

Integration of molecular quantum bits with semiconductor spintronics

Von der Fakultät Chemie der Universität Stuttgart
zur Erlangung der Würde eines Doktors der Naturwissenschaften
(Dr. rer. nat.) genehmigte Abhandlung

Vorgelegt von

Ing. Michal Kern

aus Bratislava, Slowakei

Hauptberichter:	Prof. Dr. Joris van Slageren
Mitberichter:	Prof. Dr. Peer Fischer
Prüfungsvorsitzender:	Prof. Dr. Dr. h.c. Guido Schmitz

Tag der mündlichen Prüfung: 17.12.2021

Erklärung über die Eigenständigkeit der Dissertation

Ich versichere, dass ich die vorliegende Arbeit mit dem Titel

Integration of molecular quantum bits with semiconductor spintronics

selbständig verfasst und keine anderen als die angegebenen Quellen und Hilfsmittel verwendet habe. Aus fremden Quellen entnommene Passagen und Gedanken sind als solche kenntlich gemacht.

Declaration of Authorship

I hereby certify that the dissertation entitled

Integration of molecular quantum bits with semiconductor spintronics

is entirely my own work except where otherwise indicated. Passages and ideas from other sources have been clearly indicated.

Name: Michal Kern

Unterschrift/Signed:

Datum/Date:

Acknowledgements

This thesis would not be possible without the help and support of a very large number of people and I will do my best to try and acknowledge all of them.

First of all, I want to thank my advisor and mentor Prof. Dr. Joris van Slageren. Joris, I cannot thank you enough for all the things you did for me in the last six years: giving me the opportunity to work on such a vast and challenging topic, being always there when I needed guidance and letting me work by myself when I wanted, pushing me to broaden my horizons, having endless understanding for life getting in the way, extensively correcting this thesis, freely sharing your knowledge and experience and, of course, the great music tips. Not many people have enough luck to find such mentors and I am deeply grateful for that.

I want to thank Prof. Dr. Peer Fischer for kindly agreeing to be my GRADUS mentor and to referee my thesis, and thank Prof. Dr. hc. Guido Schmitz for agreeing to chair the examination committee.

A large part of my thesis was done in close collaboration with the Institute of Semiconductor Engineering of the University Stuttgart. Thanks to Prof. Dr. Jörg Schulze who directed the efforts from their side, as well as Dr. Stefan Bechler for years of good company during long and challenging measurements. Many thanks to Hannes S. Funk and David Weißhaupt for their constant help, great discussions and uncountable number of substrates they prepared for me.

Another significant portion of the thesis was done in close collaboration with the Institute of Polymer Chemistry of the University of Stuttgart. I want to thank Prof. Dr. Sabine Ludwigs for allowing me to use their great facilities for sample preparation. Huge thanks to Dr. Yannic M. Groß for teaching me how to handle and prepare semiconducting polymer samples and to David Neußer for his help in studying some of them.

Thanks to Dr. Andreas Sperlich and Dr. Stefan Väth as well as Prof. Dr. Wolfgang Harneit and Dr. Svetlana Kucher for showing me their EDMR spectrometers and helping me understand the technique.

Many thanks to Dr. Petr Neugebauer, for his advice and for opening all the doors that he could for me. Dr. Lorenzo Tesi, thank you for helping me push my final project to the

finish line and for, together with Dr. Mauro Perfetti, making me love Italy.

Thanks to all of the undergraduate students who helped me with various parts of the project over the years: Benjamin Gerlach, Anastasia Tsianaka, Nadine Rußegger, Mario Winkler and Alexander Allgaier.

I had the good fortune to work in an amazing environment, filled with very talented people, many of which I consider friends now, not only past colleagues. The generation of PhD students, now all of them doctors, who so warmly welcomed me in the group as an undergraduate and taught me the basics of the wonderful spectroscopies I did over the years: Yvonne, María, Katharina, Maren, Phillip, Dominik Dengler. Raphael, many thanks for the great hours spent measuring HFEPR in the basement and getting me my first apartment in Germany. Thanks to my peers: Dominik Bloos, Heiko and Samuel. Our randomly chosen group chat name has proven to be too prophetic for my liking. Dominik, thank you for sharing your knowledge of electronics and LabView with me, from which I profited greatly, but mainly for your amazing friendship, company, adventures and indulgence in our shared hobbies. Heiko, thank you for being a great friend, DM and for our unforgettable bike trip. Samuel, thank you for your friendship and patient explanations of everything regarding magnetic resonance. Mario, David, thanks for the great LAN parties and D&D evenings. And of course, I have to thank everyone else in the van Slageren group, for the genuinely great and inspiring atmosphere at every time of the day or night: Philipp, Dennis, Peng, Oleksii, all the ERASMUS students and undergraduates over the years.

I want to thank my mom, dad and sister, for believing in me and making all of my studies possible.

And finally, to my fiancée Veronika: thank you for your unconditional love, for being always there for me, for your understanding and help to see this through.

Contents

List of Abbreviations	IX
Zusammenfassung	XII
Summary	XVIII
1 Introduction	1
1.1 Aim of This Work	5
1.2 Investigated Systems and Experiments	5
1.3 Organization of the Thesis	8
2 Theoretical Background	10
2.1 Magnetism and magnetometry	10
2.2 Magnetoresistance Effects	13
2.2.1 Ordinary magnetoresistance and the Hall effect	13
2.2.2 Weak (anti)localization	14
2.2.3 Electrical spin injection	16
2.3 Electron spin resonance	23
2.3.1 Basics of ESR	23
2.3.2 Pulsed ESR	26
2.3.3 Electrically detected magnetic resonance	32
2.3.4 Ferromagnetic Resonance	37
2.4 (Organic) field effect transistors	37
2.5 Low-level electrical measurements	40
3 Towards CMOS compatible spintronics	44
3.1 Introduction	44
3.2 Experimental methods	47
3.3 Formation of Mn_5Ge_3 by thermal annealing	49
3.4 Development of a low temperature magnetoresistance measurement set-up	53

3.4.1	Proof-of-principle measurements	54
3.4.2	Design, assembly and testing	58
3.4.3	AC measurements, summary and outlook	63
3.5	Spintronics in <i>p</i> -doped germanium	67
3.5.1	Three terminal spin injection measurements	67
3.5.2	Four terminal spin injection measurements	70
3.5.3	Weak antilocalization measurements	73
3.5.4	Mn ₅ Ge ₃ /Ge(100) as a platform for Ge spintronics	75
3.6	Conclusion	80
4	Electrically detected magnetic resonance of potential molecular qubit hosts	82
4.1	Introduction	82
4.2	Experimental methods	84
4.3	Development of an electrically detected magnetic resonance spectrometer	85
4.3.1	Sample holder	85
4.3.2	Microwave circuit	90
4.3.3	Magnetic field	91
4.3.4	Electrical circuit	94
4.3.5	Experimental control and data acquisition	94
4.4	EDMR on P3HT	96
4.5	EDMR on (Per) ₂ Pt _{0.75} Au _{99.25} (mnt) ₂	101
4.6	Conclusion	104
5	Molecular quantum bits in organic semiconductors	106
5.1	Introduction	106
5.2	Experimental methods	109
5.2.1	Optimization of semiconductor film preparation	112
5.3	Results and discussion	118
5.3.1	Thin film sample characterization	118
5.3.2	Drop casting as a method for increasing the number of spins	121
5.3.3	Low-temperature conductivity and mobility	123
5.3.4	Pulsed ESR spectroscopy	126
5.4	Conclusion	133
6	Appendices	134
A	Appendix to chapter 3	134
A.1	Influence of Ge doping on formation of Mn ₅ Ge ₃ layers	134

B	Appendix to chapter 5	135
B.1	Room temperature electrical characteristics for transistors based on films deposited by spin-coating	135
B.2	Room temperature electrical characteristics for transistors based on films deposited by drop-casting	138
B.3	Variable-temperature electrical characteristics for transistors based on films deposited by drop-casting	140
B.4	Spin dynamics of hybrid films of P3HT and [Cu(dbm) ₂]: [Cu(dbm) ₂] signal	141
B.5	Spin dynamics of hybrid films of P3HT and [Cu(dbm) ₂]: Charge carrier signal	145
	Bibliography	147
	Curriculum Vitae	156

List of Abbreviations

2DEG Two-Dimensional Electron Gas

3T Three Terminal

4T Four Terminal

AC Alternating Current

AFC Automatic Frequency Control

AFM Atomic Force Microscopy

BNC Bayonet Neill-Concelman

CMOS Complementary Metal-Oxide-Semiconductor

cw continuous wave

DC Direct Current

DUT Device Under Test

EDMR Electrically Detected Magnetic Resonance

ESE Electron Spin Echo

ESR Electron Spin Resonance

F₄TCNQ 2,3,5,6-tetrafluoro-tetracyanoquinodimethane

FET Field-Effect Transistor

FM ferromagnetic

FMR Ferromagnetic Resonance

FPR Fabry-Pérot Resonator

HLN Hikami-Larkin-Nagaoka

HMF Half-Metallic Ferromagnet

HRTEM High-Resolution Transmission Electron Microscopy

IHT Institute of Semiconductor Engineering, University of Stuttgart

IPC Institute of Physical Chemistry, University of Stuttgart

IRDS International Roadmap for Devices and Systems

IRDS International Roadmap for Devices and Systems

LIA Lock-In Amplifier

MBE Molecular-Beam Epitaxy

MOSFET Metal-Oxide-Semiconductor Field-Effect Transistor

MQB Molecular Qubit

MW Microwave

OFET Organic Field-Effect Transistor

OMR Ordinary Magnetoresistance

P3HT poly(3-hexylthiophene-2,5-diyl)

PCB Printed Circuit Board

PID Proportional-Integral-Derivative

PSD Phase-Sensitive Detection

PTFE Polytetrafluoroethylene

SDR Spin-dependent Recombination

SMU Source-Measure Unit

SNR Signal-to-Noise Ratio

SQUID Superconducting QUantum Interference Device

TDESR Torque Detected Electron Spin Resonance

TEM Transmission Electron Microscopy

UCLA University of California, Los Angeles

VRH Variable-Range Hopping

VTI Variable Temperature Insert

WAL Weak Antilocalization

XRD X-Ray Diffraction

Zusammenfassung

Das übergeordnete Forschungsfeld zu dem diese Arbeit beitragen möchte, ist die Entwicklung funktionaler quantenspintronischer Bauelemente basierend auf molekularen Quantenbits (Molecular Qubits (MQBs)). Das Ziel dieser Arbeit war das elektrische Auslesen von MQBs. Um dies zu verwirklichen haben wir einige Problemstellungen adressiert, darunter die effiziente Spininjektion in konventionellen Halbleitern (Kapitel 3), die Ladungsträger-Spin-Manipulation durch Mikrowellenstrahlung (Kapitel 4) und der Nachweis der Quantenkohärenz in Anwesenheit mobiler Ladungsträger (Kapitel 5). Die hierzu erforderlichen Messmethoden wurden ebenfalls entwickelt. Unter dem elektrischen Auslesen eines Quantenbits versteht man die Fähigkeit den Spin-Zustand eines MQBs durch Messung einer elektrischen Eigenschaft des Systems bestimmen zu können, beispielsweise seiner Leitfähigkeit oder einem Spannungssignal an bestimmten Anschlüssen. Damit beispielsweise eine dipolare Wechselwirkung oder sogar eine Austauschwechselwirkung zwischen den MQBs und den mobilen Ladungsträgern stattfinden kann, müssen diese nahe genug beieinander sein. Abhängig vom gewählten Material, der Art des Ladungstransports und dem Abstand der MQBs zu den mobilen Ladungsträgern, kann sich die gegenseitige Beeinflussung in einer Vielzahl physikalischer Phänomene äußern, wie dem Kondo-Effekt in Metallen bis hin zur spinabhängigen Rekombination von Ladungsträgern in Halbleitern. Wir haben drei vielversprechende Ansätze gewählt, um MQBs in die Nähe von mobilen Ladungsträgern zu bringen und ihre Wechselwirkung zu untersuchen: die Abscheidung von MQBs auf anorganischen Halbleitern mit spinpolarisierten Ladungsträgern, die Suche nach einem Material, das sowohl ein MQB, als auch die mobilen Ladungsträger in seiner Kristallstruktur bereithält, oder ein Hybridmaterial aus einem organische Halbleiter und MQBs.

Im ersten Teil dieser Arbeit wurde die Möglichkeit einer komplementären Metal-Oxid-Halbleiter (engl. Complementary Metal-Oxide-Semiconductor (CMOS))-kompatiblen Spintronik-Plattform für molekulare Quantenbits untersucht. Die Vision ist eine Schicht aus MQBs auf einem Halbleiterkanal, in dem spinpolarisierte Ladungsträger injiziert werden. Die magnetischen Momente der Ladungsträger könnten dann mit den MQBs wechselwirken, was ihre Spinpolarisierung beeinflussen würde. Die Änderung der Spinpolarisierung

der Ladungsträger könnte dann anhand magnetoresistiver Effekte, wie einer Spinventilmessung, abgelesen werden. Um dieses Ziel zu erreichen wurde in Zusammenarbeit mit dem Institut für Halbleitertechnik der Universität Stuttgart sowohl die Halbleiterplattform als auch der nötige Versuchsaufbau entwickelt. Als Material hierfür wurde Germanium gewählt, da auf diese Weise CMOS-Kompatibilität gewährleistet werden konnte und dieses über eine ausreichend große Spin-Diffusionslänge (auch Spin-Flip-Länge genannt) verfügt. Germanium kann auf Si-Wafern sowohl mit (111)- als auch (100)-Orientierung nach Industriestandard gezüchtet werden und ist bereits in vielen CMOS-Prozessen integriert. Ein weiterer wesentlicher Vorteil von Germanium ist die Existenz der ferromagnetischen Mn_5Ge_3 -Legierung, deren Curie-Temperatur von 296 K sehr nahe an der Umgebungstemperatur liegt, welche durch C-Dotierung sogar auf bis zu 450 K erhöht werden kann und, was noch wichtiger ist, seine Leitfähigkeit liegt nahe der von dotiertem Germanium, was eine Notwendigkeit für dessen Nutzung als Tunnelbarriere zur Spininjektion ist. Solche ferromagnetische Legierung mit anderen führenden Halbleitern wie Silizium ist bisher nicht bekannt.

Wir entschieden, einen einfachen Weg zur Herstellung von Mn_5Ge_3 zu untersuchen, welcher sich die Nutzung der thermischen Verdampfung von Mn auf eine kristalline Ge-Oberfläche zunutze macht, gefolgt von einem *ex-situ*-Tempern. Wir konnten durch eine Kombination aus Magnetometrie mit variabler Temperatur und Transmissionselektronenmikroskopie zeigen, dass die Bildung von Mn_5Ge_3 durch *ex-situ*-Tempern ein einfaches, schnelles und robustes Verfahren zur Herstellung dünner ferromagnetischer Filme mit einer atomar scharfen Grenzfläche zu Ge darstellt. Wir haben darüber hinaus auch untersucht, ob dieser Prozess beeinflusst wird durch die Art oder die Konzentration der Dotierstoffe in Ge, wobei die gewonnenen Ergebnisse darauf hindeuten, dass die Dotierstoffe keinen bzw. nur einen zu vernachlässigenden Einfluss haben. Die relativ niedrigen Temperaturen und die kurze Expositionszeit, in welcher das System den Temperaturen ausgesetzt ist in Kombination mit der Möglichkeit Mn *ex-situ* zu verarbeiten, machen diesen Prozess potenziell geeignet für die Implementierung in der CMOS-Technologie. Angesichts all dieser Vorteile haben wir dieses Verfahren verwendet, um die Proben, die für Spin-Injektionsexperimente verwendet wurden, herzustellen. Um die Spin-Injektionsexperimente durchzuführen musste außerdem ein geeignetes Messsystem entwickelt werden, das rauscharme elektrische Messungen bei kryogenen Temperaturen und hohen Magnetfelder erlauben sollte. Hierfür konnte ein am Institut für Physikalische Chemie der Universität Stuttgart vorhandener Oxford Instruments Spectromag-Magnet mit einem kundenspezifischen Tieftemperatur-Sondenkopf genutzt werden um eine geeignete Verkabelung, Messelektronik und Messsoftware zu entwickeln. Durch eine geeignete Erdung und Schirmung war es möglich ausreichend niedrige Rauschpegel zu erreichen, um alle temperaturabhängigen elektrischen Messungen

dieser Arbeit durchzuführen. Sowohl Drei- als auch Vierpunkt-Hanle-Messungen wurden durchgeführt, um die Spininjektion aus einem Mn_5Ge_3 -Ferromagneten in einen p -dotierten Ge-Kanal zu bestimmen. Beim Ausführen von Dreipunkt (Three Terminal (3T))-Hanle-Messungen haben wir ein anomales Verhalten des Systems beobachtet, das nicht mit reiner Spininjektion erklärt werden kann. Dieses Ergebnis war höchstwahrscheinlich ein Resultat der Kombination aus einer relativ großen Fläche der Messkontakte mit einer magnetischen Streifendomänenstruktur der ferromagnetischen Schicht außerhalb der Ebene. Daher wurde eine Vierpunkt (Four Terminal (4T))-Hanle-Messung basierend auf mehrstufiger Elektronenstrahlitographie entwickelt. Der Herstellungsprozess ergab jedoch nur eine sehr geringe Ausbeute an funktionierenden Systemen und selbst wenn die Herstellung des Systems erfolgreich war, enthielt die Metallisierung aufgrund der Bauteilgeometrie einen Flächenhals, der dazu führte, dass die Systeme sehr empfindlich auf angelegten Strom reagierten und im Allgemeinen unzuverlässig waren. Trotzdem ist es gelungen, an einem funktionsfähigen System 4T-Hanle-Messungen durchzuführen. Hier wurde ein Signal beobachtet, das zwar gut mit dem Hanle-Effekt erklärbar war, jedoch war es unempfindlich auf die Richtung des angelegten Magnetfelds. Auch bei einer Drehung um 90° zeigte die Messung immer noch das gleiche Signal, ohne einen Hinweis auf einen Spin-Ventil-Effekt. Dieses Verhalten wird in der Literatur bisher nicht berichtet und ist bisher nicht verstanden, jedoch hängt auch dies sehr wahrscheinlich mit der komplexen magnetischen Domänenstruktur unserer Mn_5Ge_3 -Schichten zusammen. Die Messungen wurden mit einem eindimensionalen Spindrift-Diffusionsmodell ausgewertet, unter der Annahme, dass die beobachteten Signale tatsächlich mit Spininjektion zusammenhängen. Die Größe und das Temperaturverhalten der Spinlebensdauern und Spindiffusionslängen stimmen mit der veröffentlichten Literatur über p -Ge überein. Um die erhaltenen Werte weiter untermauern zu können, wurden Messungen des Tieftemperatur-Magnetowiderstandes des p -Ge(111)-Substrates durchgeführt und die beobachtete schwache Antilokalisierung mit dem Hikami-Larkin-Nagaoka-Modell ausgewertet. Es zeigte sich eine gute Übereinstimmung der Daten mit dem Modell und es konnten die Phasenkohärenz und die Spin-Bahn-Längen abgeleitet werden. Die extrahierten Werte sind konsistent mit den Literaturwerten und, obwohl sie ungefähr eine Größenordnung niedriger sind als die aus den 4T-Messungen extrahierten Werten, können sie angesichts der Streuung in den 4T-Daten als genauer als letztere eingestuft werden. Dies unterstützt die Hypothese, dass in der nicht-lokalen Messung tatsächlich ein Hanle-Signal beobachtet worden ist. Das Fehlen eines Spin-Ventil-Signals macht das System jedoch ungeeignet für das Hauptziel des elektrischen Auslesens von molekularen Spinzuständen. Um diese Schwierigkeit umzugehen, wurden Messungen des Magnetwiderstandes an einem p -Ge(100)-Wafer, sowie Magnetometrie und Ferromagnetische-Resonanz-Messungen (FMR) an einem auf diesem Wafer hergestellten Mn_5Ge_3 -Schicht durchgeführt. Wir haben

beobachtet, dass der p -Ge(100)-Wafer zwar aufgrund der längeren Spinphasenkohärenz und der längeren Diffusionslängen (etwa das Doppelte von Ge(111)) für Spintronikanwendungen besser geeignet ist, jedoch die FMR-Messungen darauf hindeuten, dass die bevorzugte Magnetisierungsrichtung der Mn_5Ge_3 -Schicht zwischen 45° und 90° liegt in Bezug auf die Probenoberfläche. Dies bedeutet, dass auch $\text{Mn}_5\text{Ge}_3/\text{Ge}(100)$ -Schichten für unsere Anwendungen ungeeignet sind. Um diese Hürden zu überwinden gibt es mehrere Möglichkeiten, die in zukünftigen Arbeiten untersucht werden könnten. Zunächst müssen die Geometrie und der Herstellungsprozess der 4T-Hanle-Messstrukturen überarbeitet werden. Der Ladungs- und Spintransport findet in einem hochdotierten Ge-Kanal statt, der in Form einer Mesastruktur auf der Oberseite des Substrats gebildet wird. Diese Erhöhung des Kanals verursacht Stromengpässe an den Rändern der Mesa, an welchen die elektrischen Kontakte mit dem Kanal verbunden sind. Die Mesastruktur muss daher in das Substrat abgesenkt werden, um Stufen in den elektrischen Zuführungen zu vermeiden. Diese Modifikation sollte einen Herstellungsprozess mit höherer Ausbeute und zuverlässigeren Messstrukturen gewährleisten. Weiterhin wäre interessant zu untersuchen, ob es möglich ist, Mn_5Ge_3 auf Ge(111) für die Spintronik zu verwenden, indem verschiedene Glühparameter und Mn-Dicken untersucht werden, um herauszufinden, ob es möglich ist, Mn_5Ge_3 -Schichten dünner als 10 nm zu bilden. Es wurde gezeigt, dass solch dünne Schichten eine einzelne Domäne bilden, wobei ihre gesamte Magnetisierung in der Ebene liegt, was zu funktionsfähigen Spinventilen führen könnte. Schlussendlich wäre die Umstellung auf des Substrates auf Ge(100) aus der Anwendungssicht interessant, da diese Waferorientierung in der Industrie häufiger verwendet wird und die Spindynamik in dieser Orientierung günstiger zu sein scheint. Mn_5Ge_3 auf Ge(100) ist ein relativ neues Forschungsgebiet mit dem Potenzial, vollständig in der Ebene magnetisiertes Mn_5Ge_3 zu erzeugen.

Im zweiten Teil dieser Arbeit wurde ein Spektrometer für elektrisch detektierte Magnetresonanz (Electrically Detected Magnetic Resonance (EDMR)) basierend auf dem Bruker EMX X-Band Elektronenspinresonanz(Electron Spin Resonance (ESR))-Spektrometer am Institut für Physikalische Chemie der Universität Stuttgart entworfen, konstruiert und getestet. Wir haben das bestehende Spektrometer um eine zusätzliche Mikrowellenquelle, eine elektrische Ausleseschaltung, eine Möglichkeit zur Kontrolle der Probenhalteratmosphäre und der Probenbestrahlung, und eine selbstgeschriebene Messsoftware erweitert, um erfolgreich EDMR durchzuführen. Darüber hinaus haben wir zwei verschiedene EDMR-Substrate entwickelt, hergestellt und getestet, wobei das eine sowohl für dünne Filme als auch für Einkristalle geeignet ist und ein weiteres speziell auf dünne Filme zugeschnitten worden ist. Mit diesem neuen Versuchsaufbau wurde Poly-3-Hexylthiophen-2,5-diyl (P3HT) gemessen, das entweder durch das Aussetzen gegenüber den Umgebungsbedingungen oder

durch 2,3,5,6-Tetrafluoro-Tetracyanoquinodimethan (F_4TCNQ) unter inerten Bedingungen dotiert wurde. In beiden Fällen haben wir den Einfluss verschiedener experimenteller Parameter auf das Signal getestet und eine Kombination identifiziert, die reproduzierbar ein messbares EDMR-Signal liefert. Besonders bewährt hat sich F_4TCNQ -dotiertes P3HT, welches vergleichsweise starke Signalen bereits bei Raumtemperatur liefert. Darüber hinaus haben wir erste EDMR-Messungen an Proben der $(Per)_2M(mnt)_2$ ($M = Pt, Au, mnt^{2-}$ = Maleonitridithiolat)-Verbindungsfamilie durchgeführt und eine deutliche EDMR-Signatur beobachtet, sowohl bei Raumtemperatur als auch ein noch stärkeres Signal bei 200 K. Gepulste ESR-Messungen haben gezeigt, dass diese speziellen Verbindungen keine Quantenkohärenz aufweisen, jedoch könnte eine andere Verbindung aus derselben Familie mit einem leichterem Metall als paramagnetischem Zentrum, wie Ni, eine nennenswerte Quantenkohärenz aufweisen. Diese ersten Schritte in die EDMR ebnen den Weg für viele hochinteressante Untersuchungen. Zum Beispiel wäre eine intensivere Untersuchung des mit F_4TCNQ dotierten P3HT-Systems interessant. Zuerst um sein Verhalten bei niedrigen Temperaturen zu untersuchen und die physikalischen Prozesse zu verstehen, die das EDMR-Signal verursachen, und weiterhin auch in Kombination mit einem in das Gitter eingebetteten molekularen Quantenbits. Eine weitere spannende Perspektive ist die weitere Erforschung der $(Per)_2M(mnt)_2$ -Verbindungsfamilie mittels EDMR, da diese Untersuchungen völlig neu sind und das Potenzial haben, die Wechselwirkungen zwischen lokalisierten magnetischen Momenten und wandernden Ladungsträgern in einer optimalen Geometrie direkt abzubilden.

Im dritten und letzten Kapitel haben wir die Auswirkungen einer Mischung eines polymeren Halbleiters P3HT mit einem molekularen Quantenbit $Cu(dbm)_2$ ($Hdbm$ = dibenzoylmethan) auf die jeweiligen Materialeigenschaften untersucht, sowohl mit als auch ohne bewegliche Ladungsträger, welche durch chemische Dotierung von P3HT durch F_4TCNQ induziert werden. Wir haben durch Feldeffekttransistor-Messungen bei Raumtemperatur festgestellt, dass $Cu(dbm)_2$ die elektrischen Eigenschaften von P3HT nur minimal beeinflusst. In einem Temperaturbereich zwischen 7 K und 70 K haben wir die Leitfähigkeit des gemischten Materials sowohl mit als auch ohne Dotierung untersucht und beobachtet, dass im undotierten Material die Ladungsträger festgehalten werden und sich bis 40 K nur durch Tunneln bewegen, danach treten sie in ein Bereich mit variabler Sprungreichweite ein. Im dotierten Material treten sie jedoch schon oberhalb von 10 K in diesen Bereich ein, wahrscheinlich weil die meisten Zustände, in welchen die Ladungsträger festgehalten werden können, bereits durch die durch chemische Dotierung eingebrachten Ladungsträger gefüllt sind. Außerdem haben wir die Auswirkungen des Mischens der beiden Materialien auf $Cu(dbm)_2$, wiederum sowohl mit als auch ohne Dotierung, mit gepulster ESR im Q-Band untersucht. Wir haben beobachtet, dass die Misch-, Dotierungs- und

Präparationsmethoden wenig bis gar keinen Einfluss auf den statischen Spin-Hamiltonian von $\text{Cu}(\text{dbm})_2$ haben, welcher zwischen den verschiedenen Hybridproben und einem Pulver von $\text{Cu}(\text{dbm})_2$ in $\text{Pd}(\text{dbm})_2$ vergleichbar war. Außerdem ist nach der Dotierung ein Zweikomponentensignal entsprechend dem Signal der Ladungsträger und dem F_4TCNQ -Radikal aufgetreten. Durch die Untersuchung der Spindynamik der Hybridmaterialien haben wir beobachtet, dass die Quantenkohärenz nicht nur das Mischen, sondern auch die Anwesenheit beweglicher Ladungsträger überlebt, da wir diese bei Temperaturen bis 30 K beobachten konnten, bei welchen sich die Ladungsträger im Bereich einer variablen Sprungreichweite befinden. Es gibt einen großen Spielraum, die Eigenschaften des Materials weiter zu verbessern, beispielsweise dadurch die elektrischen Eigenschaften durch Nachbearbeitung zu verbessern und die Kohärenzeigenschaften durch Deuterierung zu verbessern. Die notwendigen nächsten Schritte umfassen die Anpassung und die Optimierung des Materials, die Suche nach Signaturen einer Qubit-Ladungsträger-Wechselwirkung in Transportmessungen und eine geeignete Modellierung, um den Wechselwirkungsmechanismus zwischen dem Qubit und den Ladungsträgern zu verstehen.

Die Ergebnisse dieser Arbeit stellen eine einzigartige Untersuchung verschiedener Wege dar molekulare Quantenbits mit organischer und anorganischer Spintronik zu integrieren. Die Integration mit anorganischer Spintronik hat sich durch das Bestreben eine CMOS-kompatible Spintronikplattform zu nutzen als kompliziert erwiesen, dies könnte jedoch bei Verwendung etablierterer Materialkombinationen einfacher gelingen. Eine elektrisch nachgewiesene magnetische Resonanz wurde sowohl an einem Qubit-kompatiblen Polymerhalbleiter als auch an einem molekularen Kristall nachgewiesen, die beide das Potenzial haben, das Ziel des elektrischen Auslesens des Qubit-Zustands zu erreichen. Schließlich konnte erstmals gezeigt werden, dass die Quantenkohärenz eines molekularen Qubits in Gegenwart beweglicher Ladungsträger in einem dotierten organischen Halbleiter erhalten bleibt. Diese neuen Erkenntnisse ebnen den Weg, MQBs mittels elektrischer Ströme zu adressieren und damit Hybridpolymer/MQB-Materialien als neuartige Plattform für die Quantenspintronik zu nutzen.

Summary

The overarching goal of this research is to develop functional quantum spintronic devices based on Molecular Qubits (MQBs). The aim of this thesis was to achieve electrical readout of MQBs. To this end, we have addressed several objectives, including efficient spin injection in conventional semiconductors (Chapter 3), charge carrier spin manipulation by microwave radiation (Chapter 4) and demonstration of quantum coherence in the presence of mobile charge carriers (Chapter 5). The measurement capabilities required to investigate these architectures were developed as well. Electrical readout of a quantum bit means the ability to infer the spin state of a MQB by measuring an electrical property of a device - its conductivity or voltage signal on some terminals. For such an effect to manifest, the MQB and a mobile charge carrier need to be close enough to each other for a dipolar or even exchange interaction to be operative. Depending on the exact materials, type of charge transport, and distance, the mutual interaction can take many forms, resulting in a wide variety of possible phenomena, from the Kondo effect in metals to spin-dependent recombination of charge carriers in semiconductors. We have identified three possible approaches to bring MQBs into the vicinity of mobile charge carriers and study their interaction: depositing MQBs on top of inorganic semiconductor channels with spin polarized charge carriers, finding a material containing both MQBs and conductive paths in its crystal structure or creating a hybrid material composed of an organic semiconductor and MQBs.

In the first part of our studies, we explored the possibility to develop a CMOS compatible spintronic platform for molecular quantum bits. The vision is to have a layer of MQBs on top of a semiconductor channel, into which spin-polarized charge carriers would be injected. The magnetic moments of the charge carriers could then interact with the MQBs, which would influence their spin polarization. The change in spin polarization of the charge carriers could then be read out using magnetoresistive effects, such as a spin valve measurement. To achieve that goal, however, both the semiconductor platform as well as the experimental set-up had to be developed, which was done in close collaboration with the Institute of Semiconductor Technology at the University of Stuttgart. Germanium was chosen as the material for spin transport to ensure CMOS

compatibility and sufficient spin-diffusion length (also called spin-flip length). Germanium can be grown on industry standard Si wafers, with both (111) and (100) orientation and is already integrated in many CMOS processes. Another significant advantage is the existence of the ferromagnetic Mn_5Ge_3 alloy, since its Curie temperature is very close to ambient temperatures (296 K, can be extended up to 450 K by C doping) and more importantly, its conductivity is close to that of doped Ge, removing the necessity of using a tunneling barrier for spin injection. Such a ferromagnetic alloy with other leading semiconductors, such as silicon, is not known. We decided to investigate a facile way of Mn_5Ge_3 fabrication utilizing simple thermal evaporation of Mn onto a crystalline Ge surface, followed by an *ex-situ* annealing step. We demonstrated, through a combination of variable temperature magnetometry and transmission electron microscopy, that the formation of Mn_5Ge_3 through *ex-situ* annealing is a simple, fast, and robust process leading to the fabrication of thin ferromagnetic films with an atomically sharp interface to Ge. We have also investigated if this process is influenced by the type or concentration of dopants in Ge, with results suggesting no or negligible influence. The relatively low temperatures and short exposure to them, along with the *ex-situ* processing of Mn, make this process potentially suitable for implementation into CMOS technology. Given all of these benefits, we have used this process to fabricate the samples used for spin injection experiments. To perform the spin injection experiments, a suitable measurement system which allows for low noise electrical measurements at low temperatures and high magnetic fields had to be developed. Taking advantage of the Oxford Instruments Spectromag magnet available at the Institute of Physical Chemistry, a custom low-temperature probe head, together with suitable cabling, measurement electronics and software was developed. By employing proper shielding and grounding strategies, it was possible to reach sufficiently low noise levels to perform all variable temperature electrical measurements performed in this thesis. Both three and four terminal Hanle measurements were performed to study spin injection from a Mn_5Ge_3 ferromagnetic layer into a *p*-doped Ge channel. When performing 3T Hanle measurements, we have observed anomalous behavior not consistent with spin injection. This was most probably caused by the relatively large size of the contacts in combination with an out-of-plane stripe domain magnetic structure of the ferromagnetic layer. A fabrication process for 4T structures based on multiple-step electron beam lithography was therefore developed. The fabrication process, however, proved to have a very low yield of functioning devices. Even if the device's fabrication was successful, the metallization contained a bottleneck point due to the device geometry, which made the devices very sensitive to applied current and generally unreliable. Nevertheless, it was possible to obtain a functioning device and study it using 4T Hanle measurements. We have observed a signal mostly consistent with the Hanle effect, it was however insensitive to the direction of the

applied magnetic field. Even upon rotation by 90° , the measurements still demonstrated the same features, without any hint of a spin-valve effect. This behavior is hitherto unreported in literature and so far not understood. However, it is most probably related to the complex magnetic domain structure of our Mn_5Ge_3 layers. The measurements were evaluated using a one-dimensional spin drift diffusion model, under the assumption that the observed signals are indeed related to spin injection. The obtained values and behavior in temperature for spin lifetimes and spin diffusion lengths are consistent with published literature on p -Ge. To obtain further support of the obtained values, we have performed low-temperature magnetoresistance on the p -Ge(111) substrate and fitted the observed weak antilocalization with the Hikami-Larkin-Nagaoka model. We have obtained accurate fits to the data and extracted spin phase coherence and spin-orbit lengths. The extracted values are consistent with the literature, and while they are approximately one order of magnitude lower than those extracted from 4T measurements, given the scatter in the 4T data, they can be considered consistent. This supports the hypothesis that we have indeed observed a Hanle signal in the non-local measurement. The lack of a spin-valve signal, however, renders the device unsuitable for our main goal electrical read-out of molecular spin states. As a possible way forward, we performed magnetoresistance measurements on a p -Ge(100) wafer, as well as magnetometry and Ferromagnetic Resonance (FMR) measurements on a Mn_5Ge_3 fabricated on a Ge(100). We have observed that while the p -Ge(100) wafer is indeed more suitable for spintronic applications due to longer spin phase coherence and diffusion lengths (approximately double those in Ge(111)), the FMR measurements suggest that the preferred magnetization direction of the Mn_5Ge_3 layer is between 45° and 90° from the sample plane. This would mean that the obtained $\text{Mn}_5\text{Ge}_3/\text{Ge}(100)$ layers are unsuitable for our applications as well. As an outlook in this direction of research, there are multiple ways forward. First, the geometry and fabrication process of the 4T structures needs to be reworked. The charge and spin path is defined through a highly doped Ge channel formed into a mesa structure on top of the substrate. This elevation of the channel causes current bottlenecks at the edges of the mesa, where current leads are connecting to the channel. This mesa structure needs to be lowered into the substrate in order to avoid any steps in the current leads. This modification should assure a manufacturing process with higher yield and more reliable devices. To investigate if it is possible to use Mn_5Ge_3 on Ge(111) for spintronics, it would be interesting to explore various annealing parameters and Mn thicknesses further, to find out if it is possible to form layers thinner than 10 nm. Such thin layers were shown to be single domain, with all of their magnetization in-plane, which could lead to functional spin-valves. Lastly, moving to Ge(100) as a substrate would be interesting from an application point of view, since the wafer orientation is more commonly used in the industry and the spin dynamics in

this orientation seem to be more favorable. Mn_5Ge_3 on top Ge(100) is a relatively new area of research, with the potential to create fully in-plane magnetized Mn_5Ge_3 .

In the second part of this thesis, we designed, constructed and tested an electrically detected magnetic resonance spectrometer based on the Bruker EMX X-Band spectrometer at the Institute of Physical Chemistry, University of Stuttgart. We have extended the existing ESR spectrometer with additional Microwave (MW) source, electric read-out circuitry, sample holder atmosphere control, sample irradiation and custom software to successfully perform EDMR measurements. At the same time, we have designed, manufactured and tested two different EDMR substrates, one suitable for both thin films and single crystals and one more tailored to thin films specifically. With this new experimental setup, we have measured poly(3-hexylthiophene-2,5-diyl) (P3HT) doped either by exposure to ambient conditions or by 2,3,5,6-tetrafluoro-tetracyanoquinodimethane (F_4TCNQ) under inert conditions. In both cases, we have tested the influence of various experimental parameters on the signal and identified a combination which reproducibly provides a measurable EDMR signal. F_4TCNQ doped P3HT proved especially useful, with comparatively large signals already at room temperature. Additionally, we have performed first EDMR measurements on samples from the $(\text{Per})_2\text{M}(\text{mnt})_2$ ($\text{M}=\text{Pt}, \text{Au}$, mnt^{2-} =maleonitriledithiolate) family of compounds and observed a clear EDMR signature, both at room temperature and an even stronger signal at 200 K. Pulsed ESR measurements have revealed that this particular compound doesn't display any quantum coherence. However, another compound from the same family with lighter metal as the paramagnetic species, such as Ni, could be potentially tested. These first steps into EDMR spectroscopy pave the way for many highly interesting investigations. One would be a deeper study of the F_4TCNQ doped P3HT system. First by itself, to investigate its low-temperature behavior and understand the physical processes causing the EDMR signal, and later in combination with a molecular quantum bit embedded in the lattice. Another exciting prospect is further study of the $(\text{Per})_2\text{M}(\text{mnt})_2$ family of compounds via EDMR, as these investigations are completely novel and hold the potential to observe the interaction between localized magnetic moments and itinerant charge carriers directly, in an ideal geometry.

In the third and last chapter, we investigated the consequences of mixing a polymeric semiconductor P3HT with a molecular quantum bit $\text{Cu}(\text{dbm})_2$ (Hdbm =dibenzoylmethane), both with and without itinerant charge carriers induced by chemical doping of P3HT. We have established, through room temperature field-effect transistor measurements, that $\text{Cu}(\text{dbm})_2$ only minimally affects the electronic performance of P3HT. We have studied the conductivity of the mixed material, both with and without chemical doping of P3HT through F_4TCNQ , in the temperature range between 7 K and 70 K and observed that in the undoped material, the charge carriers are trapped and move only via tunneling up

to 40 K, after which they enter a variable range hopping regime. In the doped material, however, they enter the hopping regime already above 10 K, probably because most of the trap states are already filled by the charge carriers introduced via chemical doping. Finally, we have studied the effects of mixing the two materials, both with and without doping, on $\text{Cu}(\text{dbm})_2$ with pulsed ESR at Q-Band. We have observed that the mixing, doping and preparation methods have little to no effect on the static spin Hamiltonian of $\text{Cu}(\text{dbm})_2$, which was comparable between both various hybrid samples and a powder of $\text{Cu}(\text{dbm})_2$ in $\text{Pd}(\text{dbm})_2$. Additionally, after doping, a two-component signal corresponding to the charge carriers and F_4TCNQ radical has appeared. By studying the spin dynamics of the hybrid materials, we have observed that quantum coherence survives not only the mixing, but the presence of mobile charge carriers as well, since we could observe it at temperatures where variable range hopping of the charge carriers was active (up to 30 K). There is ample scope to further improve the properties of the material, such as to improve the electrical properties by post-processing, and to improve the coherence properties by deuteration. Next steps will include tailoring and optimization of the material, the search for signatures of qubit-charge carrier interaction in transport measurements, and appropriate modeling to understand the interaction mechanism between the qubit and the charge carriers.

The results of this thesis constitute a unique exploration of different pathways to integrate molecular quantum bits with both organic and inorganic spintronics. The integration with inorganic spintronics has proven to be hindered by the development of a CMOS compatible spintronic platform, this could be, however, solved by using more established material combinations. We demonstrated electrically detected magnetic resonance on both a qubit-compatible polymeric semiconductor and a molecular crystal, both which hold real potential of achieving the goal of electrical readout of the qubit state. Finally, we could show, for the first time, that quantum coherence of a molecular qubit survives in the presence of mobile charge carriers in a doped organic semiconductor. This novel results pave the way to addressing MQBs by means of electric currents and thus to using hybrid polymer/MQB materials as a novel platform for quantum spintronics.

1 Introduction

Observing the ubiquity and computing power of today’s computers, it is easy to forget that the underlying mathematical and design principles were developed in the 30’s and 40’s of the previous century. Almost ten years after Alan Turing described a hypothetical ‘universal computing machine’ in his seminal paper in 1936 [1], John von Neumann wrote the formally unpublished *First Draft of a Report on the EDVAC* in 1945, which laid the foundational architecture on which digital computers are built [2]. The realization of a transistor by Bardeen, Brattain and Shockley in 1947 [3] and the Metal-Oxide-Semiconductor Field-Effect Transistor (MOSFET) in 1960 by Attala and Kahng [4] ushered in the era of modern digital computers and integrated circuits. Noting the wide range of possible applications of digital technologies, as well as rapid technological progress, in 1965 Moore predicted that the number of components per integrated circuit will double each year [5]. Ten years later, he modified this projection to doubling of components every two years [6]. This observation and projection is the well-known Moore’s law, which has been at the center of semiconductor industry planning ever since. As can be seen in Figure 1.1, the industry has kept up with the law well.

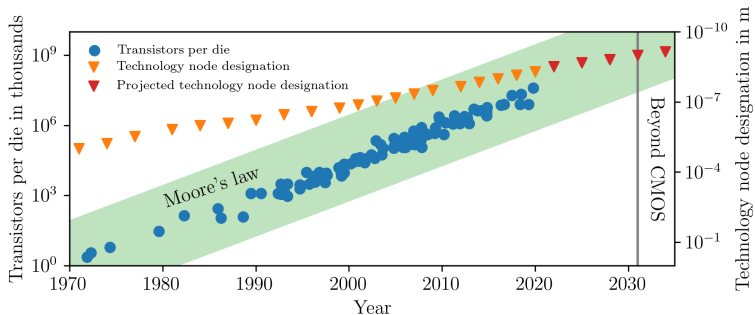


Figure 1.1: Evolution of computer technology. The green area represents Moore’s law. After the year 2031, marked with a gray line, the onset of *Beyond CMOS* technologies is projected. Transistor data from [7], technology node data from [8] and [9].

In the same figure, however, we can see that the end Moore’s law is only five to ten years away, as the size of technology node¹ reaches the fundamental physical limits of CMOS technology. The International Roadmap for Devices and Systems (IRDS) predicts the commercial onset of so-called *Beyond CMOS* technologies around the year 2031 [9]. *Beyond CMOS* in this case encompasses a wide variety of possibilities on how to extend or replace functionality of current transistors and memory devices. One of the most important *Beyond CMOS* technologies is quantum computing.

Quantum computing represents a completely different paradigm of computation. The main difference is that while Turing machines are implicitly classical, relying on deterministic processes and language of classical physics to process information, quantum computers take advantage of the processes and concepts that are dominating on the atomic scale, such as state superposition, coherence, and entanglement. Already in 1985, Deutsch showed that a “universal quantum computer” would have many remarkable properties that Turing’s “universal computing machine” could not reproduce, such as generation of true random numbers, perfect simulation of arbitrary finite physical systems, parallel computation on a serial computer and exploitation of quantum correlations [11]. Even though Deutsch has shown that a quantum computer *can* perform these tasks, he did not specify *how* would these operations be implemented. Since then, the area of quantum information processing has grown tremendously and we have a much better understanding of which problems are suited for quantum computers and even how exactly to perform them. The most famous examples are the algorithms of Shor and Grover; the former performs prime number factorization exponentially faster than classical computers [12], the latter locates entries in a database quadratically faster than its classical counterparts [13]. There are, however, many more and the exploration of which problems to solve on quantum computers and how is a very active research area still.

The physical realization of a quantum computer is a separate, and very broad, research domain. As the bit is the basic unit on which a classical computer operates, so is the quantum bit (qubit) the basic unit of a quantum computer. In general, any quantum two-level system can be considered a qubit. To evaluate the suitability of a system to be used as a qubit, we can consider some practical requirements, summarized by DiVincenzo [14]:

1. The qubit system must be scalable and well characterized.
2. It must be possible to initialize the system into a simple state at will, with a speed comparable with the times necessary to perform operations on the qubits (quantum gate times).

¹The technology node used to refer to the transistor gate length, it was changed to *approximately* the pitch of gate metalization at the 700 nm node[10]. However, since approximately the 22 nm node, there is no consensus among different manufacturers about the relation between node’s size and a specific physical dimension. As such, “technology node” is nowadays mostly just a marketing term.

3. The lifetime of the superposition state (also called decoherence time or phase-memory time T_M) must be $10^4 - 10^5$ times longer than gate time.
4. There has to exist a 'universal' set of quantum gates, i.e., it has to be possible to control the interactions between individual qubits.
5. There has to be the ability to manipulate and read out specific qubits.

It is not at all trivial to fulfill all of these requirements at the same time, as some of them are placing directly opposite constraints on the system: on one hand, the system has to be sufficiently isolated from the environment and other qubits in order to maximize its T_M ; on the other hand, the qubits need to communicate with each other for certain operations and, at the end of the calculation, we need to be able to read out the final state of the system. Finding the physical system that strikes the right balance between these requirements is an ongoing worldwide effort. Some of the most prominent physical realizations of qubits are superconducting circuits with Josephson junctions, trapped neutral or charged atoms, photons, and various qubits based on the electron spin: quantum dots, semiconductor defects, and the system studied in this work, MQBs. [15]

MQB denotes any paramagnetic molecular species, either a coordination compound or a purely organic radical. Compared to their inorganic counterparts, MQBs have a number of advantages, which all have to do with the ability to precisely tune properties of the molecule with the power of chemical synthesis. Molecules can be synthesized in a way that leads to formation of precise frameworks of metal coordination compounds, with the distance between individual metal centers (i.e., qubits) tunable with atomic precision by choosing a desired number of linker molecules (fulfilling requirement 1) [16]. Over years of careful research, factors influencing decoherence in molecules were identified, providing design guidelines to push T_M times in molecules to lengths of tens [17], even hundreds of microseconds [18] at low temperatures (fulfilling requirement 3), and still displaying coherence even at room temperature. Interactions between qubits can be tailored either statically, by tuning the distance and type of linker between individual metal centers, or even dynamically by employing, for example, photoactive linkers, which can be used to control the interaction between two qubits by light [19] (requirement 4). Until recently, all MQBs relied on relatively slow initialization procedure via thermal polarization processes, hampering fulfillment of requirement 2. By taking inspiration from the electronic structure of semiconductor defects, such as the nitrogen vacancy center in diamond, Bayliss et al. have demonstrated optical initialization and coherent spin manipulation in a series of chromium(IV) compounds [20].

The last requirement, manipulation and read out of individual qubits, is one of the biggest challenges for realization of quantum computer using MQBs. Most of the studies performed on MQBs use ESR spectrometers to perform these tasks on bulk samples.

While this work is necessary to characterize the molecules and find the best candidates to serve as qubits, there are significantly fewer studies dealing with the topic of integration of these molecules into functional devices and the effect this integration has on the properties of these molecules. More importantly, standard ESR detection through absorption of MW photons, also known as inductive detection, is fundamentally unsuitable to read out single molecules, mainly due to the limited amount of energy in a single microwave photon. In state-of-the-art, quantum-mechanics-limited inductive ESR spectrometers, the achieved sensitivity is $12 \text{ spins}/\sqrt{\text{Hz}}$ [21]. Even though there is still room for improvement in this direction, for example by "squeezing" the microwave fields [22], these measurements are still far from practical single spin sensitivity. An alternative approach is to find a material system where the electron spin transition is governing another process with larger energy, such as a charge or optical transition. These alternative detection methods of electron spin transitions have already achieved single spin sensitivity for a variety of qubit systems. Most notable for MQBs is the implementation of the Grover algorithm using a single TbPc_2 molecule [23]. The approach of Wernsdorfer and collaborators relies on a few unique properties of the TbPc_2 molecule [24][25]. After immobilizing the molecule in a nanoscopic break junction, the system can be considered a single molecule transistor. The specific structure and magnetic properties of TbPc_2 then allow for control of the qubit state using electrical fields and at the same time, electrons can hop on to the Pc ligands of the molecule, interact with the magnetic Tb ion, and hop on to the next electrode. Conductivity of this hopping transport is dependent on the spin state of the Tb ion. This experiment is therefore a demonstration of a MQB system with completely electrical control and read out. While this work is a phenomenal achievement, there are two main downsides to this approach. One, for the system to work it has to be cooled down to a temperature of 50 mK, and two, there is no clear pathway how to scale up the number of individually addressable, interacting qubits beyond a few units. Optical methods are widely used for control and readout of inorganic semiconductor defects, most notably for nitrogen vacancy centers in diamond, where single-spin measurements have become commonplace and with more advanced measurement methods even allowing for single-shot, single-spin readout at low temperatures [26]. With optical detection of molecular spin transitions being demonstrated only recently [20], this direction will certainly be of great importance for MQBs in the future. Another promising approach is to use a Scanning Tunneling Microscope to coherently manipulate and read out the spin states of individual qubits [27], even though low temperatures of 1.2 K are required in this case as well. This approach has, however, not yet been demonstrated on a molecular system and the mechanism inducing the ESR transition is still debated.

Apart from the above-mentioned studies of Wernsdorfer, there is a severe lack of

experimental investigations of electrical readout of MQBs. To explore if such measurements are possible at temperatures above a few mK and if there are more efficient system architectures, we have decided to perform an investigation into different platforms for molecular qubits.

1.1 Aim of This Work

The aim of this thesis was to achieve electrical readout of molecular quantum bits. To this end, we explored various possibilities of integration of MQBs with different material systems, with the goal of efficient spin-to-charge conversion at temperatures of a few Kelvin, in contrast to approaches relying on mK environments. The physical mechanisms chosen for these investigations are described in the following section. After identification of possible materials and experiments, the measurement capabilities required to investigate these were developed. For a useful electrical readout of a spin state, mobile charge carriers are required in the immediate vicinity of the MQB. Since the effects of bringing MQBs and mobile charge carriers near each other were not known, the effects of their interaction on both the charge carriers and the MQBs were studied in novel hybrid material displaying both conductivity and charge carrier mobility.

1.2 Investigated Systems and Experiments

Electrical readout of a quantum bit means the ability to infer the spin state of a MQB by measuring an electrical property of a device — its conductivity or voltage signal on some terminals. For such an effect to manifest, the MQB and a mobile charge carrier need to be close enough to each other for a magnetic interaction to occur. Depending on the exact materials, type of charge transport, and distance, the mutual interaction can take many forms, resulting in a wide variety of possible phenomena, from the Kondo effect in metals to spin-dependent recombination of charge carriers in semiconductors. In the context of quantum computation, the most relevant interactions are those related to EDMR, where a number of different processes can be found in the literature. A schematic overview of these mechanisms is depicted in Figure 1.2.

One of the most common mechanisms of EDMR is spin-dependent recombination of charge carriers within a semiconductor bandgap. Charge carrier recombination rate in a material directly influence the conductivity of a material and in some systems, this process can be significantly affected by the spin permutation symmetry of the participating positive and negative charges. If the two charges form a triplet, the recombination is less likely than in the case of a singlet configuration due to the Pauli exclusion principle. If one

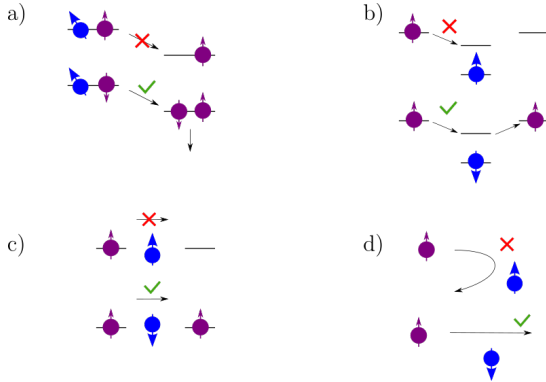


Figure 1.2: Spin-to-charge conversion mechanisms reported in literature relevant for electrical readout of quantum bits. Blue discs with arrows represent the spin qubit, while purple ones represent charge carriers. a) Spin-dependent recombination of charge carriers weakly coupled to a qubit. b) Spin-dependent transport through a quantum dot weakly coupled to the qubit. c) Spin-dependent tunneling through or hopping in the vicinity of the qubit. d) Spin-dependent scattering of charge carriers on the qubit.

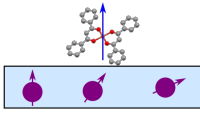
of the spins within a pair flips, for example due to spin resonance, the singlet-to-triplet ratio changes, which can be directly detected as a change in conductivity². Additionally if one of the charge carriers is coupled to another spin, such as a spin qubit, their interaction would also affect the recombination dynamics and therefore allowing for a readout of the qubit (Figure 1.2a). This method has been demonstrated as a route to read out the quantum state of a ³¹P quantum bit in silicon [28].

A second process, widely used for readout of various qubits, is to construct a system where the qubit is weakly coupled to an empty, isolated state, such as an artificial quantum dot or an empty orbital in a molecule. After forming electrical contacts to the isolated state, the charge transport through this state will be dictated by the spin permutation symmetry of the charge carrier and the qubit (Figure 1.2b). This method has been used for qubits in inorganic semiconductors [29], and is the only electrical readout method demonstrated on MQBs as well [24]. The following processes are variations on the previous one: charge carriers can tunnel through or hop around a qubit, with the probability of the process being influenced by their mutual spin orientations (Figure 1.2c) [30, 31], and in the case of delocalized charge transport, the scattering cross-section of charge carriers on a localized qubit will be spin-dependent as well (Figure 1.2d) [32].

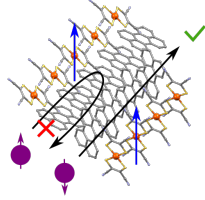
Considering the readout mechanisms above, as well as the particularities of MQBs, we have identified three possible approaches to bringing MQBs into the vicinity of mobile

²More detailed description of this process can be found in Section 2.3.3.

I. Semiconductor channel



II. Conducting channel



III. Semiconducting polymer

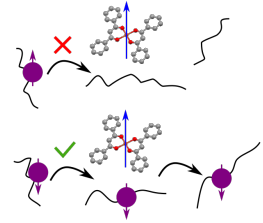


Figure 1.3: Schematic images of our selected possibilities for integration of MQBs with conductive material systems. I. MQBs on top of a semiconducting channel with spin-polarized electrons. Spin state of the MQB changes the spin polarization of charge carriers via dipolar interaction. II. MQBs inside a molecular crystal with conducting channels. Spin-dependent scattering influences conductivity in the channel. III. MQBs inside a polymeric semiconductor. Spin-dependent hopping influences overall conductivity of the material.

charge carriers and studying their interaction:

- I. Depositing MQBs on top of inorganic semiconductor channels with spin-polarized charge carriers.
- II. Employing a material containing both MQBs and conductive channels in its crystal structure.
- III. Creating a hybrid material composed of an organic semiconductor and MQBs.

Figure 1.3 shows a schematic visualization of the three approaches. In the first approach, our vision is to have a layer of MQBs on top of a semiconductor channel, into which spin-polarized charge carriers would be injected. The magnetic moments of the charge carriers could then interact with the MQBs, which would influence their spin polarization. The change in spin polarization of the charge carriers could then be read out using magnetoresistive effects, such as a spin-valve measurement. Apart being completely novel, this geometry would provide us with an easily tunable dipolar interaction between the MQBs and charge carriers, where the strength of the interaction could be tuned by a thin non-conductive layer between the MQBs and conductive channel. Another significant advantage of this approach is that the spintronic platform could be developed using industry-standard processes, therefore paving the way for molecular quantum bits integrated with CMOS compatible spintronics. The second approach came from the realization that a molecule which has one of the longest T_M times and held the record for the longest T_M for a few years ($(PPh_4)_2[Cu(mnt)_2](mnt^{2-} = \text{maleonitriledithiolate})$ [17], could also be found in the crystal structure of a fascinating family of materials that display metal-like conductivity. Due to the interaction between the localized magnetic moments of the qubits with the itinerant charge carriers inside the conducting channel, spin-dependent

scattering could potentially take place in an almost ideal geometry. The disadvantage of these organic magnetic conductors is their non-trivial synthesis. Inspired by these materials, we wanted to investigate a facile manufacturing of a material displaying both quantum coherence and conductivity by mixing MQBs and organic semiconductors, which are cheap and easily processable. Hopping between individual polymer chains could then be influenced by the spin states of the charge carrier and MQBs, providing a pathway for electrical readout of the MQB spin state.

Regardless of the interaction mechanism and the chosen approach, the presence of the charge carriers has to affect the properties of the MQB as little as possible and at the same time, we need to be able to detect a signature of the qubit through the charge carrier properties. It is therefore not only necessary to study how the charge carriers interact with the MQBs; the inverse effect, i.e., how the presence of the charge carriers affect the MQB and its properties, has to be considered as well. Additionally, in all of the approaches mentioned above, the proof-of-concept measurement would be the observation of a modulation of conductivity of a system upon excitation of the MQB ESR transition. For investigation of all aspects of these complex systems, we had to choose suitable experimental techniques. To interrogate the MQBs using spin-polarized charge carriers, a system which can detect small changes in magnetoresistance of spintronic devices at low temperatures is required. Such a system was not available at the Institute of Physical Chemistry, University of Stuttgart (IPC), it was therefore necessary to develop it. To study the MQBs and how their properties change when charge carriers are introduced into their vicinity, ESR spectroscopy, both continuous wave (cw) and pulsed, is the most suitable technique. To facilitate electric readout of the MQB spin state in the approaches with hybrid material systems displaying both conductivity and magnetism, the technique of EDMR was chosen. The experimental setup for this technique also needed to be developed.

1.3 Organization of the Thesis

After a general introduction to the field, aim of the thesis and a brief introduction to the investigated systems in this chapter, some theoretical principles underlying this study will be described in Chapter 2. A section dedicated to ESR will introduce the basics of the technique, its relation to spin qubits and the special case of electrically detected magnetic resonance. Development of experimental techniques constitutes a large portion of this thesis, the basics of sensitive electrical measurements will therefore be introduced in Chapter 2 as well, along with other experimental methods employed for analysis of samples in the course of this work. Chapter 3 will describe the development of a low-temperature

magnetoresistance measurement set up, as well as application of this apparatus to our efforts in developing a CMOS compatible spintronic platform for MQBs. Chapter 4 deals with the development of a EDMR spectrometer, its testing on an organic semiconductor and our first steps in studying molecular crystals containing both MQBs and itinerant charge carriers. Chapter 5 presents our results obtained by studying a hybrid material composed of an organic semiconductor and MQBs, showing the influence of a different environment and presence of charge carriers on the spin dynamics of MQBs.

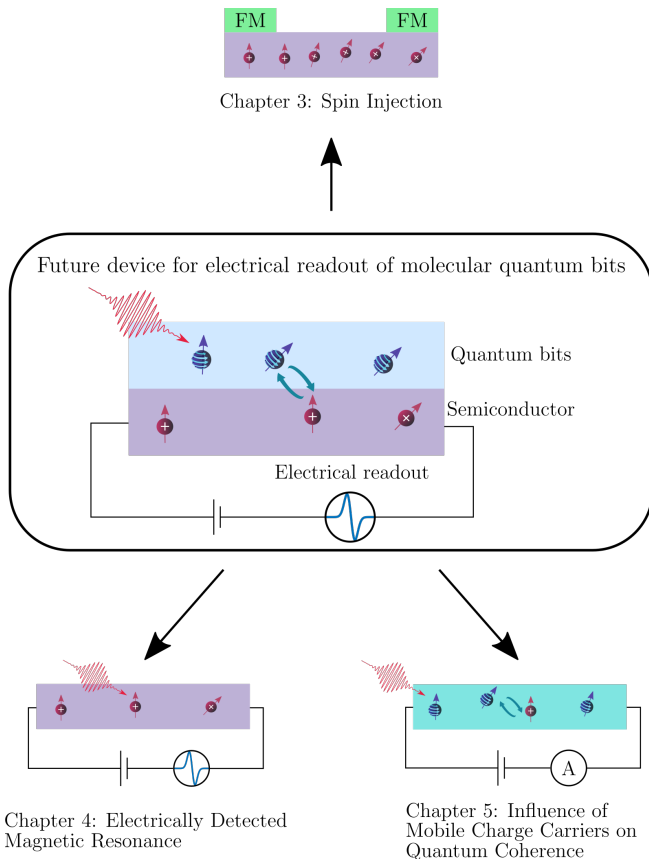


Figure 1.4: A conceptual roadmap for this thesis. The overarching goal was electrical readout of molecular quantum bits, as illustrated by a hypothetical future device. To this end, we have explored various integration possibilities with different material systems, as well as developed the required measurement capabilities.

2 Theoretical Background

This chapter should serve as a reference point for discussions later in the thesis, mainly for the relatively large number of experimental techniques used in the course of this work. After a brief discussion of magnetism and magnetometry, the various magnetoresistance effects relevant to this thesis are discussed. The technique most important for molecular quantum bits, Electron Spin Resonance (ESR), is then discussed in more detail, as well as the electrical detection of spin resonance transitions. Ferromagnetic resonance is discussed in the same section, even though it observes excitations of correlated spins, in contrast to isolated magnetic moments in standard ESR. Extraction of charge carrier mobility from organic field effect transistors is then shortly introduced and finally, considering that a significant portion of this work deals with development of experimental setups, a short discussion of small signal measurements from an electrical point of view is included.

2.1 Magnetism and magnetometry

A thorough discussion of magnetism in matter is beyond the scope of this thesis, but the interested reader is referred, for example, to the excellent book by Blundell [33], on which this section is loosely based. Here, we will focus on the introduction of basic, relevant quantities and the techniques to measure them.

The fundamental object in magnetism is the *magnetic moment*. We can recall from classical electromagnetism that a single loop of wire with surface area S carrying a current flow I has a magnetic moment of

$$\boldsymbol{\mu} = I \cdot \boldsymbol{S} \tag{2.1}$$

with its direction normal to the surface of the loop. This object is also called a magnetic dipole, due to its analogous behavior to the electric dipole. The magnetism of matter is mostly determined by its electrons and their various interactions. In addition to its mass (m) and charge (e), an electron has an intrinsic angular momentum called *spin angular momentum* \boldsymbol{S} , commonly referred to simply as *spin*. This angular momentum produces a

spin magnetic moment

$$\boldsymbol{\mu}_s = -\frac{e}{m}\mathbf{S}. \quad (2.2)$$

Given the quantum nature of spin, it cannot be directly measured. The only measurable quantity is its projection along a quantization axis (assumed to be the z -axis in this discussion), $S_z = \hbar m_s$, with \hbar being the reduced Planck's constant and m_s the spin quantum number, equal to $\pm\frac{1}{2}$ for a free electron. It follows that only the projection of the spin magnetic moment can be measured as

$$\mu_{s,z} = \pm\frac{e\hbar}{2m} = \pm\mu_B, \quad (2.3)$$

with μ_B known as the Bohr magneton. In reality, due to quantum relativistic effects, the spin magnetic moment of a free electron is

$$\boldsymbol{\mu}_s = -g\mu_B\mathbf{S} \quad (2.4)$$

with g being a factor required to account for deviations of the behavior of a quantum object to the behavior of a classical charged particle. The electron g -factor is one of the most precisely measured quantities in physics (0.7 parts per billion uncertainty) with the value of roughly $g_e = 2.0023193$ [34].

In an atom, the electron has an orbital angular momentum, \mathbf{L} , as well. The total electron angular momentum of the electron is then a vector sum of its angular momenta, $\mathbf{J} = \mathbf{L} + \mathbf{S}$. The resulting magnetic moment is then calculated based on \mathbf{J} rather than \mathbf{S} . How exactly is \mathbf{J} calculated and how it behaves across the periodic table elements is a topic not entirely pertinent to this thesis, there is, however, an important concept worth mentioning, namely the spin-orbit interaction. As the name suggests, it is the interaction between the spin and orbital parts of an electron's wave function. It arises from purely relativistic considerations; simplistically, consider an electron orbiting a nucleus. In the rest frame of the nucleus, there is no magnetic field acting on the electron. However, in a frame comoving with the electron, the nucleus is orbiting the electron, thus forming a current loop producing a magnetic field, which interacts with the electron's spin angular momentum. It is important to realize that this relativistic *magnetic* field coming from the nucleus is actually related to its *electric* potential. This means that spin-orbit interaction provides a pathway for *electric* fields to interact with the spin magnetic moment. The strength of this interaction is proportional to the 4th power of the atomic weight. In $S = 1/2$ systems, deviations of the effective g -value from that of a free electron are usually due to spin-orbit coupling.

A solid consists of many atoms with magnetic moments. All the individual magnetic

moments add up to a macroscopic magnetic moment. The macroscopic *magnetization* of an ensemble of N spins is simply the net magnetic moment per unit volume (V)

$$\mathbf{M} = \frac{1}{V} \sum_{i=1}^N \boldsymbol{\mu}_i. \quad (2.5)$$

Magnetic field in space can be described by the vector fields \mathbf{B} and \mathbf{H} , related in free space by

$$\mathbf{B} = \mu_0 \mathbf{H} \quad (2.6)$$

with μ_0 being the permeability of vacuum. Standard convention dictates that these fields are called *magnetic induction* and *magnetic field strength* respectively. In modern literature and common usage, however, the simpler term *magnetic field* is used for both and the corresponding letter is used indicate which one is meant.

In a magnetic solid, the relation between \mathbf{B} and \mathbf{H} is more complicated. Generally

$$\mathbf{B} = \mu_0(\mathbf{H} + \mathbf{M}). \quad (2.7)$$

If \mathbf{M} depends linearly on \mathbf{H} , the solid is in a linear regime¹ and we can write

$$\mathbf{M} = \chi \mathbf{H} \quad (2.8)$$

with χ being a dimensionless quantity called magnetic susceptibility, which is in the general case a second rank tensor. We can use χ to characterize materials based on their magnetic response. Diamagnetic materials have relatively small, negative susceptibility, their internal magnetic fields being always opposite to an applied external field. Paramagnetic materials have relatively small, positive susceptibilities. In ferromagnetic (FM) materials, the magnetic susceptibility is non-linear ($\chi = \partial M / \partial H$) and orders of magnitude larger than in dia- and paramagnetic materials. Additionally, in FM samples demagnetizing fields have to be considered in most cases.

To measure magnetization and magnetic susceptibility of various materials, *magnetometers* are used. Some of the most common devices are vibrating sample magnetometers (VSMs) which vibrate a sample through two counter-wound coils, which generate a sinusoidal electrical signal proportional to the magnetic moment of the sample. The most sensitive commercially available method, used in the course of this work as well, is Superconducting QUantum Interference Device (SQUID) magnetometry. Here, superconducting rings with one or more Josephson junctions are used to convert small changes in magnetic

¹Materials which do not saturate under ambient conditions and field strengths in a chosen application are commonly referred to as linear materials, even though they can become non-linear under different conditions.

flux to voltage through observation of an electron-pair interference pattern change. Due to the small size of SQUID loops, they are usually inductively coupled to pickup coils through which the magnetic sample is moved. The interested reader is referred to [35] for an exhaustive review of SQUID technology and to [36] for a more practical tutorial.

2.2 Magnetoresistance Effects

Magnetoresistance, i.e., the change of electrical resistance of a material as a response to applied magnetic field, is one of the most important physical phenomena behind modern data storage technology as well as the whole field of spintronics. This general term encompasses a large number of effects with vastly different physical origins, and as such we will introduce here only the effects observable in samples investigated in this thesis and pertinent to our envisioned electrical read-out of molecular quantum bits.

2.2.1 Ordinary magnetoresistance and the Hall effect

The two most common magnetoresistance effects can be derived from some basic semiclassical considerations based on the Drude model of conductivity in metals and semiconductors where the charge carriers can be considered free. The discussion of the Drude model can be found in any physics textbook, such as the classic by Kittel [37].

First, we can recall that a charged particle (such as a free electron with charge e) with mean velocity \mathbf{v} subject to electric (\mathbf{E}) and magnetic (\mathbf{B}) fields experiences the Lorentz force

$$\mathbf{F} = -e(\mathbf{E} + \mathbf{v} \times \mathbf{B}). \quad (2.9)$$

Based on the Drude model, we can then write the equation of motion for this system as

$$m^* \left(\frac{d}{dt} + \frac{1}{\tau} \right) \mathbf{v} = -e(\mathbf{E} + \mathbf{v} \times \mathbf{B}) \quad (2.10)$$

with m^* being the effective mass and τ the mean scattering time of the electron. We now assume that the magnetic field is applied along the z -direction, that the \mathbf{E} field is static and we focus only on the steady state (i.e., the time derivatives are 0). With these assumptions, we can write

$$v_x = -\frac{e\tau}{m^*}E_x - \frac{eB}{m^*}\tau v_y \quad (2.11)$$

$$v_x = -\frac{e\tau}{m^*}E_y - \frac{eB}{m^*}\tau v_x \quad (2.12)$$

$$v_x = -\frac{e\tau}{m^*}E_z. \quad (2.13)$$

In order to obtain an expression for conductivity (σ), we can recall that the current density $\mathbf{j} = -nev = \sigma \mathbf{E}$, where n is the charge carrier density. Additionally recognizing that the expression eB/m^* is the cyclotron frequency ω_c , we obtain

$$j_x = \sigma_0 E_x - \omega_c \tau j_y \quad (2.14)$$

$$j_y = \sigma_0 E_y - \omega_c \tau j_x \quad (2.15)$$

$$j_z = \sigma_0 E_z, \quad (2.16)$$

with $\sigma_0 = ne^2\tau/m^*$ being the well-known Drude conductivity. Since the solution in the z -direction is trivial, it is usually not considered. We can therefore see that the conductivity is a second rank tensor of the form

$$\boldsymbol{\sigma} = \begin{pmatrix} \sigma_{xx} & \sigma_{xy} \\ \sigma_{yx} & \sigma_{yy} \end{pmatrix}, \quad (2.17)$$

and with a bit of arithmetic it can be shown that in an isotropic material

$$\sigma_{xx} = \sigma_{yy} = \frac{\sigma_0}{1 + (\omega_c \tau)^2} \quad (2.18)$$

$$\sigma_{xy} = -\sigma_{yx} = \frac{\sigma_0 \omega_c \tau}{1 + (\omega_c \tau)^2}. \quad (2.19)$$

From these equations we can readily see that magnetoconductivity strongly depends on the term $\omega_c \tau$. In the regime where the experiments in this thesis usually operate, i.e., low temperatures and high magnetic fields, $\omega_c \tau$ is usually much larger than one. Therefore the conductivity along the current flow (σ_{xx}) varies as B^{-2} (ordinary magnetoresistance) and across the current flow (σ_{xy}) proportionally to B^{-1} (Hall effect).

2.2.2 Weak (anti)localization

A qualitative discussion of the weak localization and antilocalization will now follow. For a more rigorous description, the interested reader is referred to the book by Schäpers [38], which served as a basis for this section.

The previously described magnetoresistance effects could all be understood semiclassically; they are a consequence of curving charge carrier paths under the Lorentz force. The charge carriers in this picture behave as solid, localized particles. We know, however, that they are actually quantum objects, with a wavelength and phase associated with them. Weak localization and antilocalization are purely quantum phenomena originating from electron interference. The parameter which determines if such phenomena are observed is the phase coherence length l_ϕ , which is the distance the charge carrier can travel before

its phase is randomized. It is important to note that elastic scattering events (such as charged impurity scattering) do not randomize the phase, even though they shift it - the crucial point is that they shift consistently, i.e., they shift the phase by the same amount if the electron travels the same path again. The distance between two elastic scattering events is called the elastic mean free path, l_e . At low temperatures l_ϕ is in many cases larger than l_e . Under such conditions, the electron can undergo many elastic scattering events before it loses its phase information. Imagine then an electron nearing a scattering center. It can split into two partial waves, scattering off the following centers once in a clockwise and once in a counter-clockwise fashion, before arriving to the starting point and interfering with itself (Figure 2.1a). It can be shown that in the absence of a magnetic field, this interference will always be constructive, regardless of the size of the loop [38, p. 194]. This constructive interference leads to *weak localization* of the electron near such loops with the consequence of slightly decreased conductivity at zero magnetic field. If we now apply a magnetic field such that the magnetic flux is penetrating the closed loop, the electrons will acquire a phase shift, equal for both directions. However, since in a real material there are many of these loops with random sizes, this phase shift will be different for each loop, the constructive interference will be averaged out to zero (Figure 2.1b).

The previous discussion, however, neglects the electron spin. This is warranted as long as the spin orientation, i.e., its phase, is preserved during propagation along a closed loop. Indeed, elastic scattering on charged impurities, should not affect the spin at all. However, as we briefly mentioned in the section 2.1, spin-orbit coupling allows for electric fields to affect the spin. The spin can also scatter on magnetic impurities. If we now again consider the closed loop in Figure 2.1a, taking into account that the spin either precesses between the scattering events (D'yakonov-Perel' spin relaxation) or is flipped at each scattering center (Elliot-Yafet spin relaxation), we can see that the final phase of the spin after traveling along the loop will depend on the loop size and/or the number of scattering

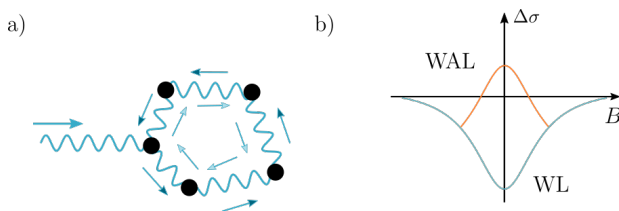


Figure 2.1: a) Elastic scattering of an electron in a closed loop, leading to weak localization (WL) and antilocalization (WAL) effects. b) Quantum correction to conductivity as a function of the magnetic field: due to weak localization, the conductivity at zero field is reduced. Inversely, weak antilocalization increases conductivity.

centers. Thus each particular loop in a material causes different spin rotation (i.e., a different phase shift) and on average, destructive interference dominates the conductivity at zero magnetic field, causing a slight increase in conductivity. This effect is called *weak antilocalization*.

The mathematical description of these effects is rather involved and is beyond the scope of this section. In short, the problem depends not only on the dimensionality of the system in question, but on the type of spin relaxation as well. For systems with D'yakonov-Perel' spin relaxation, the Iordanskii, Lyanda-Geller and Pikus (ILP) model is used. In this thesis, magnetoresistance was measured on heavily doped germanium at low temperatures, where spin relaxation of the Elliot-Yafet type is more dominant [39]. For such systems, Hikami, Larkin and Nagaoka (HLN) developed an elegant model which describes both weak localization and weak antilocalization. The samples investigated in this thesis can be considered two-dimensional, for which the HLN model of change of conductance (ΔG) in the magnetic field can be written as

$$\Delta G(B) = \frac{e^2}{2\pi^2\hbar} \cdot \left[\psi \left(\frac{1}{2} + \frac{B_\phi}{B} + \frac{B_{SO}}{B} \right) + \frac{1}{2} \psi \left(\frac{1}{2} + \frac{B_\phi}{B} + 2 \frac{B_{SO}}{B} \right) - \frac{1}{2} \psi \left(\frac{1}{2} + \frac{B_\phi}{B} \right) - \ln \left(\frac{B_\phi + B_{SO}}{B} \right) - \frac{1}{2} \ln \left(\frac{B_\phi + 2B_{SO}}{B} \right) + \frac{1}{2} \ln \left(\frac{B_\phi}{B} \right) \right], \quad (2.20)$$

where $\psi(x)$ is the digamma function, $B_\phi = \hbar/4el_\phi$ and $B_{SO} = \hbar/4el_{SO}$ are effective magnetic fields required to break phase coherence and spin coherence between spin-orbit scattering events, respectively. This equation can be directly used to fit data obtained from magnetoconductance measurements of an appropriate material, such as the ones shown in the section 3.5.3. If the mean free path between spin-orbit induced spin scattering (l_{SO}) is sufficiently large, i.e., the spin-orbit interaction is weak in given system, the spin-orbit terms related to weak antilocalization disappear and the equation can be substantially simplified to

$$\Delta G(B) = \frac{e^2}{2\pi^2\hbar} \cdot \left[\psi \left(\frac{1}{2} + \frac{B_\phi}{B} \right) - \ln \left(\frac{B_\phi}{B} \right) \right]. \quad (2.21)$$

This equation can be directly used to fit weak localization magnetoconductance curves.

2.2.3 Electrical spin injection

Previously described magnetoresistance effects are intrinsic to semiconductors and metals and either do not depend on spins at all or they are a consequence of equilibrium spin polarization within the material. For any spintronic device, however, a way to manipulate spin populations is required. Namely, we must be able to generate a non-equilibrium spin population in a desired material such as a semiconductor (spin injection), let the

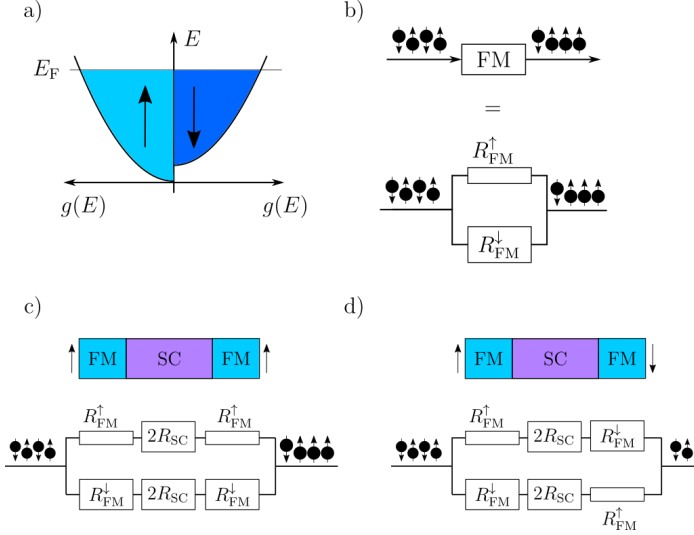


Figure 2.2: a) A schematic representation of the split density of states for spin-up and spin-down electrons in a FM metal, with a consequence of a spontaneous electron spin polarization at the Fermi level E_F . b) The resistor model of an FM electrode. Magnitude of resistance is represented here by the size of the resistors. c) and d) Schematic representations of a FM/SC/FM material stack. When the FM electrodes are magnetized in parallel, the resistance of the network is low, whereas in an anti-parallel orientation, the resistance is high.

spin polarization evolve or be manipulated, and afterwards detect the final state (spin detection). While both spin injection and detection can be done optically in a very efficient manner, purely electrical pathway would be much more easily integrated with current technology, and as such we will focus on those only. The most common examples of possible devices, as well as our proposal for implementation, are introduced in chapter 3. In this section, we will briefly introduce the most important concepts for our measurements and the employed detection techniques. The interested reader is again referred to the book by Schäpers [38], which provides a broader, more detailed view.

It is well known that the density of states in ferromagnets is different for the two electron spin orientations, leading to spontaneous magnetization [33, p.145]. Figure 2.2a shows a schematic representation of this fact in FM metals. As a consequence, we can see that at the Fermi level there is majority of, for example, spin-up electrons and minority of spin-down electrons. A simple yet powerful way of describing an FM electrode and electrical spin injection is the so-called resistor model. Neglecting any spin scattering, we can consider the two spin orientations separately. Since there are different densities

of states for each orientation, we can plausibly assume that the conductivity differs as well. Figure 2.2b demonstrates how we can treat an FM electrode as two parallel resistors with different resistances for the two spin orientations (represented by the size of the resistors). With this model, we can define spin polarization β through the spin-dependent conductivity as

$$\beta = \frac{\sigma_{\text{FM}}^{\uparrow} - \sigma_{\text{FM}}^{\downarrow}}{\sigma_{\text{FM}}^{\uparrow} + \sigma_{\text{FM}}^{\downarrow}} \quad (2.22)$$

where $\sigma_{\text{FM}}^{\uparrow}$ and $\sigma_{\text{FM}}^{\downarrow}$ are the conductivities of spin-up and spin-down electrons in the ferromagnet, respectively. For experimental purposes it is sometimes more instructive to use resistances instead of conductivities. Summing up the parallel resistances as usual and with a bit of arithmetic, we can write

$$\frac{1}{R_{\text{FM}}} = \frac{1}{R_{\text{FM}}^{\uparrow}} + \frac{1}{R_{\text{FM}}^{\downarrow}} \quad (2.23)$$

$$R_{\text{FM}}^{\uparrow} = \frac{2R_{\text{FM}}}{1 + \beta} \quad (2.24)$$

$$R_{\text{FM}}^{\downarrow} = \frac{2R_{\text{FM}}}{1 - \beta}. \quad (2.25)$$

With a single FM electrode connected to, for example, a semiconductor, we can generate spin-polarized current just on the basis of the spontaneous electron polarization in the ferromagnet. Such a device, however, would not be able to electrically detect flipping of the electrode magnetization, since the change in resistance for the two spin orientations is equal and opposite. The essential spintronic device is therefore a ferromagnet/semiconductor/ferromagnet (FM/SC/FC) material stack, also known as a spin valve. Figure 2.2c and d show a schematic representation of this material stack, along with its resistor model and resulting current flow. The resistance of the semiconductor is assumed to be spin independent, it is therefore represented by two spin channels, each with a resistance of $2R_{\text{SC}}$. Considering the resistance network formed in such a material stack, it is clear that we expect to observe a higher, spin polarized current if the FM electrodes are magnetized parallel to each other, since the current will predominantly flow through the low resistance spin-up channel. If the two FM electrodes are magnetized in antiparallel, a lower, spin-unpolarized current is to be expected. The relative difference between resistance between the parallel (R_{par}) and antiparallel configurations (ΔR) can be calculated based on the resistor network in Figure 2.2 as

$$\frac{\Delta R}{R_{\text{par}}} = \frac{\beta^2}{1 - \beta^2} \frac{R_{\text{FM}}^2}{R_{\text{SC}}^2} \frac{4}{4 \frac{R_{\text{FM}}^2}{R_{\text{SC}}^2} + 2 \frac{R_{\text{EM}}}{R_{\text{SC}}} + (1 - \beta^2)}. \quad (2.26)$$

This result provides an important insight, namely that the observable signal (which depends on the spin polarization in the semiconductor channel) strongly depends on the ratio between the conductivities of the ferromagnetic electrode and the semiconductor channel. If there is a large difference between the two, as is often the case for a FM metal and a semiconductor, the spin injection is very inefficient. This is known as the conductivity mismatch problem in spintronics. One of the solutions to this problem is to insert a tunneling barrier between the FM electrode and the semiconductor, the other is to find such a combination of materials as to maximize this ratio. An example of both solutions in practice can be found in chapter 3.

Detection of spin injection

In the previous section, we have established that creating a non-equilibrium spin polarization in a semiconductor between two ferromagnets leads to a measurable difference in conductivity of such a material stack. Let us now consider such a device, as in Figure 2.2c. If we wanted to prove that we have a spin-dependent effect, we would measure the resistance of this material stack while changing the magnetic field. We would expect that at a certain field, when the configuration of magnetizations of the two FM electrodes changes from parallel to antiparallel, a change in the resistance would be observed. Such an experiment is known as a spin-valve measurement. This particular configuration, however, would be plagued by the common pitfalls of two-terminal measurements, as well as some additional ones: significant contributions from contact resistance, effects of stray fields of the electrodes or contributions from anisotropic magnetoresistance. Due to these reasons, such two-terminal measurements are usually not considered a definite proof of successful electrical spin injection into a material. One widely used practice to avoid these problems is to employ optical methods, such as the magneto-optical Kerr effect, to directly measure the spin polarization inside a material. We are, however, interested in electrical read-out of our systems due to easier integration and a higher compatibility with existing technology, and as such will focus only on those. The other possibility is to increase the number of electrical terminals from two to four. With four terminals, it is possible to realize a so-called non-local spin valve structure, which significantly reduces the number of possible measurement artifacts. A qualitative description of non-local effects follows, based on references [40] and [41], which contain more rigorous descriptions as well as the pioneering experiments.

The main idea behind nonlocal measurements is the separation of charge and spin currents. This is possible because of the fact that spin diffuses away from the injection point independently of the charge flow, similarly to heat. One can therefore distinguish between spin-polarized charge current and pure spin current with appropriate experiments.

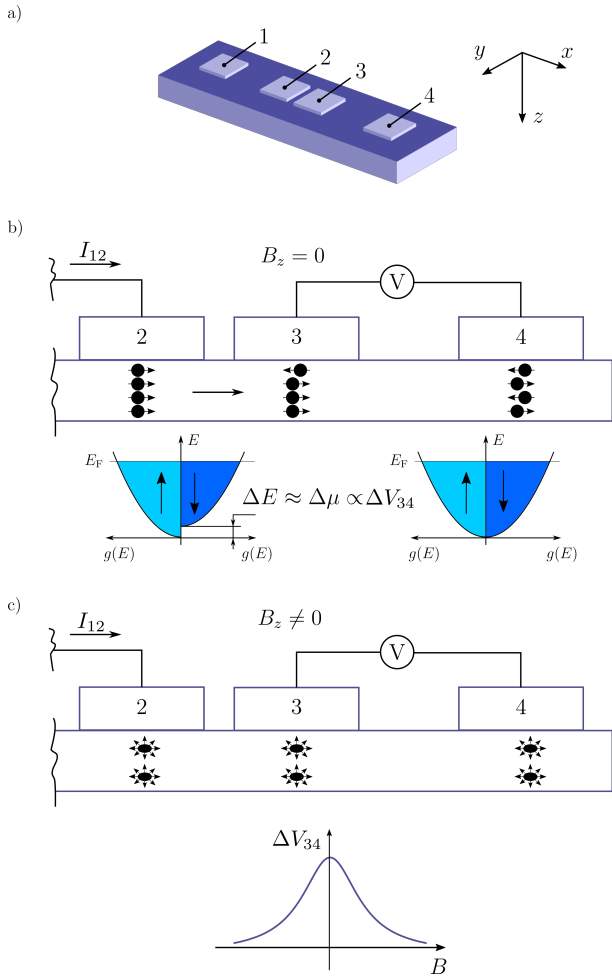


Figure 2.3: a) A nonlocal magnetoresistance measurement setup, assuming that the substrate (purple) is a doped semiconductor and electrodes (light blue) are ferromagnetic. b) A schematic demonstrating spin diffusion from electrode 2 to electrode 3, causing a voltage drop across electrodes 3 and 4 (ΔV_{34}). c) Applying a magnetic field in the z direction causes all of the spins to precess, resulting in a loss of spin accumulation and therefore a decrease in ΔV_{34} .

Let us now consider a four-terminal device geometry such as the one shown in Figure 2.3, assuming that the substrate is a doped semiconductor and the contacts are ferromagnetic. After applying a constant current between terminals 1 and 2, spin-polarized electrons would be injected from terminal 2 into the semiconductor. From the point of injection, spin-polarized electrons would flow from terminal 2 to terminal 1 with the drift velocity, while pure spin polarization would homogeneously diffuse from terminal 2 in all directions. The polarization would decay with increasing distance from terminal 2 with a certain spin-diffusion length, l_{sf} . If the distance between terminals 2 and 3 is smaller or comparable to l_{sf} , there would be a non-equilibrium spin polarization under terminal 3 as well. Assuming that the distance between terminals 3 and 4 is much larger than l_{sf} means that under terminal 4 there is no spin polarization. The different number of electrons polarized 'up' and 'down' under terminals 3 and 4 results in different values of the chemical potential in those regions. As a consequence, there is a measurable voltage drop between terminals 3 and 4, even though there is no charge current present. A modulation of the spin polarization by some external means could therefore be directly measured on terminals 3 and 4, proving a spin accumulation under terminal 3. Furthermore, since all of our electrodes are ferromagnetic, these structures are also sensitive to the relative orientation of magnetizations between terminals 2 and 3. The nonlocal spin-valve experiment would therefore entail manufacturing terminals 2 and 3 with different coercive fields, for example by making them of different sizes, and applying a magnetic field in the y direction (B_y). After flipping one of the electrodes, reaching an antiparallel configuration, we would observe a jump in the measured nonlocal voltage. Upon increasing B_y , the second electrode would flip as well and the voltage would return to its previous level.

The gold standard in proving spin injection and transport is probing the spin dynamics by measuring the Hanle effect in a non-local spin-valve device. The difference to the spin-valve measurement lies in the orientation of the magnetic field. In a Hanle experiment, a constant current is maintained between terminals 2 and 1, and the magnetization orientations of terminals 2 and 3 are assumed to be parallel and pointing along the y direction during the whole time. The external magnetic field is applied along the z -axis (B_z). As described above, at zero magnetic field, spin polarization is diffusing from terminal 2 to all directions, eventually reaching terminal 3 as well, which induces a voltage drop between terminals 3 and 4. The injected spins are oriented the same way as the electrodes, i.e., along the y -axis. Upon application of B_z , the spins will start to precess around it due to Larmor precession (see Section 2.3). With increasing B_z , the spin polarization is increasingly destroyed, eventually equalizing the spin populations and therefore removing the voltage drop between terminals 3 and 4. In order to mathematically describe this effect, usually a one-dimensional drift diffusion model is used, which describes the diffusion of

spin polarization from the injection point (x_1) along with Larmor precession under applied field. It can be shown that the resulting (measurable) y component of the steady-state spin polarization at the detector (x_2) is [41, 42]

$$S_y(x_1, x_2, B_z) = S_0 \int_0^\infty \frac{1}{\sqrt{4\pi Dt}} e^{(-x_2 - x_1 - v_d t)^2 / 4Dt} \times \cos(\omega_L t) e^{-t/\tau_s} dt, \quad (2.27)$$

where S_0 is the spin injection rate, D is the electron diffusion constant, v_d the electron drift velocity and $\omega_L = \frac{g\mu_B B}{\hbar}$ the Larmor frequency with g the electron g factor and μ_B the Bohr magneton. To evaluate the integral, we take advantage of the fact that we measure purely diffusive spin current and set the drift velocity to zero and integrate over the widths of the electrodes in order to obtain $S_y(B)$, which is proportional to the nonlocal voltage. D and g can be extracted from other measurements, such as Hall magnetoresistance and ESR, respectively, leaving only S_0 and τ_s as free parameters. As such, nonlocal Hanle measurements are not only a proof of electrical spin injection, but another method of quantifying spin lifetimes as well.

The only disadvantage of nonlocal Hanle measurements is that the distance between the injection and detection electrodes must be on the order of the spin-diffusion constant. In material systems where this is technologically difficult, one can resort to an easier, albeit less unambiguous version of the experiment. In a local or three-terminal Hanle experiment, the injection and detection electrodes (2 and 3) are merged into one. The rest of the experiment is identical with the non-local variety. The measurement curve is afterwards again a Lorentzian line; however, we cannot use equation (2.27) anymore. Given that there is no distance between the injection and detection of the spin polarization, we lose all quantitative information about injection rates and the diffusion of spin polarization. Nevertheless, we can still obtain an estimate of the spin lifetime, which will be proportional to the linewidth of the measured line. To facilitate that, a phenomenological equation

$$\Delta V = \frac{V_0}{1 + \omega_L \tau_s} \quad (2.28)$$

is commonly used, where ΔV is the measured voltage drop between the injection/detection terminal and terminal 4. Given the local nature of this measurement, it is also more prone to measuring other magnetoresistance effects compared to the non-local measurement, and it is therefore usually not considered a definitive proof of spin injection.

2.3 Electron spin resonance

2.3.1 Basics of ESR

Electron spin resonance is widely used in the study of paramagnetic species, which play a key role across a wide range of disciplines and natural processes, from life sciences across chemistry all the way to materials science and physics. In addition to detecting the presence of unpaired electrons, ESR and its variations can provide us with unmatched insight into the microscopic environment of the sample, as well as into the various dynamic processes within. In the last few years, it has become highly relevant in the field of quantum computing as well, due to the emergence of various spin qubits, which take advantage of ESR to perform all of their operations. In the following, we will briefly introduce the foundations of the technique, as well as a few of its modifications pertinent to this work. For a more extensive and rigorous description, the interested reader is referred to the classic books by Schweiger and Jeschke [43] or Weil and Bolton [44], from which this section drew heavily.

We can recall from equation (2.3) in section 2.1 that the spin magnetic moment of a free electron has two possible projections along a quantization axis. Without any external magnetic fields, these two projections, i.e., energy states, are degenerate. Applying a static magnetic field B_0 lifts this degeneracy and aligns the quantization axis along this field. Each of these discrete energy levels has a so-called Zeeman energy of:

$$E = -\boldsymbol{\mu}_s \cdot \mathbf{B}_0. \quad (2.29)$$

with $\boldsymbol{\mu}_s = -g\mu_B\mathbf{S}$ as discussed in equation (2.4). In the absence of further interactions, \mathbf{B}_0 is chosen along the z -axis and the magnetic moment is $\mu_z = -g\mu_B B_0 m_s$. By irradiating the electron with radiation corresponding to the energy difference between these two levels, $\Delta E = g\mu_B B_0$, we can induce transitions between them. In commercial ESR instruments, magnetic fields from approximately 300 mT up to almost 10 T are used, corresponding to radiation in the range from 9 GHz up to 270 GHz. Spectrometers using either lower or higher fields and frequencies are used as well, even though not as commonly, since they are typically made for very specific applications.

The Zeeman energy term is often the dominant term for ESR, there is, however, a plethora of other interactions that affect an ESR signal. The total spin Hamiltonian commonly used, for example in the simulation and analysis package EasySpin [45], has

the form

$$\begin{aligned} \hat{\mathcal{H}} = & \sum_i \left[\hat{\mathcal{H}}_{\text{EZI}}(i) + \hat{\mathcal{H}}_{\text{ZFI}}(i) \right] + \sum_k \left[\hat{\mathcal{H}}_{\text{NZI}}(k) + \hat{\mathcal{H}}_{\text{NQI}}(k) \right] + \\ & + \sum_i \sum_{j>1} \hat{\mathcal{H}}_{\text{EEI}}(i, j) + \sum_i \sum_k \hat{\mathcal{H}}_{\text{HFI}}(i, k) \end{aligned} \quad (2.30)$$

with the following terms:

- $\hat{\mathcal{H}}_{\text{EZI}}(i) = \mu_B \mathbf{B} \cdot \mathbf{g} \cdot \hat{\mathbf{S}}_i$: Electron Zeeman Interaction of electron spin i . We should note that \mathbf{g} is generally a second-rank tensor, which is usually symmetric and can therefore be described by three principal values g_{xx} , g_{yy} and g_{zz} .
- $\hat{\mathcal{H}}_{\text{ZFI}}(i)/h = \hat{\mathbf{S}}_i \cdot \mathbf{D} \cdot \hat{\mathbf{S}}_i$: Zero-Field Interaction of electron spin i . The second rank tensor \mathbf{D} describes the electron-electron interaction in spin systems with $S > 1/2$. In this work, we will be analyzing only spin systems with $S = 1/2$, we will therefore not need it.
- $\hat{\mathcal{H}}_{\text{NZI}}(k) = \mu_n g_n \mathbf{B} \cdot \hat{\mathbf{I}}$: Nuclear Zeeman Interaction of nucleus k , with μ_n being the nuclear magneton, g_n the nuclear g-factor and I the nuclear spin operator.
- $\hat{\mathcal{H}}_{\text{NQI}}(k)/h = \hat{\mathbf{I}}_k \cdot \mathbf{Q} \cdot \hat{\mathbf{I}}_k$: Nuclear Quadrupole Interaction of nucleus k , described by the second rank tensor \mathbf{Q} . Nuclei with spin quantum number $I > 1/2$ have an electric quadrupole moment that can interact with the local electric field gradient. This is usually a weak effect and can be neglected for systems investigated in this work.
- $\hat{\mathcal{H}}_{\text{EEI}}(i, j)/h = \hat{\mathbf{S}}_i \cdot \mathbf{J} \cdot \hat{\mathbf{S}}_j$: Electron-Electron Interaction between electrons i and j described by the second-rank tensor \mathbf{J} . This term is relevant in all systems where the individual spins are not isolated and interact.
- $\hat{\mathcal{H}}_{\text{HFI}}(i, k)/h = \hat{\mathbf{S}}_i \cdot \mathbf{A} \cdot \hat{\mathbf{I}}_k$: Hyperfine interaction between electron spin i and nuclear spin k , described by the second-rank tensor \mathbf{A} . Similarly to \mathbf{g} , it is often symmetric and can be diagonalized to just three principal values.

A more rigorous description of all the parameters, as well as their manifestation in ESR spectra, can be found for example in [44]. As a demonstration pertinent to this thesis, let us first consider a system with a single unpaired electron, therefore only $S = 1/2$ and later add a hyperfine interaction with a nucleus with $I = 3/2$, such as a Cu^{2+} ion in a square-planar coordination environment.

At zero applied magnetic field, all of the energy states are degenerate, since there is only one unpaired electron. The spin operator $\hat{\mathbf{S}}$ of a single electron has two eigenvalues, $m_S = \pm \frac{1}{2}$. Glancing upon the electron Zeeman interaction Hamiltonian above, we can therefore expect two energy states in an applied magnetic field B_0 . These two states are conventionally referred to as α and β for the higher and lower energy state, respectively.

The energy of each electron spin state will be

$$E_\alpha = +\frac{1}{2}g\mu_B B_0 \quad (2.31)$$

$$E_\beta = -\frac{1}{2}g\mu_B B_0. \quad (2.32)$$

In an ESR experiment, the important value is the difference between these two energy levels, since this corresponds to the energy needed to excite the system from one state to the other and therefore the energy absorbed. By simply subtracting the two energies, we arrive at the well-know ESR resonance condition:

$$\Delta E = E_\alpha - E_\beta = g\mu_B B_0 \quad (2.33)$$

If the electron interacts with an additional nucleus, for example a Cu with $I = 3/2$, we have to consider the nuclear Zeeman and hyperfine interaction terms of the total Hamiltonian as well. An $I = 3/2$ system has four allowed projections, $m_I = \pm\frac{1}{2}, \pm\frac{3}{2}$. When coupled to a single electron, this results in eight total energy levels and four allowed transitions (selection rule $\Delta m_S = 1, \Delta m_I = 0$). It can be shown that while the energy levels are shifted by the nuclear Zeeman interaction, the resulting transition energies depend only on the hyperfine coupling tensor \mathbf{A} . The energy level diagram, as well as the corresponding EPR spectra, are shown in Figure 2.4. The Hamiltonian in equation (2.30) completely describes the static behavior of the spin system and suffices for extraction of the corresponding parameters from spectroscopic data. For quantum information processing, however, we also need to describe and control the spin dynamics, which is the realm of pulsed ESR.

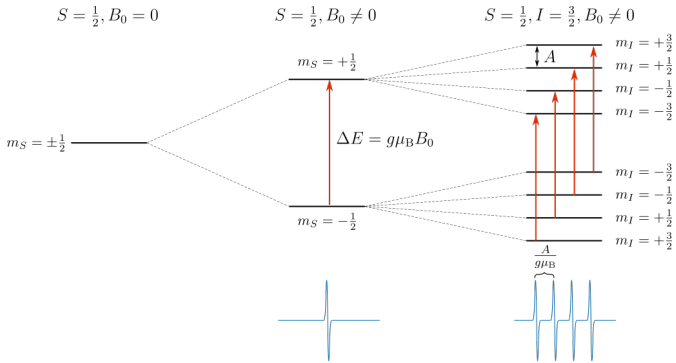


Figure 2.4: Energy splittings as well as the corresponding ESR spectra of an $S = 1/2, I = 3/2$ system.

2.3.2 Pulsed ESR

Pulsed ESR allows for coherent control of spin systems, which enables not only the performance of quantum logic operations, but also the study of many interactions and parameters not accessible by continuous wave methods - the most widely spread example would be double electron-electron resonance, commonly referred to as DEER or PELDOR, which can provide the exact distance between two electrons in the range of 1 to 10 nm. This method is invaluable in biology for structural studies of proteins and their conformations [43]. A rigorous description of pulsed ESR experiment requires the use quantum mechanics and the density operator formalism. While powerful and strictly necessary for more than two-level systems, it lacks the clarity and intuitive understanding that a (semi-)classical, vectorial picture can provide. We will therefore introduce the basics of pulse ESR, relaxation and the most relevant experiments using *Bloch equations* and refer the interested reader to [43] for a more rigorous treatise.

Pulsed ESR experiments are most commonly performed on large spin ensembles, as such we can recall equation 2.5 and consider a magnetization vector \mathbf{M} instead of the individual magnetic moments. In the absence of relaxation, if we expose the spin ensemble to a static and homogeneous field \mathbf{B}_0 , the magnetization vector would experience a torque and precess according to

$$\frac{d\mathbf{M}}{dt} = \gamma_e \mathbf{M} \times \mathbf{B}_0, \quad (2.34)$$

with $\gamma_e = \frac{g\mu_B}{\hbar}$ being the electron gyromagnetic (magnetogyric) ratio. Aligning the magnetic field with the z -axis, $\mathbf{B}_0 = (0, 0, B_0)$, we obtain

$$\frac{dM_x}{dt} = \gamma_e B_0 M_y \quad (2.35a)$$

$$\frac{dM_y}{dt} = -\gamma_e B_0 M_x \quad (2.35b)$$

$$\frac{dM_z}{dt} = 0. \quad (2.35c)$$

The solution to these differential equations is

$$M_x = M_{\perp}^0 \cos \omega_L t \quad (2.36a)$$

$$M_y = M_{\perp}^0 \sin \omega_L t \quad (2.36b)$$

$$M_z = M_z^0, \quad (2.36c)$$

where we can see that the magnetization precesses about B_0 with the Larmor frequency $\omega_L = -\gamma_e B_0$ if M_{\perp}^0 is non-zero. The longitudinal component of magnetization M_z is constant. We can now consider relaxation processes by imagining a sudden change of B_0

orientation. The magnetization component along the new field direction, i.e., the new z -axis, would follow an exponential rise with time constant commonly referred to as T_1 or longitudinal relaxation time. As is usual, we would assume that M_x and M_y relax with the same time constant T_2 or transverse relaxation time. Adding this to our original equations of motion results in

$$\frac{dM_x}{dt} = \gamma_e B_0 M_y - \frac{M_x}{T_2} \quad (2.37a)$$

$$\frac{dM_y}{dt} = -\gamma_e B_0 M_x - \frac{M_y}{T_2} \quad (2.37b)$$

$$\frac{dM_z}{dt} = \frac{M_z^0 - M_z}{T_1}. \quad (2.37c)$$

By solving these differential equations, we obtain solutions much like the ones in equations (??), however, with a decay of the components to zero. We should note the relaxation times mentioned here are only empirical ensemble parameters, which provide no physical insight about the source of these relaxation processes.

In an EPR experiment, we are using radiation to induce transitions between the different spins states, or in the vector picture, to manipulate the magnetization of the sample. Commonly, this radiation is in the microwave region of the electromagnetic spectrum, but these equations are equally valid at other frequencies. The radiation is represented as an additional, circularly polarized, sinusoidally oscillating magnetic field B_1 with the components

$$B_{1x} = B_1 \cos \omega_{\text{mw}} t \quad (2.38a)$$

$$B_{1y} = B_1 \sin \omega_{\text{mw}} t \quad (2.38b)$$

$$B_{1z} = 0 \quad (2.38c)$$

By adding these terms to the equations of motions, we obtain the full Bloch equations:

$$\frac{dM_x}{dt} = \gamma_e (B_0 M_y - B_1 \sin \omega_{\text{mw}} t M_z) - \frac{M_x}{T_2} \quad (2.39a)$$

$$\frac{dM_y}{dt} = \gamma_e (B_1 \cos \omega_{\text{mw}} t M_z - B_0 M_x) - \frac{M_y}{T_2} \quad (2.39b)$$

$$\frac{dM_z}{dt} = \gamma_e (B_1 \sin \omega_{\text{mw}} t M_x - B_1 \cos \omega_{\text{mw}} t M_y) - \frac{M_z^0 - M_z}{T_1}. \quad (2.39c)$$

We can see that the equations are rather unwieldy due to the time dependence of the B_1 field. Since we know that M is continually precessing about B_0 , we can simplify the problem by transforming the static coordinate frame into frame rotating around the z -axis at the frequency of the impinging microwave radiation, ω_{mw} . In this new, *rotating*

frame with coordinates x_r , y_r and z , and B_1 being along x_r , the equations of motion simplify to

$$\frac{dM_x}{dt} = -(\omega_L - \omega_{mw})M_{yr} - \frac{M_{xr}}{T_2} = -\Omega M_{yr} - \frac{M_{xr}}{T_2} \quad (2.40a)$$

$$\frac{dM_y}{dt} = (\omega_L - \omega_{mw})M_{xr} + \gamma_e B_1 M_z - \frac{M_{yr}}{T_2} = \Omega M_{xr} + \omega_1 M_z - \frac{M_{yr}}{T_2} \quad (2.40b)$$

$$\frac{dM_z}{dt} = \gamma_e B_1 M_{yr} - \frac{M_z^0 - M_z}{T_1} = \omega_1 M_{yr} - \frac{M_z^0 - M_z}{T_1}. \quad (2.40c)$$

Ω is commonly referred to as the resonance offset and ω_1 is the so-called Rabi frequency. The above equations fully describe dynamics of a two-level system under microwave irradiation. They can be used to describe the evolution of magnetization either during or after a microwave pulse and the steady-state solutions describe a continuous wave experiment as well. In pulsed ESR, signals are recorded in the x_r and y_r plane in the rotating frame using quadrature detection, i.e., both the x_r and y_r projections of magnetization are recorded, because they couple slightly to the MW resonator. Usual setups are not sensitive to the M_z component. Additionally, due to the relatively high power of used pulses compared with the strength of the ESR signal, detection can only take place after the MW irradiation has been turned off and most of the energy stored in the microwave resonator has dissipated. The time after the end of a pulse and earliest measurement is called the dead time of a resonator. This leads to a number of practical limitations to what signals can be detected. Using equations (2.40), it can be shown that after a MW pulse of duration t_p ($B_1 = 0$), the magnetization evolves as:

$$M_{xr}(t) = M_0 \sin \beta \sin(\Omega t) \exp\left(-\frac{t}{T_2}\right) \quad (2.41a)$$

$$M_{yr}(t) = -M_0 \sin \beta \cos(\Omega t) \exp\left(-\frac{t}{T_2}\right) \quad (2.41b)$$

$$M_z = M_0 \cos \beta \left[1 - \exp\left(-\frac{t}{T_1}\right)\right] \quad (2.41c)$$

where $\beta = \omega_1 t_p$ is the magnetization flip angle. The complex signal $M_{xr} - iM_{yr}$, which is then detected, is called the *free induction decay* or FID. We can see that observation of the signal is limited by the transverse relaxation T_2 , which in combination with the dead time mentioned previously, leads to the main limitation of pulsed ESR. Reality is, however, even more complicated in the fact that T_2 , usually referred to as the spin-spin relaxation time, is only one of the possible transversal relaxation mechanisms and is non-trivial to measure. Decay of the free induction decay is actually governed by the so-called *phase memory time* T_M , which is an umbrella term for multiple relaxation mechanism influencing the directly observed transversal relaxation and is usually shorter than T_2 . T_M is also

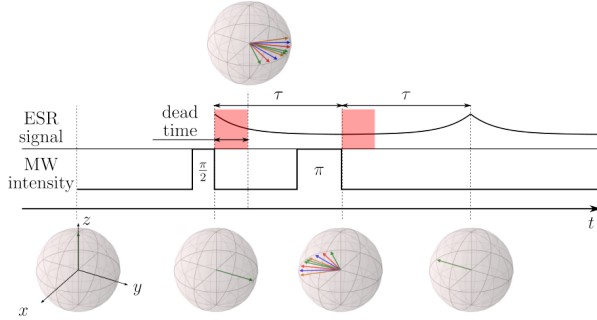


Figure 2.5: An illustration of the evolution of magnetization (colored arrows) in time during a pulsed ESR experiment, inducing a FID and a spin echo. In this experiment, B_0 is oriented along the z -axis, while B_1 along the x -axis.

the parameter most interesting for spin qubits, as this the time during which all of the quantum logic operations have to be performed.

Based on the vectorial analysis presented so far, there is very little that one could do to mitigate the dead-time limitation in a magnetic resonance experiment. Luckily, we can take advantage of a few phenomena that are not captured by the Bloch equations to shift our detection window outside of the dead-time, at least to a certain extent. Now consider a situation directly after a short pulse with $\beta = \frac{\pi}{2}$. It is important to realize that even though we can represent the spin ensemble by the collective magnetization M , this quantity is not necessarily constant. Since a real sample is made up of mostly independent spins, one easily imagine that in a realistic magnetic field B_0 , which has some spatial inhomogeneity, some spins have different frequency offsets Ω as others. This leads to 'fanning out' of the transverse magnetization, as some of the spin rotate faster or slower than others (also called de-phasing). Eventually, the average transverse magnetization will be zero. However, Erwin Hahn realized in 1950 that if we now applied another pulse corresponding to a flip angle of π , we would effectively reverse the direction of the spin precession; spins that were 'fanning out' are now 'fanning in' (or refocusing) and will meet again. As the transverse magnetization builds back up, the FID is observable again in reverse, after which it decays as previously. This process is called a spin echo and is the foundation of all pulsed magnetic resonance spectrometers, since it effectively shifts the signal by a time τ , corresponding to the interpulse delay, further away from the second pulse. This process is illustrated in Figure 2.5. Due to the relatively short T_2 times in most investigated samples, the vast majority of ESR experiments, including those performed in this thesis, detect only spin echoes.

For our purposes, only three pulsed ESR experiments are immediately relevant. First is the echo-detected spectrum. In this experiment, spin echo intensity is measured as a function of the applied magnetic field B_0 , effectively reproducing continuous wave ESR spectrum, since an echo can only be visible when the resonance condition is matched. This serves to verify that all species of interest are present in the sample, as well as the interactions between them. To gain insight into spin dynamics, we additionally want to obtain both the longitudinal and transversal relaxation times.

Extraction of the longitudinal relaxation time T_1

During longitudinal electron spin relaxation, the magnetic quantum number m_s and therefore the energy of the system changes. In solids, thermal motion is usually described by phonons, the quasiparticles of lattice vibrations. Longitudinal relaxation is caused by absorption or stimulated emission of phonons. For the spin system to interact with environmental phonons, a coupling between the two systems is needed and this type of relaxation is therefore often referred to as *spin-lattice relaxation*. Fluctuating magnetic fields, induced by lattice vibrations, mediate the energy transfer. The main spin-lattice relaxation processes are the direct process (absorption/emission of a single phonon), Raman process (two-phonon process involving a virtual excited energy level) and Orbach process (resonant two-phonon process involving a real excited energy level). These processes can usually be distinguished by the temperature scaling of T_1 . The measurement of T_1 therefore provides a pathway to investigate the microscopic origin of spin relaxation in a given environment.

There are multiple options regarding how to extract T_1 from different experiments, each with their own advantages and disadvantages. We have used two of them at different instances. The most commonly used experiment is the *inversion recovery measurement*. First, the magnetization is fully inverted by a π pulse. After a variable time τ_s , during which the magnetization freely evolves, a 'probe' echo sequence ($\pi/2 - \tau - \pi - \tau$) and the echo intensity is read out and plotted as a function of τ_s . The full pulse sequence is therefore $\pi - \tau_s - \pi/2 - \tau - \pi - \tau$. The curve will follow a rising exponential as the magnetization evolves from $-M_0$ (inversion) to $+M_0$ (recovery) and can be fitted by either of the functions

$$I(\tau) = I_0 + A \exp\left(-\frac{\tau}{T_1}\right) \quad (2.42a)$$

$$I(\tau) = I_0 + A_s \exp\left(-\frac{\tau}{T_{1s}}\right) + A_f \exp\left(-\frac{\tau}{T_{1f}}\right) \quad (2.42b)$$

$$(2.42c)$$

where I_0 , A , A_s and A_f are constants. Equation (2.42b) is needed in case the observed spin-lattice relaxation process is biexponential, with a slow (T_s) and a fast (T_f) component.

For long T_1 times, such as those at low temperatures, this experiment becomes inconvenient or even impossible to perform, because the pulse sequence becomes too long and the repetition time² too low. In those cases, it's possible to estimate the T_1 time by observing the intensity of the primary echo as a function of the repetition time. At fast repetition rates, the spin system will become saturated and the echo intensity will decrease. The resulting curve can be then fitted by an exponential recovery function as in equations (2.42).

Extraction of the phase memory time T_M

In contrast to longitudinal relaxation, transverse relaxation does not require exchange of energy with the environment. The quantity that diminishes during transversal relaxation is phase coherence, i.e., the phase information between individual excited spins. If an excited spin experiences a spin flip (longitudinal relaxation), this destroys the correlation of the precession phase between the affected spin and the other excited spins, thus contributing to transverse relaxation. A spin flip can also provide energy for a second spin to transition into the excited state, however, without the phase information. This flip-flop process is twice as effective at destroying coherence than a single flip. This process is energy conserving and is called *spin-spin relaxation*. The transverse relaxation rate $1/T_2$ is then a sum of the spin-spin relaxation rate $1/T_2'$ and the longitudinal relaxation rate $1/2T_1$. In solids, T_2 is often not well defined due to the large number (virtually infinite) of coupled spins and other metrics have to be used to reasonably quantify transverse relaxation. The phase-memory time T_M , is often used as such and is associated with the decay of the primary echo as a function of the interpulse delay τ , with the previously described pulse sequence $\pi/2 - \tau - \pi - \tau$. The resulting curve can be fitted by either of the functions

$$I(\tau) = I_0 + A \exp\left(-\frac{\tau}{T_M}\right) \quad (2.43a)$$

$$I(\tau) = I_0 + A_s \exp\left(-\frac{\tau}{T_{Ms}}\right) + A_s f \exp\left(-\frac{\tau}{T_{Mf}}\right) \quad (2.43b)$$

$$I(\tau) = I_0 + A \exp\left(-\frac{\tau}{T_M}\right)^k, \quad (2.43c)$$

depending on if the observed relaxation process is mono-, bi- or a stretched exponential with a stretching factor k .

²A single acquisition of an echo is rarely sufficient to obtain a good signal-to-noise ratio. Multiple measurements, usually on the order of tens and hundreds, are commonly acquired and averaged. Repetition time is the time between subsequent 'shots' of the same measurement and needs to be at least five times longer than T_1 to prevent unintended saturation of the signal.

T_M corresponds to the inverse homogeneous linewidth and is sometimes simply called T_2 in literature. However, there may be contributions to T_M which can be refocused (instantaneous diffusion, see below) and mechanisms other than spin-spin relaxation and lifetime broadening ($1/2T_1$), which will be briefly outlined in the following. *Instantaneous diffusion* is caused by dipolar couplings between electron spins and cannot be neglected even at low spin concentrations. If a MW pulse excites dipole-coupled spins, the spin flips change the local field at each particular spin. Since the spatial distributions of neighboring spins is in general different for each spin, the changes in local fields are also different. Consequently, spins that had the same resonance frequency before the pulse, can have different resonance frequencies after the pulse. Pulse lengths are usually negligible compared to relaxation times and this phenomenon is therefore known as instantaneous diffusion of magnetization in the spectral dimension. Magnetization can also spread from the excited (A) spins to non-excited (B) spins, if the dipolar couplings are on the order of the difference in the resonance frequencies in a process known as *spin diffusion* or *spectral spin diffusion*. The dipolar coupling between A and B spins also directly decreases T_M , since the spin-lattice relaxation of B spins causes fluctuations of the local fields at the A spins. A similar relaxation mechanism is of importance in systems with abundant protons, such as the molecular solids investigated in this work. The protons play the role of the B spins, but relax predominantly by spin-spin relaxation rather than spin-lattice relaxation, due to the comparatively long T_1 times. This causes fluctuations of the hyperfine field at the observed electron spins. A more extensive description of the various spin relaxation mechanisms, as well as the equations describing them, can be found in the book by Schweiger and Jeschke [43].

2.3.3 Electrically detected magnetic resonance

EDMR is an umbrella term covering all experimental techniques which detect an electron magnetic resonance transition via a change in conductivity of the sample. This makes the navigation and search of relevant literature fairly difficult, due to the number of different techniques and nomenclatures. Most commonly, however, the term refers to spin-dependent transitions of charge carriers in semiconductors. For an in-depth review of the whole topic, the reader is referred to the paper by Boehme and Malissa [46]. Due to the plethora of fundamentally different mechanisms that are known to cause an EDMR signal, it would be beyond the scope of this thesis to even list all of them. We will therefore focus only on selected processes in semiconductors, as they are the main focus of this thesis and account for most of the EDMR signals reported in literature. First, we need to define a few terms from semiconductor physics.

Consider a simplified model of semiconductor energy band gap, as illustrated in

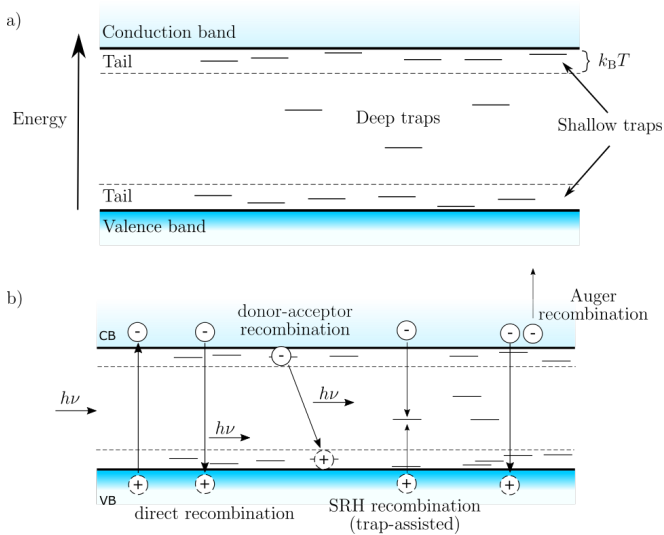


Figure 2.6: a) A simplified model of a semiconductor bandgap, b) the most important charge recombination processes within.

Figure 2.6a. Apart from the valence and conduction bands, in a real material there are some additional states that need to be taken into account. Most semiconductors use dopants to increase the number of free charge carriers and therefore their conductivity. These dopants, either electron acceptors (*p*-type) or electron donors (*n*-type), create isolated states in the band gap, usually energetically close³ to the valence (*p*) or conduction (*n*) bands. Due to the proximity of these states to the bands in which free charge carriers are being transported, they often act as traps, into which electrons and holes can be temporarily trapped, effectively decreasing the conductivity of a material. The energy spectrum close to conduction and valence bands is called the band tail, and the states within are known as tail states or shallow traps. Some types of defects can create shallow traps as well. Additionally, there are so-called deep traps, which are states 'deep' within the band gap, commonly caused by metal contaminants. Charge carriers require much more energy to free themselves from a deep trap and spend there considerably longer time than in shallow traps - they are therefore much more detrimental to the performance of a semiconductor.

When using a semiconducting material, i.e., driving current through it, excess electrons

³Meaning on the order of thermal energy $k_B T$, where k_B is the Boltzmann constant and T the absolute temperature.

and holes are constantly being generated, either by injection from electrodes or by photoexcitation. These electrons and holes can either be bound (forming an exciton), or they can be independent. After generation, they move freely through their respective energy bands or they hop between the isolated states in the band tails. Finally, they are either extracted at their respective electrodes or they recombine. Recombination is undesirable, since it decreases the amount of free charge carriers available and therefore the conductivity, and additionally, in applications such as solar cells, we want to extract as many charge carriers from the material as possible. There are three main recombination pathways: direct, trap-assisted (also known as Shockley-Read-Hall, or SRH recombination) and Auger. These processes are sketched in Figure 2.6b. When an electron in the conduction band recombines with a hole in the valence band while emitting a photon with corresponding energy, this is a direct process. This process is prevalent in sufficiently clean, direct semiconductors⁴ such as Ge. This process can be assisted with a trap, where the charge carriers 'meet' at a trap in the bandgap. Given the smaller energy difference compared to a direct transition, this process is much more probable if there is a sufficient number of traps, leading to unwanted, non-radiative recombination. Lastly, an electron can give the energy difference to another electron, effectively exciting to a higher energy state (Auger process) and recombine with a hole in the valence band. We won't go into detail with any of these processes, we will just note that the trap-assisted recombination (and its variations) is the most relevant for EDMR and is usually directly related to the observed signal. The interested reader is referred to standard solid-state and semiconductor physics textbooks for more details. [37, 47].

EDMR can be observed when some charge carrier transition in a material is spin-dependent. The basic underlying principle under all of the spin-dependent process is the Pauli exclusion principle, or the Pauli blockade; two identical fermions⁵ cannot occupy the same quantum state simultaneously. Consider the trap-assisted charge carrier recombination described above, this time with the addition of spin. If an electron would like to recombine with a hole in a trap, the particles need to have opposite spin (forming a singlet); otherwise they would have the exact same state (forming a triplet), which is Pauli forbidden. In other words, the relative spin orientation, or spin-permutation symmetry, governs the transition probability between singlet and triplet states (under spin conservation conditions). Applying resonant microwave excitation that flips the one of the spins, makes more (or less) of these transitions allowed (or forbidden), therefore changing the recombination rates in the sample and effectively altering its conductivity.

⁴A direct semiconductor has a *direct bandgap*, i.e., the highest point of the conduction band and lowest point of the valence band are along the same direction in reciprocal (k) space. This transition can therefore happen without the assistance of phonons.

⁵Particles with half-integer spin, such as electrons,

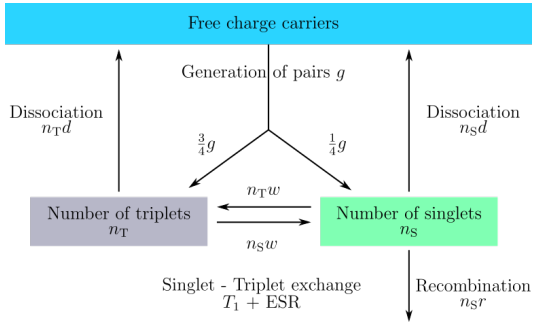


Figure 2.7: A visual representation of the KSM model based on rate equations.

Charge carrier hopping through singly occupied paramagnetic states can be imagined in a similar manner.

Historically, quantitative description of these processes has been a matter of much contention and it took a considerable time to formulate models that would reproduce the observed experiments. One unfortunate conclusion that makes the topic of EDMR rather complicated is that almost any model has to be tailored to the specific sample under investigation and there are very few general statements that one can make. However, most of the EDMR signals reported in literature can be described by the so-called Kaplan-Solomon-Mott, or KSM model, which we will briefly introduce. Other models of note are the Lépine and donor-acceptor recombination model. A more in-depth discussion of these and other various models can be found in [46] and [48]. The KSM model is a refinement of the Lépine model and introduces the concept of intermediate spin pairs, which are formed prior to the recombination event. Such pairs can form when the charge carriers come close to one another, for example when an electron is trapped in a band tail state close to a neutral dangling bond on the surface. After formation of such a pair, the charge carriers either recombine or dissociate, with the outcome dictated by relative orientation of the two spins. While this process can be described rigorously by quantum mechanics, here we take a more illustrative approach based on rate equations, as presented by Boehme and Lips in [49]. The model is illustrated in Figure 2.7 as well. A reservoir of free charge carriers generates singlet and triplet states with equal probability with a generation rate g . Since there are three times more triplet than singlet states, the generation rate of triplets is also three times higher. The system is represented by a number of singlet $n_S(t)$ and triplet states $n_T(t)$. The dissociation of these pair states is spin independent and has a probability of d , while recombination can only take place from a singlet state with the rate r . A singlet state can be transformed into a triplet state either by a longitudinal

spin relaxation or by resonant microwave excitation with a probability w . Based on these considerations, one can build a simple system of first-order ordinary differential equations [49]:

$$\partial_t \begin{pmatrix} n_T \\ n_S \end{pmatrix} = \begin{pmatrix} -[d+w] & w \\ w & -[d+r+w] \end{pmatrix} \begin{pmatrix} n_T \\ n_S \end{pmatrix} + \frac{g}{4} \begin{pmatrix} 3 \\ 1 \end{pmatrix}. \quad (2.44)$$

The change in conductivity, observable as an EDMR signal, is then directly related to the change in singlet recombination rate $n_S r$. These equations can then be solved and modified for a particular system or experiment. Examining these equations qualitatively, we can notice a number of peculiarities when compared to conventional ESR. The intensity of the radiation in the resonant case is connected to the exchange rate w with a square root dependence. In the KSM model, saturation of the ESR transition leads to a maximum signal, instead of line broadening as in conventional ESR. Additionally, the intensity of the EDMR line is independent of spin polarization, i.e., the same relative variation of conductivity would be observed at different magnetic fields and temperatures, which was confirmed experimentally as well. This holds for EDMR signals originating from intermediate spin pairs in general, but can fail for experiments performed at non-negligible polarization conditions, such as low temperatures and high magnetic fields; in those cases, the original EDMR model developed by Lépine becomes significant [46]. We can also see that the EDMR signal is closely related to the dynamics of charge carriers through the rate coefficients. This is advantageous on one hand, since it allows for determination of these rate coefficients using time-domain ESR experiments, but disadvantageous for continuous-wave measurements. Conventional ESR is usually performed with the help of a lock-in amplifier, which modulates the sample at a rate of 100 kHz. Electron spin dynamics are usually on the order of nano- and microseconds, which is much faster than the applied modulation rates. Charge carrier dynamics can, however, be both faster and slower, depending on various factors, such as charge carrier concentration, defect densities, injected current and others. This can easily lead to situations where the chosen modulation frequency is on the same order or faster than the dynamic behavior of the sample, and as a result, enhance, distort, or suppress the EDMR signal. Lee *et al.* have extensively studied various scenarios and found combinations of parameters where an EDMR signal is measurable only at high frequencies, only at low frequencies, or even just within a frequency window [50]. A modulation frequency dependence is therefore a requirement when searching for an EDMR signal.

Since we have not performed any quantitative analysis of EDMR signals in this thesis, this introduction to the topic should serve only as qualitative explanation of the observed signals and basis for further investigations. We should note that essentially all pulsed ESR

experiments have their EDMR equivalent, however, since no pulsed EDMR was performed in this thesis, we will omit this topic.

2.3.4 Ferromagnetic Resonance

Ferromagnetic resonance is analogous to electron spin and nuclear magnetic resonances. The main difference is that in the case of ferromagnet, the sample is not made up of an ensemble of isolated spin species, but strongly exchange-coupled spins, the excitations are therefore of collective nature. We can describe the macroscopic behavior of the sample similarly to the previously derived Bloch equations; however, we need to take into account the internal fields of a sample. As mentioned in passing in Section 2.1, a ferromagnetic material is strongly anisotropic and shape effects due to demagnetizing fields have to be considered. Demagnetizing factors, usually denoted as \mathbf{N} have rigorous meaning only for a small select number of shapes which can be derived from ellipsoids. For these special cases, Kittel has shown that the resonance frequency at which an FMR takes place can be expressed as [37].

$$\omega_{\text{FMR}}^2 = \gamma_e^2 (B_0 + (N_y - N_z)\mu_0 M)(B_0 + (N_x - N_z)\mu_0 M), \quad (2.45)$$

with the static magnetic field being applied along z and the MW field along the x -axis. For the case of a flat plate sample with B_0 perpendicular to the plate ($N_x = N_y = 0; N_z = 4\pi$), $\omega_{\text{FMR}} = \gamma_e(B_0 - \mu_0 M)$ and for a sphere ($N_x = N_y = N_z$) $\omega_{\text{FMR}} = \gamma_e B_0$. Additionally, in the case of single crystals, the resonance position will depend on the magnetocrystalline anisotropy. This makes FMR uniquely suited to extract the magnetic anisotropy constant K , which of interest in many applications such as magnetic recording and storage. The exact way how anisotropy affects the resonance position strongly depends on the symmetry of crystal of interest. The above equations also do not take into account magnetic domains and their interactions. In practice, it is usually necessary to complement FMR measurements with magnetometry and micromagnetic simulations in order to extract all necessary parameters and tailor the analytical model to the sample under study.

2.4 (Organic) field effect transistors

In the course of this thesis, we will use Organic Field-Effect Transistors (OFETs) to characterize the charge transport through various materials. The field-effect transistor and its variations, being a cornerstone of modern technology, have entire chapters and books dedicated to it. A rigorous treatment of the physics can be found, for example, in the standard textbook by Sze [47]. Here we will limit our discussion to the extraction of

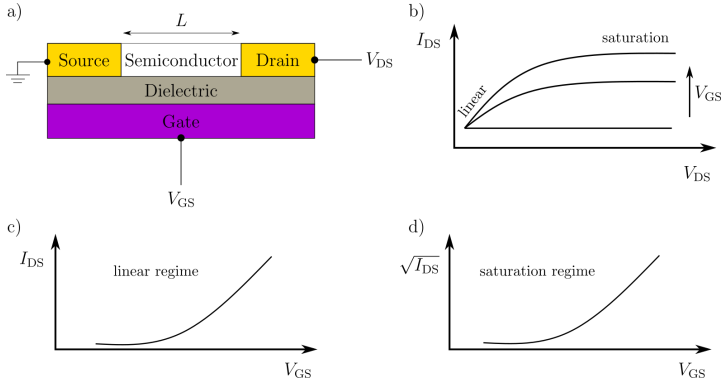


Figure 2.8: a) A schematic illustration of a field-effect transistor. b) Output characteristic of a FET at different V_{GS} . c) Transfer characteristic of a FET in the linear regime. d) Transfer characteristic of a FET in the saturation regime.

charge carrier mobility from the basic operational characteristics of a field-effect transistor, either organic or inorganic.

The essential components of a OFET can be seen in Figure 2.8a. It is composed of (usually metallic) source and drain electrodes on top of an electrically insulating layer, with a third electrode called the gate underneath. The semiconductor is only located between the source and drain electrodes. The source and drain electrodes have width W (channel width) and are separated by length L (channel length). Voltage is usually applied on the gate electrode and the drain electrodes, while the source electrode is usually grounded, therefore creating a potential difference between gate and source (V_{GS}) and drain and source (V_{DS}). Applying a negative V_{GS} will induce positive charge at the semiconductor-insulator interface, since the gate and source electrodes act as a capacitor. For p type semiconductors, this is desirable, whereas for n type semiconductors, positive V_{GS} inducing negative charges is needed. Not all of these induced charges will be mobile and contribute to a current, however, since deep traps caused by defects and contaminants have to be first filled. After filling of these trap states at a threshold voltage V_{th} , all additional charges will be free and will increase the conductivity of the semiconductor. The effective gate voltage is therefore $V_{GS} - V_{th}$. At $V_{DS} = 0$, the charge carrier concentration is uniform in space across the transistor channel. At small values of V_{DS} , there is a linear gradient of charge density between source and drain electrodes and the drain-source current I_{DS} is linearly dependent on V_{DS} . This is the so-called linear regime of a transistor. However, when increasing the drain-source voltage to a point where $V_{DS} = V_{GS} - V_{th}$, the local potential at the drain electrode is lower than the threshold voltage; therefore the

semiconductor is not conductive anymore and the channel is said to be 'pinched off'. After this, further increase of V_{DS} doesn't increase the current between drain and source and the current is said to be saturated. We should note that to study these phenomena, two experimental voltage-current characteristics are usually recorded: I_{DS} as a function of V_{DS} at different constant V_{GS} , known as *output characteristic* of a FET, and I_{DS} as a function of V_{GS} at a constant V_{DS} , corresponding to either linear or saturation regimes, known as *transfer characteristic* of a FET.

It can be shown that under usual operating conditions in transistors with relatively long channel lengths⁶, the drain-source current can be described as [51]:

$$I_{DS} = \frac{W}{L} \mu C_i \left[(V_{GS} - V_{th}) V_{DS} - \frac{1}{2} V_{DS}^2 \right], \quad (2.46)$$

with, μ being the charge carrier mobility and C_i the capacitance per unit area of the gate dielectric. In the linear regime $V_{DS} \ll V_{GS}$, equation (2.46) can be simplified to

$$I_{DS} = \frac{W}{L} \mu_{lin} C_i (V_{GS} - V_{th}) V_{DS}. \quad (2.47)$$

This equation can be easily solved for μ_{lin} to obtain the field-effect mobility in the linear regime (Figure 2.8b and c). After reaching the saturation regime, however, the current cannot increase anymore and the above equation is no longer valid. To obtain the saturation current, we can substitute $V_{DS} = V_{GS} - V_{th}$ to obtain:

$$I_{DS,sat} = \frac{W}{2L} \mu_{sat} C_i (V_{GS} - V_{th})^2. \quad (2.48)$$

In the saturation regime, the square root of the current is directly proportional to the gate voltage and it is therefore often plotted as such in the literature (Figure 2.8d). In OFETs, the mobility is, however, often a function of the gate voltage. For our application it is therefore better to take this into account and write

$$\mu_{lin} = \frac{L}{WC_i V_{SD}} \frac{\partial I_D}{\partial V_G} \quad \text{for } V_{DS} \leq V_G - V_{th} \quad (2.49)$$

$$\mu_{sat} = \frac{2L}{WC_i} \left(\frac{\partial \sqrt{I_D}}{\partial V_{DS}} \right)^2 \quad \text{for } V_{DS} \geq V_G - V_{th}. \quad (2.50)$$

⁶The so-called gradual channel approximation, where the electric field perpendicular to current flow (from V_{GS}) is much larger than the field parallel to the current flow (from V_{DS}). This approximation fails for very short channel lengths, but is valid in our experiments.

2.5 Low-level electrical measurements

Measurements of weak signals is an intrinsic part of experimental science. In the course of this thesis, two distinct measurement setups to detect changes in the conductivity of a sample, both small and large, were developed. To explain some of the decisions and the terminology used, a brief introduction to electrical measurements will be given in the following. Most information here was taken from the excellent Low-Level Measurements Handbook from Keithley [52] and from data sheets of the relevant instruments.

Virtually all experiments can be (or should be) reduced to measuring either voltage, current or resistance. Whether it's a Hall probe monitoring a magnetic field, a photomultiplier tube registering impacts of single photons or an ESR spectrometer probing spin dynamics of a sample, all of the physical processes have to be in the end converted to electrical signals, since that is what our current technology can reliably measure. The three most important electrical quantities are related by the well-known Ohm's law:

$$V = I \cdot R, \tag{2.51}$$

with V being the voltage, I the current and R the resistance. The fundamental limit on sensitivity in most measurements determined by the noise generated by resistances in the circuit⁷, which include the sample (or Device Under Test (DUT) in engineering) and the complete measurement instrumentation. The noise produced by thermal movement of charges with the circuit is called Johnson or thermal noise and its power is

$$P = 4k_{\text{B}}TRB \tag{2.52}$$

with T being the absolute temperature, and B the measurement bandwidth in Hz. Since Johnson noise is a so-called white noise, i.e., uniformly distributed over the frequency spectrum, how much of the spectrum are we integrating into our measurements is important. This is related to the measurement time - if we're averaging each point for 1 second, our measurement bandwidth is 1 Hz⁸. Metallic conductors approach this theoretical noise limit, other materials, however, such as semiconductors, can have additional internal processes that produce higher noise at certain frequencies. The most important example is the flicker noise with its typical $1/f$ frequency dependence, which comes from charges getting trapped and released by shallow traps in band tails (see Section 2.3.3). For

⁷There are two main additional noise sources in electrical measurements, flicker ($1/f$) noise and shot noise, which can become dominant under special conditions.

⁸The real measurement bandwidth also depends on the input capacitance of the instrumentation being used for the measurement, since it forms an RC circuit with the DUT and wiring, which will have a certain rise and fall times and therefore limit the achievable B .

practical purposes, we can use the equations

$$V_{\text{noise}} = \sqrt{4k_{\text{B}}RB} \quad (2.53a)$$

$$I_{\text{noise}} = \frac{\sqrt{4k_{\text{B}}RB}}{R}, \quad (2.53b)$$

to obtain the expected RMS values of voltage and current noise, respectively. All real voltage and current sources contain an internal resistance and as such, they exhibit Johnson noise in addition to the sample, or DUT.

Direct Current (DC) Voltages and current are most commonly measured by digital multimeters with unshielded cables. Generally, these are sufficient for signals greater than 1 μV , 1 μA , or less than 1 $\text{G}\Omega$. These devices, however, don't approach the theoretical limits of sensitivity. To be able to reliably read out smaller signals, more sensitive, dedicated instruments have to be used, such as Source-Measure Units (SMUs), nanovoltmeters or a switch to AC methods, such as lock-in amplification has to be made. When comparing different devices and choosing one for a particular measurement, one has to consider a number of instrumental parameters. The most important one is the sensitivity, which is closely related to resolution and accuracy. Sensitivity is the smallest change in the signal that can be detected. It is determined by the instrument resolution and measurement range. For example, a nanovoltmeter can have a 7.5 digit resolution in a 10 mV range, meaning it can display 7 whole digits (each between 0 and 9) plus a leading half digit which is either 0 or ± 1 . A signal of 10 mV would be displayed as 10.00000 mV, meaning that the nanovoltmeter has indeed 1 nV sensitivity. Each instrument also has a defined accuracy, which is the agreement between a measured value and its true value. This is usually specified as (\pm ppm of reading + ppm of range). This is especially important when making absolute, quantitative measurements. It is not to be confused with precision, which is a more qualitative term related to the reproducibility of a measurement.

Of course, the more sensitive our instruments are to the signals of interest, the more easily disturbed are they by unwanted signals, in general called noise. These can come either from other instruments in the laboratory or even from other instruments connected to the electrical circuit in the building. Consideration of noise sources and their elimination or filtering is therefore of paramount importance in low-level measurements. Some best practice recommendations for practical experimental setups, going from least effort and most common to more exotic:

- Twisting of the measurement leads to minimize noise induced from electromagnetic waves in the environment. Each loop of wire acts as an antenna and twisting reduces the area of such loops.
- Separating low-level signals from noisy ones. Where the signal and power cables

must cross, cross them at right angles and maximum separation.

- Using coaxial shielded cables.
- Choosing a single grounding point for all instruments to minimize ground loops.
- Using triaxial shielded cables.
- Filtering and amplifying the signals of interest before measuring them.
- Adding filters between the power supply of the instruments and the electrical network.
- Using batteries to power measurement equipment.
- Transfer digital signals from the measurement equipment to the PC using optical links, to galvanically separate the two electrical networks.

The above discussion and selection of tips are but a small fraction of the available knowledge. Much more details can be found in [52] and the older but useful Handbook of Measurement Science [53].

Among other sources of errors, thermoelectric voltages can play a large role in low-voltage measurements. These voltages are generated when conductors made of different materials are joined together. Microvolts of thermal voltages can be caused by temperature gradients in the test circuit, for example due to fluctuating temperatures in the lab. Common ways of minimizing these effects are using the same materials for all conductors and minimizing temperature gradients in the circuit, which is, however, not always possible. In those cases, one useful method to eliminate thermoelectric fluctuations and temperature drift is the Delta method. With this method, the current sourced to the DUT is periodically reversed, usually at a rate of a few Hz and voltage measurements are taken after each reversal. Each data point is a moving average of three voltage readings, which leads to canceling of any thermoelectric voltages, linear drifts and leads to a decrease of noise due to the averaging.

An additional possibility of reducing noise in measurements, if the speed of the DUT allows it, is to shift the signal of interest from DC to a different frequency. A very common method of achieving this is using a Lock-In Amplifier (LIA). LIAs extract signals in a defined frequency band around a reference frequency, effectively rejecting all other frequency components. This is done by multiplying the measured signal with a reference signal and applying a low-pass filter to the result. The reference signal can be generated by the LIA or provided from an external source. Modern instruments can extract a signal of interest which is buried in noise up to a million times higher in amplitude. As an example, LIAs are used in virtually all continuous wave ESR spectrometers. The signal is modulated by additional modulation coils near the sample, which modulate the B_0 field by a small amount (around 0.1 mT) at frequency of usually 100 kHz. Since this scheme modulates the resonance position, the resulting signal after amplification is proportional

to the slope of the measured curve at any given point, resulting in the first derivative of absorption shape typical of ESR.

3 Towards CMOS compatible spintronics

In this chapter, the development of a CMOS compatible spintronic platform for potential integration with molecular quantum bits is discussed. To this aim, a novel manufacturing method of the ferromagnetic semiconductor alloy Mn_5Ge_3 directly on top of a doped Ge(111) channel was developed. By thermal annealing of a Mn/Ge material stack, a thin layer of Mn_5Ge_3 is formed at the material interface with atomically sharp transition. This process was shown to be robust with respect to annealing conditions and doping of the Ge substrate. To be able to study the electrical properties of our spintronic devices, a low-temperature magnetoresistance experimental set-up was designed, assembled, tested and optimized at the IPC. This set-up was subsequently used to perform three- and four-terminal Hanle measurements on devices with our novel ferromagnetic electrodes to assess their potential for studying the interaction between spin-polarized charge carriers and MQBs. After identifying some challenges with our chosen materials and processes, a possible way forward by switching to Ge(100) is explored by magnetometry and FMR experiments. Parts of this chapter were published in [54]. This part of the thesis was carried out in close collaboration with Dr. Stefan Bechler, Dr. Li-Te Chang, Hannes S. Funk, David Weißhaupt, Prof. Dr. Inga A. Fischer and Prof. Dr. Jörg Schulze from the Institute of Semiconductor Engineering of the University of Stuttgart. High-Resolution Transmission Electron Microscopy (HRTEM) analysis was performed by Dr. Gerard Colston and Dr. Maksym Myronov from the University of Warwick.

3.1 Introduction

Spintronics, or spin electronics, refers to the study of spin phenomena in solids, be it metals, semiconductors or insulators, as they pertain to information processing and transfer. The goal of spintronics, apart from fundamental research, is the usage of the spin of a charge carrier in addition to or instead of its charge as a degree of freedom for information processes [41]. Some spintronic devices are already a part of everyday technology, such as

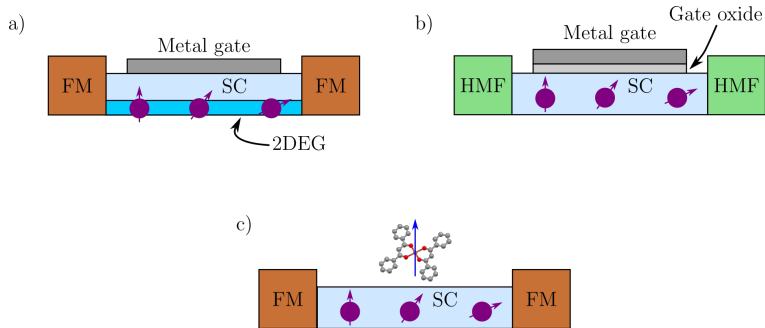


Figure 3.1: a) Spin-FET proposed by Datta and Das. b) Spin-MOSFET proposed by Sugahara and Tanaka. c) Our proposed architecture for electrical read out of MQBs.

giant magnetoresistance read heads in hard drive magnetic storage. Other information storage technologies are either already integrated into CMOS processes, such as magnetic random access memory or the spin-transfer-torque random access memory [9]. Information processing, however, is still in the proof-of-concept stage. One of the most promising concepts in CMOS extension is the spin transistor, of which there are two variants: the spin-Field-Effect Transistor (FET) proposed by Datta and Das [55] and the spin-Metal-Oxide-Semiconductor Field-Effect Transistor (MOSFET) by Sugahara and Tanaka [56] (Figure 3.1a and b, respectively). While both of the devices work as transistors and take advantage of magnetoresistive effects for, their operating principles are quite different. The original spin-FET proposal used FM electrodes (such as Fe) for electrical injection and detection of spin-polarized electrons into a Two-Dimensional Electron Gas (2DEG), while the metallic gate served to control the spin orientation of the injected charge carriers with applied electric field through the Rashba effect. The magnitude of the output current is dependent on the angle between the electron spin and magnetization of the second FM electrode. In the spin-MOSFET, the gate performs the same function as in a usual MOSFET, the drain-source current, however, depends on the angle between magnetizations of the Half-Metallic Ferromagnet (HMF) electrodes. In both cases, this expands the capabilities of usual FET transistors by adding the possibility of having a non-volatile information storage unit directly in the transistor. We have decided to take some inspiration from these concepts and modify them to be able to design a platform for electrical read out of MQBs. Figure 3.1c shows a schematic image of the concept. An FM electrode electrically injects a spin-polarized charge carrier into the semiconductor channel. While drifting through the channel, this charge carrier interacts with the magnetic moment of a MQB deposited on top of the channel via dipolar interaction. This influences the

spin polarization of the charge carrier. Since the magnetoresistance of the whole device depends on the angle between the charge carrier spin and the second FM electrode, it should be theoretically possible to observe this interaction, by carefully monitoring the current while the spin of the MQB is manipulated.

To realize this vision, a few prerequisites have to be met. Spin polarized charge carriers have to be efficiently injected and extracted, which requires low conductivity mismatch between the FM electrodes and the semiconductor channel (see Section 2.2.3). At the same time, the spin polarization of the charge carriers has to travel from the injector to the detector, meaning the spin diffusion length in the semiconductor channel has to be on the order of distance between the electrodes. Finally, maintaining CMOS compatibility in the manufacturing process would ease the potential transition to real-world applications. Naturally, there are some constraints on the MQBs as well; however, they will be partially dictated by the spintronic platform. To ensure CMOS compatibility and sufficient spin-diffusion length (also called spin-flip length, l_{sf}), we decided to use germanium as the material for the semiconductor channel. Germanium can be grown on industry standard Si wafers, with both (111) and (100) orientation and is already integrated in many CMOS processes. l_{sf} depends only on the mobility of the charge carriers and the spin lifetime. Compared to silicon, germanium has a higher mobility for both electrons and holes¹, promising higher l_{sf} . Another significant advantage is the existence of the ferromagnetic Mn_5Ge_3 alloy. Mn_5Ge_3 has been proposed as a promising material for spintronics since the 2000s [57]. Its Curie temperature is very close to ambient temperatures, 296 K, and can be extended up to 450 K by C doping [58]. Even more importantly, its conductivity is close to the conductivity of doped Ge, removing the necessity of using a tunneling barrier for spin injection. Mn_5Ge_3 has a hexagonal crystal structure and can be grown epitaxially on Ge(111) surface with 3.7 % lattice mismatch, with almost no threading dislocations [59]. Mn_5Ge_3 can be grown on top of Ge with a wide variety of methods. Generally, they consist of successive evaporation or co-evaporation of Ge and Mn in either high or ultra-high vacuum (molecular beam epitaxy systems), while being heated to substrate temperatures varying from room temperature to 650 °C or being annealed at temperatures from 350 °C to 650 °C post-deposition *in situ* [57–63]. These methods, while providing a high degree of control and offering possibilities to study the material during growth, often include steps which are not CMOS compatible, such as molecular beam epitaxy techniques or prolonged exposure to high temperatures. To explore routes to more application-relevant fabrication methods, we decided to investigate a facile way of Mn_5Ge_3 fabrication utilizing simple thermal evaporation of Mn onto a crystalline Ge

¹The mobility of electrons and holes at 300 K in Ge is $3900 \text{ cm}^2 \cdot \text{V}^{-1} \cdot \text{s}^{-1}$ and $1900 \text{ cm}^2 \cdot \text{V}^{-1} \cdot \text{s}^{-1}$, respectively, compared to $1450 \text{ cm}^2 \cdot \text{V}^{-1} \cdot \text{s}^{-1}$ and $500 \text{ cm}^2 \cdot \text{V}^{-1} \cdot \text{s}^{-1}$ in Si.[47]

surface, followed by an *ex situ* annealing step. This method is inspired by the industry-standard self-aligned silicide process (Salicide), which is used in CMOS technology to produce ohmic contacts on Si-based devices through a solid-state reaction between thin metallic films on top of Si subjected to a series of annealing and etching processes. Abbes *et al.* investigated such a self-aligned germanide process in 2013 using *in situ* X-Ray Diffraction (XRD) measurements [64]. They deposited Mn on amorphous Ge on top of SiO₂ and monitored the XRD pattern upon annealing, revealing that Mn₅Ge₃ starts forming at $T \approx 210^\circ\text{C}$ and disappears at $T = 650^\circ\text{C}$. However, already at $T \approx 310^\circ\text{C}$, the antiferromagnetic Mn₁₁Ge₈ starts forming, which precludes electrical spin injection experiments. Building upon this process, we developed and studied potential spintronic structures and measurement equipment for the electrical read out of MQBs.

3.2 Experimental methods

Sample fabrication

All of these steps were performed in a clean room at the Institute of Semiconductor Engineering, University of Stuttgart. The samples were fabricated starting with the growth of Ge on p^- Si(111) wafers using molecular beam epitaxy. After the growth of a 50 nm Si-buffer and 100 nm of Ge at a substrate temperature of 330 °C, the samples were annealed at 820 °C to form a Ge-virtual substrate (for details on the formation of thin virtual substrates we refer to [65]). This was followed by the growth of 300 nm of undoped Ge and 100 nm of doped Ge with varying dopant concentrations using B and Sb as dopant materials. For all samples, Mn₅Ge₃ was formed as follows: the deposition of Mn was carried out using thermal evaporation from a W boat at room temperature followed by deposition of 30–80 nm of Al to prevent Mn from oxidizing. Before deposition of the metals, the samples were dipped in buffered HF for 10 s and rinsed in deionized water to clean the Ge surface and remove the native Ge oxide. Samples were then subjected to an *ex situ* thermal annealing step under N₂ atmosphere in a Steag ASH SHS 200 RTP system. For magnetometry studies, the samples were diced into 3×3 mm² dies.

In the case of structured samples for magnetoresistance measurements, device fabrication started with the structuring of a mesa using photolithography and reactive ion etching. SiO₂ was then deposited as a passivation layer in a plasma-enhanced chemical vapor deposition system. After opening of contact holes using photolithography and reactive ion etching, the contact metals Mn and Al were deposited and structured with a liftoff process. Four-terminal Hanle structures were structured using additional electron beam lithography process. More details on the process itself can be found in [66].

Magnetometry

Magnetometry measurements were performed in a Quantum Design MPMS3 Superconducting QUantum Interference Device (SQUID) magnetometer. Samples were $3 \times 3 \text{ mm}^2$ dies within standard straws and fixed using PTFE tape and Mylar foil. To extract the saturation magnetization from the low-temperature magnetization measurements, the diamagnetic background was fitted and subtracted from the data. Coercive fields were extracted via linear interpolation of points near to zero magnetization. Reported errors are errors of fit of the magnetic moment calculated by the magnetometer and propagated using Gaussian error statistics where applicable.

High-resolution Transmission Electron Microscopy

HRTEM measurements were carried out at the University of Warwick using a JEOL 2100 TEM operating at an accelerating voltage of 200 kV. Sample cross sections were prepared through mechanical grinding and Ar milling within a precision ion polishing system to achieve electron transparency.

Magnetoresistance

Magnetoresistance measurements were performed in lab-built set-up developed in this thesis. It includes an Oxford Instruments 10 T Spectromag with a variable temperature insert and custom probe head that allows for electrical measurements. To monitor the resistance of the sample, either a Keithley 2400 Source-Measure Unit, a Keithley 2450 Source-Measure Unit or a Keithley 6220 current source was used, together with a Keithley 2182A Nanovoltmeter. More details can be found in Section 3.4.

Ferromagnetic Resonance

Ferromagnetic resonance measurements were performed on a Bruker EMX X-Band EPR spectrometer at the IPC. Samples were $3 \times 3 \text{ mm}^2$ dies, fixed with Mylar foil and Apiezon N grease within standard 3 mm X-Band EPR tubes rotated with a goniometer accessory.

3.3 Formation of Mn_5Ge_3 by thermal annealing

Building upon previous studies of Mn_5Ge_3 (Section 3.1), we decided to investigate the influence of annealing parameters on Mn_5Ge_3 formation based on a solid-state reaction of elemental Mn on top of crystalline Ge(111), as well as the influence of Ge doping. An aluminum cap layer on top of Mn was used to prevent oxidation, as well as to provide electrical contact. A schematic representation of the reaction can be seen in Figure 3.2a. With the first sample series, we investigated two annealing parameters: maximum temperature and heating rate. Figure 3.2b shows a visualization of the annealing processes, while an overview of the parameters and sample designation can be found in Table 3.1.

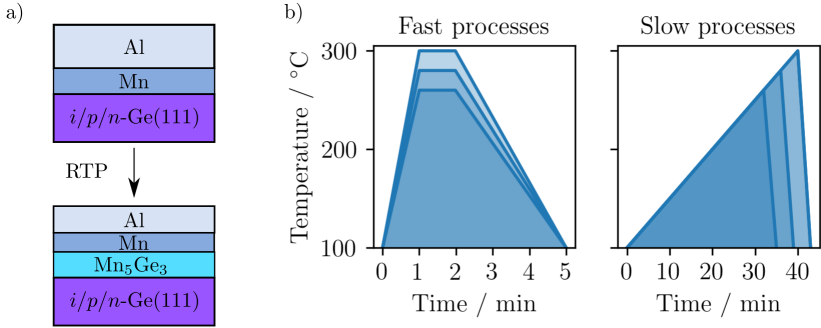


Figure 3.2: a) Schematic representation of the solid-state reaction investigated. b) Nominal temperature profiles used in this study.

Table 3.1: Annealing parameters for Mn_5Ge_3 formation investigations. In all protocols, the starting temperature was 100°C and the ramp-down time 3 minutes.

Sample designation	Ramp / $^\circ\text{C min}^{-1}$	End / $^\circ\text{C}$	Plateau / min
260fast	160	260	1
280fast	180	280	1
300fast	200	300	1
260slow	5	260	-
280slow	5	280	-
300slow	5	300	-

After sample fabrication, SQUID magnetometry was used to study the magnetic properties of the layers. Figure 3.3a shows the in-plane (B_{\parallel}) magnetization dependence on temperature of all the samples investigated in this series of measurements. All of the

samples display a rapid increase in magnetization at $T_C = (300 \pm 5)$ K, with a subsequent almost monotonic increase of magnetization while cooling down to 5 K. As a representative example, Figure 3.3b shows the magnetization curves of the **300fast** sample with the magnetic field applied both in- and out-of-plane (B_{\perp}) of the sample at $T = 5$ K. In both orientations, the samples display an open hysteresis loop with almost identical coercive fields (B_C), but clearly different saturation magnetizations (m_{sat}) and remanence (m_{rem}). This behavior was consistent across all samples, as can be seen in Figures 3.3c and d. When compared against each other, we can see that samples exhibit almost identical B_C , while the variations are mainly in m_{rem} and m_{sat} . Of interest is also the ratio $m_{\text{rem}}/m_{\text{sat}}$, which can be related to the thickness of the ferromagnetic layer [67]. All of the extracted parameters can be found in Table 3.2. We can observe a trend of increasing both m_{rem} and m_{sat} at higher annealing temperatures, while their ratio decreases slightly for the fast recipes and stays within the experimental error for the slow recipes, with the exception of **280slow**, which seems to be an outlier.

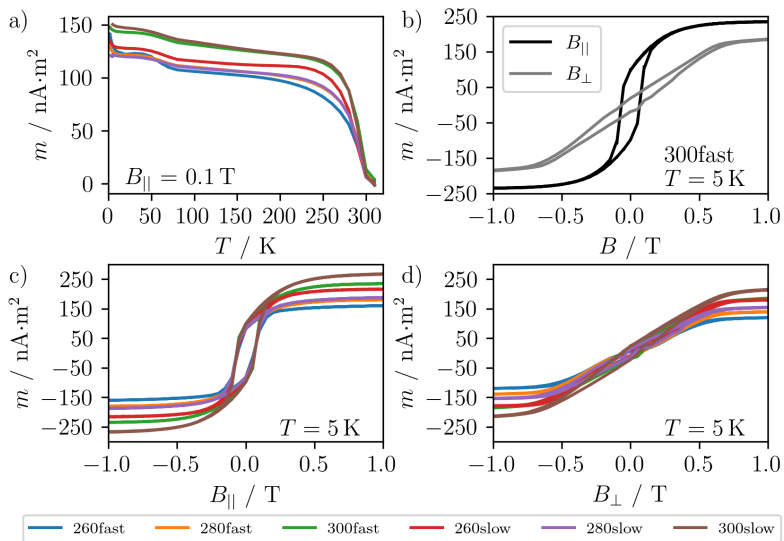


Figure 3.3: a) In-plane magnetization temperature dependence with an applied field of 0.1 T. b) Magnetization measurement of the **300fast** sample at 5 K. c) In-plane magnetization measurements of the investigated samples at 5 K. d) Out-of-plane magnetization measurements at 5 K. © IOP Publishing. Reproduced with permission from [54]. All rights reserved.

The temperature dependent measurements reveal that the same magnetic phase is dominant in all samples, with the ordering temperature of $T_C = (300 \pm 5)$ K being

Table 3.2: Summary of the sample properties extracted from magnetometry measurements.

	260fast	280fast	300fast	260slow	280slow	300slow
$m_{\text{rem}} / \text{nA}\cdot\text{m}^2$	79 ± 4	84 ± 4	99 ± 5	83 ± 4	85 ± 4	101 ± 5
$m_{\text{sat}} / \text{nA}\cdot\text{m}^2$	162 ± 8	180 ± 5	236 ± 8	217 ± 5	190 ± 8	270 ± 11
$m_{\text{rem}}/m_{\text{sat}} / \%$	49 ± 3	47 ± 3	42 ± 3	38 ± 2	45 ± 3	37 ± 2
B_c / mT	65 ± 8	64 ± 9	67 ± 8	65 ± 9	65 ± 8	66 ± 8

consistent with Mn_5Ge_3 . Low-temperature magnetization measurements further confirm that all samples are ferromagnetic, since they all exhibit magnetic saturation and possess a remanent magnetization at zero magnetic field. Due to the higher saturation and remanence measured with the magnetic field oriented parallel to the sample plane, we can conclude that the magnetization is mostly in-plane, however, with significant out-of-plane components as well. While there is no simple, analytical expression between the film thickness and $m_{\text{rem}}/m_{\text{sat}}$ ratio, we can at least estimate it, based on the data presented in [67] and discuss this qualitatively. A decrease of $m_{\text{rem}}/m_{\text{sat}}$ indicates an increase in layer thickness. Observing the trends in our sample series, we can see that for the “fast” group of recipes, higher temperatures lead to an increase in layer thickness, as well as that for the same final temperature, a slower ramp will result in a thicker layer. A possible reason is that higher temperatures increase material interdiffusion, since the diffusing atoms have more thermal energy, and that prolonged exposure allows for more material mixing, thus creating a thicker layer. Within the “slow” recipes, there are two curiosities. One, there are only marginal differences between the $m_{\text{rem}}/m_{\text{sat}}$ ratio of **260slow** and **300slow**, even though there is a notable increase in saturation magnetization, suggesting that more ferromagnetic material is present. Two, sample **280slow** has a notably lower saturation magnetization than **260slow**, while the remanence is the same within experimental error. More study would be needed to understand why this is the case. Comparing the extracted $m_{\text{rem}}/m_{\text{sat}}$ values with the data from [67], we can estimate that the Mn_5Ge_3 thicknesses in our samples range between 15 nm and 20 nm. Transmission Electron Microscopy (TEM) Analysis of the **300fast** sample was performed at the University of Warwick to measure the thickness exactly and assess the quality of the samples. Figure 3.4 presents the images obtained in (111) diffraction condition. In Figure 3.4 a and b, we can observe the cross-section of the sample at the same magnification in bright and dark fields, respectively. The sample is composed of four layers: the Molecular-Beam Epitaxy (MBE) grown Ge in direct contact with Mn_5Ge_3 , residual Mn not consumed during the annealing, and an Al cap layer. The thickness of the Mn_5Ge_3 is ≈ 12 nm, while the residual Mn is ≈ 10 nm thick. This data confirms the approximate calculations of Mn_5Ge_3 layer thickness based on the $m_{\text{rem}}/m_{\text{sat}}$ ratio. The nominal thickness of the deposited Mn layer was 18 nm, meaning that 8 nm of Mn

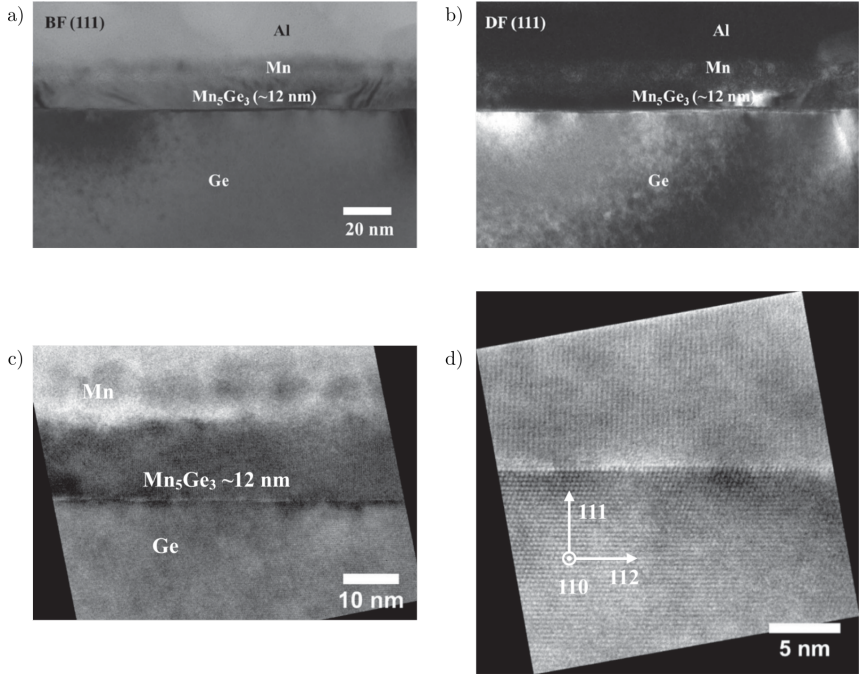


Figure 3.4: Cross-sectional TEM images of the **300fast** sample in a) bright field and b) dark field. c) HRTEM image of the Mn/Mn₅Ge₃/Ge region of the sample cross-section. d) HRTEM image of the interface between Mn₅Ge₃ and Ge. © IOP Publishing. Reproduced with permission from [54]. All rights reserved.

transformed into 12 nm of Mn₅Ge₃. From the dark field image, we can deduce that the Mn₅Ge₃ layer is most likely polycrystalline, given its low intensity. Figure 3.4c shows an HRTEM image of the Mn/Mn₅Ge₃/Ge region. Here we can observe in more detail that the interface between the residual Mn and Mn₅Ge₃ is relatively rough and not well defined, while the transition between Mn₅Ge₃ and Ge is flat. Figure 3.4d brings the Mn₅Ge₃/Ge interface into an even closer focus. This image shows a definite, atomically sharp transition between the diamond cubic lattice of Ge and the hexagonal lattice of Mn₅Ge₃, with the Mn₅Ge₃ *c*-axis parallel to the Ge(111) direction, confirming epitaxial growth of Mn₅Ge₃ on Ge.

We can now assess the obtained information in the context of spin injection. As discussed at length in [67], due to the competing magnetostatic and magnetocrystalline anisotropies, there are two distinct magnetic regimes in Mn₅Ge₃ thin films. When the

film thickness is under 10 nm, the film can be considered single-domain, with all of the magnetization being in-plane. When the thickness reaches 20 nm and higher, the magnetocrystalline anisotropy forces the magnetization into stripe domains, with their magnetization pointing alternatively up and down completely out-of-plane. There is a gradual transition between the two regimes at the intermediate thicknesses, in which our samples find themselves. For spin injection experiments, such as Hanle or spin-valve measurements (Section 2.2.3), the magnetization of the injection electrodes must be well defined, homogeneous, and in-plane. The atomically sharp interface between Mn_5Ge_3 and Ge observed in the TEM measurements is therefore ideal for such experiments, as any roughness would cause stray fields, leading to depolarization of the injected charge carriers. The variation in thickness of the Mn_5Ge_3 layer, as seen at the interface between the ferromagnet and the residual Mn, could be potentially problematic, as it could create domains with different magnetization orientations. Similarly, the fact that the thickness of the fabricated layers, while close to the monodomain regime, contains out-of-plane domains is non-ideal, leading to the aforementioned stray fields and injection of charge carriers with varying spin orientation. Both of these problems could be potentially solved by depositing a lower amount of Mn, such that the final Mn_5Ge_3 layer would be entirely in the monodomain regime, and all of the Mn would be consumed. It is, however, difficult to predict what would happen with the Al cap layer after the consumption of Mn. This process would require further study of the annealing parameters.

We have demonstrated that the formation of Mn_5Ge_3 through *ex situ* annealing is a simple, fast, and robust process leading to the fabrication of thin ferromagnetic films with an atomically sharp interface to Ge. We have also investigated if this process is influenced by the type or concentration of dopants in Ge, with results suggesting no or negligible influence (Appendix A). The relatively low temperatures and short exposure to them, along with the *ex situ* processing of Mn, make this process potentially suitable for implementation into CMOS technology. Given all of these benefits, we have used this process to fabricate the samples used for spin injection experiments described in this chapter.

3.4 Development of a low temperature magnetoresistance measurement set-up

In order to pursue the aim of this work, namely the electrical read-out of a molecular qubit spin state, a new experimental set-up was needed at the Institute of Physical Chemistry, University of Stuttgart (IPC). We have considered the following requirements:

1. Variable temperatures between 300 K and 2 K - the interactions and excitations of interest in the systems chosen for initial investigations are observable mainly at cryogenic temperatures. At the same time, the ability to reach room temperature is useful for evaluation of application feasibility of the developed systems.
2. Magnetic fields up to at least 3 T - the materials and interactions in this work are all based on magnetism; therefore, a variable magnetic field is necessary to study them. To eventually manipulate MQBs using ESR, magnetic fields compatible with our compatible microwave sources should be reachable.
3. Electrical access - to study the behavior of charge carriers and manipulate them in a manner closest to applications, electrical access to the samples is required. Care has to be taken to allow for measurements of weak signals, i.e., mitigate noise as much as possible.
4. Optical access - to allow for potential manipulation of the qubits with light, microwaves, or both, an optical access is needed.

The Oxford Instruments Spectromag SM4000 was already available at our institute and fulfilled three out of the four requirements: it has a Variable Temperature Insert (VTI) capable of reaching temperatures between 1.5 K and 300 K, a split-coil magnet with maximum fields of ± 10 T, and optical access from 4 sides. To allow for electrical measurements, we decided to modify an existing VTI probe, which I had previously developed for Torque Detected Electron Spin Resonance (TDESER) measurements [68][69]. The development had three main stages: proof-of-principle set-up, design of a new set-up, along with assembly and testing, and finally optimization with outlining of possible upgrade paths.

3.4.1 Proof-of-principle measurements

As a first step in the project, the verification of suitability of the selected magnet was necessary. To this end, we attempted to reproduce spin injection from a $\text{Mn}_5\text{Ge}_3\text{C}_{0.8}$ layer into a germanium channel in a 3T Hanle measurement configuration (Section 2.2.3). Such measurements were previously performed at the University of California, Los Angeles (UCLA) by Dr. Li-Te Chang and published in [70]. The original device (sample **3Tref**) used in [70] was used for these measurements. Figure 3.5 displays the architecture and composition of the sample. It consisted of three rectangular terminals with sputtered $\text{Mn}_5\text{Ge}_3\text{C}_{0.8}$ on top of a degenerately n -doped Ge(111) channel, with a 2 nm Al_2O_3 tunneling barrier between them. More details about the sample can be found in [70].

As can be seen in Figure 3.5a, at least three current/voltage leads are required for the measurements. For more flexibility and redundancy, we used four cables for the initial experiments. We wanted to modify the existing TDESER probe as little as possible so that

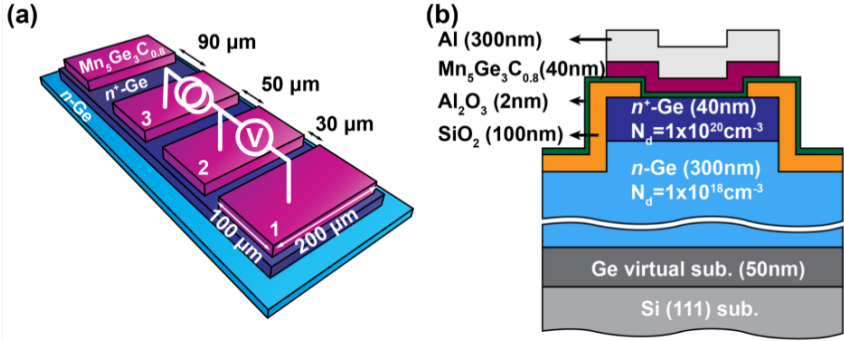


Figure 3.5: 3Tref device used for the proof-of-principle measurements. (a) Architecture and terminal numbering, (b) terminal cross-section. Reproduced from [70], with the permission of AIP Publishing.

it could be easily returned to its original state after the fabrication of a dedicated probe for electrical measurements. We focused on the bare minimum requirements to run the measurements, namely

- mount the sample in the VTI,
- connect the sample to a feedthrough at the top of the VTI,
- connect the feedthrough connectors to a current source and a voltmeter.

Figure 3.6 shows the original TDESr probe before any modification. For the initial measurements, we removed the stepper motor along with its mounting bracket (1) and slider (2) since no detailed angular dependence was necessary. We have also decided not to use the static exchange gas chamber (8), since it unnecessarily increased the system’s complexity and the measurements were not expected to be sensitive to He gas flow. The Bayonet Neill–Concelman (BNC) port was exchanged for a feedthrough with four individual DEE101-A004 hermetic receptacles from Fischer connectors. Four single-core, epoxy-insulated, unshielded copper cables were soldered to the plugs and routed down to the probe head (10), where precision pin receptacles were soldered onto the ends. The sample holder (11) was exchanged for simpler, older variant into which two threaded holes were drilled. Afterward, the sample was glued and wire-bonded to an expander Printed Circuit Board (PCB), and the whole PCB was attached to the sample holder with two screws. The direct connection between the PCB and the sample holder ensured good thermal contact. The used sample holder is photographed in Figure 3.7. Outside of the VTI, we have used custom made, shielded cables with S101-A004 plugs from Fischer connectors on one side and a standard BNC connector on the other. The BNC connectors were connected to the used Keithley 2400 SMU through banana plug adapters.

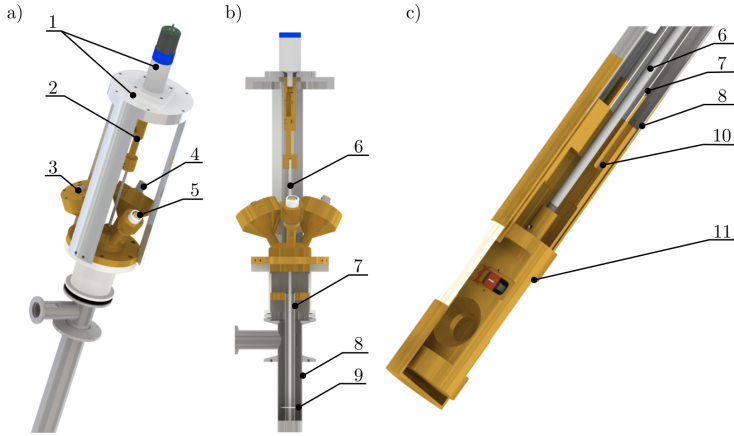


Figure 3.6: The original TDESER probe, before modifications. a) Upper part of the probe. b) Partial section of the upper part. c) Partial section of the lower part. Individual components of the probe: 1 - stepper motor with mounting bracket, 2 - up/down slider, 3 - BNC feedthrough, 4 - optical fiber feedthrough, 5 - temperature sensor feedthrough, 6 - sample holder rod, 7 - sample holder rod housing, 8 - static exchange gas chamber, 9 - temperature shields/cable guides, 10 - probe head, 11 - sample holder. Pictures adapted from [68].

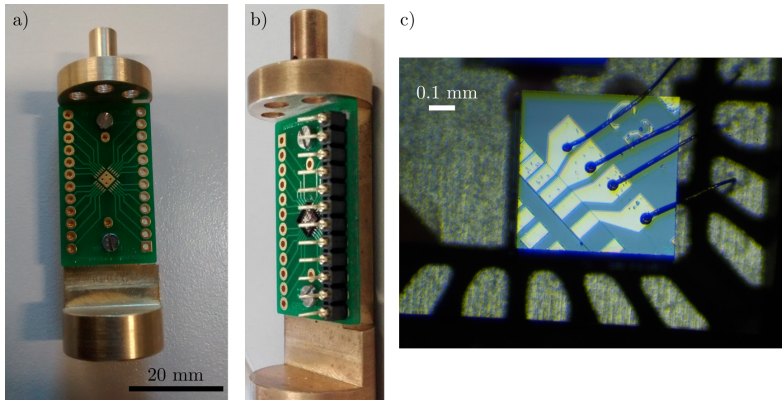


Figure 3.7: Sample holder used for the first measurements. a) Sample holder with a blank PCB chip, b) sample holder PCB on which the sample is glued and wire-bonded, c) microscope image of the prepared sample.

The **3T**ref sample was mounted (Figure 3.7b and c and connected the same way as in [70] (Figure 3.5a). As a first test, we performed temperature-dependent $I - V$ measurements between terminals 1 and 2, to verify the basic electrical behavior of the sample. Figure 3.8a and b compares the $I - V$ measurements performed at IPC and UCLA, respectively. We can observe that at room temperature, the sample displays linear, ohmic behavior which becomes increasingly non-linear around $V_{12} = 0$ with decreasing temperature. The non-linear behavior is a direct consequence of the Al_2O_3 tunneling barrier between the $\text{Mn}_5\text{Ge}_3\text{C}_{0.8}$ and Ge layers. We can also observe that the overall resistance between the two contacts increases with decreasing temperature, as is expected for a semiconducting material. There are slight differences observable in the absolute currents measured at comparable temperatures between the two experimental set-ups, e.g., at 300 K, with $V_{12} = 1$ V, $I_{12} = 18$ mA at IPC while at UCLA $I_{12} \approx 16$ mA. The small differences are probably caused by a lower serial resistance of the whole experimental set-up used at the IPC, given that these are 2-point measurements, measuring the resistance of the whole current path between the terminals of the source-meters. Besides that, we can observe that the measurements are essentially the same, confirming that both the sample and experimental set-up work as desired. After cooling the sample down, we have applied a constant current of $I_{23} = -1$ mA and monitored the voltage V_{12} while sweeping the magnetic field applied perpendicularly to the layers (B_{\perp}).

The resulting raw data can be seen in Figure 3.8c. A peak around $B_{\perp} = 0$ on top of a shifted parabolic background is clearly recognizable. The background signal is expected from Ordinary Magnetoresistance (OMR) and can be easily fitted and subtracted for better comparison (Section 2.2.1). Figure 3.8d shows the signal without the background. The height of the Hanle peak around zero is $\Delta V_{\text{peak}} \approx 0.08$ mV, while the noise level, shown in Figure 3.8d as red area, is ≈ 25 μ V. To have an idea what magnitude of noise would be expected under given experimental conditions, we can calculate the Johnson noise in our experiment (Section 2.5):

$$V_{\text{J,pp}} = 5 \cdot \sqrt{4 \cdot k_B \cdot T \cdot \frac{V_{12}}{I_{23}} \cdot bw} = \sqrt{4 \cdot k_B \cdot 3.4 \cdot 201 \cdot 10} \approx 3 \text{ nV} \quad (3.1)$$

With the improvised set-up, we are approximately 4 orders of magnitude away from the theoretical limit. In comparison, Figure 3.8e shows measurements under comparable conditions on the same sample performed at UCLA, with $\Delta V_{\text{peak}} \approx 0.14$ mV and noise level ≈ 1 μ V or less. The higher ΔV_{peak} observed at UCLA seems to be only due to the broader sweep range, however, the difference in the observed noise level is stark. Given the simplicity of used set-up at IPC and lack of shielding on the cables used inside the VTI, this is not unexpected. Qualitatively, we have been able to observe the 3T Hanle

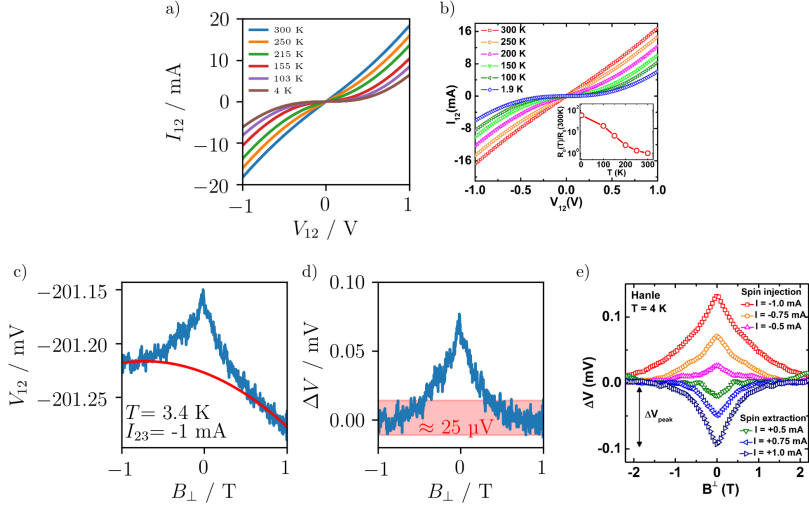


Figure 3.8: First magnetoresistance measurements on the **3Tref** sample at IPC. a) Temperature dependent $I - V$ measurements between terminals 1 and 2, measured at IPC. b) Same as a), measured at UCLA. Inset shows zero-bias resistance normalized to room temperature resistance of the device. c) $3T$ Hanle measurements measured at IPC. Raw data in blue circles, red line shows fitted Ordinary MagnetoResistance (OMR) background. d) Data from c) after background subtraction. Red area highlights approximate noise floor of $\approx 25 \mu\text{V}$. e) Measurements on the same device, performed at UCLA. b) and e) reproduced from [70], with the permission of AIP Publishing.

effect and therefore found the magnet itself to be a suitable basis for a new experimental set-up dedicated to electrical measurements. With the proof-of-concept measurements successful, we have proceeded with the design of a new experimental set-up.

3.4.2 Design, assembly and testing

After gaining some familiarity with the measurements during the proof-of-principle phase, we could formulate the requirements for a new, dedicated experimental set-up:

- To be able to test multiple samples after cooling down the sample holder, we have modified the sample holder such that it will be able to accommodate 5 samples at once, each sample with four electrical connections, requiring 20 contacts in total.
- To improve noise performance and flexibility, we integrated a dedicated current source and voltmeter.
- Implement at least coaxial shielded cables in every step, triaxial where possible.

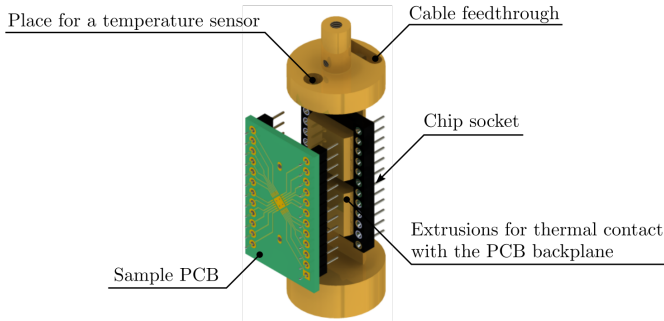


Figure 3.9: Sample holder redesigned for electrical measurements.

- Write dedicated National Instruments Labview software for safe and comfortable control of the experiment.

Figure 3.9 shows the redesigned sample holder. To simplify the mounting of the sample and ensure good electrical contact, we used a dual-in-line socket with 28 sockets for precision pins. The number 28 was chosen due to commercial availability. The sample holder was subsequently designed around this socket, with care taken to include extrusions in the middle part which serve a dual purpose: to stabilize the socket in place and, since they are machined to precisely touch the backplane of a PCB mounted in the socket, and to ensure thermal contact between the sample holder and the PCB. The PCBs used for our experiments have metallic plates on the front, where the sample is glued, and on the back as well. These two plates are connected with multiple vias², effectively transferring heat between the brass sample holder and the sample. The rest of the probe remained mostly unchanged. To carry the electrical signals with minimal external influences, ten individually shielded miniature twisted pairs of brass wires were chosen (Twisted Pair Brass in CuNi Shield, CMR-Direct). The cables were spiraled around the sample rod housing and fastened using Polytetrafluoroethylene (PTFE) tape. On the upper part of the probe, one of the feedthroughs was sealed off, and one was redesigned to house a hermetic 24-pin Fischer connector socket. Two additional wires were added to the temperature sensor feedthrough to provide power to the heater incorporated into the probe head (part number 10 in Figure 3.6).

Figure 3.10 displays a schematic comparison between the proof-of-concept and the redesigned set-up. Outside of the magnet, the feedthrough was connected to a lab-built aluminum breakout box with a cable consisting of 10 pairs of insulated, multi-core copper

²Via is an electrical connection between different layers of a PCB, consisting of multiple coaxial openings in the PCB connected with a copper tube.

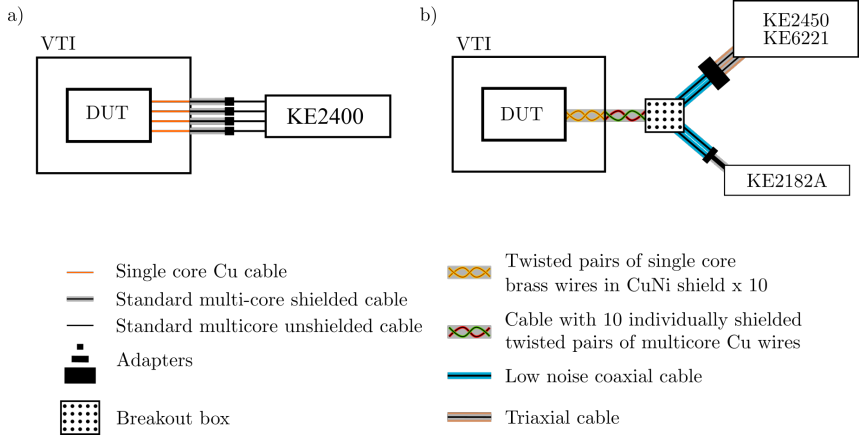


Figure 3.10: Simplified schematic diagrams of a) initial proof-of-principle and b) redesigned, dedicated experimental set-ups.

cables, with each pair individually shielded and the whole cable additionally guarded. The breakout box consisted of 20 isolated BNC connectors, with the BNC shield connected to the twisted pair shielding, while the whole box is connected to the cable guard. To supply the sample with current, we have used a Keithley 2450 Source-Measure Unit for most of the three- and four-terminal experiments, which was later replaced with a Keithley 6221 AC and DC current source. While the 2450 proved to be sufficient for our measurements, and has slightly higher resolution, accuracy and lower noise (in DC measurements), the 6221 offers better integration with the Keithley 2182A Nanovoltmeter, allowing for pulsed and Alternating Current (AC) measurements. Both the KE2450 and KE6221 have triaxial output connectors, which were used to perform all measurements. Custom adapters, allowing for a transition to BNC connectors to be used with the breakout box, while connecting the guard to the breakout box exterior, were made in-house. Standard coaxial cables between the adapters and the breakout box were exchanged for low noise cables (CAB-LN1, Femto). The 2182A has a four-pin Lemo socket as input (2 channels), for which a custom BNC adapter box was made in-house.

After assembly and initial testing, care was taken to minimize additional sources of noise. The first issue we have investigated was to choice of the proper power plug as the grounding point. If the grounding point used for all of the shielding is noisy by itself, the gains in noise reduction would be smaller. The building has two main electrical circuits: *Experimental* and *EDV*, or computer network. The experimental circuit is used for all of the high-power devices at the faculty, such as pumps and electromagnets,

while the computer circuit is meant for low power, office devices. A Hewlett-Packard 35660A analog frequency analyzer was used to investigate the frequency spectra of these two networks in the range from 0.1 kHz to 1.6 kHz³. The experimental network was substantially more noisy, with not only the expected 50 Hz peak, but also 50 Hz harmonics in the whole range and many additional peaks. The noise floor in the computer network was substantially lower, with the 50 Hz peak being present but much lower and no other dominant frequencies. Given that the source and measurement devices are low-power devices, we have chosen a single power plug on the computer network as the grounding point. The magnet is, however, a high-power device, which should be connected to the experimental network. In order to avoid accidentally connecting to the noisy ground, care was taken to disconnect the shields and guards of the measurement equipment from the magnet housing, which is connected to the power supply ground.

Dedicated software written in National Instruments LabView was developed to control the experiment, front panel of which can be seen in Figure 3.12. The software allows access to the settings, control, and read-out of the magnet power supply, the temperature controller, and all of the previously mentioned Keithley devices (2450, 6221, 2182A). Both magnetic field and temperature sweeps can be recorded, along with all of the experimental settings. Taking advantage of the two voltage measurement channels on the 2182A, it is possible to fully characterize a Hall bar device (measure both longitudinal and transversal resistance) in a single temperature sweep. The modular nature of the source code allows for simple extensions, which makes experiments on multiple devices easy to perform - a version of the code was written to set current on both 2450 and 6221 and record data from the voltage channel of 2450 and two 2182A nanovoltmeters to a total of two current and five voltage channels. All of these features allowed for fast, reliable, and safe sample screening, with the option to perform complex experiments when necessary.

After implementing all of the improvements, we have remeasured the **3Tref** sample. Figure 3.11 shows the comparison between measurements performed with the initial and the improved set-ups. We can see that while the noise level with the simple set-up was around 25 μV , all of the upgrades reduced the noise at least 10 times, to level of 2 μV or lower. A more exact comparison would require dedicated noise measurements. This configuration of the set-up was sensitive enough to perform all of the spintronic experiments described in this chapter with a sufficient signal-to-noise ratio.

³The measurement device displays its data on a cathode-ray display. As such, no data are displayed here.

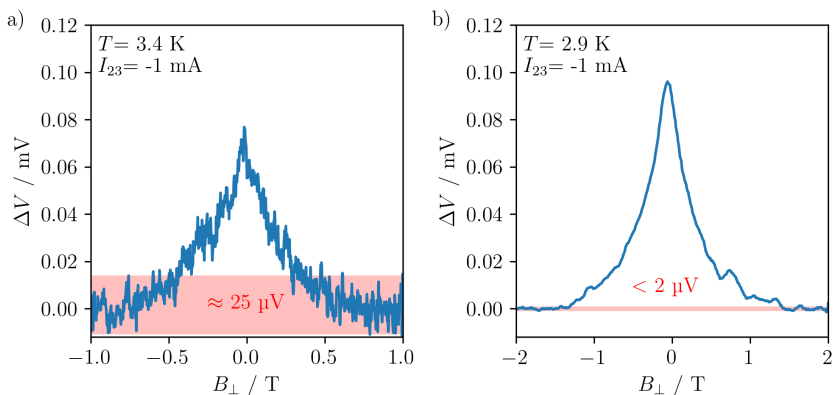


Figure 3.11: 3T Hanle measurements on the **3Tref** sample measured with a) the proof-of-principle and b) the upgraded set-up. Red areas highlight the approximate noise floors. The difference in signal magnitude is due to the slightly different temperatures.

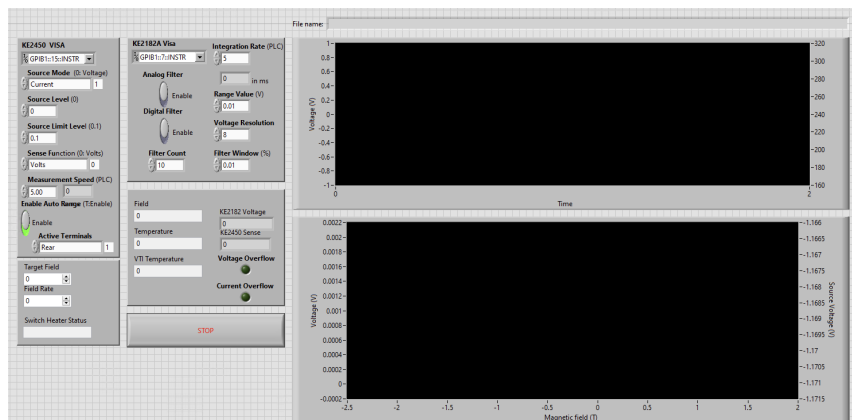


Figure 3.12: Front panel of the magnetoresistance measurement LabView program.

3.4.3 AC measurements, summary and outlook

All of the electrical measurements described in this chapter were performed in DC mode. We have also experimented with the integration of AC measurement schemes to see if they would benefit the noise performance of our set-up. Two AC detection techniques were readily available to use: delta mode measurements and phase-sensitive detection. A detailed description of both modes can be found in Section 2.5. In short, in delta mode, the current source periodically reverses its polarity, while the voltmeter calculates a running average of at least three measurements to reduce thermoelectric drift and noise. For phase-sensitive detection, a Lock-In Amplifier (LIA) is used. The LIA outputs a sinusoidal signal, which is used to drive the DUT, after which it demodulates the DUT output at the same frequency, effectively rejecting other signal components, significantly reducing noise.

Instead of measuring raw noise performance on a resistor, we have decided to test the measurement methods on a 'real' sample, to see if they provide any benefits to our typical experiments. As a test sample, a Hall bar manufactured on top of p -doped Ge was used, the same sample as used in subsection 3.5.3. A magnetoresistance measurement at 2 K was a good representative of a routine experiment. To test the delta mode measurements, Keithley 6221 and 2182A were used, the same devices as used for the DC measurements. For phase-sensitive detection, we have integrated the Zürich Instruments MFLI LIA into the measurement set-up. While the usage of the delta mode system is relatively straightforward since it was made specifically for this purpose, using an LIA to perform magnetoresistance measurements requires some additional considerations. To characterize the sample without the influence of contact and lead resistances, a 4-point measurement scheme is used: a constant current is applied on the longitudinal axis of the Hall bar, while the voltage drop along this axis is measured with two additional contacts. During a magnetic field sweep, the resistance of the sample changes - maintaining a constant current ensures that this resistance change is detected as a change in the measured voltage. Typical LIAs, however, only have a voltage output, rendering such measurements impossible. The easiest, and the most common, workaround is to simply connect a resistor with resistance high compared with the DUT in series with the voltage output and assume that the set-up is operating in constant current mode. This approach, while functional, has several significant disadvantages. The two biggest are that to ensure constant-current operation, the DUT's behavior has to be entirely predictable and stable, which is rarely the case, and that to eventually monitor the current, additional measurement equipment is necessary. The Zürich Instruments MFLI offers a different approach: the device has a current input, which can be used to monitor the current flowing through the DUT and

dynamically adjust the voltage output to maintain a constant current using a Proportional-Integral-Derivative (PID) controller. The company did not yet test the application of this method to magnetoresistance measurements; as such, these experiments were made in collaboration with Dr. Claudius Riek from Zürich Instruments. Figure 3.13c and d shows the measurement with and without the PID control, clearly demonstrating its necessity. With the regulation off, most of the resistance change manifests only as a current change, with only a small effect on the measured voltage. With the PID on, the current is maintained, and a clear signal can be observed in the voltage channel.

Figure 3.13a shows which inputs and outputs of the various devices were used to connect to the Hall bar. Figure 3.13b displays measurements performed using the three different experimental schemes. The data displayed is raw, with the minimum of the curves shifted to zero for clarity. We can observe that all of the curves are similar, with the shape of the background being slightly different each time. The shape and size of the peak in the middle, however, is always the same. In terms of noise performance, we can see that there are only small differences, with the DC measurement being the one with the lowest noise. While the LIA measurement has similarly clean curves, a number of 'wiggles' is visible. They are an artifact of the PID regulation, which could be eventually removed by additional tuning of the controller. The delta mode measurements are the noisiest of the three, though not by much, and could potentially be also improved with different settings. Nevertheless, DC measurements offer the least complexity and best results directly. The fact that moving to higher frequencies does not reduce the observed noise suggests that its source is either external interference or internal processes of the sample. Further measurements could shed more light on the noise sources; for example, observing the noise level as a function of the LIA modulation frequency could be helpful to identify noise sources by their typical frequency dependencies.

We can see from the above that the performance of the set-up is sufficient, even though there are still some open questions and possible improvements. One of the things that has not been sufficiently systematically investigated was the effect of various grounding schemes. We have investigated the noise components of the two available electrical networks, however, without directly measuring their effects on the electrical performance. Similarly, the grounding scheme used was made according to various 'best practices' and recommendations, but the direct effect on noise performance in measurements was not evaluated, meaning there could be some additional systematic errors missed and potential improvements. In terms of sample rod design, two flaws have emerged over the years of usage. The fastening of the 24-pin hermetic socket at the top of the probe is on the inside of the feedthrough, and is done using a nut. This internal fastening means that after soldering all of the cables, there is no way to re-tighten the nut, which eventually

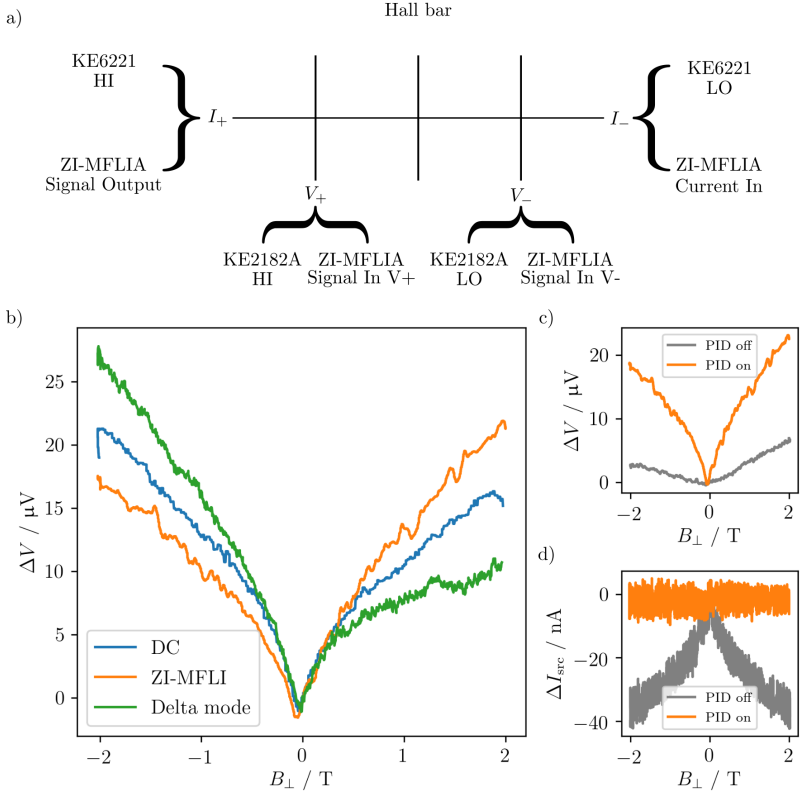


Figure 3.13: a) Schematic image of a Hall bar with the connections used for the different measurement schemes. Both DC and Delta mode measurements were performed with the Keithley 6221 and 2182A devices. b) Magnetoresistance of a Hall bar on top of p -doped Ge at 2K measured using different measurement schemes. c) and d) Same measurement as in b) using ZI-MFLIA with the PID compensation off and on.

did come a bit loose after 1–2 years of careful handling, introducing a leak into the VTI. While this was solved by applying GE varnish around the socket, a more elegant solution would improve the handling of the connector. Another long-standing problem was the use of cartridge heaters in the lower part of the probe. A number of them seemingly stopped working after a short time. It was not clearly established if the cause was insufficient heat-sinking or some electrical connection problems. The lack of an additional heater significantly prolonged the warmup time of the probe.

To conclude, we demonstrated that the newly manufactured set-up for low-temperature electrical measurements in high magnetic fields has sufficient noise performance for all of the measurements presented in this thesis. The versatile design with a large number of connections allows for investigations of various samples in combination with a wide variety of excitations - not only temperature and magnetic field, but optical and microwave radiation as well. Both DC and AC measurements can be performed if necessary. It has been successfully used to investigate inorganic semiconductors, semiconductor devices, spintronic effects, organic field effect transistors and provides a solid platform for more future investigations at the Institute of Physical Chemistry, University of Stuttgart.

3.5 Spintronics in *p*-doped germanium

3.5.1 Three terminal spin injection measurements

As described in detail in the section 3.4, the first measurements of electrical spin injection from Mn_5Ge_3 into Ge at the IPC were performed on the **3Tref** sample. In that case, the ferromagnetic layer was doped with C to increase its Curie temperature ($\text{Mn}_5\text{Ge}_3\text{C}_{0.8}$) and had an Al_2O_3 oxide barrier to overcome the conductivity mismatch problem (Section 2.2.3). While the measurements were successful, two disadvantages are connected with the usage of an oxide barrier:

1. The contact resistance (ρ_c) is relatively high already at room temperature ($\rho_c \approx 4 \Omega \cdot \text{cm}^2$ [66]). This leads to unnecessary heating of the sample during operation and limits possible downscaling of the device. For context, the requirement set by the IRDS for integration into CMOS technology is $\rho_c < 1 \cdot 10^{-8} \Omega \cdot \text{cm}^2$ [71].
2. When the sample is cooled down to temperatures necessary for observation of spin injection, the electrical behavior becomes highly non-linear (Figure 3.8 e) and the contact resistance rises by three orders of magnitude [66], leading to higher heat dissipation, noise, and further limiting the usage of smaller contacts.

To overcome these problems, we decided to investigate the possibility of using Mn_5Ge_3 without the oxide barrier, fabricated using the newly developed process described in the section 3.3. The conductivity mismatch was not expected to be significant, since Mn_5Ge_3 without C doping has conductivity comparable to highly doped Ge, as used in this study⁴. Additionally, during our investigation of the Mn_5Ge_3 formation, we have found the contact resistance of these devices to be 6 to 8 orders of magnitude smaller, when compared to the sample with tunneling oxide at room temperature, between $1.6 \cdot 10^{-8}$ and $1.8 \cdot 10^{-6} \Omega \cdot \text{cm}^2$ [54]. With these advantages in mind, we fabricated three devices with the same architecture as **3Tref**. One sample had the same doping type and level as **3Tref**, i.e., *n*-type with nominal dopant concentration $n = 10^{20} \text{ cm}^{-3}$ (designated **3Tn20**). The other two samples were both *p*-doped, once with $p = 10^{19} \text{ cm}^{-3}$ (**3Tp19**) and once with $p = 10^{20} \text{ cm}^{-3}$ (**3Tp20**).

Figure 3.14 compares the temperature dependence of the electrical behavior of sample contacts with and without an oxide barrier between the ferromagnetic layer and the transport channel. Figure 3.14a shows the $I - V$ curves of the **3Tref** sample, where we can observe non-linear behavior already at 250 K. In contrast, Figure 3.14b demonstrates that the **3Tp20** sample obeys Ohm's law even at 20 K, with only a marginal change in

⁴The ratio between the resistivity of Mn_5Ge_3 ($\rho_{\text{Mn}_5\text{Ge}_3}$) and Ge (ρ_{Ge}) was larger than 0.2 in all investigated samples, with the absolute values being between $1 \cdot 10^{-4}$ and $1 \cdot 10^{-3} \Omega \cdot \text{cm}$ [66].

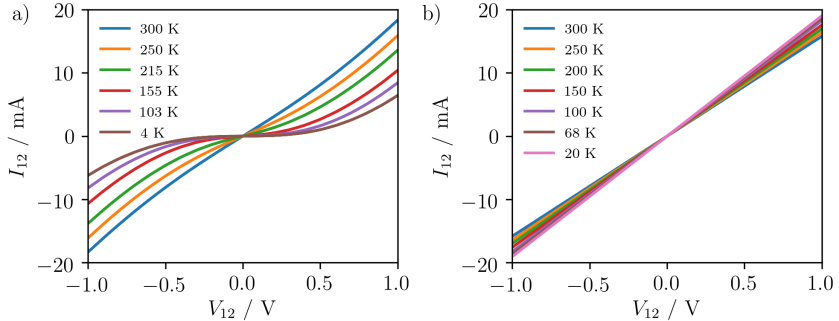


Figure 3.14: Comparison of temperature dependent $I - V$ curves. a) **3Tref** sample with an Al_2O_3 barrier between $\text{Mn}_5\text{Ge}_3\text{C}_{0.8}$ layer and Ge. b) **3Tp20** sample without an oxide layer, allowing for ohmic behavior down to cryogenic temperatures.

overall resistance.

We performed 3T Hanle measurements on all three samples at low temperatures and in all cases observed a peak around $B_{\perp} = 0\text{ T}$. Figure 3.15 shows the data of the **3Tp20** sample, it is, however, representative of all three samples, which had qualitatively the same behavior. Figure 3.15a displays the temperature dependence of the measured voltage signal. While it is tempting to assign the peak to spin accumulation, upon closer inspection, we can conclude that the Hanle effect cannot explain the observed behavior. As explained in Section 2.2.3, in a 3T Hanle measurement, a Lorentzian peak centered around $B_{\perp} = 0\text{ T}$ is expected. The linewidth of this peak is inversely proportional to the spin lifetime, τ_s . With increasing temperature, the magnitude of the signal is expected to lower, while the linewidth should increase due to the lowering of τ_s . In contrast, Figure 3.15a shows a peak that is becoming smaller and narrower at the same time, implying significantly longer τ_s at higher temperatures. This is highly improbable and was not reported in Ge before, suggesting that the measured signal is not related to spin injection and accumulation. Two additional observations support this. Figure 3.15b shows the measurement at $T = 1.5\text{ K}$ under different polarities of the injection current I_{23} and orientations of the sample. While signs of the signal are consistent with the ones measured on **3Tref** sample⁵, the rotation of the sample by 90° has virtually no effect on the signal. In a 3T Hanle measurement, it was demonstrated that a so-called inverted Hanle effect is observed upon 90° rotation, with opposite sign and a different shape [72]. While the inverted Hanle effect was not observed in **3Tref**, there was some angular dependence present, and τ_s behaved as expected with

⁵The sign of the signal in the **3Tref** samples is already inverted when compared to theory. The exact origin of this sign inversion is not clearly established and it was observed in other materials as well [70].

temperature. Figure 3.15c presents the dependence of the signal shape on the rate of the magnetic field sweep. While the shape could be considered approximately Lorentzian at a sweep rate of 1 T/min, at lower rates it becomes clear that the signal is not of a Lorentzian shape. We can observe a visible plateau between ≈ -0.1 and 0.1 T. This precludes its origin in the Hanle effect, even though it is possible that a peak related to spin accumulation is present underneath. As mentioned in section 3.3 and explained in depth by Michez [67], a 12 nm thick layer of Mn_5Ge_3 such as ours has both in-plane magnetic domains and out-of-plane up/down stripe magnetic domain structure under our experimental conditions. It is therefore possible that the observed change in 3T voltage is related to the alignment of the out-of-plane magnetic domains with the applied field. Figure 3.15d compares the 3T measurement at $T = 1.5$ K and 0.05 T/min magnetic field sweep rate with the magnetization measurement of the **300slow** sample at $T = 5$ K. We can observe a possible correlation between the two measurements, with the plateau in the 3T voltage approximately fitting the coercive field of the Mn_5Ge_3 layer.

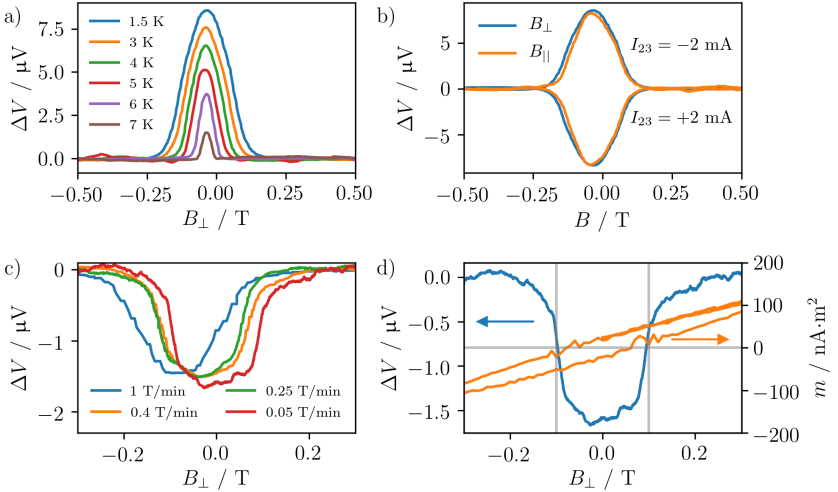


Figure 3.15: 3T measurements on the **3Tp20** sample. a) Temperature dependence of the central peak measured with magnetic field sweep rate of 0.4 T/min. b) Measurements at $T = 1.5$ K with different injection current polarities and sample orientations. c) Dependence of the central peak shape on the magnetic field sweep rate, $T = 1.5$ K. d) Comparison of the 3T measurement taken at $T = 1.5$ K with a magnetic field sweep rate of 0.05 T/min (blue, left vertical axis) with the magnetization measurement of **300slow** sample recorded at 5 K (orange, right vertical axis). Gray lines highlight the approximate intersections of the curves.

While an exact explanation of the mechanism behind these observations would require further study, it is clear that these samples are unsuitable for our purposes since they do not provide us with a clear proof of spin injection. The complexity of the observed signal, in addition to the inherent disadvantages of 3T measurements (large electrode size, merging of the spin injection/detection electrodes), prompted us to develop a fabrication technology to manufacture devices suitable for 4T, nonlocal Hanle measurements.

3.5.2 Four terminal spin injection measurements

4T measurements are generally more suitable for spintronic experiments, with the caveat that they significantly increase the complexity of device fabrication. In 3T measurements, since the spin injection and spin detection happen locally, i.e., at the same point in space, the overall dimensions of the device do not depend on the spin diffusion length, also called spin-flip length, l_{sf} . The electrodes can, therefore, be made such that optical lithography has sufficient resolution to define them. In nonlocal measurements, however, the spin polarization has to diffuse from the injector to the detector electrode (Section 2.2.3). The distance between those two electrodes then has to be on the order of l_{sf} , which was shown to be on the order of tens of nanometers in moderately doped p -Ge [39]. A design for non-local spin injection and detection in a highly p -doped Ge channel was developed by Dr. Stefan Bechler at the Institute of Semiconductor Engineering, University of Stuttgart (IHT), along with a fabrication process based on a multi-step electron beam lithography [66]. Figure 3.16a shows a schematic image of the structure used for the measurements. Similarly to the 3T architecture, the current is injected into a highly doped Ge channel ($p = 1 \cdot 10^{20} \text{ cm}^{-3}$) defined by a mesa structure on top of i -Ge. Four electrodes contact the channel, each containing the Mn_5Ge_3 layer along with Al metalization on top (Figure 3.16b), sample **4Tp20**). When performing the measurements, a constant current is injected between electrodes 1 and 2 (I_{12}), while the voltage change is being monitored on electrodes 3 and 4. The distance between the inner electrodes (numbers 3 and 4), i.e., the distance the spin polarization has to diffuse over, is $d_{34} = 195 \text{ nm}$. The fabrication process, however, proved to have a very low yield of functioning devices. Even if the device's fabrication was successful, the metalization contained a bottleneck point on the edge between the substrate and semiconductor channel, which made the devices very sensitive to the applied current and generally unreliable. Despite those problems, we have obtained a functioning device and studied it using low-temperature 4T measurements. More details about the growth and structuring of the device can be found in the dissertation of Dr. Bechler [66].

Figure 3.17 shows selected measurements performed on the **4Tp20** sample. After observing a signal, we performed several control measurements based on our experience

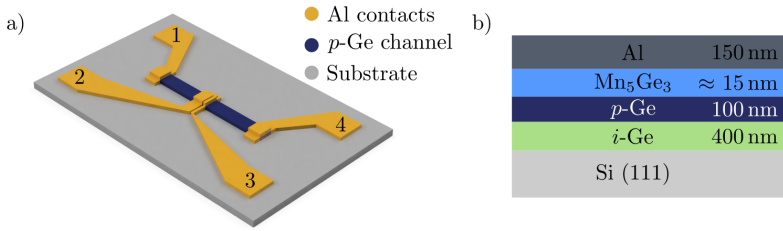


Figure 3.16: a) Schematic drawing of the 4T device structure. The distance between the inner electrodes (3 and 4) is 195 nm. b) The material stack active in each electrode of the **4Tp20**.

with the 3T devices. Figure 3.17a shows the temperature dependence of the signal, which decreases in magnitude and broadens at higher temperatures, behavior consistent with a Hanle signal. The magnitude and polarity of the signal is now consistent with the standard theory of spin injection as well, i.e., it scales with the injection current without reversing polarity, is positive for positive injection current and vice versa (Figure 3.17b and c). And finally, the shape of a Lorentzian peak is preserved regardless of the magnetic field sweep rate (Figure 3.17d). Given all this expected behavior, it is therefore rather curious that the signal shows essentially no change upon rotation of the sample by 90° . (Figure 3.17b). In a typical 4T measurement, when the field is applied in-plane of the sample, a spin-valve signal is expected, i.e., a step-change in voltage at the coercive fields of the individual electrodes. At the same time, the Hanle signal should not be visible. No such observations could be made. This could again be related to the multi-domain magnetic structure of Mn₅Ge₃, however, a hypothesis consistent with all of the observations is not readily apparent and further investigations of the system would be necessary.

An analysis based on the one-dimensional drift diffusion model (Section 2.2.3) is nevertheless possible and was performed by Bechler [66]. Figure 3.18a shows a signal taken at $T = 5$ K and $I_{12} = -30 \mu\text{A}$, along with a fit to the model. For the fitting, the only fitting parameters were the polarizations of the electrodes and spin lifetimes, τ_s , while the g -factor was taken from literature as 7.2 [73]. Other parameters were extracted from Hall measurements performed on the sample. Figure 3.18b shows the extracted spin lifetimes as a function of temperature. Both the behavior and the order of magnitude is consistent with the measurements of Rortais *et al.* [39], who extracted τ_s using three methods: 3T Hanle measurements, fitting of weak antilocalization signal in magnetoresistance and spin pumping experiments. It should be noted, however, that the 3T measurements in [39] show a significantly smaller linewidth (≈ 0.2 T), which is closer to linewidths

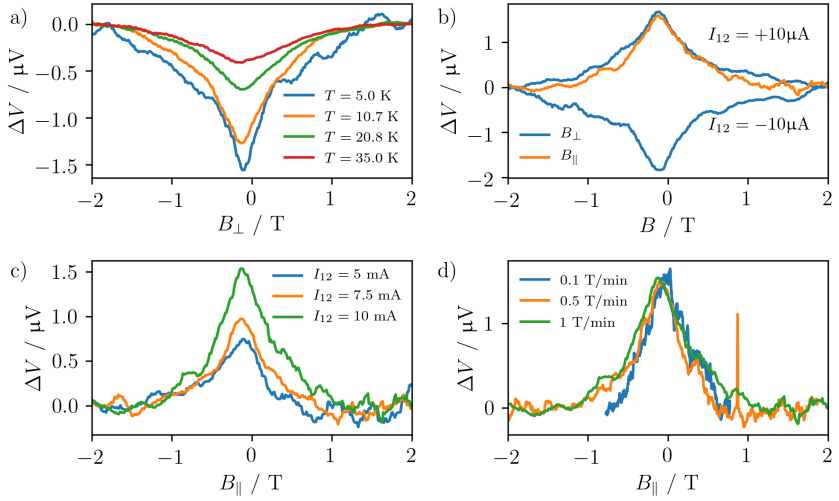


Figure 3.17: 4T measurements performed on the 4Tp20 sample. a) Temperature dependence of the signal at $I_{12} = -10 \mu\text{A}$. b) Dependence of the signal on the magnetic field orientation and current polarity at $T = 5 \text{ K}$. c) Dependence of the magnitude of the signal on the injected current at $T = 5 \text{ K}$. d) Dependence of the signal on the magnetic field sweep rate at $T = 5 \text{ K}$.

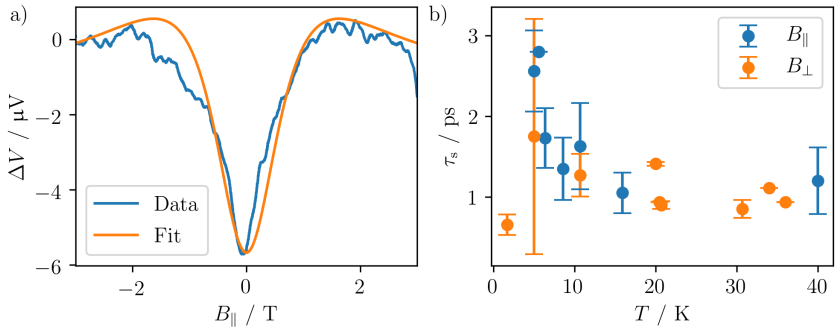


Figure 3.18: a) 4T measurement at $T = 5 \text{ K}$ and $I_{12} = -30 \mu\text{A}$ fitted using the 1D drift diffusion model. b) Temperature dependence of the spin lifetime τ_s extracted from the 4T measurements. Data courtesy of Stefan Bechler.

commonly observed for both three and four terminal Hanle measurements ([72]). Using the extracted τ_s , as well as the charge diffusion constant $D = 14.5 \text{ cm}^2 \cdot \text{V}^{-1} \cdot \text{s}^{-1}$ obtained from Hall measurements [66], we can calculate the spin diffusion length using $l_{\text{sf}} = \sqrt{D \cdot \tau_{\text{sf}}}$. Assuming that the spin and charge diffusion constant are the same, we obtain values between of $l_{\text{sf}} \approx 30 - 70 \text{ nm}$, which is comparable to the values obtained by Rortais [39]. The polarizations of the Mn_5Ge_3 electrodes obtained from the fit of our data are of the order of 1%. The values of Mn_5Ge_3 polarization in literature are a matter of contention and range from -10% to -42% [74].⁶ While the obtained 1% is significantly lower, it should be noted that this is the effective spin polarization measured from injector to detector, which can be reduced during the injection/detection steps and could potentially be influenced by the polycrystalline, multi-domain nature of our electrodes.

In summary, we have observed a nonlocal voltage signal using a 4T device structure, the results are, however, only partially consistent with a Hanle signal. While the obtained spin lifetimes are consistent with literature values for p -Ge, the absence of a spin-valve behavior, along with the absence of rotational dependence, remain unsolved problems. It is probable that the reason for this anomalous behavior is the multi-domain magnetic structure of our Mn_5Ge_3 layer with significant out-of-plane components. To probe the spin dynamics of p -Ge without the influence of Mn_5Ge_3 , we have decided to perform low temperature magnetoresistance measurements to observe the weak antilocalization effect.

3.5.3 Weak antilocalization measurements

In order to verify the spin diffusion lengths and spin lifetimes in p -Ge obtained from 4T Hanle measurements, we performed low-temperature magnetoresistance measurements on the same Ge substrate as used in **4Tp20**, without the ferromagnetic Mn_5Ge_3 layer. A standard triple Hall cross, same as schematically depicted in Figure 3.13a was used as a measurement structure, with both the longitudinal and transversal voltages being measured during a magnetic field sweep.

Figure 3.19a shows the measured change in longitudinal resistance (ΔR) as a function of the magnetic field and temperature. The individual curves are offset by 0.5Ω for clarity. A clear Weak Antilocalization (WAL) peak, on top of OMR, can be seen close to $B_{\perp} = 0 \text{ T}$. This peak decreases and broadens with increasing temperature up to 40 K, after which it was no longer visible. Figure 3.19b displays the data recalculated into a change in magnetoconductance (ΔG) and fitted using the Hikami-Larkin-Nagaoka (HLN) model (Section 2.2.2). The fitting was performed by David Weißhaupt from IHT and very good, robust fits were obtained for each temperature. Figure 3.19c depicts the

⁶In a 4T Hanle measurement, the product of the individual electrode polarizations enters the equation, it is therefore insensitive to the sign if the electrodes are identical.

extracted fitting parameters: the phase-coherence length (l_ϕ) and spin-orbit length (l_{so}). These parameters can be easily recalculated into the more relevant spin diffusion length $l_{sf} = (\sqrt{3}/2) \cdot l_{so}$ and spin lifetime $\tau_s = l_{sf}^2/D$, where D is the diffusion constant extracted from measurements of the transversal (Hall) voltage. The recalculated values can be seen in Figure 3.19 d, along with a comparison to the values obtained from 4T measurements. The spin lifetimes obtained from WAL fits are approximately one order of magnitude shorter, however, given the uncertainty of the values obtained from Hanle measurements, it is not unreasonable to consider them comparable. These results support the hypothesis that the observed signal in 4T measurements was indeed a Hanle-type signal, even if it shows some hitherto unreported behavior. Nevertheless, even if the signal observed in 4T measurements was a proof of spin injection, the absence of spin-valve behavior makes the Mn_5Ge_3 electrode unsuitable for the molecular qubit read-out mechanism described in Section 3.1. Assuming that the problem lies in the magnetic domains of ferromagnetic layers pointing out-of-plane, we have considered to solve it by changing the crystallographic orientation in which the Mn_5Ge_3 grows in the following section.

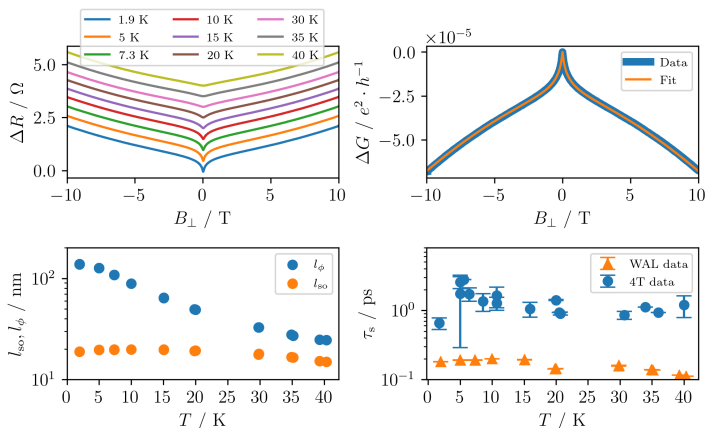


Figure 3.19: a) Magnetoresistance of the Ge substrate used for the 4Tp20 sample at various temperatures. b) Magnetoresistance at 1.9 K recalculated into magnetoconductance, along with a fit to the HLN model. c) Spin-orbit (l_{so}) and phase-coherence lengths (l_ϕ) extracted from the magnetoresistance measurements using the HLN model. d) Comparison of the spin lifetimes extracted from both magnetoresistance and 4T-Hanle measurements. Fits to the WAL data courtesy of David WeiBhaupt.

3.5.4 $\text{Mn}_5\text{Ge}_3/\text{Ge}(100)$ as a platform for Ge spintronics

In the previous sections, the $\text{Mn}_5\text{Ge}_3/p\text{-Ge}(111)$ material stack was thoroughly investigated as a potential platform for spintronics, with the goal of using a spin-valve structure to read out the spin state of a molecular qubit. As we have seen, the Mn_5Ge_3 layers manufactured using a slow annealing process had thicknesses between 10 nm and 20 nm, which meant that the competition between shape and magnetocrystalline anisotropies lead to a multi-domain structure with significant out-of-plane components. This has proven to be severely detrimental to both three and four-terminal measurements. Even though we were able to observe a signal in the 4T measurements, the absence of a spin-valve behavior limits the usability of this platform for our desired application. Assuming we want to maintain the potential CMOS compatibility by using Mn_5Ge_3 , there are two potential solutions: making the ferromagnetic layer thinner and limiting the effect of magnetocrystalline anisotropy, or re-orienting the crystal growth. We decided to perform preliminary exploration measurements of the latter option. By growing the layer on top of a $\text{Ge}(100)$ surface, instead of (111), the c -axis of the hexagonal crystal should lie in the plane of the sample. Since the c -axis is the easy axis of the magnetocrystalline anisotropy, this should force the overall magnetization in-plane. Additionally, the $\text{Si}(100)$ orientation is much more commonly used in the industry than (111), which would be an advantage from an application point of view. There are only a few reports on Mn_5Ge_3 grown on $\text{Ge}(100)$ in the literature, most of them focused on nanoislands [75][76], or polycrystalline microstructures [61]. There are only four articles explicitly investigating the formation of Mn_5Ge_3 thin films on $\text{Ge}(100)$. Lungu *et al.* [77] deposited a 100 nm thick Mn layer on top of $\text{Ge}(100)$ heated to a substrate temperature $T_s = 350^\circ\text{C}$ and observed that the Mn mostly dilutes in the Ge matrix, and forms inclusions of Mn_5Ge_3 and $\text{Mn}_{11}\text{Ge}_8$ phases. This method is, therefore, unsuitable for spin injection applications. Olive-Méndez *et al.* published two reports dealing with Mn_5Ge_3 on $\text{Ge}(100)$ in 2018. In the first report, they observed that when depositing either Mn or co-depositing Mn and Ge onto a $\text{Ge}(100)$ substrate with $T_s = 250^\circ\text{C}$, the c -axis of the resulting Mn_5Ge_3 layer makes a 45° angle with the substrate plane [78]. This orientation results in both in-plane and out-of-plane anisotropy, with the in-plane one being slightly more dominant, resulting in behavior similar to what we have observed in our annealed layers. In the second report, they fabricated epitaxial $\text{Mn}_5\text{Ge}_3\text{C}_{0.6}$ layers on $\text{Ge}(100)$ by magnetron sputtering (co-deposition of Mn, Ge, and C at $T_s = 350^\circ\text{C}$) and observed a large in-plane anisotropy, ten times larger than that observed for $\text{Mn}_5\text{Ge}_3\text{C}_{0.6}$ on $\text{Ge}(111)$. They remark that the C atoms may modify the surface free energy such that this epitaxial relationship is preferred to the one observed in undoped Mn_5Ge_3 samples. At the same time, Xie *et al.* reported epitaxial

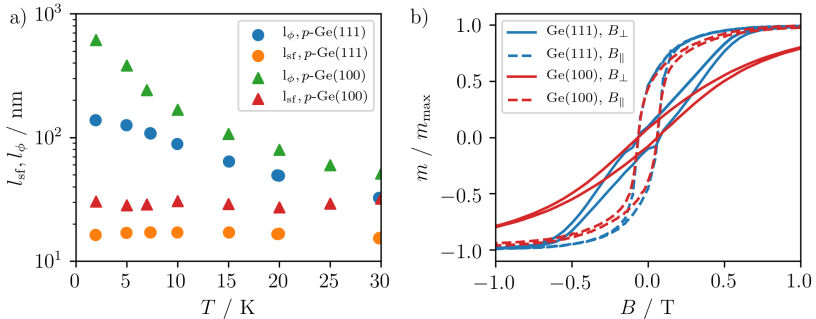


Figure 3.20: a) Spin-flip (l_{sf}) and phase coherence (l_ϕ) length of p -Ge(111) and p -Ge(100) samples extracted from WAL measurements. Extracted data courtesy of David Weißhaupt. b) Comparison of magnetization curves of the **300fast** sample grown on Ge(111) and **300fastGe(100)** at $T = 5$ K. **300fastGe(100)** data courtesy of Hannes S. Funk.

Mn_5Ge_3 layers on Ge(100) obtained by flash lamp annealing [79]. In their method, a 30 nm thin film of Mn was deposited on a Ge(100) wafer and annealed for 20 ms with an energy density of $95 \text{ J}\cdot\text{cm}^{-2}$. This process results in an epitaxial Mn_5Ge_3 layer, with an atomically sharp interface and the Mn_5Ge_3 c axis in-plane. While the magnetization was found to be preferentially in-plane, there was still remanence present in the out-of-plane direction as well.

We performed low-temperature magnetoresistance measurements on p -Ge(100) (sample **pGe100**), to see if there are any differences in spin dynamics. Additionally, we fabricated a magnetic sample by depositing 100 nm of Mn on a commercial Ge(100) wafer with subsequent annealing at 300°C for 1 minute (sample **300fastGe(100)**). We have then performed SQUID magnetometry to investigate the sample. Additionally, as a first step in trying to gain more insight into the complex magnetic properties of our samples, FMR experiments were performed on the sample.

Figure 3.20a compares the spin-flip and phase coherence lengths extracted from magnetoresistance measurements on p -Ge(111) and p -Ge(100). Both compared values are significantly higher in the p -Ge(100) sample. The charge carrier concentration at low temperatures extracted from Hall measurements was comparable, $p = 1.83 \cdot 10^{20} \text{ cm}^{-3}$ in the p -Ge(100) sample, compared to $p = 8.6 \cdot 10^{19} \text{ cm}^{-3}$. If anything, one would expect the slightly higher concentration of dopants in the p -Ge(100) to decrease the spin diffusion lengths. The data, however, suggests that the p -Ge(100) substrate is more favorable for spintronic experiments. Figure 3.20b shows the magnetization measurements performed on the **300fastGe(100)** sample, along with **300fast** data. We can see that the in-plane

magnetization of the layers behaves almost identically, while out-of-plane direction is noticeably 'harder' in **300fastGe(100)**, i.e., the sample reaches saturation at higher fields. However, the remanence is virtually identical in both directions, indicating that there are still domains in the sample with out-of-plane magnetization, approximately the same amount as in **300fast**. Temperature dependence of the magnetization was also measured, confirming that we have created a ferromagnetic layer with a $T_C \approx 290$ K. This means that our fabrication method, while resulting in Mn_5Ge_3 on a Ge(100) substrate as well, does not result in a layer with higher anisotropy than on Ge(111).

To gain some more insight into the magnetization structure of our ferromagnetic layers, and to validate that we can perform this technique, FMR measurements were performed at the IPC for the first time. Figure 3.21a defines the coordinate system used for the description of the experiment and shows the orientation of the sample in the static magnetic field (B_0) and the microwave magnetic field (B_1). Figure 3.21b shows the first measurements at room temperature, one with B_0 in-plane of the sample ($\theta_B = 90^\circ$) and one with B_0 out-of-plane ($\theta_B = 0^\circ$). We can observe two clear resonance lines; however, there is at least one more signal hidden underneath, due to the observed shape of the sharper line. The same measurement performed at $T = 5.6$ K is in Figure 3.21c. The intensity of the signals decreased significantly, while their resonance fields shifted to higher values. We can observe this in the more detailed temperature dependence in Figure 3.21f. The magnetic field was oriented out-of-plane of the sample in these measurements. The resonance field is strongly dependent on temperature between room temperature and 250 K, due to the proximity to T_C . The signal shifts ever closer to the position of $g \approx 2$ with higher temperatures, demonstrating the transition from a ferromagnet into a paramagnet. The signal seems to disappear between 50 K and 250 K, then reappearing at 25 K. The small, sharp features visible between 25 K and 50 K are due to the residual oxygen present in the sample tube undergoing magnetic phase transitions⁷ and is unrelated to our sample. Below 50 K, the only signal originating from the sample is a broad, featureless peak with relatively low intensity. The large signal between 0 T and 0.3 T is the background of the used resonator. Complete out-of-plane angular dependencies using a manual goniometer were performed at both at room temperature and 5.6 K, shown in Figure 3.21d and e, respectively. At both temperatures, we can observe that the resonance fields of the main signal have extremes at $\theta_B \approx 60^\circ$ and $\theta_B \approx 150^\circ$. These extremes are, however, not identical: the one at $\theta_B \approx 60^\circ$ is 'flatter', i.e., the resonance field changes only slightly between $\theta_B \approx 45^\circ$ and $\theta_B \approx 90^\circ$. We can observe the same behavior at low temperatures, with two main differences: all of the resonance curves are shifted ≈ 0.3 T to higher fields,

⁷Solid oxygen has three distinct magnetic phases at low temperatures, with two of them being antiferromagnetic and one paramagnetic. The para-antiferromagnetic transition occurs around 45 K [80].

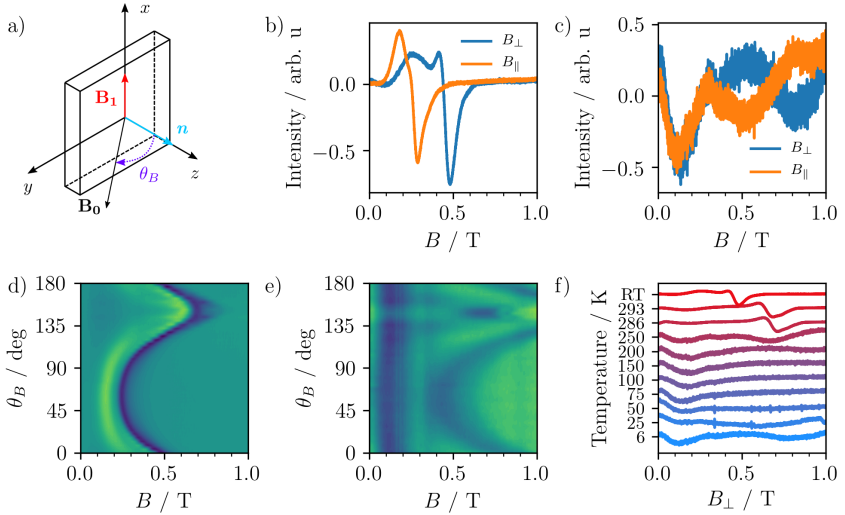


Figure 3.21: FMR measurements performed on the **300fastGe(100)** sample. a) Sketch of the sample orientation in the experiment, along with definition of the coordinate system used. b) Comparison of measurements with the magnetic field in- and out-of-plane at room temperature. c) Comparison of measurements with the magnetic field in- and out-of-plane at $T = 5.6$ K. d) Complete angular dependence measured at room temperature. e) Complete angular dependence measured at $T = 5.6$ K. f) Temperature dependence of the signal with the field perpendicular to sample plane. Intensity of the signals is normalized and offset by 1 for clarity, temperature on the vertical axis serves only as label.

and that the peak near $\theta_B \approx 140^\circ$ appears to be inverted.

Due to the complexity of the Mn_5Ge_3 system, a complete analysis of these data would require further measurements (in-plane angular dependence), the construction and solution of an appropriate analytical model, along with micromagnetic simulations, as was done in [81]. We can, however, at least qualitatively discuss our observations, based on comparisons with thick Mn_5Ge_3 layers grown on Ge(111) and extensively analyzed in [81]. If we compare the observed signals with the magnetization measurements in Figure 3.20b, one can notice that the sharp feature always occurs close to the field when the sample reaches saturation at a given orientation⁸. This might suggest that its origin is the acoustic (in-phase) mode of aligned domains, similarly to $\text{Mn}_5\text{Ge}_3/\text{Ge}(111)$. As we increase θ_B , we can observe a shift towards lower resonance fields, i.e., we can excite this mode with less energy. Interestingly, the lowest resonance field, which, based on the analysis in [81], would correspond to the magnetic easy axis of the layer, does not occur

⁸The magnetization curve at 300 K is comparable to the one at 5 K in terms of onset of saturation.

at $\theta_B \approx 90^\circ$, as would be expected from the magnetometry. The easy axis seems to lie in a relatively broad region near $\theta_B = (60 \pm 15)^\circ$. If we compare the angular dependence with the one measured on $\text{Mn}_5\text{Ge}_3/\text{Ge}(111)$, we can indeed see that it is very similar in shape, however, shifted by approximately $45\text{--}75^\circ$. This supports the findings in [78], that the c axis of an undoped Mn_5Ge_3 on $\text{Ge}(100)$ grows at a 45° angle to the $\text{Ge}(100)$ plane. The assignment of the other observed signals is difficult without further data, however, in $\text{Mn}_5\text{Ge}_3/\text{Ge}(111)$ broad, unresolved signals were assigned to magnetization trapped in magnetic flux closure caps [81]. The shift of the resonances to higher fields at lower temperatures could be a sign of ‘stiffening’ of the ferromagnetic layer, i.e., increasing of the magnetic field required to reach the resonance mode. Stiffening of the ferromagnetic layer was observed, although on a different scale, in the $\text{Mn}_5\text{Ge}_3/(111)$ system as well. In that case, the signal assigned to the acoustic mode of the stripe domains became more intense and sharp with decreasing temperature, however, whereas we observed a line broadening upon cooling. This discrepancy, along with the observation of multiple signals, might suggest that our sample’s domain structure is even more complex due to, e.g., multiple crystallographic or magnetic phases. While we cannot make any definite statements without further analysis and measurements, these first experiments demonstrate that FMR is an invaluable part in the toolkit of magnetic analysis.

3.6 Conclusion

In this chapter, we have set out to investigate the possibility of fabricating a spintronic platform suitable for electrical read-out of a molecular qubit spin state, while maintaining as much compatibility as possible with the current CMOS manufacturing technology. We have shown that by a facile, *ex situ* annealing of a Mn layer on top of a Ge(111) surface, a ferromagnetic Mn_5Ge_3 layer with an atomically sharp interface to Ge can be fabricated. This process results in ferromagnetic layers with ohmic behavior, very low contact resistance, and T_C close to room temperature, all properties highly relevant for spintronic applications. Furthermore, this process can be fine-tuned by the amount of deposited Mn and used annealing parameters. Afterward, we have developed a new experimental set-up at the IPC for performing variable temperature magnetoresistance measurements with high sensitivity. This set-up was extensively optimized in both hardware and software, and various measuring techniques were evaluated to find the best fit for our application. The new experimental set-up was subsequently used to evaluate spintronic devices with a Mn_5Ge_3 layer fabricated using our newly developed method. When performing 3T Hanle measurements, we have observed anomalous behavior not consistent with spin injection. This was most probably caused by the relatively large size of the contacts in combination with an out-of-plane stripe domain magnetic structure of the ferromagnetic layer. A fabrication process for 4T structures based on multiple-step electron beam lithography was therefore developed. The fabrication process, however, proved to have a very low yield of functioning devices. Even if the device's fabrication was successful, the metalization contained a bottleneck point due to the device geometry, which made the devices very sensitive to the applied current and generally unreliable. Nevertheless, it was possible to obtain a functioning device and study it using 4T Hanle measurements. We have observed a signal mostly consistent with the Hanle effect, it was, however, insensitive to the direction of the applied magnetic field. Even upon rotation by 90° , the sample still demonstrated the same peak, without any hint of a spin-valve effect. This behavior is hitherto unreported in literature and so far not understood; however, it is most probably related to the complex magnetic domain structure of our Mn_5Ge_3 layers. The measurements were nevertheless evaluated using a one-dimensional spin drift diffusion model, under the assumption that the observed signals are indeed related to spin injection. The obtained values and behavior in temperature for spin lifetimes and spin diffusion lengths are consistent with published literature on *p*-Ge. To obtain further support of the obtained values, we have performed low-temperature magnetoresistance on the *p*-Ge(111) substrate and fitted the observed WAL with the HLN model. We have obtained accurate fits to the data and extracted spin phase coherence and spin-orbit lengths. The extracted

values are consistent with the literature, and while they are approximately one order of magnitude lower than those extracted from 4T measurements, given the scatter in the 4T data, they can be considered consistent. This supports the hypothesis that we have indeed observed a Hanle signal in the nonlocal measurement. The lack of a spin-valve signal, however, renders the device unsuitable for our main goal electrical read-out of molecular spin states. As a possible way forward, we performed magnetoresistance measurements on a *p*-Ge(100) wafer, as well as magnetometry and FMR measurements on a Mn₅Ge₃ fabricated on a Ge(100). We have observed that while the *p*-Ge(100) wafer is indeed more suitable for spintronic applications due to longer spin phase coherence and diffusion lengths (approximately double than in Ge(111)), the FMR measurements suggest that the preferred magnetization direction of the Mn₅Ge₃ layer is between 45° and 90° from the sample plane. This would mean that the obtained Mn₅Ge₃/Ge(100) layers are unsuitable for our applications as well.

As an outlook in this direction of research, there are multiple ways forward. First, the geometry and fabrication process of the 4T structures need to be reworked. The current and spin path is defined through a highly doped Ge channel formed into a mesa structure on top of the substrate. This elevation of the channel causes current bottlenecks at the edges of the mesa, where current leads are connecting to the channel. This mesa structure needs to be lowered into the substrate in order to avoid any steps in the current leads. This modification should assure a manufacturing process with higher yield and more reliable devices. To investigate if it is possible to use Mn₅Ge₃ on Ge(111) for spintronics, it would be interesting to explore various annealing parameters and Mn thicknesses further, to find out if it is possible to form layers thinner than 10 nm. Such thin layers were shown to be single domain, with all of their magnetization in-plane, which could lead to functional spin valves. Lastly, moving to Ge(100) as a substrate would be interesting from an application point of view, since the wafer orientation is more commonly used in the industry and the spin dynamics in this orientation seem to be more favorable. Mn₅Ge₃ on top Ge(100) is a relatively new area of research, with the potential to create fully in-plane magnetized Mn₅Ge₃.

4 Electrically detected magnetic resonance of potential molecular qubit hosts

This chapter presents the development of an EDMR spectrometer at X-Band frequencies. After introducing the various components that compose the spectrometer, we discuss each of them in detail, along with their evolution throughout the project and their influence on the measurement. The set-up was tested by performing EDMR measurements on P3HT, both nominally undoped and chemically doped. After investigation of the various experimental parameters, we present the first EDMR measurements on $(\text{Per})_2\text{Pt}_{0.75}\text{Au}_{99.25}(\text{mnt})_2$. While we have observed a clear EDMR signal, both at room temperature and 200 K, we have discovered that the investigated sample was of the semiconducting β phase. These measurements represent the first steps in investigation of crystalline organic conductors as potential hosts of MQBs.

4.1 Introduction

Electrically detected magnetic resonance is an umbrella term covering the detection of an electron magnetic resonance transition¹ via a change in the conductivity of a sample [46]. Most commonly it is the result of spin-dependent recombination or transport, which will be the main focus of this chapter, there are, however, a variety of other processes responsible for this effect (Section 2.3.3). Compared to traditional, inductively detected ESR, this technique has a number of advantages: no need for microwave detection circuitry; experimental access to processes directly influencing the charge transport; and, depending on the process responsible for the EDMR signal, potentially higher sensitivity. On the other hand, only very specific samples can manifest EDMR and due to complexity of the processes leading to an EDMR signal, the parameter space determining conductivity signal

¹Meaning both electron spin resonance and ferromagnetic resonance.

is larger compared to inductive ESR. This can be partially remedied by performing pulsed experiments, which are more complex than their classic counterpart. Nevertheless, this technique has proven very useful in studying defects in technologically relevant materials and devices such as amorphous silicon [82] or organic light emitting diodes [83] and is intrinsically suited for the electrical read-out of quantum bits [84].

Despite the age² and usefulness of EDMR spectroscopy, there is only a handful of such spectrometers in the world, all of them being lab-built, tailored to the specific needs and resources available to the groups who built them. EDMR has been implemented in a frequency range almost as broad as ESR: from 200 MHz low-field tabletop spectrometers [88], through broadband stripline set-ups [89], up to W-band [90] and even state-of-the-art cw/pulsed 263 GHz spectrometers [91]. The most common way, however, to realize EDMR spectroscopy, is by modifying the relatively ubiquitous X-Band spectrometers, where even a tabletop version was developed [92]. We decided to use our X-Band ESR spectrometer as a basis as well.

To test and benchmark our system, we have chosen to use the well-known organic semiconductor poly(3-hexylthiophene) (P3HT), a general discussion of which can be found in Chapter 5. Curiously, considering the staggering volume of literature on this material and its relevance to modern technology, there are only two articles discussing EDMR on the pure material, one from 2018 [93] and one from 2019 [94]. Other EDMR reports deal with P3HT only in blends with other materials in, for example, solar cells [95, 96]. We have chosen to use P3HT as a test sample mainly due to its availability and ease of processing, with the outlook of potentially gaining some new insights into the material, given the low number of EDMR reports on it and our interest in it as host for MQBs.

Finally, we wanted to investigate the possibility of using a one-dimensional molecular metal as a host for MQBs. This idea was motivated by the realization that a molecule which has one of the longest T_M times and held the record for the longest T_M for a few years, $\text{Cu}(\text{mnt})_2$ [17], could also be found in the crystal structure of a fascinating family of molecular materials that display metal-like conductivity. The material family in question, $(\text{Per})_2\text{M}(\text{mnt})_2$ ($M = \text{Fe}, \text{Co}, \text{Ni}, \text{Cu}, \text{Au}, \text{Pt}, \text{Pd}$), has been investigated since the 1970s due to the interplay between localized magnetic moments of the transition metal ions with electrons delocalized along the perylene stack [97]. A short discussion of the material and our preliminary experiments can be found in Section 4.5.

²First reports of EDMR are due to a bolometric effect in InSb from 1965 [85], after which came various reports of EDMR in other materials, such as rutile [86] and Si [32, 87].

4.2 Experimental methods

The equipment developed and used for EDMR measurements is described in detail in Section 4.3.

Materials

Solvents were acquired commercially and used as received. Regioregular P3HT was bought from Merck and used without further purification. The number average molar mass extracted from gel permeation chromatography was $\overline{M}_n = 28.7 \text{ kg}\cdot\text{mol}^{-1}$ with a polydispersity index of $\text{PDI} = 1.77$. 2,3,5,6-tetrafluoro-tetracyanoquinodimethane (F_4TCNQ) (98.0%) was bought from TCI. 2,2,6,6-Tetramethyl-1-piperidinyloxy (TEMPO) was purchased from Sigma-Aldrich. $(\text{Per})_2\text{Pt}_{0.75}\text{Au}_{99.25}(\text{mnt})_2$ (mnt=malesonitriledithiolate) was received from Prof. Manuel Almeida from the University of Lisbon, where it was prepared as described in [98].

Sample preparation

Substrates were prepared as described in Section 4.3.1 and cleaned in an ultrasonic bath using acetone and isopropanol.

Sample **P3HT-9D**: film of P3HT was deposited on top of a quartz substrate from a 3 g/L toluene solution by static spin coating at 1000 rpm using a Süss MicroTec Delta-6RC spin coater under N_2 atmosphere in a glovebox. The sample was taken out and soldered by hand under ambient conditions to copper wires (< 15 min exposure). After soldering and sealing the tube with a custom feedthrough described in Section 4.3.1, the tube was pumped and flushed with He three times and kept under a slight overpressure of He gas. It was kept under these conditions for nine days before the presented spectra were recorded. We should note that an EDMR signal was visible only after two days and that only due to slow leakage of ambient oxygen inside of the sample holder, which doped the P3HT film over time.

Sample **TEMPO:P3HT**: film was prepared from a solution of 6 g/L of P3HT with 5wt% of in toluene with the same procedure as described above and measured immediately. It should be noted that later investigations revealed that the TEMPO molecule is not stable in the P3HT matrix [99] and bears no effect on the properties of P3HT or its EDMR signal.

Sample **F4:P3HT**: P3HT layers (6 g/L in chlorobenzene) sequentially doped with F_4TCNQ ($1.3 \text{ g}\cdot\text{L}^{-1}$ in acetonitrile) were spin-coated onto Si substrates under inert

conditions, followed with the same procedure as described previously and measured immediately.

Sample **Per-Pt**: a single crystal of $(\text{Per})_2\text{Pt}_{0.75}\text{Au}_{99.25}(\text{mnt})_2$ (mnt=maleonitriledithiolate) was glued to a quartz substrate using silver paste. The compound crystallizes in the form of needle-like crystals, with the b -axis of the lattice being the long axis of the crystal. The crystal was mounted parallel to the long axis of the substrate, i.e., bridging the two electrodes at the tip.

4.3 Development of an electrically detected magnetic resonance spectrometer

While the general requirements to perform EDMR experiments are relatively simple to formulate and do not differ much from standard ESR, the exact experimental execution can be, depending on the sample, relatively complex. Due to the nature EDMR, even obtaining a sample and experimental conditions for which one can be reasonably certain that a EDMR signal should be visible is a non-trivial task. To somewhat mitigate these difficulties, the design of the spectrometer was discussed with Dr. Andreas Sperlich and Dr. Stefan V ath (University of W urzburg) as well as with Prof. Dr. Wolfgang Harnett and Dr. Svetlana Kucher (University of Osnabr uck). Figure 4.1 shows a schematic representation of the various interacting components of an EDMR spectrometer. The set-up can be roughly divided into five components: computer, microwave and electrical circuits, magnetic fields, and sample holder. The computer facilitates control and data acquisition from the other systems. The microwave circuit ensures critical coupling to the cavity in which the sample is held and microwave excitation. “Magnetic field” entails the control and read-out of both the static and the modulation fields. While these components are identical to those used in a conventional ESR spectrometer, an additional electrical circuit is necessary for the read-out of spin transitions. Finally, the sample holder needs to be tailored to this technique: appropriate substrates, electrical connections, illumination and when dealing with air-sensitive samples, atmosphere management. In the following subsections, each of these systems will be described in detail.

4.3.1 Sample holder

When designing the sample holder of an EDMR experiment, we had to consider the following points:

- To be able to perform the experiment both at room and low temperatures using the flow cryostat already installed in the spectrometer, both the sample and sample

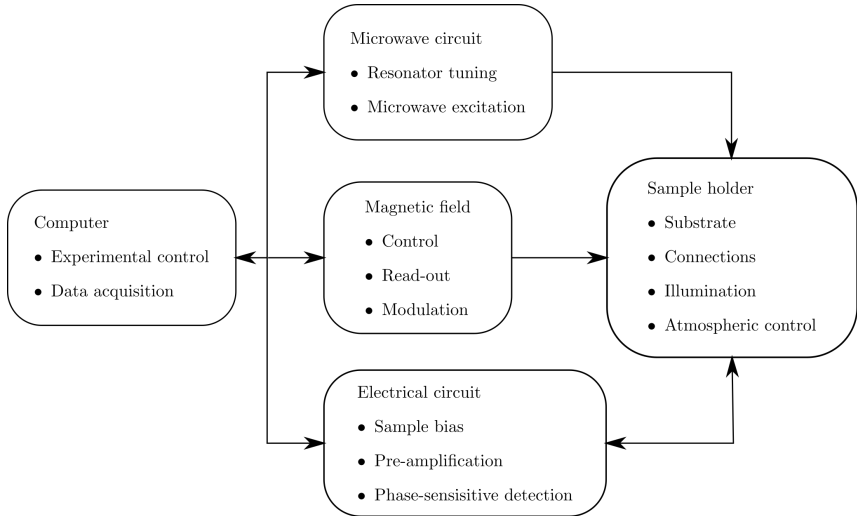


Figure 4.1: Schematic representations of the various systems and their interaction in a EDMR spectrometer.

holder had to be compatible with standard ESR tubes, with 3 mm to 4 mm inner diameters and 1 mm thick walls.

- The electrically active area of the sample has to be in the maximum of the B_1 field. However, metal disturbs the shape of the resonant mode inside the MW cavity. To disturb the MW field as little as possible, the electrical contacts have to be thinner than the skin depth at those frequencies.
- Some of the samples that we wanted to investigate using EDMR, such as organic semiconductors, are often air-sensitive. Some way of managing inert atmospheric conditions is required.
- Similarly, some samples might require light excitation to excite charge carriers into the conduction band in order to show an EDMR signal.

Considering all of the above points, the feedthrough in Figure 4.2a and b was designed. It consists of a brass body with 3 openings: one compatible with the DBEE 102 A051-130 hermetic receptacle from Fischer connectors, one for the ESR tubes, and one compatible with the QH-QS-6 miniature ball valve from Festo. The hermetic receptacle serves as the feedthrough for electrical connections and is screwed directly into the brass body. Its counterpart for connecting with the rest of the electrical circuit is the WSO 102 A051-130 right-angle plug from Fischer connectors. The right-angle variant ensures minimal strain on the quartz ESR tube coming from the weight of the cable itself. The cable had to be

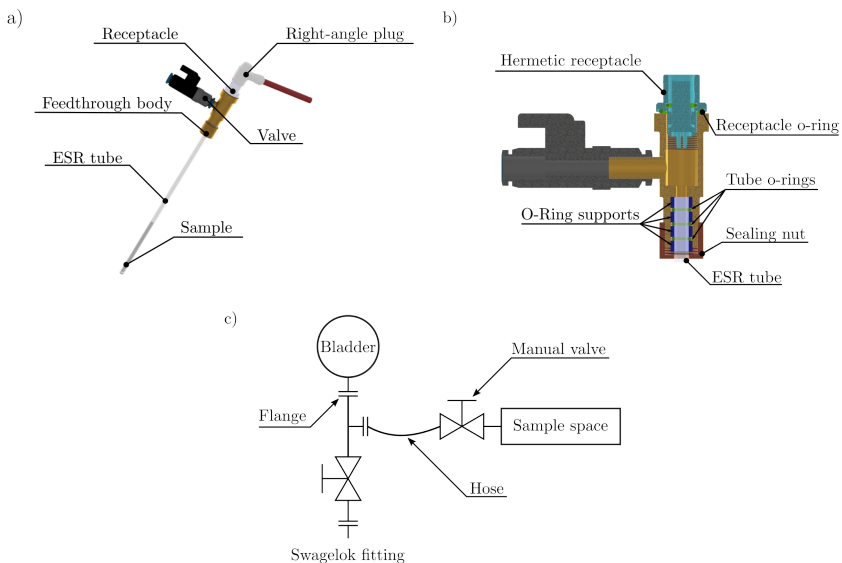


Figure 4.2: a) Overview of the EDMR sample holder designed in this work. b) Section view of the upper part of the sample holder. c) Schematic of the sample space atmospheric management system.

routed in a right angle to the tube due to space and cable length constraints. To seal off the ESR tube, a simple mechanism based on 3 o-rings between 4 supports squeezed by a nut at the bottom of feedthrough was implemented. Figure 4.2c shows the schematic of an atmospheric management system designed for our set-up. The sample space is connected to the rest of the system through the manual valve, which is in turn connected to a T-tube with a hose. The rest of the T-tube is connected to a rubber bladder (commonly used to pressurize He dewars) on one end and to a Swagelok fitting on the other. With this system, the sample space can be connected to a pumping line with the Swagelok fitting and either just evacuated and sealed off, or filled with an inert gas, such as N_2 , He, or Ar. To ensure minimal contamination with air, the balloon can be filled with the chosen gas to maintain overpressure of the inert gas after disconnection from the pumping line. For sample illumination, an LED lamp covering the visible spectrum was bought. The model chosen was KL2500 LED from Schott, due to its relatively high luminous flux a long light guide, simplifying the integration into the set-up. For fastening the light guide onto the resonator, a 3D-printed holder designed by Mario Winkler was used.

The samples we planned on investigating using EDMR included both films of organic

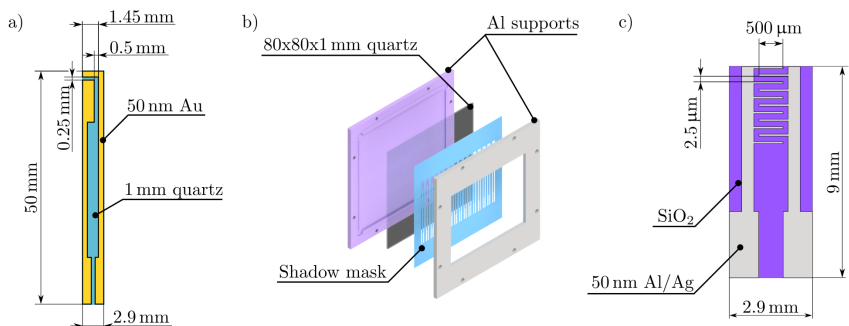


Figure 4.3: a) Design of the electrodes used for first experiments, suitable for all samples, e.g., thin films and single crystals. b) Exploded view of the assembly used for batch production of the electrodes shown in a). c) Electrodes developed for thin films of organic semiconductors.

semiconductors and single crystals, therefore, a substrate compatible with spin coating, soldering and contacting with silver paste was needed. We developed two types of sample holders. For the first, quartz was chosen as the substrate material and plates cut to 80 mm squares with 1 mm thickness were purchased from GVB GmbH. To electrically contact the samples, suitable electrodes had to be designed and fabricated. To facilitate easy manufacturing of the electrical connections using techniques available to us, a design compatible with simple shadow mask metal deposition was designed. Figure 4.3a shows the design of the individual electrode pair. The width of the electrodes was set to 2.9 mm for compatibility with both 3 and 4 mm ESR tubes, while the minimal distance between the electrodes, i.e., where the current will be flowing in the experiment, is 0.25 mm. This dimension is at the limits of metal stencil manufacturing, which we have chosen for creation of the shadow mask. While it is possible to create much finer stencils using polyimide as a substrate or UV photolithography techniques, we have chosen the simplest technique for the first experiments due to commercial availability and simplicity. The final assembly for the metal deposition can be seen in Figure 4.3b. This assembly was then inserted into a metal evaporation chamber and 50 nm of Au, on top of a 2 nm of Cr adhesion layer, was deposited by Dr. Yannic M. Gross. The quartz plate, together with the deposited electrodes, was then sent to A.L.L. Lasertechnik GmbH, where they cut out the individual electrodes using a CO₂ laser. These sample holders are suitable for general use and for applications where optical access from both sides of the sample is required.

For samples requiring electrical gating or larger effective electrode area, we developed a second design (Figure 4.3c). To increase the current flowing through the sample, the design uses multiple interdigitated electrodes, as well as a doped silicon substrate to

allow for application of gate voltage. In this case, the substrates were manufactured from p -Si(100) with 200 nm SiO₂ layer on top. The structures were fabricated from Al or Ag using photolithography and metal evaporation. After metal deposition, the individual samples were cut out using a diamond saw. The whole fabrication was done by Hannes S. Funk.

Finally, the electrodes have to be connected to the rest of the electrical circuit. Since the samples for EDMR are best fabricated directly on the substrates via spin coating or evaporation, the connections should be both mechanically stable and easy to perform. In view of the limited space inside a 3 mm ESR tube, this proved to be a challenge that was not completely solved. Multiple options were tried and successful measurements were performed; however none of the tested procedures can be described as ideal. Single core, isolated copper wires were soldered to the feedthrough and on most of the samples, these wires were then directly soldered onto the electrodes by hand. This, however, frequently led to destruction of the electrodes or short-circuits. Additionally, there is no way to perform the soldering in the glovebox used for sample preparation, making this highly unsuitable for air-sensitive samples. To try to and circumvent this, we have tried soldering pin sockets directly to the electrodes before sample depositions, and subsequently connecting the wires via pins while still in the glovebox; this has, however, also proven unreliable due to short-circuits and low mechanical stability.

As an outlook to solve these problems, some inspiration can be taken from the procedure developed by Schott *et al.*, and described in the Supplementary information to [100]. While the authors do not perform EDMR and do not have air-sensitive samples, they also use electrical contacts inside 3 mm ESR tubes. After the deposition of a batch of their electrodes onto a quartz substrate, they cut grooves around the individual electrode pairs. Afterward, they spin coat their polymer over the whole batch (to avoid problems with irregular spin coating on individual electrode pairs) and only then they separate the samples by applying pressure around the grooves. For contacting, they glue and wire bond their samples onto a carrier, which is then permanently soldered to the cables in their feedthrough. Some preliminary tests with wire-bonding of the interdigitated electrodes were performed, we have however encountered problems with adhesion of the metallic layer (Ag on quartz in that case). These problems could be solved by using a different substrate, adhesion layer, metal or wire bonding parameters. For our application, we could optimize the design of the feedthrough to accommodate a clamping mechanism for a sample carrier made out of simple copper-clad PCB. Our clean substrates could then be wire bonded to these carriers, taken into the glovebox for sample deposition, clamped into the feedthrough and sealed before transport to the spectrometer.

4.3.2 Microwave circuit

Even though it would be possible to observe EDMR with the maximum 200 mW output MW power of a Bruker EMX spectrometer in some samples, that is not a general rule. If the mechanism responsible for the EDMR signal is Spin-dependent Recombination (SDR), as we expected in our organic semiconductor samples, the signal-to-noise ratio will always benefit from higher MW intensities, since the signal cannot be saturated as in standard ESR. To expand the capabilities of our spectrometer, we implemented the Anritsu MG3692C/5-14-15A-27 MW signal generator. In this configuration, the generator can synthesize signals with frequencies between 8 MHz and 20 GHz with power of up to 1 W, optionally with amplitude modulation. To couple the signal generator to the waveguide circuit, a coax-to-waveguide adapter was used. Since we are using a resonator to enhance the MW intensity at the sample position, the signal generator cannot be used on its own. The MW bridge from the ESR spectrometer is still required in order to tune the circuit and sufficiently couple to the resonator. To facilitate easy switching between the two MW sources, a manual 3-port waveguide switch was implemented. During the experiment, the circuit was tuned using the MW bridge at 200 mW (maximum available power), after which the bridge output was turned off, the switch was changed to couple to the signal generator, where the exact same frequency was manually set used to excite the sample. Figure 4.4 shows a schematic representation of the microwave circuit.

While this system is working quite well, there is one possible quality-of-life and safety improvement available. To better protect the MW equipment against the careless user who would change the switch ports before turning off either the MW bridge or generator outputs, causing high-power reflections, exchange of the switch either to an electrically controlled one or a 4-port switch with an attenuator at the 4th port (or both) would be useful. If an electrically controlled switch were used, this procedure could be implemented in the control program with all the adequate safety precautions.

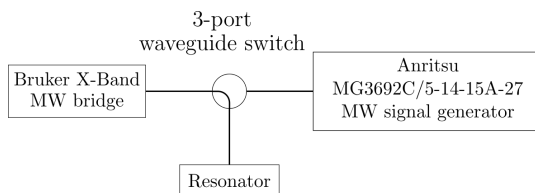


Figure 4.4: Simplified diagram of used microwave circuit.

4.3.3 Magnetic field

The magnetic field requirements for an EDMR experiment are the same as for an ESR experiment. Up to three magnetic fields have to be considered: the B_0 field that is being swept to fulfill the resonance condition; the magnetic component of the microwave radiation, B_1 ; and if the magnetic field modulation is used for Phase-Sensitive Detection (PSD), the modulation field B_{mod} . The B_1 field was considered together with the rest of the microwave circuit in the previous subsection; here we will mention it only with regard to MW amplitude modulation and focus on the B_0 and B_{mod} fields.

For generation of the B_0 field the X-Band ESR spectrometer already had a functional 1 T electromagnet ready to use, requiring no further parts. The control and read-out of the field are handled via the winEPR software from Bruker, supplied with the spectrometer. While this is fully sufficient for ESR experiments, in EDMR we need to correlate the measured electrical signal with the applied magnetic field, in order to gain spectroscopic information. Since our electrical circuit is fully custom and the Bruker software is compiled and proprietary, there is no straightforward way how to communicate the actual magnetic field to our data acquisition software. There are at least two relatively simple approaches to solving this problem. One is to integrate a separate magnetic field probe into the set-up, one that can be read out via our software. We have first tried this approach, using an older gaussmeter supplied with the spectrometer. The gaussmeter has, however, proven unsuitable for this application—the communication with the instrument was very slow and it was periodically losing the field value. While we had another, more modern gaussmeter available, there is an additional problem with this approach. If the data acquisition is not synchronized with the individual field steps, data is integrated over multiple field values, leading to smearing out of sharp lines or shifts in the apparent resonant field. To solve these problems, we have studied how the X-Band spectrometer operates during an ESR experiment. First, the user specifies the magnetic field range he wishes to sweep over by choosing a central field, sweep width and number of points. The software then simply divides the field range by the number of points to obtain a table of desired field values. Using this table of values, it subsequently uses a calibrated Hall probe together with (probably) a PID controller to reach each of the field values. The transitions between individual field points are triggered using a digital signal sent to a connector on the EMX console marked SWADV (Sweep ADVance). We have found that we can access this signal line using a T-connector and read out this trigger signal without any detriment to spectrometer function. For EDMR experiments, we can create an identical table of field values and use the SWADV signal to trigger our data acquisition accordingly. More details on how this signal needs to be modified to be used as a trigger

are in Subsection 4.3.5.

Phase-Sensitive Detection (PSD) is indispensable for both ESR and EDMR. In short, a LIA is used to generate a periodic signal at a specific frequency (f_{mod}), which is then used to modulate the signal of interest, after which the resulting signal is demodulated at that frequency, effectively suppressing unwanted frequencies. The demodulated output has two components: in-phase (X) and out-of-phase (Y). These are often recalculated into polar coordinates with $R = \sqrt{X^2 + Y^2}$ and $\theta = \arctan \frac{Y}{X}$ for convenience or phase correction, where all of the signal is recalculated into one channel. ESR most commonly uses a field-modulation scheme, where the physical quantity modulated is the B_0 field. By attaching a pair of coils to the sides of the resonator, the resonance field can be modulated with a sinusoidal signal, usually at 100 kHz. It is possible to modulate either the amplitude or the frequency of the MW radiation as well, depending on the used experimental set-up. While for the vast majority of ESR experiments a single modulation frequency is sufficient, EDMR, or spin-dependent recombination specifically, was shown to require access to multiple frequencies, since depending on the charge carrier dynamics, which are difficult to predict, a signal may be observable only at low frequencies, high frequencies or even just within a frequency window [50] (Section 2.3.3). The amplitude of the field modulation should be such that it does not distort the spectral lines of interest³, commonly between 0.01 and 2 mT. LIAs, such as the Zürich Instruments MFLI (ZI-MFLI), usually have only limited output power, which is not sufficient to effectively drive a set of modulation coils. The modulation signal, therefore, has to be amplified in order to drive a sufficient current through the coils. In our set-up, we have tested three methods of performing field modulation, as well as MW amplitude modulation, in order to assess their suitability in terms of accessible modulation frequencies and signal-to-noise ratio.

In the first approach (method FM A, Figure 4.5a), we can take advantage of the EMX consoles internal amplifier by supplying a modulation signal generated by the ZI-MFLI to the EXT. REF port on the console. The console then drives the coils as in its normal operation. This approach has the advantage that we have a direct access to the modulation frequency and amplitude parameters, without the need to use the proprietary winEPR software. The disadvantage is that we don't know the exact magnetic field that is being generated by a given modulation amplitude. The workaround is to measure the current in the circuit by adding a multimeter between the console and the coils, and compare it with the current that flows there during normal ESR operation using the calibrated modulation field values in the winEPR software. Another approach to field modulation is to drive the coils directly through the EMX console and send a reference signal to the ZI-MFLI for synchronization (Method FM B Figure 4.5b). With this method, the

³Usual recommendation is to modulate by less than 20% of linewidth.

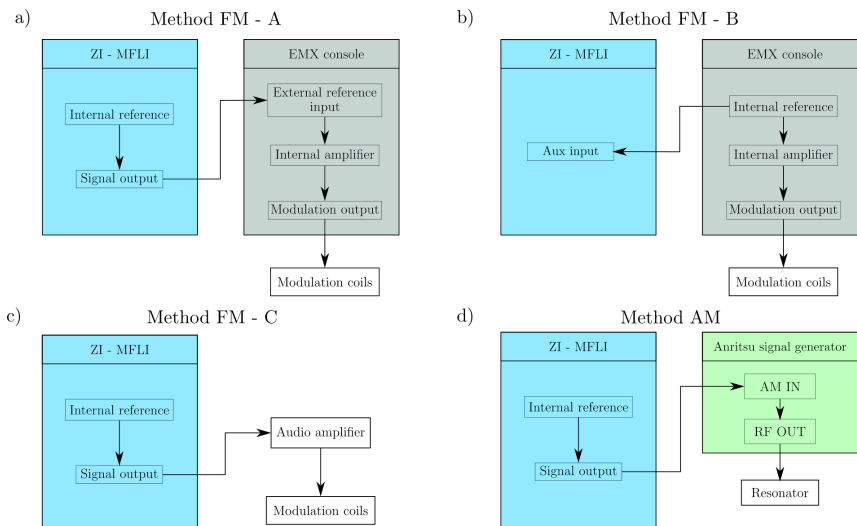


Figure 4.5: Four different signal modulation schemes tested in our set-up. a) Using the ZI-MFLI as the reference and EMX console as an amplifier. b) Using the EMX console internal reference and amplifier, with the ZI-MFLI synchronizing with the EMX reference signal. c) Using the ZI-MFLI together with a commercial audio amplifier. d) Performing MW amplitude modulation using the Anritsu signal generator synchronized with the ZI-MFLI reference signal.

modulation frequency and amplitude are controlled by the winEPR software, however, now we can take advantage of the calibration of the spectrometer. While this approach has proven to be easy to perform and works for the two samples investigated, it is still limited by the frequency range of the EMX console, which is effectively restricted to 100 kHz due to the modulation coil being part of an LC circuit (Figure 4.8c). To circumvent the EMX console entirely, we can use the ZI-MFLI with a separate amplifier to drive the coils (Method FM C, Figure 4.5c). While the audio amplifier we had at hand to perform these tests (InterM L-1400 Audio Amplifier) also limits the usable frequency range (20 Hz to 20 kHz with optimal performance, up to 70 kHz with -3 dB attenuation), it adds significant flexibility to the set-up at the cost of losing the calibration information. Finally, we have tested abandoning field modulation altogether in favor of MW amplitude modulation. One of the options on our Anritsu signal generator (option number 14) allows for an external signal to drive the amplitude of the generated MWs. We can then simply connect the signal output of the ZI-MFLI to the AM IN port of the signal generator, set the depth and sensitivity of the modulation (e.g., 1 V corresponds to 50 % amplitude) and have another modulation method independent of the EMX console circuitry.

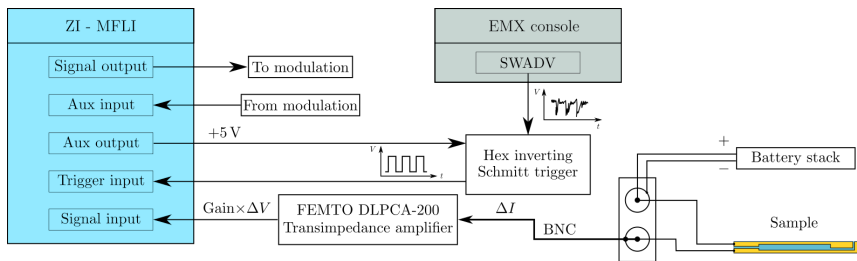


Figure 4.6: Schematic representation of the electrical circuit used for EDMR experiments. The modulation circuit is omitted for clarity and detailed in Figure 4.5.

4.3.4 Electrical circuit

Figure 4.6 shows a schematic representation of the electrical circuit responsible for detecting the magnetic resonance transition, along with triggering of the data acquisition. In case of an unknown sample, it is first necessary to measure the $I - V$ characteristics using the Keithley 2450 Source-Measure unit in order to find a suitable working point. Once the electrical behavior of the sample is known, one of the electrodes is biased by an interconnected stack of 9V batteries. The batteries provide a more stable bias when compared to the source-measure unit, which proved to be unusable for this purpose (Figure 4.9f). The other electrode is connected to the FEMTO DLPCA-200 variable gain transimpedance amplifier. The amplifier converts the current flowing between the electrodes into a voltage signal, while amplifying from 10^3 to 10^{11} times, depending on the available bandwidth and absolute magnitude of the signal. This pre-amplified signal is then fed into the signal input of the ZI-MFLI LIA. As mentioned in the previous section, the data acquisition is triggered by the SWADV signal from the EMX console. The raw signal on the SWADV output is, however, unsuitable for triggering the ZI-MFLI: it has inverted polarity to what the ZI-MFLI expects and is rather noisy. To overcome this, a hex-inverting Schmitt trigger (74HC14) is necessary to invert and clean-up the signal. The Schmitt trigger requires 5V bias voltage to operate, which is supplied by the ZI-MFLI Aux output. The clean trigger signal is sent to the trigger input of the ZI-MFLI. Modulation of the sample signal is handled with the signal output and aux input of the ZI-MFLI, which was discussed in the previous section and is omitted here for clarity.

4.3.5 Experimental control and data acquisition

A desktop personal computer is attached to the spectrometer to facilitate most of the experimental control and data acquisition. The EMX ESR spectrometer and its parts

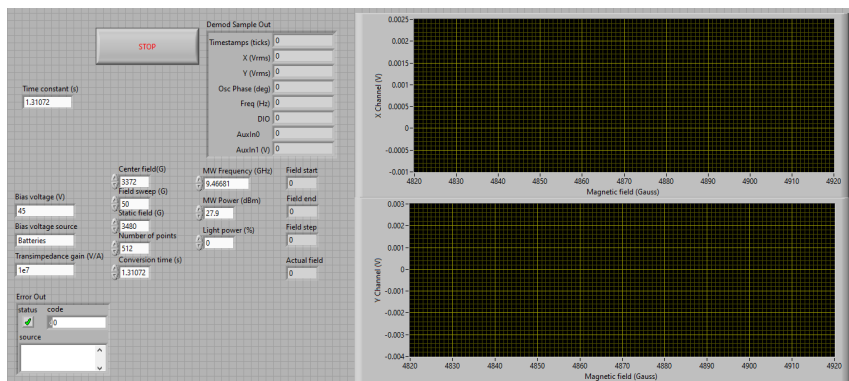


Figure 4.7: Front panel of the EDMR data acquisition software.

are only controllable via the included winEPR software, providing no access point for custom-made software. This means that the control of the MW bridge and the magnetic field can only be performed through winEPR and none of the data reported back from those parts of the spectrometer can be read out. For control of the ZI-MFLI and data acquisition, custom program was written in LabView. Given the limitations imposed on us by the ESR spectrometer, several workarounds had to be implemented into the measurements protocol. Figure 4.7 shows the front panel of the measurement program. All of the fields with the white background, except for the 'Error Out' window, have to be filled out manually. The values, along with additional LIA settings from the ZI-MFLI, are then saved alongside the measurement values in the data file. The magnetic field axis is calculated within the software based on user input. In order to synchronize it with the EMX spectrometer field sweep, one has to start the LabView program, after which the field sweep has to be started inside the winEPR software. The LabView program then starts the data acquisition synchronized with the field steps, thanks to the SWADV signal from the console.

While the software fulfills its function, there is significant potential for improvement. The EMX MW bridge and magnetic field cannot be controlled or read-out without the proprietary software, there are, however, ways how to simulate mouse and keyboard operation from within LabView, as well as read out values displayed on the monitor using image processing. With such implementation, the whole experiment could be controlled from within one program. Additionally, the Anritsu signal generator and the LED light source could be integrated into the software, to minimize tasks which the user has to do manually outside of the program.

4.4 EDMR on P3HT

As a test sample, the organic semiconductor P3HT was chosen, due to the relatively easy processing and availability. Since pure P3HT doesn't have enough free charge carriers to observe an EDMR signal, the material has to be doped first, either by exposure to ambient air and light (sample **P3HT-9D**) or, in a more controlled manner, with the electron acceptor F_4TCNQ . After assembly and initial testing of the set-up, we studied the influence of various experimental parameters on the EDMR signal.

A comparison of the performance of various modulation schemes can be seen in Figure 4.8a. The measurements were performed on the **P3HT-9D** sample, with $f_{\text{mod}} = 6.267$ kHz. We can observe that there are essentially no differences in terms of Signal-to-Noise Ratio (SNR), with the small changes in amplitudes of the signals a consequence of the different modulation currents. We can therefore use all of the three methods interchangeably. The overall low magnitude of the signals was later explained by measuring the dependence of the signal on the used f_{mod} (Figure 4.8c), where it became clear that the field modulation was highly optimized for 100 kHz only. Figure 4.8b shows the comparison of the FM B ($B_{\text{mod}} = 2$ mT, $f_{\text{mod}} = 100$ kHz) and AM modulation (95% modulation depth, $f_{\text{mod}} = 6.137$ kHz) schemes performed on the **F4:P3HT** sample. While the AM scheme seems to provide slightly lower noise floor, the amplitude is almost halved when compared to the signal from FM B. When measuring the f_{mod} dependence, however, we have observed that the signal could be potentially much higher with lower modulation frequencies (Figure 4.8d) — it could, however, lead to higher noise as well. Nevertheless AM modulation also seems a viable option for the experiments should a modulation method not connected to coils or AC magnetic fields be required.

Figures 4.9a to e shows another round of test measurements performed on the **F4:P3HT** sample at room temperature. In Figure 4.9a, we can see the dependence of the signal intensity on field modulation amplitude (B_{mod}), with Figure 4.9b showing the second integral of the measured signal as a function of B_{mod} . We can clearly see an expected, linear increase in the signal intensity with increasing B_{mod} . We have fitted the signal to a single Gaussian line to quantify the influence of measurement parameters on the signal. A comparison to a Lorentzian fit can be seen in the same figure as well. While at lower modulation amplitudes the difference between the two lineshapes is not that prominent, at 2 mT we can clearly see that the line is of a Gaussian lineshape. Table 4.1 contains all the parameters extracted from the depicted measurements, along with errors of fits. It should be noted that the g values should be taken into account only in terms of relative change between measurements, as we did not perform a field offset check with a calibration sample (the offset in our magnet can reach values of up to 0.5 mT). Since the g value

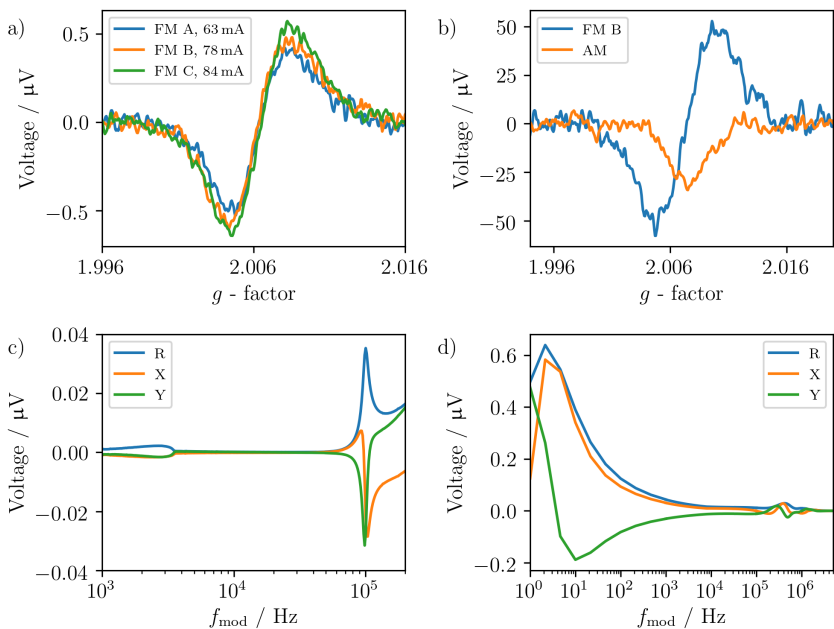


Figure 4.8: a) Comparison of the three different field modulation schemes performed on the **P3HT-9D** sample. The current noted in the legend is the I_{rms} flowing through the modulation coils at $f_{\text{mod}} = 6.267$ kHz. b) Comparison of the FM B ($B_{\text{mod}} = 2$ mT, $f_{\text{mod}} = 100$ kHz) and AM modulation (95% modulation depth, $f_{\text{mod}} = 6.137$ kHz) schemes performed on the **F4:P3HT** sample. c) Frequency response of the EDMR signal measured at a fixed field using the FM A scheme on the **F4:P3HT** sample. d) Frequency response of the EDMR signal measured at a fixed field using the AM scheme on the **F4:P3HT** sample. All measurements performed at room temperature.

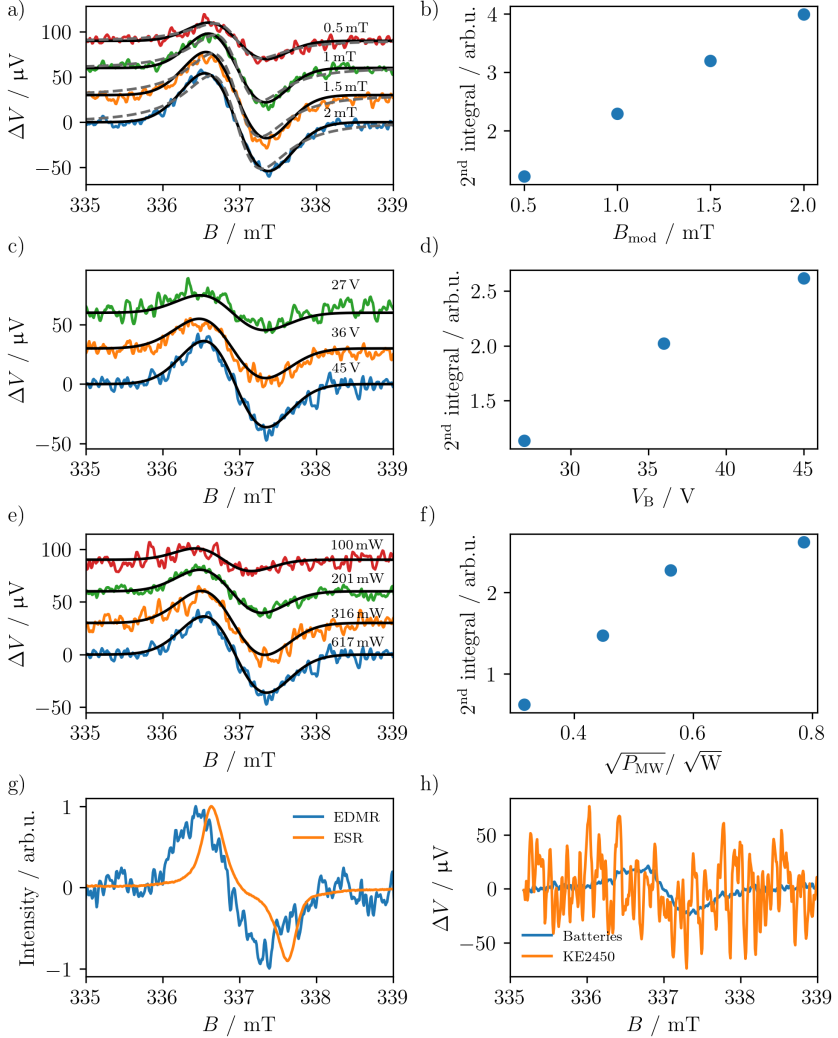


Figure 4.9: Various EDMR test measurements. Unless otherwise noted, the measurement parameters were: $B_{\text{mod}} = 2$ mT, $V_B = 45$ V, $P_{\text{MW}} = 617$ mW. Panels a to e show measurements performed on the **F4:P3HT** sample at room temperature. Black lines are fits of a Gaussian function, dashed gray lines are Lorentzian. a) and b) Field modulation amplitude dependence, modulation scheme FM B. c) and d) bias voltage dependence. e) and f) MW power dependence. g) Comparison of a simultaneously recorded ESR and EDMR signal, normalized for clarity, $P_{\text{MW}} = 201$ mW. h) Comparison of different sources of bias voltage, performed on sample **TEMPO:P3HT** at $T = 140$ K.

should not depend on B_{mod} , and there is no observable trend in the measurements, the mean value and the standard deviation (2.00729 ± 0.00004) of the measurements can be indicative of the experimental error of the magnetic field. The linewidth, however, clearly increases from $\Delta B_{\text{pp}} = 0.621 \pm 0.003$ mT at $B_{\text{mod}} = 1$ mT to $\Delta B_{\text{pp}} = 0.687 \pm 0.003$ mT at $B_{\text{mod}} = 2$ mT. A modulation amplitude of 1 mT is the upper limit before we start to artificially increase the linewidth at room temperature. Figures 4.9c and d show the dependence of the signal on the applied bias voltage (V_{B}). The clear trend in this case is the increase in signal intensity at higher bias voltages, which is consistent with EDMR theory—higher current in the sample means more recombination/hopping events can take place. Similarly, Figures 4.9e and f compare measurements at different MW powers (P_{MW}). From the KSM model of EDMR coming from spin-dependent recombination, we would expect the signal intensity to have square root dependence on P_{MW} (Section 2.3.3). This is not the case above 300 mW, where the difference between 316 mW and 617 mW is marginal, suggesting that we are close to a complete saturation of the spins. In contrast, in conventional ESR we would expect to observe significant line broadening (Section [44]), which is clearly not the case. Upon observing that an EDMR signal is still visible even with $P_{\text{MW}} = 201$ mW, which is the maximum output power of the EMX MW bridge, we have decided to record an ESR and EDMR signal simultaneously using the MW bridge as the source. Figure 4.9g shows both of the normalized signals. This comparison shows us that the two signals are not directly connected, i.e., the species that absorb the MW radiation the most during an ESR experiment is not the same as the one responsible for the EDMR signal. This hypothesis is supported by three observations. First, the two signals have clearly different g -values, assuming there is no systematic error responsible for the shift. Second, the two signals have different lineshapes; while the EDMR signal is inhomogeneously broadened, the ESR signal is single Lorentzian line [99]. Third, the linewidth is significantly different as well; the ESR measurement is strongly overmodulated, both at $B_{\text{mod}} = 2$ mT and $B_{\text{mod}} = 1$ mT, while the EDMR signal shows barely any signs of distortion. Both signals, however, appear only after doping. It is widely accepted that the conductivity in organic semiconductors is of hopping nature, as we have observed as well in the F_4TCNQ doped P3HT system at low temperatures (Section 5.3.3). With this in mind, the observed EDMR signal could be a consequence of spin-dependent hopping of polarons between individual P3HT chains. The F_4TCNQ doping would then simply provide sufficient amount of charge carriers to observe this effect. Another possibility could be that the F_4TCNQ dopant itself serves as a recombination center, the EDMR signal would therefore be a consequence of spin-dependent recombination at the dopant site. Further experiments would be necessary to investigate the origin of the signal. As a final remark, we have tested using the Keithley 2450 SMU as a source for the bias voltage

Table 4.1: Parameters extracted from Gaussian fits to the test EDMR measurements on **F4:P3HT**. Errors are errors of fits.

Exp. parameter	Value	$B_{\text{res}} / \text{mT}$	g	$\Delta B_{\text{pp}} / \text{mT}$
B_{mod}	0.5 mT	336.971 ± 0.006	2.00724 ± 0.00003	0.621 ± 0.009
	1.0 mT	336.965 ± 0.003	2.00728 ± 0.00002	0.621 ± 0.005
	1.5 mT	336.954 ± 0.003	2.00734 ± 0.00002	0.655 ± 0.006
	2.0 mT	336.959 ± 0.002	2.00731 ± 0.00001	0.687 ± 0.003
V_{B}	27 V	336.906 ± 0.012	2.00763 ± 0.00007	0.705 ± 0.021
	36 V	336.905 ± 0.006	2.00763 ± 0.00004	0.721 ± 0.010
	45 V	336.941 ± 0.004	2.00742 ± 0.00002	0.680 ± 0.007
P_{MW}	100 mW	336.789 ± 0.014	2.00833 ± 0.00008	0.608 ± 0.024
	201 mW	336.888 ± 0.005	2.00774 ± 0.00003	0.678 ± 0.009
	316 mW	336.915 ± 0.006	2.00757 ± 0.00004	0.692 ± 0.010
	617 mW	336.941 ± 0.004	2.00742 ± 0.00002	0.680 ± 0.007

instead of the batteries. And example measurement on the TEMPO:P3HT sample at a temperature of 140K can be seen in Figure 4.9h. This has proven completely unsuitable, either because of an incorrect grounding scheme employed or due to higher voltage noise coming from the SMU.

To conclude, we have shown that doped P3HT is an easily accessible test sample for EDMR measurements and investigated parts of the experimental parameter space to find combinations which provide measurable signals. The determination of the exact mechanism responsible for the observed signal is beyond the scope of this study, but given the lack of publications on EDMR of doped P3HT, a detailed investigation in terms of dopant concentration and temperature would be warranted.

4.5 EDMR on $(\text{Per})_2\text{Pt}_{0.75}\text{Au}_{99.25}(\text{mnt})_2$

Crystalline molecular metals, also called molecular or organic conductors, are a fascinating class of materials, which, despite their molecular nature, display metallic or even superconducting behavior. This conductivity is often strongly anisotropic, in certain compounds to such an extent that it can be considered only one-dimensional. One-dimensional organic conductors have a special place in the history of molecular metals, since the first molecular crystal exhibiting metallic conductivity was found when the perylene molecule (Figure 4.10a) was exposed to Br in 1954 [101]. It was then realized

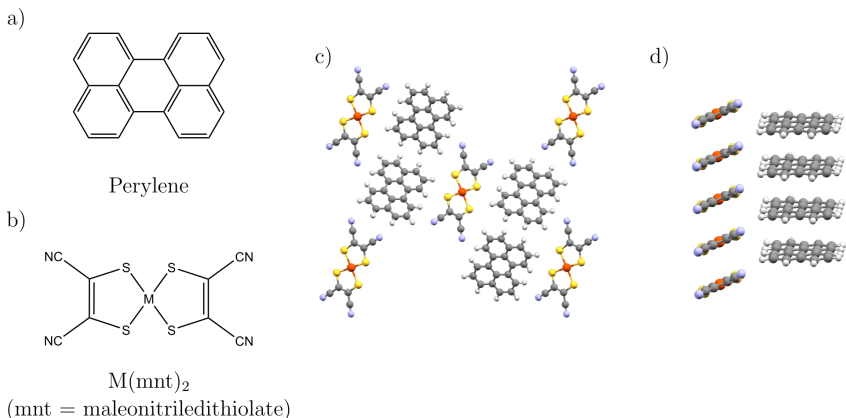


Figure 4.10: a) Chemical structure of the perylene molecule. b) Chemical structure of $\text{M}(\text{mnt})_2$ family of complexes. c) Crystal structure of the $\alpha\text{-(Per)}_2\text{M}(\text{mnt})_2$ as viewed along the crystallographic b axis. d) Stacking of the (Per) and $\text{M}(\text{mnt})_2$ moieties in the $\alpha\text{-(Per)}_2\text{M}(\text{mnt})_2$ crystal. Crystallographic data from [102].

that this is a consequence of the extended interaction between the π -electrons in the highest occupied molecular orbitals of the planar perylene molecules, which are stacked on top of each other in a crystal [103]. After oxidation, these perylene stacks form an effectively one-dimensional conducting channel. Perylene-halogen complexes have the honor of being the first in the vast field of organic conductors. For the purposes of this thesis, however, the complexes containing metal anions are much more relevant. Among these, none were studied in such detail as the perylene conductors with $\text{M}(\text{mnt})_2$ (mnt = maledonitriledithiolate), with $\text{M} = \text{Fe}, \text{Co}, \text{Ni}, \text{Cu}, \text{Au}, \text{Pt}, \text{Pd}$ (Figure 4.10b). All of these compounds are essentially isostructural and depending on the metal, the resulting anion can be either diamagnetic or paramagnetic. This allows for creating materials in which localized magnetic moments reside in defined, reproducible distances from a conducting

channel. It should be noted, however, that the compounds can crystallize in one of two phases: α and β . Figure 4.10c shows the crystal structure of a α -(Per)₂M(mnt)₂ molecular conductor, viewed along the crystallographic b axis, representing a slice from the stacked structure. Figure 4.10c shows an individual stack of perylene and M(mnt)₂ molecules. Due to the isostructurality of the various transition metal variants, one can combine a pair of metals, such as Pt and Au, to obtain a mostly diamagnetic material doped with relatively small amounts of paramagnetic molecules, effectively suppressing the interactions between the metal anions to observe the interaction between the isolated spins and the conducting channel [98, 104]. The β phase, however, has a disordered structure and behaves as a semiconductor with temperature activated hopping transport [105]. These two phases are sadly indistinguishable by eye, the only way to identify the phase being conductivity, x-ray diffraction, or thermopower measurements. A complete overview of all the investigations performed on these materials is beyond the scope of this section, the interested reader is therefore referred to [103]. For a more recent overview of some of the physics in these materials, especially the structural and magnetic instabilities within them, see [106].

To our knowledge, there is no report of an EDMR experiment performed on a single crystal of a molecular metal. We have chosen to perform the first preliminary measurements in this area, with the hopes of observing a spin-dependent electrical transport process, such as scattering in the α phase or hopping in the β phase. Indeed, as discussed in [106], some of the α -(Per)₂M(mnt)₂ variants, with M = Pd, Ni, and Pt, represent a realization of a one-dimensional Kondo lattice, i.e., a material where the spins of the itinerant electrons are strongly coupled to the localized spins, creating a magnetic scattering center. The synthesis of these materials is non-trivial [103], we were, however, able to obtain a sample of (Per)₂Au_{1-x}Pt_x(mnt)₂, with $x = 0.0075$ from Prof. Manuel Almeida (University of Lisbon). A needle-like single crystal of the **Per-Pt** sample was glued to our quartz substrates using silver paste, with its b -axis bridging the two electrodes, being perpendicular to B_0 after mounting in the spectrometer. Given the relatively high conductivity of these materials, care has to be taken when applying bias voltages — during first attempts to measure IV curves in the range from -10 to 10 V, the crystal was immediately burned. Figure 4.11a shows an IV curve in a more appropriate range (± 0.5 V) at three different temperatures.

We can see that at room temperature the sample shows completely ohmic characteristics, while at $T = 150$ K the sample shows a clearly non-linear onset of current around zero. We can also see that the resistance increases with decreasing temperature. There are two possible explanations to this, which may be true simultaneously. First is that the contacts between the Au electrodes and the crystal are non-ohmic due to imperfect application of the silver paste. Since these are only two-point measurements, we are measuring the conductivity of all the leads and contacts as well. Second, the mounted crystal is the β

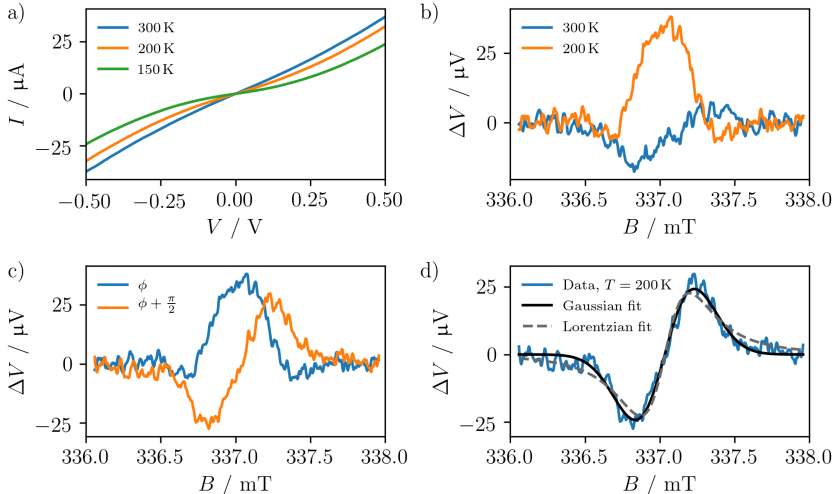


Figure 4.11: Measurements of the **Per-Pt** sample. a) IV curves recorded at various temperatures. b) EDMR spectra at two different temperatures. c) Comparison of the EDMR curve recorded at 200 K without any MW phase manipulation (ϕ) and with a $\pi/2$ phase shift ($\phi + \frac{\pi}{2}$). d) Fits of the corrected EDMR curve recorded at 200 K.

phase of the compound, which is a semiconductor instead of metal. Unfortunately, these two phases are distinguishable only by conductivity, thermopower or XRD measurements. We can estimate the conductivity of the measured sample to be on the order of 10^{-1} - $10^1 \text{ S}\cdot\text{cm}^{-1}$, which is well below the reported $700 \text{ S}\cdot\text{cm}^{-1}$ reported for α -(Per) $_2$ Au(mnt) $_2$ and closer to the $50 \text{ S}\cdot\text{cm}^{-1}$ of the β phase [103]. This further suggests that the measured sample was indeed a crystal with the disordered, β phase of the compound. Figure 4.11b shows the EDMR signals recorded at room temperature and $T = 200 \text{ K}$ after baseline correction. The used bias voltage was $V_B = 0.5 \text{ V}$, supplied by one of the ZI-MFLIs Aux outputs. No light irradiation was used. Of note is the fact, other than an observation of a signal at all, that while at room temperature we can see a typical absorption lineshape, this changes to a pure dispersion signal at the lower temperature. To verify this, we can mathematically recalculate the lineshapes by changing the MW phase ϕ (the angle between real and imaginary parts of the signal after a Hilbert transformation). Indeed, as we can see in Figure 4.11c, after shifting ϕ by $\frac{\pi}{2}$, we obtain the familiar absorption lineshape. The appearance of dispersion is the consequence of using a fixed frequency MW source. When recording an ESR spectrum using the EMX bridge, it uses a so-called Automatic Frequency Control (AFC) to lock the source frequency to the resonator frequency. When

the sample starts absorbing radiation due to ESR, it slightly shifts the resonator frequency due to change of the magnetic susceptibility and temperature inside the resonator. When this shift is not compensated, as in our case, the signal contains dispersion components. The reason why this effect is not that visible at room temperature is related to how much the resonator frequency shifts - the EDMR signal is quite weak at room temperature as is the distortion, while with the stronger signal the effect is much more pronounced. After correcting the lineshape, we can try to fit the signal. Figure 4.11d shows a comparison of fitting the signal with either a Gaussian or a Lorentzian line. While the difference is small, the Gaussian fit reproduces the line better. The obtained values are $g = 2.00669 \pm 0.00001$, with $\Delta B_{pp} = 0.330 \pm 0.003$ mT. The errors are errors of fits. As in the previous section, the g value could be shifted due to a field offset which was not measured. While it is impossible to identify the physical process behind the observed EDMR signal without additional measurements, considering the evidence that the sample was the disordered β phase of the compound, it is very likely that it is either spin-dependent hopping or spin-dependent tunneling. While we have not observed any evidence of interaction of the charge carriers with the magnetic moments of Pt in this compound, the fact that an EDMR signal is observable at all warrants a more careful and detailed investigations. It should be noted, however, that while the **Per-Pt** shows an ESR signal both at room and low temperatures [104], we have not been able to observe any spin echo in pulsed ESR measurements. This could be related to the usage of Pt as the paramagnetic species, which has a relatively strong spin-orbit coupling due to its weight. This means that the magnetic moment is more sensitive to fluctuating electric fields, such as those originating from charge carriers within the crystal, causing fast decoherence. A usage of a compound with a lighter metal, such as Ni, could provide a system showing both high conductivity and spin coherence.

4.6 Conclusion

The goal of this chapter was the design, construction and testing of a new EDMR spectrometer at the Institute of Physical Chemistry, along with identification of possible compounds of interest to study the interaction between molecular quantum bits and mobile charge carriers. We have extended the existing Bruker EMX X-Band ESR spectrometer with additional MW source, electric read-out circuitry, sample holder atmosphere control, sample irradiation and custom software to successfully perform EDMR measurements. At the same time, we have designed, manufactured and tested two different EDMR substrates, one suitable for both thin films and single crystals and one more tailored to thin films specifically. With this new experimental set-up, we have measured P3HT

doped either by exposure to ambient conditions or by F₄TCNQ under inert conditions. In both cases, we have tested the influence of various experimental parameters on the signal and identified a combination which reproducibly provides a measurable EDMR signal. F₄TCNQ doped P3HT proved especially useful, with comparatively large signals already at room temperature. Additionally, we have performed first EDMR measurements on samples from the (Per)₂M(mnt)₂ (M=Pt, Au) family of compounds. While the tested samples turned out to be of the semiconducting β phase, instead of the metallic α phase as hoped, we have observed a clear EDMR signature. While a deeper investigation would be necessary, the signal is probably a consequence of spin-dependent hopping of charge carriers through the disordered structure of the sample.

These first steps into EDMR spectroscopy pave the way for many highly interesting investigations. One would be a deeper study of the F₄TCNQ doped P3HT system. First by itself, to investigate its low-temperature behavior and understand the physical processes causing the EDMR signal, and later in combination with a molecular quantum bit embedded in the lattice. Another exciting prospect is further study of the (Per)₂M(mnt)₂ family of compounds via EDMR, as these investigations are completely novel and hold the potential to observe the interaction between localized magnetic moments and itinerant charge carriers directly, in an ideal geometry.

5 Molecular quantum bits in organic semiconductors

This chapter describes the investigation of organic semiconductors as potential conductive hosts for molecular quantum bits. After briefly discussing our preliminary work on hybrid materials exhibiting both quantum coherence and conductivity, we focus on the preparation and extensive characterization of layers composed from the polymeric semiconductor P3HT and the molecular quantum bit $\text{Cu}(\text{dbm})_2$ (Hdbm = dibenzoylmethane). To separate the effects of charge carriers on a qubit from the effect of embedding a qubit in a P3HT matrix, we prepared both nominally undoped and chemically doped P3HT layers. We confirm the preservation of electrical properties of the polymer in both doped and undoped states through organic field-effect measurements at room temperature. Additionally, to study the behavior of charge carriers at temperatures where $\text{Cu}(\text{dbm})_2$ exhibits quantum coherence, we performed variable temperature conductivity measurements, which revealed mobile charge carriers already at 15 K. Finally, electron spin resonance measurements on the hybrid layers demonstrated quantum coherence of $\text{Cu}(\text{dbm})_2$ in the presence of charge carriers up to 30 K. The results from this chapter were published in [107].

5.1 Introduction

Organic materials, such as small molecules and conjugated polymers, are firmly established in the field of electronics. Owing to their versatility and chemical tunability, their electrical properties can range from insulating through semiconducting and conducting all the way to superconducting. The discovery of conductive polymers in the 1970s by Heeger, MacDiarmid and Shirakawa was even awarded with a Nobel Prize in Chemistry in 2000 [108]. Nowadays, the best-known application of organic materials in electronics are organic semiconductors used in solar cells and especially organic light-emitting diodes, which can be found in modern television and smartphone displays. In contrast to their inorganic counterparts, however, the usage of organic semiconductors for spintronics is still in the research phase. Organic materials offer a number of significant advantages for

electronics: they are flexible, cheaper and more easily prepared compared to inorganic semiconductors. Additionally, for spintronics, they promise longer spin lifetimes compared to silicon or germanium due to lower spin-orbit coupling, owing to the usage of materials with lower atomic weights (mostly carbon, nitrogen and oxygen). Despite the young age of the field¹, great strides have been made both in device fabrication and theoretical understanding of spin and charge transport physics in these materials. Initially, fabricated devices, mostly vertical spin valves, showed only modest spin diffusion lengths of tens of nanometers. The advantages of longer spin lifetimes were completely erased by relatively low charge carrier mobilities in organic semiconductors, which limited both spin transport and efficient spin injection due to the large conductivity mismatch. A significant step forward was made when Yu discussed the absence of Hanle effect in organic devices and proposed a model of spin transport based on exchange coupling between polarons [111]. He proposed that the limitations of low charge carrier mobilities can be overcome by separating the spin and charge transport mechanisms, which occurs at sufficient dopant concentration in organic semiconductors. His theoretical predictions have only recently been experimentally demonstrated: in 2019, Wang and co-workers reported remarkable spin diffusion lengths of over 1 μm , achieved by generation of pure spin current [112], and only as recently as in 2020, Groesbeck *et al.* investigated spin and charge transport in π -conjugated polymers separately, confirming that they occur via different mechanisms, with spin transport being 1 to 2 orders of magnitude faster than charge current [113]. These discoveries pave the way for high-performance organic spintronic devices which can be chemically tuned for specific applications.

In this project, we have focused on semiconducting conjugated polymers as hosts for molecular quantum bits. As in the previous chapters, the final goal of this project is to find out if it is possible to electrically read out the spin of an MQB via a spin-dependent transport mechanism, as illustrated in Figure 5.1. Before that, however, we need to not only find a suitable MQB/conjugated polymer pair and combine them appropriately, but establish that their respective properties of interest, i.e., quantum coherence in the MQB and charge transport in the organic semiconductor, remain unaffected by the mixing. One can imagine two possibilities of combining the two materials: attaching MQBs covalently to the polymer chains (for example through click chemistry based on a Cu-catalyzed Huisgen 1,3-dipolar cycloaddition between an azide and alkyne [114, 115]) or creating a solid dispersion of the MQB inside the organic semiconductor via mixing of the two materials. The former potentially offers a higher degree of control over position of the MQBs in the

¹The field of organic spintronics was started in 2002, when Dediu and co-workers demonstrated spin injection into the organic semiconductor sexithienyl [109] and accelerated by the first observation of giant magnetoresistance in a spin valve using a small molecule semiconductor, Alq₃, as a spin transport layer [110].

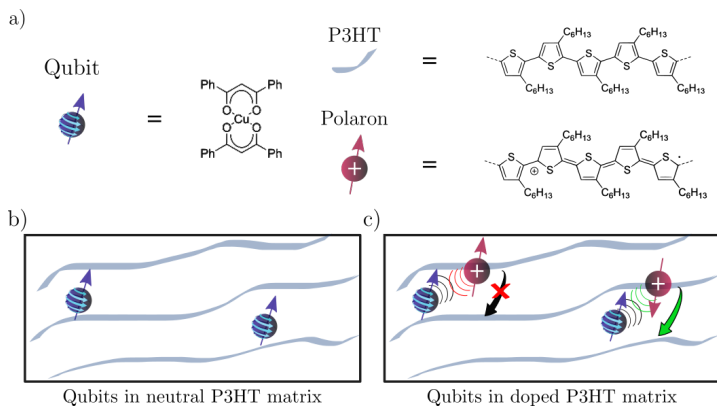


Figure 5.1: An illustration depicting a) the used materials and b) the potential mechanism of electrical read-out of an MQB in a P3HT matrix. Illustration courtesy of Dr. Lorenzo Tesi.

lattice, however it requires a synthetic effort to produce suitable polymer-qubit pair. The latter method is facile, easily modifiable and requires no further preparation other than procurement of the desired components. Given the exploratory character of this thesis, we have decided to investigate preparation of hybrid materials consisting of semiconducting conjugated polymers and MQBs via solution mixing. Different combinations of conjugated polymers with MQBs and their preparation were explored in a number of undergraduate theses under my supervision [99, 116–120]. For the investigation described in this chapter, we have decided to use the semiconducting conjugated polymer poly(3-hexylthiophene-2,5-diyl) (P3HT) and the transition metal complex $[\text{Cu}(\text{dbm})_2]$ (Hdbm=dibenzoylmethane) as the MQB (Figure 5.1a).

P3HT is one of most well known and most researched semiconducting conjugated polymers, with entire books dedicated to it [121]. First synthesized in the 1990s, it quickly garnered attention and became a “fruit fly” among polymeric organic semiconductors [121]. Reasons for the popularity of P3HT are multiple; however the main one is that it displays interesting self-assembling and electronic properties while being relatively simple to synthesize and process, in contrast to more advanced polymers. Similar to inorganic semiconductors, the conductivity of neutral P3HT can be increased by several orders of magnitude by means of chemical, electrochemical or field-effect doping. Depending on the exact method of doping and processing, the conductivities in pristine P3HT films of $\approx 10^{-4} \text{ S}\cdot\text{cm}^{-1}$ can be increased up to $224 \text{ S}\cdot\text{cm}^{-1}$ [122] in disordered films and even $570 \text{ S}\cdot\text{cm}^{-1}$ [123] in highly ordered, crystalline layers. Field-effect charge carrier mobilities can reach up to $10^{-1} \text{ cm}^2\cdot\text{V}^{-1}\cdot\text{s}^{-1}$ [121]. Given the relatively good electronic properties

and ease of processing, it has quickly found application in organic solar cells, field-effect transistors and light-emitting diodes. The best electronic properties are, however, only displayed by the regio-regular variant of P3HT (Figure 5.1a), with its alkyl chains regularly distributed along the thiophene backbone. P3HT with regioregularities $\geq 95\%$ are fortunately readily commercially available.

To separate the effects of incorporating qubits in a polymer matrix from the effect of nearby charge carriers, we used P3HT both in a nominally undoped and doped state. We employed chemical doping with the electron acceptor 2,3,5,6-tetrafluoro-tetracyanoquinodimethane (F_4TCNQ), which generates positively charged polarons and bipolarons on the thiophene backbone of P3HT by integer charge transfer from the thiophene to F_4TCNQ molecule (Figure 5.1a). This method of doping allows for very simple processing, where the dopant is dissolved in a solvent that doesn't dissolve P3HT and the resulting solution is simply drop-cast on an already prepared P3HT layer, and after a short reaction time the excess solution is spun off using a spin coater. Using this method, we investigated both the undoped and doped layers without using more sophisticated electrochemical doping procedures and we didn't need to modify our ESR spectrometer to apply voltage for field-effect doping.

The molecular qubit chosen for our investigations is the organometallic complex $[Cu(dbm)_2]$ (Hdbm=dibenzoylmethane). This qubit has been extensively studied by our group, since it possesses rather long coherence times of up to 47 μs in frozen CS_2 solution and 7.7 μs when doped into the corresponding diamagnetic palladium (II) compound [124]. Additionally, since this compound is electrically neutral, it can be easily evaporated intact [125]. Considering the wealth of data available on this compound, combined with its favorable properties and ease of synthesis, it was an ideal candidate for our first experiments.

5.2 Experimental methods

Four types of samples were investigated in this study. In this chapter, the samples will be identified by the concentrations of the solutions from which they were prepared (in g/L) of P3HT (P), $[Cu(dbm)_2]$ ([Cu]) and F_4TCNQ dopant (D), e.g., **12P/0.3[Cu]/1.3D** for a film cast from a solution of P3HT (12 g/L) and $[Cu(dbm)_2]$ (0.3 g/L), with subsequent doping by casting a solution of F_4TCNQ (1.3 g/L) in acetonitrile on top of the sample. An en-dash (–) denotes the absence of that particular component, e.g., 12P/–/– for a nominally undoped P3HT film without $[Cu(dbm)_2]$.

Materials

Solvents were acquired commercially and used as received. Regioregular P3HT was bought from Merck and used without further purification. The number average molar mass extracted from gel permeation chromatography was $\overline{M}_n = 28.7 \text{ kg}\cdot\text{mol}^{-1}$ with a polydispersity index of $\text{PDI} = 1.77$. F_4TCNQ (98.0% purity) was bought from TCI. $[\text{Cu}(\text{dbm})_2]$ was prepared as previously [124]. For the fabrication of thin-film field-effect transistors, silicon substrates were purchased from Fraunhofer IPMS. Si substrates for ESR measurements with a size of $15 \times 15 \text{ mm}^2$ were cut with a diamond saw from commercial lightly *p*-doped- 4-inch wafers with specific resistivity of $\rho = 1000$. Commercial microscope slides were used as glass substrates for UV/Vis/NIR measurements.

Semiconductor film preparation

Substrates were cleaned in three steps:

1. 10 minute ultrasonic baths in acetone and isopropanol.
2. Spraying with a CO_2 (Applied Surface Technologies SnowJet) stream with the substrate heated to 200°C .
3. Final cleaning inside a low-pressure oxygen plasma chamber (Diener electronic) for 10 minutes at 100 W power.

Semiconductor films were prepared inside the nitrogen atmosphere of a glove box. Films were deposited either by static spin-coating² of $100 \mu\text{L}$ of solution at 1000 rpm using a Süss MicroTec Delta-6RC spin-coater, starting from solutions of P3HT (12 g/L) and $[\text{Cu}(\text{dbm})_2]$ (1.8 g/L), leading to film thicknesses of around 75 nm, or by drop-casting of a solution containing P3HT (24 g/L) and $[\text{Cu}(\text{dbm})_2]$ (2.6 g/L) onto the substrate, with subsequent drying under dry nitrogen stream. The poor solubility of $[\text{Cu}(\text{dbm})_2]$ in chlorobenzene was overcome by heating to 80°C with continuous stirring. Chlorobenzene solutions of P3HT were preheated to 70°C and mixed with the $[\text{Cu}(\text{dbm})_2]$ solution immediately before film deposition. To generate *p*-type polaronic charge carriers, $100 \mu\text{L}$ of a solution of F_4TCNQ in acetonitrile was cast onto the previously prepared P3HT film and after a reaction time of 1 minute the excess solution was spun off using the spin-coater. A more detailed protocol can be found in Section 5.2.1.

Transistor fabrication

Commercial thin-film transistors obtained from Fraunhofer IPMS were fabricated in the bottom contact, bottom gate device architecture with a highly *n*-doped silicon substrate

²Static spin-coating is performed by casting the solution on a static substrate, immediately followed by starting of the spin-coater.

serving as a common gate electrode for all transistors on the substrates, and thermally grown SiO_2 serving as the gate dielectric with a thickness of 230 nm. Gold was used for the source and drain contacts with a height of 40 nm. The transistors have channel lengths of $L = 2.5, 5, 10, 20 \mu\text{m}$, the effective electrode width is $W = 10 \text{ mm}$. The architecture is sketched in Figure 5.2

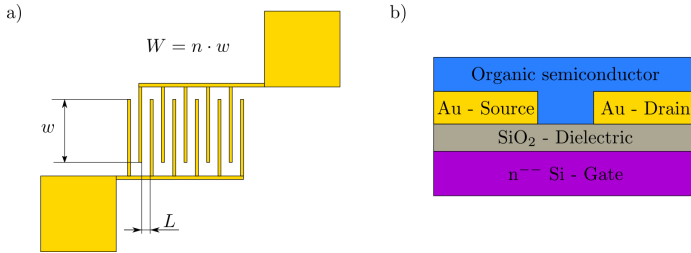


Figure 5.2: Organic field-effect transistor configuration used for the electrical characterization of our samples. a) Sketch of the geometry of the used gold electrodes, b) Sketch of a cross-section of a typical bottom-gate, bottom-contact OFET sample. Figure from [107].

Film characterization

Optical microscopy images were taken with a Zeiss Axio Imager microscope and AFM images were recorded with a Bruker Dimension Icon instrument in contact mode. AFM images were processed and analyzed using Gwyddion software [126]. UV/Vis/NIR spectra were recorded in the glovebox with a custom-built sample holder and a Zeiss MSC 621 VIS II spectrometer cassette.

Charge-transport measurements

Room temperature conductivity and transistor measurements were carried out inside the glove box, using a Süss MicroTec EP6 4-point probe station with a Keithley 2636B Source-Measure Unit. Low temperature transport measurements were carried out on a home-built setup featuring a Keithley 2636B Source-Measure Unit and an Oxford Instruments Spectromag cryomagnet (see Section 3.4 for more details). Reported output and transfer characteristics were measured on 2-4 different transistor structures for each channel size, with the reported values of field-effect mobility and effective conductivity being averages over all channel lengths. The field-effect mobilities were extracted using Equations (2.49) in Section 2.4. Geometrical parameters are specified above, the capacitance per unit area was calculated as $C_i = \epsilon_0 \epsilon_r / d$, with ϵ_0 being the permittivity of the vacuum, $\epsilon_r = 3.9$ the

relative permittivity of SiO_2 and $d = 230$ nm the thickness of SiO_2 . The mobility was extracted at $V_{\text{GS}} = -35$ V, which is within both the linear regime for $V_{\text{DS}} = -10$ V and within saturation for $V_{\text{DS}} = -80$ V. The effective conductivity was extracted from the linear part of the output curve at zero gate voltage. While this value differs from the intrinsic material conductivity due to contribution of the contact resistance, in this case, it serves just to validate the effectiveness of used doping procedure.

Pulsed ESR measurements

Measurements were carried out using a home-built pulsed Q-Band (35.000 GHz) spectrometer, equipped with an Oxford Instruments CF935O helium flow cryostat and a home-built brass Fabry-Pérot resonator [127, 128]. For the field-swept echo-detected spectra, the Hahn echo sequence was used with pulse lengths of 40 and 80 ns, as well as an interpulse delay of 300 ns. Easyspin was used for spectrum simulation [45]. The same sequence with varying interpulse delays was used for determining quantum coherence times. Spin-lattice relaxation times were determined by fast repetition or inversion recovery measurements. Saturation by fast repetition was used for undoped samples (both spin-coated and drop-cast) up to 15 K, and at higher temperatures inversion recovery was used. For doped samples, only inversion recovery was used.

5.2.1 Optimization of semiconductor film preparation

As mentioned in the introduction to this chapter, different combinations of semiconducting polymers and paramagnetic species were investigated as potential hybrid materials for this project. In the course of those experiments, it has become clear that a precise, well-understood protocol for sample preparation was necessary to reproducibly obtain a usable material. The most important parameters needed to be optimized were

- type of substrate,
- substrate cleaning protocol,
- solvent used,
- preparation of the solutions,
- spin-coating parameters.

For the hybrid material described in this thesis, some of these parameters were partially explored in undergraduate theses and projects under my supervision. However, none of this preliminary work yielded a sample preparation protocol that satisfactorily fulfill all of the following requirements:

- Homogeneity - no aggregates, crystallites or dust visible in the film.
- Stability - the hybrid material should be thermally stable at least on the time scale

of hours and resist oxidation or decomposition under ambient conditions for 1-2 minutes, which are necessary for insertion of the samples into the measurement equipment.

- Quantity - the procedure must yield a sample with a sufficient number of paramagnetic species (qubits) to be able to measure them using our pulsed ESR spectrometer (around 10^{14} - 10^{15} spins).

In the following, the main conclusions from the preliminary work relevant to this chapter will be briefly summarized. The first solvent used was chloroform, since both $\text{Cu}(\text{dbm})_2$ and P3HT were well soluble in it. After spin-coating, however, it was clear from optical microscopy that the low boiling point of the solvent leads to low quality of the films. More importantly, it was first observed by Rußegger [117] and later confirmed by an in-depth study by Winkler [118], that $\text{Cu}(\text{dbm})_2$ is not stable in a chloroform solution of P3HT. This instability manifests itself only in the presence of light and oxygen; however, even a short exposure leads to rapid oxidation of P3HT and disappearance of the $\text{Cu}(\text{dbm})_2$ ESR signal. Exchanging the solvent for toluene led to excellent thin film quality, though the number of what was most probably $\text{Cu}(\text{dbm})_2$ aggregates increased significantly. Winkler also observed that $\text{Cu}(\text{dbm})_2$ tends to crystallize inside the film after deposition, a process that is accelerated by heating. Crystallization and aggregation of the qubit are highly undesirable, since they not only increase dipolar interaction between the qubits, reducing their coherence times; if the molecules are aggregated, molecules on the perimeter of the aggregate prevent the read-out of the inner molecules.

As for used substrates, we have investigated several Si wafers doped with various amounts of p or n dopants. We have then chosen p^{--} doped Si(100) wafers since they possess the lowest amount of ESR active species of the investigated substrates. Additionally, we have briefly experimented with using Mylar foil as a substrate, which has proven very useful for other thin film studies in a cw X-band ESR spectrometer. Using a thin foil has the advantage of being cheap, readily available and easily cut to size. The fact that these foils were almost seven times thinner than the Si (just 0.075 mm compared to 0.5 mm for the Si) also gave us the impression that it would lead to a higher B_1 field homogeneity in the ESR resonator.

The first step in this work was therefore to investigate Mylar as a potential substrate material, given the promising results when using it for cw X-band ESR. We have, however, quickly realized the unsuitability of Mylar for these studies. Even though the material does not possess any measurable paramagnetic signal in X-band ESR at room temperature, upon inspection with an optical microscope a significant number of impurities and defects were observed (Figure 5.3). These defects make the evaluation of the homogeneity and quality of a deposited layer difficult. These impurities persist even after cleaning by

sonication in acetone and isopropyl alcohol. Further cleaning steps, such as using a strong CO₂ stream (the so-called snow jet) or oxygen plasma, only damaged the material. After deposition of the thin layer, it is impossible to determine the height of the layer using Atomic Force Microscopy (AFM), since any instrument used for scratching the thin film will also damage the foil underneath. Additionally, we have observed that after insertion of a 15 × 15 mm² piece of Mylar into our Q-Band Fabry-Pérot Resonator (FPR), it was impossible to tune it into resonance. This may be caused by relatively high dielectric losses of Mylar (≈ 100 times larger than Si, at least at frequencies larger than 100 GHz [129]). Following these findings, we decided to use p^{--} Si exclusively for the rest of these studies.

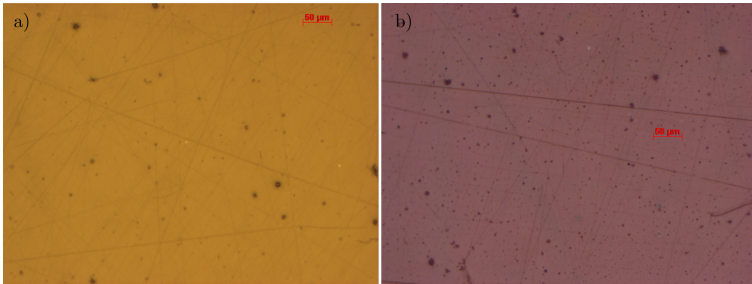


Figure 5.3: Optical microscopy images of a) cleaned Mylar foil and b) Mylar foil with a thin film of the mixed material.

The starting Si substrate cleaning procedure used was fairly standard:

1. Acetone ultrasonic bath, 10 minutes.
2. Isopropyl alcohol ultrasonic bath, 10 minutes.
3. Low-pressure oxygen plasma chamber, 10 minutes.

While this procedure gets rid of most organic residues and dirt from the surface, upon closer inspection, one can see that some particulates are present even after cleaning (Figure 5.4). These particulates can be very easily mistaken for aggregates of either P3HT or Cu(dbm)₂. In order to decrease the number of particulates on the surface, we implemented a snow-jetting step before plasma cleaning. This step entails spraying of the substrate (heated to 200 °C) with a narrow jet of high-pressure CO₂. After the procedure, we observed a significant increase in homogeneity of the surface, as can be seen in Figure 5.4. Therefore, we included snow-jetting in the cleaning procedure afterward.

Building upon the improvement in film quality when switching from a low-boiling point solvent (chloroform, $T_B = 61$ °C [130]) to higher boiling point (toluene, $T_B = 110$ ° [130]), we have decided to try a further solvent in hopes of solving the problem of Cu(dbm)₂ aggregation. We have chosen chlorobenzene because of its even higher boiling point ($T_B = 132$ °C [130]) and good solubility of P3HT in it. The solubility of Cu(dbm)₂, however,

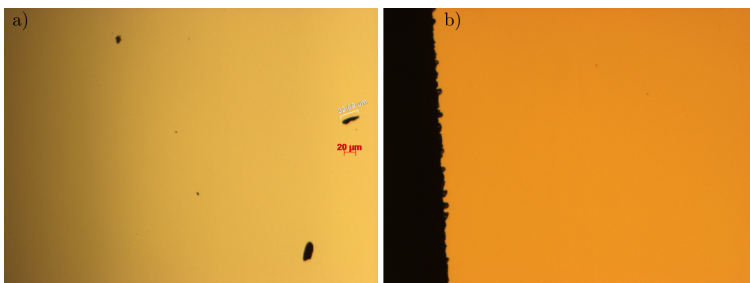


Figure 5.4: Optical microscopy images of a Si substrate a) before and b) after snow-jet cleaning.

was not ideal. After dissolving of $\text{Cu}(\text{dbm})_2$ in chlorobenzene, even after extended shaking and sonication, fine particles were visible in the solution, and subsequently, in the film (Figure 5.5a). To mitigate that, we have put a stirrer into the solution and placed the vial on a hotplate with 70°C for an hour before mixing it with P3HT (which was always warmed up to the same temperature). The $\text{Cu}(\text{dbm})_2$ solution was clear upon optical inspection, and the resulting thin films contained only minimal amounts of particulates (Figure 5.5b). Deeming the quality of resulting samples sufficient, we have used the following protocols for sample preparation.

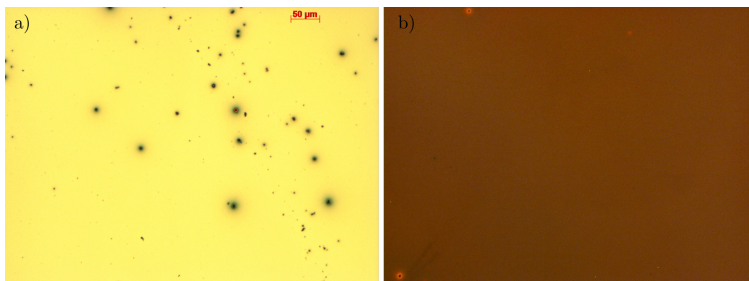


Figure 5.5: Optical microscopy images of the sample spin coated from chlorobenzene using $\text{Cu}(\text{dbm})_2$ solution a) at room temperature and b) heated to 70°C .

Protocol for spin-coated sample preparation

This protocol covers the recommended procedure for preparation of spin-coated samples. In order to maximize available time on the day of measurements and ensure sufficient dissolution of P3HT, it is advised to start the procedure the day before.

Part A - the day prior to measurements

1. Prepare a solution of P3HT in chlorobenzene of desired concentration in a brown vial with a magnetic stirrer included and place it on a hot plate heated to 70 °C with the stirrer on medium setting. Leave overnight in glovebox.
2. Clean sample substrates (either OFET or p^{-} Si):
 - I. Ultrasonic bath in acetone, 10 minutes.
 - II. Ultrasonic bath in isopropylalcohol, 10 minutes.
 - III. Snow-jet cleaning with the substrate heated to 200°C.
 - IV. Oxygen plasma cleaning for 10 minutes at 100 W power.
3. Store the cleaned substrates in a clean, closed box.

Part B - the day of the measurements

1. Approximately 15-30 minutes prior to spin-coating, prepare a solution of $\text{Cu}(\text{dbm})_2$ in chlorobenzene with a magnetic stirrer in the vial and place it on the same hot plate as the P3HT solution.
2. If chemical doping with F_4TCNQ is planned, prepare a fresh solution of F_4TCNQ in acetonitrile.
 - Fresh preparation is required especially for concentrations lower than 1.3 g/L, as we have observed deterioration of the oxidizing properties of F_4TCNQ solutions over time.
3. Set spin-coater settings:
 - Step 1: 1000 rpm for 300 s with a 5 s ramp
 - Step 2: 2000 rpm or more for 5 s to get rid of excess solution
4. Mix the desired volume of P3HT and $\text{Cu}(\text{dbm})_2$ solutions in a 1:1 ratio.
5. Spin-coat 100 μL of the mixed solution on a clean substrate.
6. If chemical doping with F_4TCNQ is desired:
 - I. Drop-cast 100 μL (or more, depending on the size of substrate) of the F_4TCNQ solution on the spin-coated layer, such that the whole surface is covered.
 - II. Leave for 1 minute to allow for complete oxidation of the film.
 - III. Run the first step of the above spin-coating program for at least 30 s to remove excess solution.

Protocol for drop-cast sample preparation

This protocol covers the recommended procedure for preparation of drop-cast samples. In order to maximize available time on the day of measurements and ensure sufficient dissolution of P3HT, it is advised to start the procedure the day before. The procedure on the day prior to measurements is identical to spin-coating sample preparation (Part A), as well as steps 1 and 2 of Part B.

Part A - the day prior to measurements

1. Prepare a solution of P3HT in chlorobenzene of desired concentration in a brown vial with a magnetic stirrer included and place it on a hot plate heated to 70 °C with the stirrer on medium setting. Leave overnight in glovebox.
2. Clean sample substrates (either OFET or p^{-} Si):
 - I. Ultrasonic bath in acetone, 10 minutes.
 - II. Ultrasonic bath in isopropylalcohol, 10 minutes.
 - III. Snow-jet cleaning with the substrate heated to 200°C.
 - IV. Oxygen plasma cleaning for 10 minutes at 100 W power.
3. Store the cleaned substrates in a clean, closed box.

Part B - the day of the measurements

1. Approximately 15-30 minutes prior to spin-coating, prepare a solution of $\text{Cu}(\text{dbm})_2$ in chlorobenzene with a magnetic stirrer in the vial and place it on the same hot plate as the P3HT solution.
2. If chemical doping with F_4TCNQ is planned, prepare a fresh solution of F_4TCNQ in acetonitrile.
 - Fresh preparation is required especially for concentrations lower than 1.3 g/L, as we have observed deterioration of the oxidizing properties of F_4TCNQ solutions over time.
3. Mix the desired volume of P3HT and $\text{Cu}(\text{dbm})_2$ solutions in a 1:1 ratio.
4. Drop-cast 100 μL (or more if desired) of the mixed solution on a clean substrate.
 - Ideally, get a second person to help you.
 - Slowly spread the solution with a pipette over the whole surface of the sample, while a second person blows dry nitrogen gas over the sample.
 - After the first layer has dried, repeat until the solution is used up.
5. If chemical doping with F_4TCNQ is desired:
 - I. Drop-cast 100 μL (or more, depending on the size of substrate) of the F_4TCNQ solution on the drop-cast layer, such that the whole surface is covered.
 - II. Leave for 1 minute to allow for complete oxidation of the film.

- III. Run the first step of the spin-coating program (Spin-coating protocol step B3) for at least 30 s to remove excess solution.

5.3 Results and discussion

In the following subsection, the microscopical, electrical and optical characterization of semiconductor film samples at room temperature will be described, establishing that the incorporation of MQBs does not adversely affect these properties of P3HT. The second subsection shows the low-temperature electrical properties of the semiconductor films, investigating charge transport at temperatures where MQBs demonstrate quantum coherence. In the final subsection, pulsed ESR measurements demonstrate sizable quantum coherence of MQBs in the presence of mobile charge carriers.

5.3.1 Thin film sample characterization

With the optimized sample procedure described in the previous section, we have prepared samples both via spin-coating and drop-casting. Figure 5.6a-c shows AFM height images of both spin-coated and drop-cast samples, which were used for electrical characterization as well. The images reveal a disordered, homogeneous film without significant aggregation in any film, regardless of incorporation of MQBs. Figure 5.6d shows a line scratch profile of a spin-coated 6P/0.9[Cu]/1.3D film with a thickness of 74 ± 7 nm.

Figure 5.7 shows the UV/Vis/NIR spectra of P3HT thin films deposited by spin-coating on glass substrates with different levels of sequential doping. The undoped film shows a clear absorption peak at 555 nm attributed to the exciton transition in P3HT. The presence of some vibronic fine structure indicates a moderate degree of ordering in the film [131]. Upon doping, the intensity of the exciton band decreases and new bands at near 800 nm and 417 nm arise. The latter is attributed to the F_4TCNQ radical anion, while the former has been reported to be due to an intrapolaron electronic transition overlapping with a further F_4TCNQ transition. These data show that the sequential doping procedure was successful.

To study the influence of introducing $Cu(dbm)_2$ into the organic semiconductor on the electrical transport properties of the material, we have manufactured OFETs and studied their output (drain current vs. drain-source voltage) and transfer (drain current vs gate-source voltage) characteristics at room temperature. A typical set of output curves recorded on a spin-coated **12P/0.3[Cu]/-** film on top of a 20 μm OFET can be seen in Figure 5.8. Qualitatively, both samples with and without [Cu] show the same transistor behavior, with a linear region at small drain-source voltages and a saturation

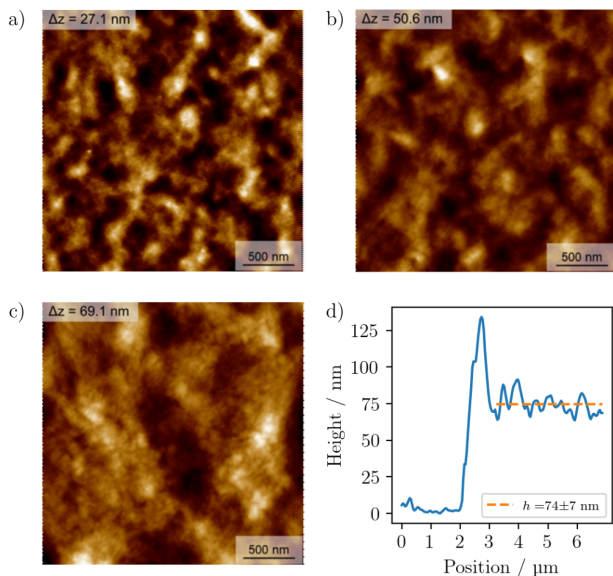


Figure 5.6: AFM height images of a) $12\text{P}/-/-$ deposited by spin-coating, b) $12\text{P}/0.3[\text{Cu}]/-$ deposited by spin-coating, c) $12\text{P}/0.3[\text{Cu}]/-$ deposited by drop-casting, d) AFM measurement of a line-scratch profile of a $6\text{P}/0.9[\text{Cu}]/1.3\text{D}$ film, deposited by spin-coating. Orange line represents a line-fit of the thickness with $t = 74 \pm 7$ nm. AFM height images courtesy of David Neusser.

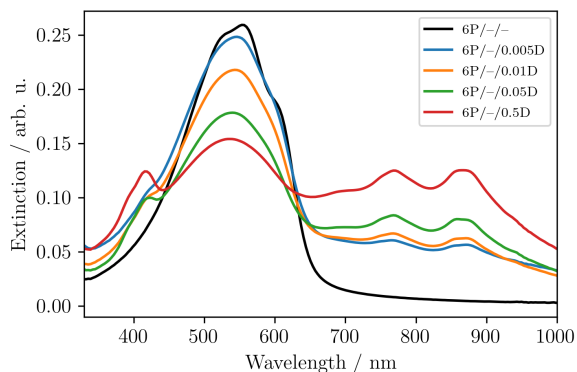


Figure 5.7: UV/VIS spectrum of a P3HT films doped with F_4TCNQ solutions of various concentrations.

region at higher drain-source voltages (Section 2.4). For the smallest channel length (2.5 μm , Figure B2 in Appendix B), the contribution of the contact resistance to the total device resistance causes a pronounced non-linearity at small drain-source voltages. At large drain-source voltages, the drain current does not saturate completely, that is, it still shows a weak dependence on the drain-source voltage, which we attribute to unintentional oxygen doping of the P3HT films. Contact resistance could be mitigated by passivating the SiO_2 surface with hexamethyldisilazane (HMDS) or a self-assembled monolayer [121, p. 119], however, as our interest was only observing relative changes of properties between samples, we did not carry out these additional steps. The transfer curves (Appendix B) reveal that the threshold voltage is significantly shifted to positive values (approximately 20 V), meaning that even without an applied gate, the transistor is turned “on”. This shift is usually a signature of unintentional p -doping by oxygen [121, p. 125]. This shift was visible in all samples, even though the solution preparation and subsequent measurements were all performed under a nitrogen atmosphere without leaving the glovebox. The unintentional background doping indicates that the unprocessed P3HT was already contaminated, possibly by the repeated exposure of the whole batch to ambient conditions while weighing the powder in solid state. The effective mobility was extracted from the transfer characteristics were $\mu_{\text{sat}} = (0.5 \pm 0.1) \cdot 10^{-3} \text{ cm}^2 \cdot \text{V}^{-1} \cdot \text{s}^{-1}$ for the **12P**/–/– sample and $\mu_{\text{sat}} = (0.6 \pm 0.3) \cdot 10^{-3} \text{ cm}^2 \cdot \text{V}^{-1} \cdot \text{s}^{-1}$ for **12P/0.3[Cu]**/–. These numbers agree well with the literature for transistors made from P3HT with similar molecular weights [121, p. 115], and they are within the margin of error of each other, showing that the incorporation of an MQB into the P3HT matrix does not influence its transport properties significantly.

The effective conductivities extracted from the linear region of the output characteristics at $V_{\text{GS}} = 0$ were almost identical between the samples, with $\sigma_{\text{eff}} = 0.34 \pm 0.04 \text{ S} \cdot \text{cm}^{-1}$ for **12P**/–/– and $\sigma_{\text{eff}} = 0.40 \pm 0.07 \text{ S} \cdot \text{cm}^{-1}$ for **12P/0.3[Cu]**/–. Upon doping, both of the samples showed an increase in conductivity by three orders of magnitude, underlining the lack of differences between them. The obtained effective conductivity values after doping are rather high (1600 and 2666 $\text{S} \cdot \text{cm}^{-1}$ for **12P**/–/**1.3D** and **12P/0.3[Cu]**/**1.3D**, respectively), with a large scatter between the different transistor channel lengths. These values are approximately three orders of magnitude larger than the ones measured with a more reliable 4-point method on comparable samples [132]. Such high numbers were observed consistently for all 3 investigated samples. The relative change in conductivity, however, is consistent with the literature. As such, we would conclude that the doping procedure works as expected, with the absolute numbers being influenced by an unknown systematic error. Nevertheless, we can conclude that the implementation of $\text{Cu}(\text{dbm})_2$ into P3HT has a negligible influence on its room temperature electrical properties.

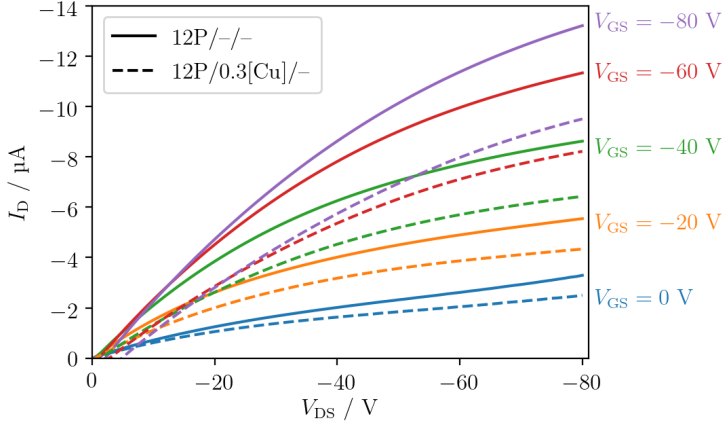


Figure 5.8: Output characteristics of OFETs with 20 μm channel length recorded on spin-coated 12P/-/- (solid lines) and 12P/0.3[Cu]/- (dashed lines) samples.

5.3.2 Drop casting as a method for increasing the number of spins

Encouraged by the results, there was one last aspect of the sample to verify - if the preparation procedure results in a sufficient number of spins to perform investigations of spin dynamics. To this end, we prepared a spin-coated **6P/0.9[Cu]/-** sample, with the [Cu] concentration corresponding to 15.4wt% of P3HT, which is the solubility limit, i.e., the maximum number of dissolved molecules in the sample. We were successful in obtaining an ESR signal in our pulsed Q-band ESR spectrometer, the intensity was, however, rather small, insufficient for studies of temperature dependence in which we were interested³. It was, therefore, apparent that we needed to increase the number of spins in our samples. Using the volume (V) of the spin-coated layer extracted from AFM measurements, we can estimate the number of $\text{Cu}(\text{dbm})_2$ molecules in the spin-coated film as:

$$N = \frac{V \cdot \rho_{\text{P3HT}} \cdot \text{wt\%Cu}}{M_{\text{Cu}(\text{dbm})_2}} \cdot N_{\text{A}}, \quad (5.1)$$

with V being the volume of the layer, ρ_{P3HT} the density of P3HT, wt%Cu the weight fraction of $\text{Cu}(\text{dbm})_2$, $M_{\text{Cu}(\text{dbm})_2}$ the molar mass of $\text{Cu}(\text{dbm})_2$ and N_{A} Avogadro's number.

³ESR signal intensity is proportional to the number of polarized spins. At low temperatures, polarization is higher (Boltzmann factor) and decreases with increasing temperatures, resulting in decrease of ESR signal.

Evaluating this expression for the spin-coated sample yields approximately $4 \cdot 10^{15}$ spins. The previously determined sensitivity of our pulsed Q-band spectrometer with the FPR is better than 10^{14} spins/mT at 7 K [127]. To compare it with our measurements, we can divide the estimated number of spins with the spectral width of the $\text{Cu}(\text{dbm})_2$ spectrum (≈ 150 mT), resulting in a sensitivity of around $3 \cdot 10^{13}$ spins/mT. This shows us that we were operating at the limit of our spectrometer. As can be seen in Equation 5.1, there are two options to increase the number of spins in a sample: increase the spin concentration or the volume. The former was not possible since the used concentration of $\text{Cu}(\text{dbm})_2$ used was already at the solubility limit and high concentrations lead to shortened coherence times due to dipolar interactions of the neighboring spins. The concentration, therefore, had to be decreased. and simultaneously, the volume and P3HT concentration had to be increased significantly. Given the shape of the Gaussian TEM002 mode in the resonator used for the pulsed ESR measurements, the maximum lateral size for our samples was 15 mm by 15 mm. The only spatial dimension left to exploit to increase the absolute number of spins in our sample was the layer height. The height of a spin-coated layer of P3HT can be predicted by the empirical formula:[133]

$$h_f = \frac{k \cdot w \cdot \eta^{0.4}}{\omega^{0.4}} \quad (5.2)$$

with k being an empirical constant, w the weight fraction of P3HT in the solvent, η the solution viscosity and ω the rotation speed. While the equation was derived for chloroform as a solvent, which will affect both k and η , following qualitative arguments should still hold. The rotation speed used for our sample was 1000 rpm, which is already the lower limit of speeds at which the use of spin-coating brings benefits in terms of sample morphology and reproducibility compared to drop-casting. The only variable left to adjust is thus the weight fraction of P3HT in solution. There are, however, practical constraints on the usable concentration range of P3HT. To avoid gelation and crystallization, we were limited to P3HT concentrations of at most 12 g/L, i.e., double of the concentration used before. Observing Equations 5.2 and 5.1, this would result in at most double of the layer height (≈ 144 nm, assuming viscosity would remain constant) and consequently doubling of the number of spins ($\approx 4 \cdot 10^{15}$). This height would still not provide us with sufficient $\text{Cu}(\text{dbm})_2$ molecules to measure up to significantly higher temperatures than before, even if we would not decrease $\text{Cu}(\text{dbm})_2$ concentration. If we wanted to obtain at least an order of magnitude higher number of spins, we needed to deposit an even thicker film, for which a method other than spin-coating had to be chosen.

While there are a large number of various polymer deposition methods, the only suitable ones available to us were doctor-blading or simple drop casting. Doctor-blading

is a highly effective technique for deposition of layers thicker than 1 μm ; it is, however, most effective for relatively large substrates, typically at least 20 mm by 80 mm. We have therefore resorted to simple drop casting. To produce our samples, we have sequentially cast 100 μL of the mixed solutions and spread them over the substrate under N_2 flow in an N_2 glovebox. To decrease spin-spin relaxation due to dipolar coupling, we have decreased the weight concentration of $\text{Cu}(\text{dbm})_2$ in P3HT to 2.5wt% (0.3 g/L in solution). Neglecting losses, this results in a number of spins:

$$N = \frac{V \cdot c}{M_{\text{Cu}(\text{dbm})_2}} \cdot N_{\text{A}} = 3.5 \cdot 10^{16}, \quad (5.3)$$

with V being the volume of the used solution and c the $\text{Cu}(\text{dbm})_2$ concentration in solution. The one order of magnitude larger number of spins thus obtained allowed us to perform pulsed ESR measurements up to 40 K, as will be discussed in subsection 5.3.4, even with the reduced concentration of $\text{Cu}(\text{dbm})_2$.

The switch from spin-coated to drop cast films naturally raises the questions if these are comparable. Even though the centrifugal forces during spin-coating do produce more homogeneous layers in terms of height, the comparatively faster drying results in more amorphous structure than with drop-casting, and order is usually introduced via an additional annealing step, which promotes crystallization. Drop-cast layers usually show slightly better electrical performance and higher crystallinity, which is attributed to slower drying of the material [121, p. 57-62]. To verify this, we have compared both room temperature transport properties (conductivity, mobility) and ESR spectra (Section 5.3.4). Both the field-effect mobility ($\mu_{\text{sat}} = (1.9 \pm 0.9) \cdot 10^{-3} \text{ cm}^2 \cdot \text{V}^{-1} \cdot \text{s}^{-1}$) and effective conductivity ($\sigma_{\text{eff}} = 1.2 \pm 0.6 \text{ S} \cdot \text{cm}^{-1}$) of a **12P/0.3[Cu]/-** drop-cast sample are higher compared to the spin-coated films, in agreement with the literature [121, p. 116]. We can see that the electrical properties of P3HT are barely influenced by the incorporation of $\text{Cu}(\text{dbm})_2$ into P3HT and that doping procedure worked consistently across all samples.

5.3.3 Low-temperature conductivity and mobility

Since the coherence time of $\text{Cu}(\text{dbm})_2$ increases with decreasing temperature [124], it is necessary to characterize the behavior of charge carriers in P3HT at these temperatures as well. To this end, we measured the output and transfer characteristics of drop cast **12P/0.3[Cu]/-** and **12P/0.3[Cu]/1.3D** samples in the temperature range between 7 and 70 K. Considering the semiconducting behavior of P3HT, the low-temperature conductivities were expected to be low, the smallest 2.5 μm channel length transistors were therefore chosen to maximize the measured current. As a consequence, the quantitative

results were strongly affected by contact resistance and high lateral electric fields [134]; qualitative temperature trends are, however, expected to be valid. In Figure B10 in the Appendix, we can observe that the output curves of **12P/0.3[Cu]/-** display much smaller drain currents than at room temperature, which increase in a highly non-linear fashion at higher drain-source voltages without saturation. These short-channel effects, already visible at room temperature, are even more emphasized at low temperatures. Output curves of **12P/0.3[Cu]/1.3D** (Figure B11, Appendix) show qualitatively similar behavior. Additionally, we can observe that at above 40 K, comparatively high currents are observable even at $V_{DS} = 0$ and non-zero V_{GS} . These leakage currents are consequence of the drop-cast solution spreading to the edges of the OFET substrate.

For comparison with the pulsed ESR measurements, output curves at $V_{GS} = 0$ are most relevant, since we didn't apply any gate voltage during ESR measurements either. The variable temperature output curves at $V_{GS} = 0$ V for both samples can be seen in Figure 5.9. **12P/0.3[Cu]/-** displays only extremely small (< 40 pA at $V_{DS} = -60$ V), linear drain currents which show no systematic dependence on temperature up to 60 K, which could come from charge carrier tunneling currents in the sample or leakage currents inside the measurements setup itself. The non-zero current at $V_{DS} = 0$ V is probably a measurement artifact⁴. In contrast, for the doped film, the drain current is more than an order of magnitude larger and shows an approximately linear dependence on the drain-source voltage for all but the two lowest temperatures measured (7 K and 10 K). These data demonstrate that in the doped films, mobile charge carriers are present at temperatures down to 15 K, even at zero gate-source voltage.

The absence of clear linear and saturation regimes in the output curves, as well as the presence of high leakage currents at higher temperatures, prevents us from reliable evaluation of the effective mobilities in these samples. Similarly, we cannot determine the effective conductivity based on the behavior of the output curves at low V_{DS} . Instead, we chose to determine the differential conductivity σ_{diff} to assess charge-transport mechanisms and their temperature dependence. We define differential conductivity as:

$$\sigma_{\text{diff}} = \left. \frac{\partial I_D}{\partial V_{DS}} \right|_{V_{DS}=V_{\text{ev}}} \quad (5.4)$$

with V_{ev} being the V_{DS} at which the value is evaluated ($V_{\text{ev}} = -60$ V for **12P/0.3[Cu]/-** and $V_{\text{ev}} = -50$ V for **12P/0.3[Cu]/1.3D**). The resulting plot of differential conductivity against temperature can be seen in Figure 5.10a. We can clearly distinguish two con-

⁴The output curves were measured by applying a voltage sweep from +60 V to -60 V with dwell time of only 50 ms. At low temperatures, the capacitance of the device is higher than at higher temperatures due to frozen charge carriers, leading to a residual current due to a slower discharge of the device. This residual current decreases at a higher temperature, which is consistent with this hypothesis.

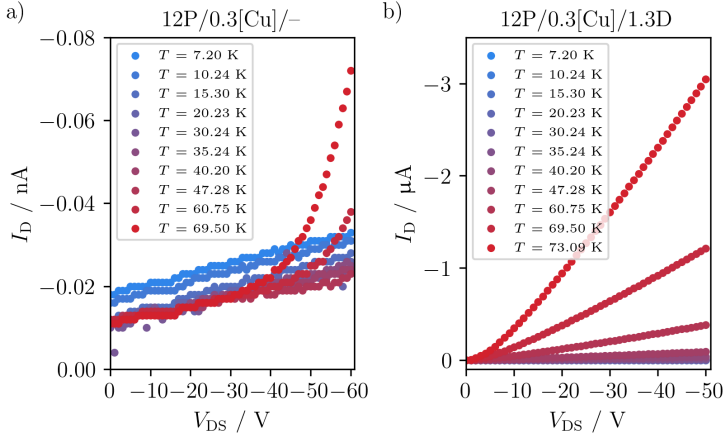


Figure 5.9: Temperature dependence of output curves at $V_{GS} = 0$ of drop-cast a) **12P/0.3[Cu]/-** and b) **12P/0.3[Cu]/1.3D** samples.

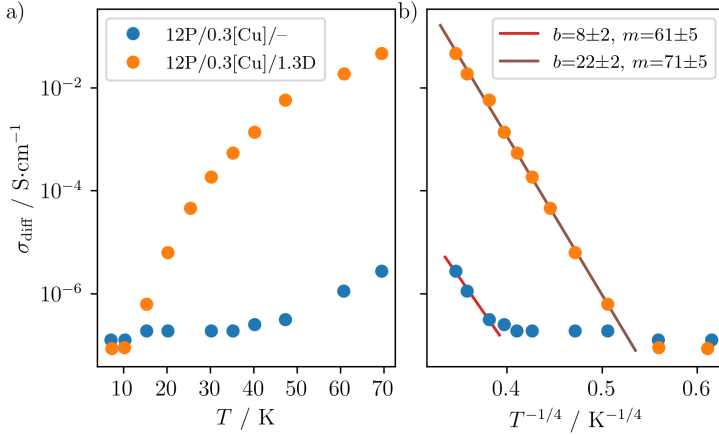


Figure 5.10: a) Differential conductivity of the two materials as a function of temperature. b) The same dataset as in a) plotted against $T^{1/4}$ along with fits to the variable range hopping model, with intercepts (b) and slopes (m) of the fitted lines shown in the legend.

ductivity regimes in both samples. At 7 K and 10 K, both samples are in a temperature independent, tunneling current regime. While the **12P/0.3[Cu]/-** sample remains in this regime up to ≈ 35 K, **12P/0.3[Cu]/1.3D** transitions to a more conductive regime already at 15 K. The undoped sample shows similar behavior at $T > 40$ K. To verify which mechanism is responsible for the observed conductivity, we have plotted differential conductivity data against $T^{-1/4}$ (Figure 5.10b). Indeed, we can now see a clear linear dependence in the high temperature region of both curves. This corresponds to Mott's 3D Variable-Range Hopping (VRH) model, defined as:[135]

$$\ln \sigma_{\text{diff}} = \ln A - \left(\frac{B}{T}\right)^{1/4} = b - m \cdot \frac{1}{T^{1/4}} \quad (5.5)$$

with b and m being the intercept and slope of the line, respectively. As we can see in Figure 5.10, this model does indeed fit the data almost perfectly. Thus, we can conclude that in **12P/0.3[Cu]/-** (**12P/0.3[Cu]/1.3D**), the charge carriers are in a temperature independent tunneling regime up to ≈ 40 K (15 K) above which the current is produced by 3D VRH up to at least 70 K.

5.3.4 Pulsed ESR spectroscopy

To study the effect of charge carriers on the spin dynamics of $\text{Cu}(\text{dbm})_2$, three samples were investigated. A spin-coated **6P/0.94[Cu]/-** sample, which was shown to possess an insufficient number of spins for the full study of the temperature dependence, and drop-cast **12P/0.3[Cu]/-** along with **12P/0.3[Cu]/1.3D** to observe the interaction of interest. Electron Spin Echo (ESE) detected spectra of all three samples recorded on our pulsed Q-band ESR spectrometer can be seen in Figure 5.11. The broad absorption band between ≈ 1.07 T and 1.23 T is a typical feature of a Cu(II) complex with axial symmetry and proves that the integration of our qubits into the P3HT matrix was successful. This part of the spectra can be reproduced by fitting an axial spin Hamiltonian of the form

$$\hat{\mathcal{H}} = \mu_{\text{B}}g\mathbf{B}\hat{\mathbf{S}} + \hat{\mathbf{S}}\mathbf{A}\hat{\mathbf{I}} \quad (5.6)$$

with the symbols as defined in Section 2.3. The obtained fit parameters (Table 5.1) agree with the ones previously obtained for a 0.001% $\text{Cu}(\text{dbm})_2$ doped powder of $\text{Pd}(\text{dbm})_2$ ($[\text{Cu}]_{\text{Pd}}$) quite well [124]. Considering that all of the spectra can be fitted with the same set of parameters which agree with the previously published ones, we can conclude that $\text{Cu}(\text{dbm})_2$ is integrated in the P3HT matrix without any significant structural changes.

At $B_0 = 1.2448$ T, corresponding to $g \approx 2$, we can observe an additional sharp

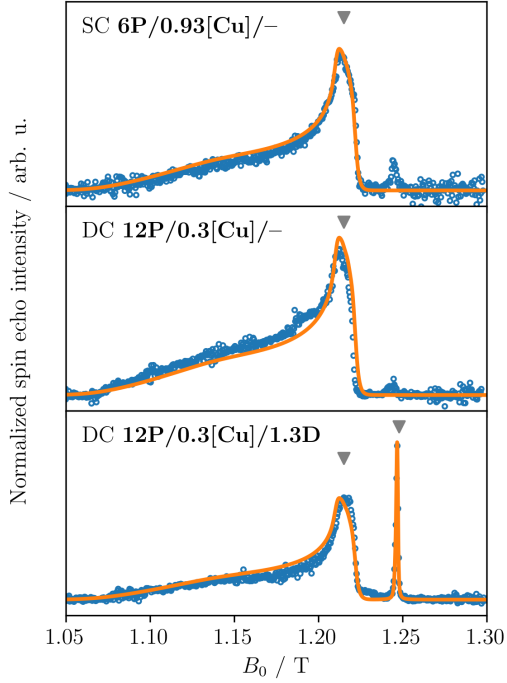


Figure 5.11: ESE detected spectra of a spin-coated **6P/0.9[Cu]/-** (top), drop cast **12P/0.3[Cu]/-** (middle) and **12P/0.3[Cu]/1.3D** (bottom). Data in blue circles, calculation with one set of spin Hamiltonian parameters as orange lines. Triangles indicate field positions at which spin dynamics times were measured, while crossed mark an impurity signal.

Table 5.1: Spin Hamiltonian parameters obtained from fitting of pulsed Q-band ESE spectra of the **12P/0.3[Cu]/1.3D** sample and $\text{Cu}(\text{dbm})_2$ embedded in a diamagnetic analog for comparison.

	g_{\parallel}	g_{\perp}	$A_{\parallel} / \text{MHz}$	A_{\perp} / MHz
$\text{Cu}(\text{dbm})_2$ in P3HT	2.27 ± 0.02	2.056 ± 0.002	550 ± 30	80 ± 10
$\text{Cu}(\text{dbm})_2$ in $\text{Pd}(\text{dbm})_2$ [124]	2.255 ± 0.005	2.050 ± 0.001	570 ± 10	78 ± 10
	g_{iso}	$\Delta B_{\text{pp,Gauss}} / \text{mT}$	$\Delta B_{\text{pp,Lorentz}} / \text{mT}$	
Charge carriers component 1	2.0055 ± 0.002	0.74		0.17
Charge carriers component 2	2.0065 ± 0.002	1.22		0.48

feature. In the undoped films, this corresponds with the unintentional p -doping through ambient oxygen already observed as a threshold voltage shift in room temperature OFET measurements (Section 5.3.1). In the **12P/0.3[Cu]/1.3D** spectrum, this feature is much more prominent and can be seen separately in Figure 5.12. The underlying chemistry of chemical doping tells us that by introducing the F_4TCNQ molecule to the P3HT matrix, an integer charge transfer between the two species creates a positive polaron in the P3HT backbone and a F_4TCNQ radical, both with spin of $\frac{1}{2}$. Since we expect two ESR active species, we will interpret the signal as a convolution of two systems with isotropic g -values, since the signal cannot be satisfactorily reproduced with a single line, either Lorentzian, Gaussian, or pseudo-Voigtian. We can see in Figure 5.12 that the signal can be deconvoluted into two pseudo-Voigtian lines with equal weight, one sharper and one broader. Even though we could analyze the differences in each linewidth contribution, it should be noted that a similarly good fit to the data can be obtained with different distributions of the Gaussian/Lorentzian contributions. The g -values, however, always converge to the indicated values. The lower g value is closer to the value of $g = 2.00395$ reported for the F_4TCNQ radical [100], we attribute it therefore as such. For a more in-depth analysis, a clearer separation between the two species would be necessary. Given the relatively small difference between the two species, frequencies higher than 200 GHz would be needed to deconvolute the signals and analyze them separately⁵. Since we cannot distinguish between the two species in our measurements, we will refer to them jointly as the charge carrier signal.

To probe the spin dynamics in the samples, we have measured the spin-lattice relaxation times and coherence time at the field position marked in Figure 5.11 as a function of temperature. The measured curves and the corresponding fits of the spin-coated

⁵The exact frequency where the two signals will be distinguishable will depend on the linewidth of the individual lines at the high magnetic fields required for such measurements. The linewidths at high fields, in turn, depend on the width of g -value distribution in the sample and the exact Gaussian/Lorentz contributions to the lineshape. More realistically, frequencies higher than 350 GHz or 400 GHz will be needed.

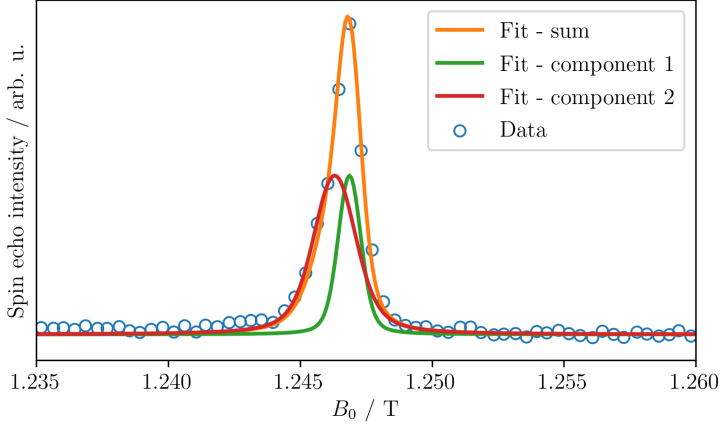


Figure 5.12: Section of the ESE detected spectrum of **12P/0.3[Cu]/1.3D** as blue circles, along with a spin Hamiltonian fit as an orange line. The fit is a linear combination of two systems (green and red lines) with the spin parameters in Table 5.1.

6P/0.9[Cu]/- sample at different temperatures can be seen in Figure B12 in Appendix. As already mentioned in subsection 5.3.2, even with the relatively high concentration of $\text{Cu}(\text{dbm})_2$ in this sample (15.4wt%), there were not enough spins to measure at temperatures higher than 13 K. Additionally, the high concentration led to shortened phase coherence times of only $T_M = 778 \pm 19$ ns, which is an order of magnitude lower than in $[\text{Cu}]_{\text{Pd}}$. Given these shortcomings, we have not investigated this sample any further and focused solely on the drop-cast samples. Spin dynamics measurements of the drop-cast **12P/0.3[Cu]/-** can be found in the Appendix (Figures B13,B14). The spin-lattice relaxation curves were found to be biexponential at low temperatures, similarly to those recorded on $[\text{Cu}]_{\text{Pd}}$. The major, slow component is reported in Table 5.2 and Figure 5.13. At 7 K, the spin-relaxation time was found to be $T_1 = 7.8 \pm 1.0$ ms which is surprisingly high, considering it is almost half of the one reported for $[\text{Cu}]_{\text{Pd}}$ (18.4 ± 0.1 ms). The spin-lattice relaxation time is related to stiffness of the lattice [17], i.e., the available vibrational (phonon) modes [136]. It is therefore surprising that P3HT, with its 'softer' lattice is not more detrimental to the MQB performance. Above 7 K, T_1 rapidly decreases, reaching a value of 0.9 ± 0.1 μs at 40 K. The temperature dependence follows a power law $T_1 \propto T^{-3.8}$, which parallels the behavior of $[\text{Cu}]_{\text{Pd}}$, suggesting that the relaxation mechanism of the Raman kind, which relies on intramolecular, rather lattice vibrations [137]. The Hahn echo decay curves at $T = 7$ K were fitted with a stretched exponential function, resulting

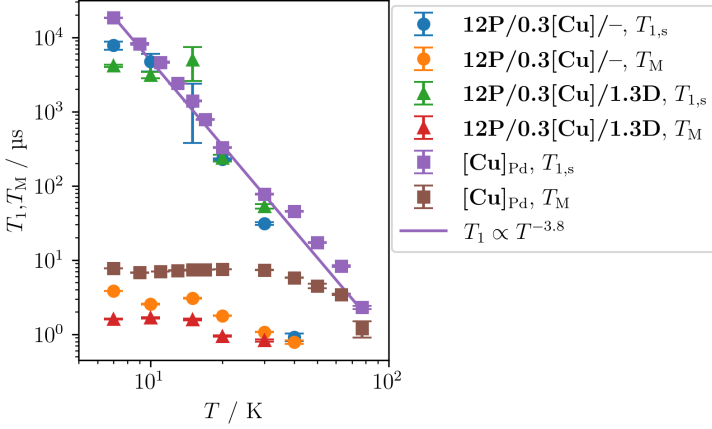


Figure 5.13: Spin relaxation times of the investigated drop cast samples, along with comparison to $[\text{Cu}]_{\text{Pd}}$ from [124]. T_1 times for all samples seem to roughly obey a $T^{-3.8}$ power law up to 30 K, after which the drop cast samples strongly deviate.

in $T_M = 3.84 \pm 0.02 \mu\text{s}$ with a stretch factor $k = 1.51 \pm 0.02$. The phase memory time is roughly half of the one of $[\text{Cu}]_{\text{Pd}}$, which is still rather high considering the three orders of magnitude higher in concentration. A stretched exponential echo decay was observed in that sample as well, however, with a stretch factor of $k = 2.86$.

This suggests that the main source of decoherence is different in the two samples. A stretch factor of 1.5 suggests that at the lowest temperatures, decoherence is caused by physical movement of nuclei in the vicinity of the electron spin, whereas stretch factors larger than 2 are indicative of nuclear spin diffusion as the dominant mechanism. This can be explained by the large number of alkyl chains in the $12\text{P}/0.3[\text{Cu}]/-$ sample, which are able to rotate through tunneling even at liquid helium temperatures (or at least their methyl end groups) [138, p. 68]. At higher temperatures, the Hahn echo decay of $12\text{P}/0.3[\text{Cu}]/-$ becomes monoexponential (indicating multiple relaxation pathways) and the phase memory times decrease rather slowly to $T_M = 0.79 \pm 0.04 \mu\text{s}$ at $T = 40 \text{ K}$. All values are reported in Table 5.2. Finally, we investigated a drop-cast film of $12\text{P}/0.3[\text{Cu}]/1.3\text{D}$, with the measurements shown in the Appendix (Figures B15, B16). Similarly to its undoped counterpart, the spin-lattice relaxation was found to be biexponential and slightly lower at 7 K ($T_1 = 4.15 \pm 0.15 \text{ ms}$). An interesting observation, as this suggests that the incorporation of F_4TCNQ into P3HT matrix modifies the phonon spectrum of the material, which is consistent with reported X-ray scattering studies

Table 5.2: Selected spin dynamics parameters of the drop-cast samples for comparison, along with selected values of $[\text{Cu}]_{\text{Pd}}$ from [124]. Tables with all parameters can be found in the appendix.

12P/0.3[Cu]/-			12P/0.3[Cu]/1.3D	
T	$T_{1,s} / \text{ms}$	$T_M / \mu\text{s}$	$T_{1,s} / \text{ms}$	$T_{M,s} / \mu\text{s}$
7	7.79 ± 0.98	3.84 ± 0.01	4.15 ± 0.14	1.61 ± 0.02
10	4.75 ± 1.26	2.56 ± 0.02	3.12 ± 0.29	1.67 ± 0.02
15	1.38 ± 1.00	3.07 ± 0.02	5.00 ± 2.43	1.59 ± 0.07
20	0.23 ± 0.01	1.78 ± 0.01	0.24 ± 0.03	0.95 ± 0.01
30	0.031 ± 0.001	1.07 ± 0.01	0.053 ± 0.004	0.82 ± 0.01
40	0.0009 ± 0.0001	0.79 ± 0.02	-	-

[Cu] _{Pd}		
T	$T_{1,s} / \text{ms}$	$T_M / \mu\text{s}$
7	18.4 ± 0.1	7.74 ± 0.03
9	8.2 ± 0.2	6.81 ± 0.04
11	4.63 ± 0.07	7.00 ± 0.02
15	1.39 ± 0.02	7.38 ± 0.03
20	0.327 ± 0.004	7.54 ± 0.02
30	0.077 ± 0.001	7.34 ± 0.03
40	0.0456 ± 0.0007	5.78 ± 0.04

showing an 11% swelling of the P3HT lattice upon doping with F_4TCNQ [132]. At higher temperatures, however, the differences between the two samples are essentially washed out, before losing the signal altogether above 30 K. Spin echoes could be measured in this temperature range as well, with the phase coherence times approximately halved compared to the undoped samples (Table 5.2). The Hahn echo decay curves were biexponential in this case, which was previously observed in frozen solutions of $\text{Cu}(\text{dbm})_2$. Biexponential decay is usually attributed to the complex residing in two different types of surroundings.

Since we've established the presence of mobile charge carriers already at 15 K (Section 5.3.3), these measurements demonstrate, for the first time, a measurable quantum coherence of molecular quantum bit in the presence of mobile charge carriers. This is in contrast to a previous report [139], where the inclusion of an MQB in a semiconductor on a molecular level resulted in a severe decrease of quantum coherence. In our study, the two functionalities are provided by two materials, with the conductivity provided by the oxidized P3HT backbone and quantum coherence localized on the [Cu] complex. This results in a lower detrimental influence of the charge carriers on the MQB. When we directly compare the coherence times with the differential conductivities in the samples (Figure 5.14), we can gain some additional insight into the observed behavior. In the undoped sample, we can observe no correlation between the two properties up to 40 K, after which the conductivity starts to increase and we lose the spin echo. With the

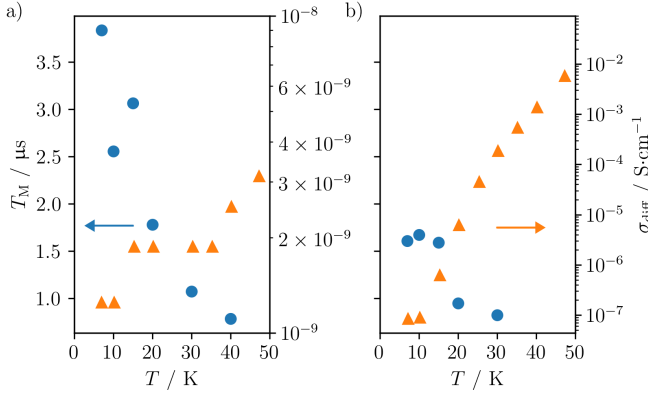


Figure 5.14: Comparison of the coherence times and differential conductivities of a) **12P/0.3[Cu]/-** and b) **12P/0.3[Cu]/1.3D** samples.

limited available data it is not possible to say if these two events are related. In the **12P/0.3[Cu]/1.3D** sample, we can see that a step-like decrease by a factor of two in T_M corresponds with the onset of VRH conductivity. This appearance of conductivity causes an increase in the local fluctuating fields in the material, both electric and magnetic, resulting in faster decoherence of the qubit. Nevertheless, we can clearly observe a temperature region with both conductivity and coherence. It would, therefore, be feasible to investigate the possibility of reading out the spin state of the MQB via electrical transport in the 15 K - 30 K temperature range.

Additionally, we have measured the spin relaxation times of the charge carrier species as well (Figures B17, B18 and Tables B5, B6 in Appendix B). Both its spin-lattice and coherence times were found to be biexponential, similarly to the [Cu] complex. While the T_1 was essentially identical to the one of [Cu] at 7 K and 10 K, at 15 K the relaxation time jumped to a significantly higher value (19.79 ms as compared to 5 ms) and maintained this offset at higher temperatures as well. While additional measurements would be necessary to validate and explain the step-like increase, the continuous decrease above 15 K is consistent with measurements of Schott *et al.* on a different F_4TCNQ doped semiconducting polymer [100], where they report 25 ms around 10 K and 10 ms around 20 K. The T_M time of the charge carrier signal in our measurements was around 1.7 μs at all measured temperatures, in contrast to T_M of the [Cu] complex, which starts with a comparable value but decreases above 15 K. This is again comparable to the measurements of Schott *et al.*, who has measured values around 1 μs at 10 K and 20 K [100].

5.4 Conclusion

The goal of this chapter was to investigate the consequences of mixing a polymeric semiconductor P3HT with a molecular quantum bit $\text{Cu}(\text{dbm})_2$ on their respective properties, as well as the influence of introduction of itinerant charge carriers into the environment of a MQB. We have established, through room temperature FET measurements, that $\text{Cu}(\text{dbm})_2$ only minimally affects the electronic performance of P3HT. We have studied the conductivity of the mixed material, both with and without chemical doping of P3HT through F_4TCNQ , in the temperature range between 7 K and 70 K and observed that in the undoped material, the charge carriers are trapped and move only via tunneling up to 40 K, after which they enter a variable range hopping regime. In the doped material, however, they enter the hopping regime already above 10 K, probably because most of the trap states are already filled by the charge carriers introduced via chemical doping. Finally, we have studied the effects of mixing the two materials, both with and without doping, on $\text{Cu}(\text{dbm})_2$ with pulsed ESR at Q-Band. We have observed that the mixing, doping and preparation methods have little to no effect on the static spin Hamiltonian of $\text{Cu}(\text{dbm})_2$, which was comparable between both various hybrid samples and a powder of $\text{Cu}(\text{dbm})_2$ in $\text{Pd}(\text{dbm})_2$. Additionally, after doping, a two-component signal corresponding to the charge carriers and F_4TCNQ radical has appeared. By studying the spin dynamics of the hybrid materials, we have observed that quantum coherence survives not only the mixing, but the presence of mobile charge carriers as well, since we could observe it at temperatures where variable range hopping of the charge carriers was active (up to 30 K). There is ample scope to further improve the properties of the material, such as to improve the electrical properties by post-processing, and to improve the coherence properties by deuteration. These results pave the way to addressing MQBs by means of electric currents and thus to using hybrid polymer/molecular qubit materials as a novel platform for quantum spintronics. Next steps will include tailoring and optimization of the material, the search for signatures of qubit-charge carrier interaction in transport measurements, and appropriate modeling to understand the interaction mechanism between the qubit and the charge carriers.

6 Appendices

A Appendix to chapter 3

A.1 Influence of Ge doping on formation of Mn_5Ge_3 layers

The samples are designated by their dopant type and the dopant concentration in cm^{-3} , i.e., n-Ge1e18 is an n doped sample with $1 \cdot 10^{18} \text{ cm}^{-3}$ dopants. For n and p doping, Sb and B was used, respectively. The Al(65 nm)/Mn(20 nm)/Ge layer stacks were annealed with 100°C starting temperature, 300°C final temperature and $5^\circ\text{C}\cdot\text{min}^{-1}$ ramp.

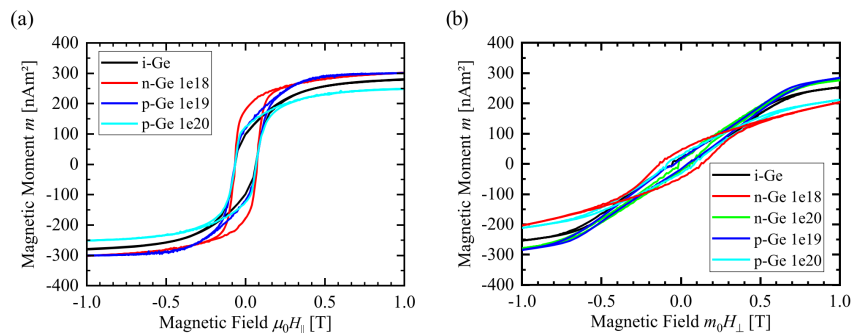


Figure A1: a) In-plane and b) out-of-plane magnetization measurements of samples with different Ge substrate dopings. © IOP Publishing. Reproduced with permission from Ref. [54]. All rights reserved.

B Appendix to chapter 5

B.1 Room temperature electrical characteristics for transistors based on films deposited by spin-coating

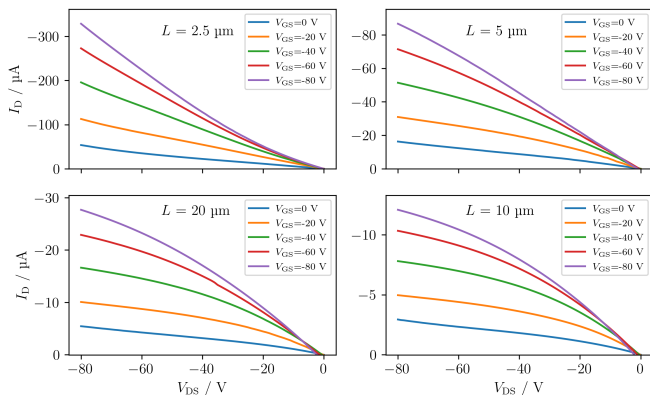


Figure B1: Room temperature output characteristics for transistors based on **12P/-/-** deposited by spin-coating from chlorobenzene. Curves are averages from 2 to 4 transistors.

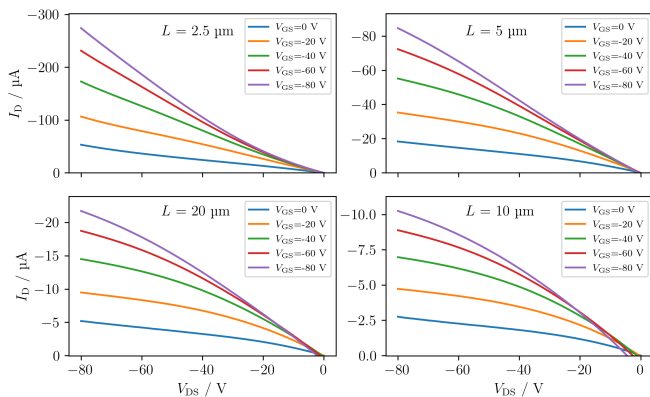


Figure B2: Room temperature output characteristics for transistors based on **12P/0.6[Cu]/-** deposited by spin-coating from chlorobenzene. Curves are averages from 2 to 4 transistors.

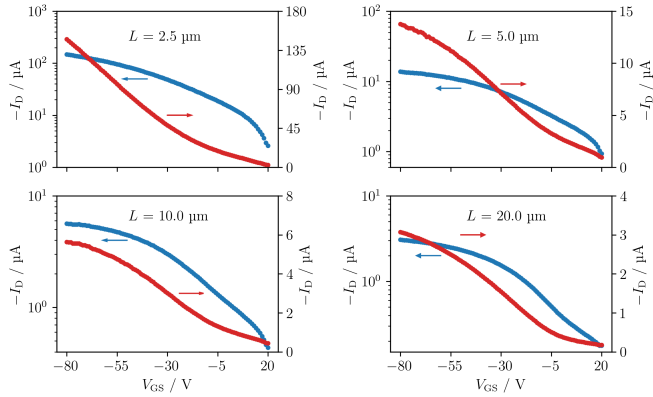


Figure B3: Room temperature transfer characteristics for transistors based on **12P**/ $-/-$ deposited by spin-coating from chlorobenzene measured in the linear regime ($V_{DS} = -10$ V). Curves are averages from 2 to 4 transistors.

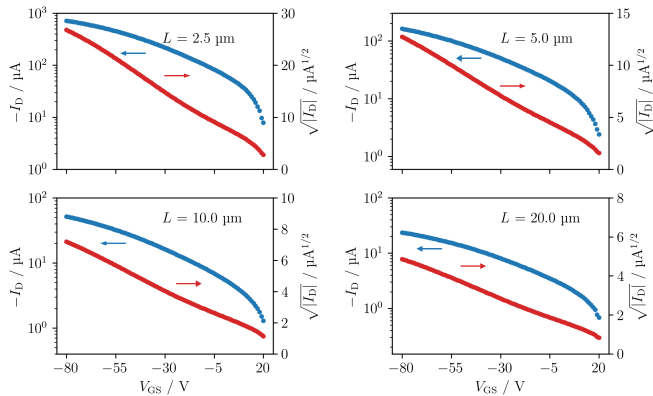


Figure B4: Room temperature transfer characteristics for transistors based on **12P**/ $-/-$ deposited by spin-coating from chlorobenzene measured in the saturation regime ($V_{DS} = -80$ V). Curves are averages from 2 to 4 transistors.

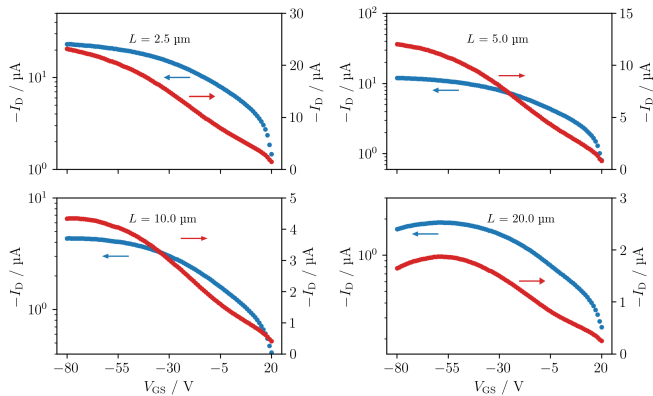


Figure B5: Room temperature transfer characteristics for transistors based on $12\text{P}/0.6[\text{Cu}]$ deposited by spin-coating from chlorobenzene measured in the linear regime ($V_{\text{DS}} = -10\text{ V}$). Curves are averages from 2 to 4 transistors.

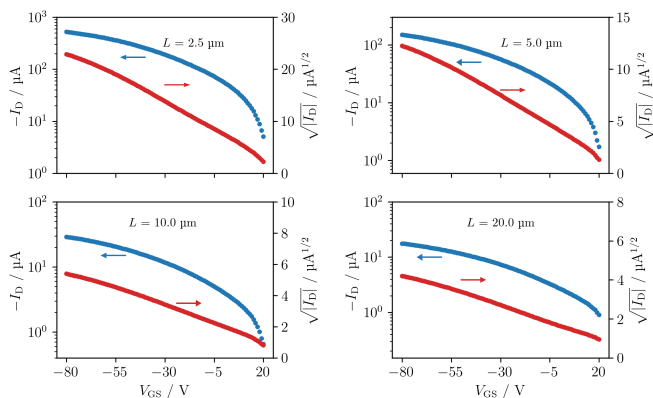


Figure B6: Room temperature transfer characteristics for transistors based on $12\text{P}/0.6[\text{Cu}]$ deposited by spin-coating from chlorobenzene measured in the saturation regime ($V_{\text{DS}} = -80\text{ V}$). Curves are averages from 2 to 4 transistors.

B.2 Room temperature electrical characteristics for transistors based on films deposited by drop-casting

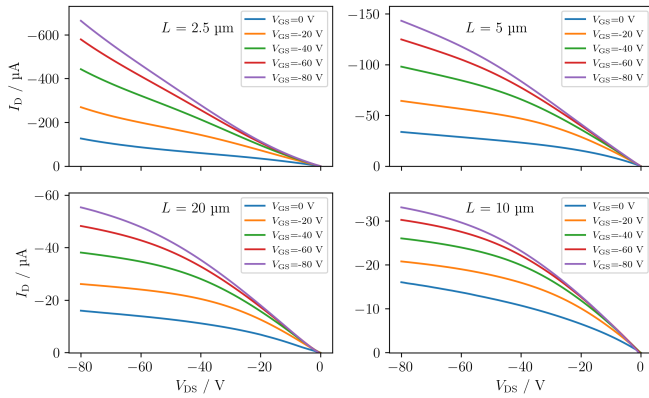


Figure B7: Room temperature output characteristics for transistors based on **12P/0.3[Cu]**-deposited by drop-casting from chlorobenzene.

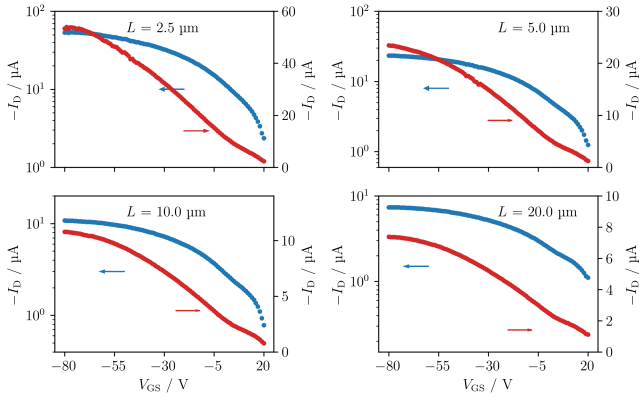


Figure B8: Room temperature transfer characteristics for transistors based on **12P/0.6[Cu]**/– deposited by drop-casting from chlorobenzene measured in the linear regime ($V_{DS} = -10$ V). Curves are averages from 2 to 4 transistors.

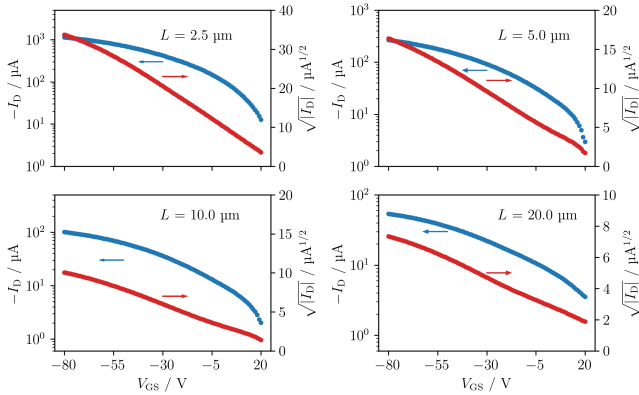


Figure B9: Room temperature transfer characteristics for transistors based on **12P/0.6[Cu]**/– deposited by drop-casting from chlorobenzene measured in the saturation regime ($V_{DS} = -80$ V). Curves are averages from 2 to 4 transistors.

B.3 Variable-temperature electrical characteristics for transistors based on films deposited by drop-casting

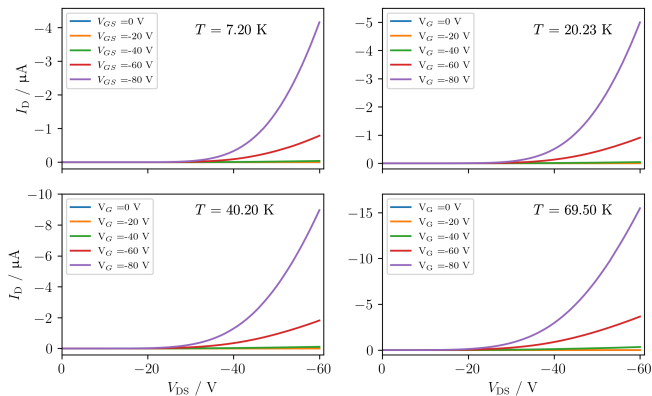


Figure B10: Output characteristics of a transistor based on **12P/0.3[Cu]/-** deposited by drop-casting. The transistor has a channel length of $2.5\ \mu\text{m}$.

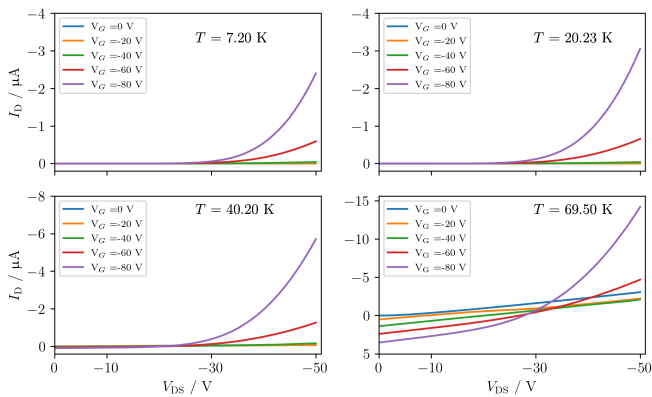


Figure B11: Output characteristics of a transistor based on **12P/0.3[Cu]/1.3D** deposited by drop-casting. The transistor has a channel length of $2.5\ \mu\text{m}$.

B.4 Spin dynamics of hybrid films of P3HT and $[\text{Cu}(\text{dbm})_2]$: $[\text{Cu}(\text{dbm})_2]$ signal

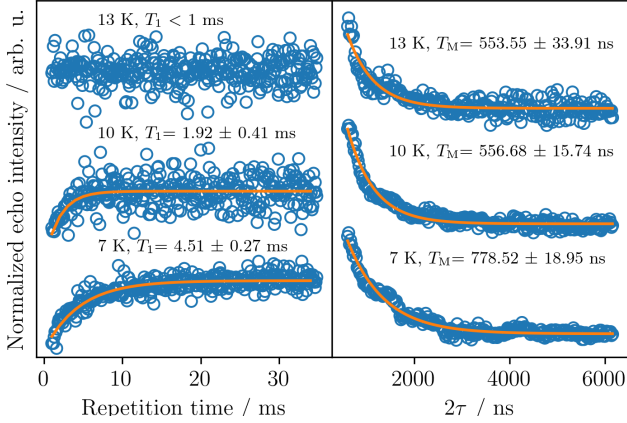


Figure B12: Measurements of T_1 (left) and T_M (right) relaxation times of a spin-coated **6P/0.9[Cu]**/– sample. T_1 and T_M were measured by saturation by fast repetition and Hahn echo pulse sequences, respectively. Data are reported as circles and fits as solid lines.

Table B1: Best-fit parameters of the mono- and biexponential fits of saturation by fast repetition (up to 15 K) and inversion recovery experiments (above 15 K) on a **12P/0.3[Cu]**/– film deposited by drop-casting.

T / K	$A_s \cdot 10^3$ / arb.u.	$T_{1,s}$ / ms	A_f / arb.u.	$T_{1,f}$ / μs
7	-591 ± 84	7.79 ± 0.98	-0.66 ± 0.07	1.69 ± 0.38
10	-492 ± 229	4.75 ± 1.26	-0.89 ± 0.16	1.40 ± 0.47
15	-968 ± 1556	1.38 ± 1.00	-4.24 ± 24.05	0.34 ± 0.86
20	-1.23 ± 0.03	0.23 ± 0.01	-	-
30	-1.2 ± 0.1	0.031 ± 0.001	-	-
40	-1.2 ± 0.1	0.0009 ± 0.0001	-	-

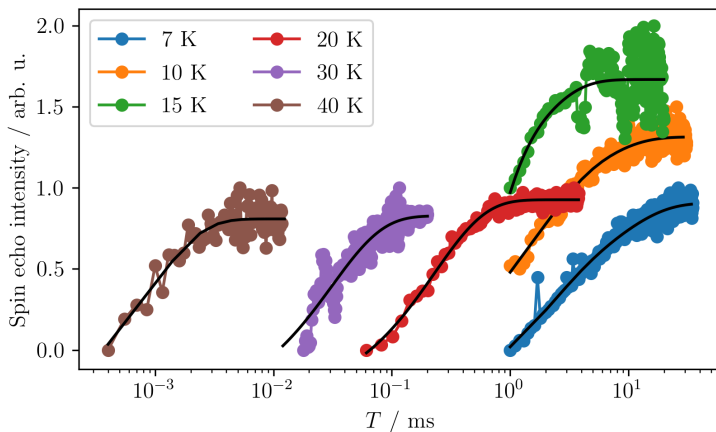


Figure B13: Spin-lattice relaxation time measurements using saturation by fast repetition (up to 15 K) and inversion recovery (above 15 K) on a $12\text{P}/0.3[\text{Cu}]/-$ film deposited by drop-casting. Data are reported as circles and fits as solid lines.

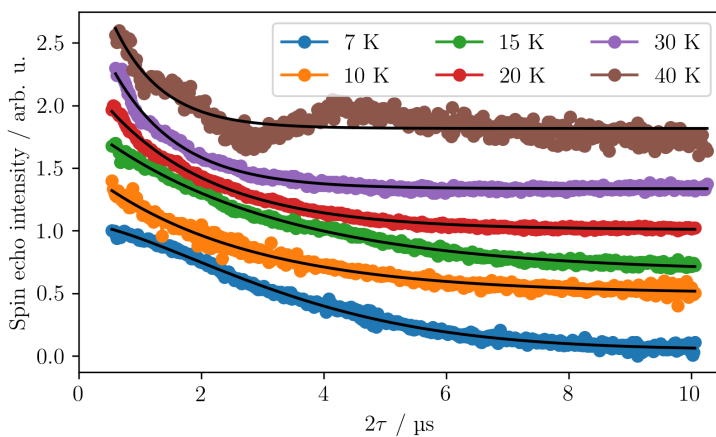


Figure B14: Hahn echo decay curves measured on a $12\text{P}/0.3[\text{Cu}]/-$ film deposited by drop-casting. Data are reported as circles and fits as solid lines.

Table B2: Best-fit parameters of the mono- and stretched exponential fits of Hahn echo decay experiments on a **12P/0.3[Cu]**- film deposited by drop-casting.

T / K	$A / \text{arb.u.}$	$T_m / \mu\text{s}$	k
7	1.01 ± 0.01	3.84 ± 0.02	1.51 ± 0.02
10	1.02 ± 0.01	2.56 ± 0.04	
15	1.21 ± 0.01	3.07 ± 0.03	
20	1.28 ± 0.01	1.78 ± 0.01	
30	1.60 ± 0.02	1.07 ± 0.01	
40	1.71 ± 0.12	0.79 ± 0.04	

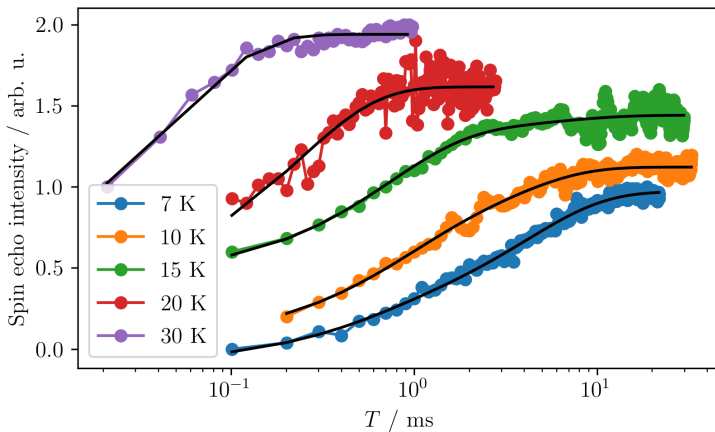


Figure B15: Spin-lattice relaxation time measurements using inversion recovery on a **12P/0.3[Cu]/1.3D** film deposited by drop-casting. Data are reported as circles and fits as solid lines.

Table B3: Best-fit parameters of the mono- and biexponential fits of inversion recovery experiments on a **12P/0.3[Cu]/1.3D** film deposited by drop-casting.

T / K	$A_s / \text{arb.u.}$	$T_{1,s} / \mu\text{s}$	$A_f / \text{arb.u.}$	$T_{1,f} / \mu\text{s}$
7	-0.80 ± 0.02	4.15 ± 0.15	-0.25 ± 0.03	0.47 ± 0.12
10	-0.54 ± 0.07	3.12 ± 0.29	-0.52 ± 0.06	0.69 ± 0.15
15	-0.13 ± 0.06	5.00 ± 2.43	-0.85 ± 0.07	0.71 ± 0.11
20	-1.21 ± 0.12	0.24 ± 0.02	-	-
30	-1.36 ± 0.08	0.053 ± 0.004	-	-

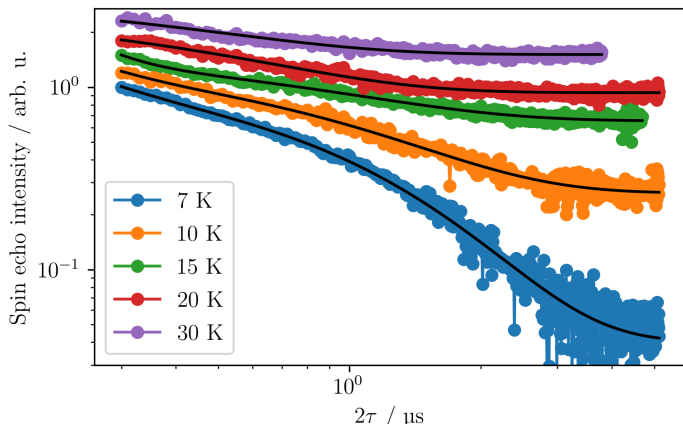


Figure B16: Hahn echo decay curves measured on a **12P/0.3[Cu]/1.3D** film deposited by drop-casting. Data are reported as circles and fits as solid lines.

Table B4: Best-fit parameters of the mono- and biexponential fits of Hahn echo decay experiments on a **12P/0.3[Cu]/1.3D** film deposited by drop-casting.

T / K	$A_s \cdot 10^3 / \text{arb.u.}$	$T_{M,s} / \mu\text{s}$	$A_f \cdot 10^3 / \text{arb.u.}$	$T_{M,f} / \mu\text{s}$
7	1.22 ± 0.02	1.61 ± 0.02	3.95 ± 2.45	0.18 ± 0.03
10	1.17 ± 0.03	1.67 ± 0.04	6.00 ± 6.10	0.16 ± 0.04
15	0.91 ± 0.03	1.59 ± 0.05	21.92 ± 18.78	0.13 ± 0.02
20	1.66 ± 0.03	0.95 ± 0.02	-	-
30	1.64 ± 0.06	0.83 ± 0.03	-	-

B.5 Spin dynamics of hybrid films of P3HT and $[\text{Cu}(\text{dbm})_2]$: Charge carrier signal

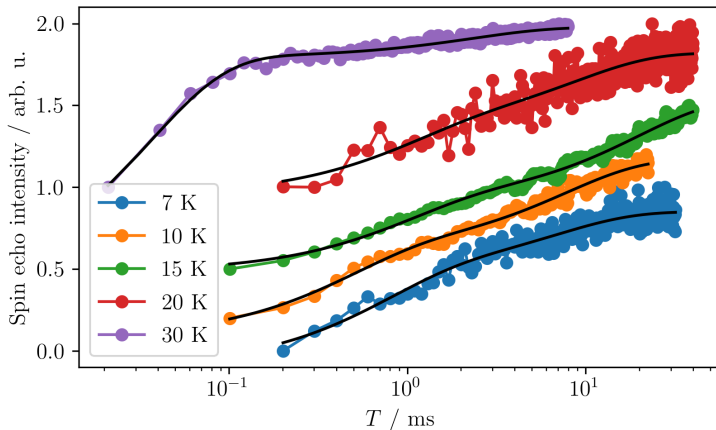


Figure B17: Spin-lattice relaxation time measurements using inversion recovery on the charge carrier signal in **12P/0.3[Cu]/1.3D** film deposited by drop-casting. Data are reported as circles and fits as solid lines.

Table B5: Best-fit parameters of the mono- and biexponential fits of inversion recovery experiments on the charge carrier signal in **12P/0.3[Cu]/1.3D** film deposited by drop-casting.

T / K	$A_s \cdot 10^3 / \text{arb.u.}$	$T_{1,s} / \text{ms}$	$A_f \cdot 10^3 / \text{arb.u.}$	$T_{M,f} / \text{ms}$
7	-0.38 ± 0.03	6.82 ± 0.86	-0.56 ± 0.06	0.71 ± 0.14
10	-0.56 ± 0.01	7.76 ± 0.44	-0.53 ± 0.03	0.45 ± 0.05
15	-0.63 ± 0.01	19.79 ± 0.93	-0.43 ± 0.02	0.94 ± 0.07
20	-0.47 ± 0.04	8.84 ± 1.16	-0.40 ± 0.07	0.95 ± 0.31
30	-185.16 ± 3.38	2.33 ± 0.12	-1397.15 ± 47.04	0.036 ± 0.001

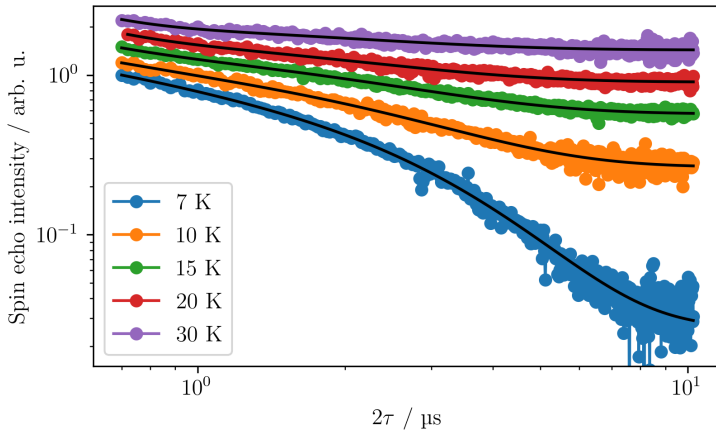


Figure B18: Hahn echo decay curves measured on the charge carrier signal in **12P/0.3[Cu]/1.3D** film deposited by drop-casting. Data are reported as circles and fits as solid lines.

Table B6: Best-fit parameters of the biexponential fits of Hahn echo decay experiments measured on the charge carrier signal in **12P/0.3[Cu]/1.3D** film deposited by drop-casting.

T / K	$A_s \cdot 10^3 / \text{arb.u.}$	$T_{M,s} / \mu\text{s}$	$A_f \cdot 10^3 / \text{arb.u.}$	$T_{M,f} / \mu\text{s}$
7	1.30 ± 0.03	1.67 ± 0.02	1.05 ± 0.32	0.32 ± 0.05
10	1.20 ± 0.04	1.79 ± 0.05	1.65 ± 1.33	0.26 ± 0.08
15	1.12 ± 0.02	1.83 ± 0.03	4.27 ± 2.49	0.21 ± 0.04
20	1.08 ± 0.04	1.69 ± 0.05	9.22 ± 9.13	0.18 ± 0.05
30	0.82 ± 0.07	1.76 ± 0.14	16.34 ± 27.85	0.17 ± 0.07

Bibliography

- [1] A. M. Turing, Proceedings of the London Mathematical Society **s2-42**, 230 (1937).
- [2] M. D. Godfrey and D. F. Hendry, IEEE Annals of the History of Computing **15** (1993).
- [3] NobelPrize.org, *The nobel prize in physics 1956*, Accessed: 01.11.2021, <https://www.nobelprize.org/prizes/physics/1956/summary/>.
- [4] Computer History Museum, *1960: Metal Oxide Semiconductor (MOS) Transistor Demonstrated*, Accessed: 01.11.2021, <https://www.computerhistory.org/siliconengine/metal-oxide-semiconductor-mos-transistor-demonstrated/>.
- [5] G. E. Moore, Electronics **38** (1965).
- [6] G. E. Moore, IEEE Solid-State Circuits Society Newsletter **11**, 36 (2006).
- [7] K. Rupp, *Microprocessor trend data*, Accessed: 01.11.2021, (2019) <https://github.com/karlrupp/microprocessor-trend-data>.
- [8] Wikipedia, *Semiconductor device fabrication*, Accessed: 01.11.2021, https://en.wikipedia.org/wiki/Semiconductor_device_fabrication.
- [9] IEEE Press, *International Roadmap for Devices and Systems: More Moore*, tech. rep. (2020).
- [10] IEEE Press, *International Technology Roadmap for Devices and Systems: Executive Summary*, tech. rep. (2018).
- [11] D. Deutsch, Proceedings of the Royal Society A **400**, 97 (1985).
- [12] P. W. Shor, in Proceedings 35th annual symposium on foundations of computer science (1994), pp. 124–134.
- [13] L. K. Grover, in Proceedings of the Twenty-Eighth Annual ACM Symposium on Theory of Computing (1996), 212–219.
- [14] D. P. DiVincenzo, Fortschritte der Physik **48**, 771 (2000).
- [15] IEEE Press, *International Roadmap for Devices and Systems: Cryogenic Electronics and Quantum Information Processing*, tech. rep. (2020).

- [16] C. J. Yu, M. D. Krzyaniak, M. S. Fataftah, M. R. Wasielewski, and D. E. Freedman, *Chemical Science* **10**, 1702 (2019).
- [17] K. Bader, D. Dengler, S. Lenz, B. Endeward, S.-D. Jiang, P. Neugebauer, and J. van Slageren, *Nature Communications* **5**, 5304 (2014).
- [18] J. M. Zadrozny, J. Niklas, O. G. Poluektov, and D. E. Freedman, *ACS Central Science* **1**, 488 (2015).
- [19] J. S. Uber, M. Estrader, J. Garcia, P. Lloyd-Williams, A. Sadurní, D. Dengler, J. van Slageren, N. F. Chilton, O. Roubeau, S. J. Teat, J. Ribas-Ariño, and G. Aromí, *Chemistry - A European Journal* **23**, 13648 (2017).
- [20] S. L. Bayliss, D. W. Laorenza, P. J. Mintun, B. D. Kovos, D. E. Freedman, and D. D. Awschalom, *Science* **370**, 1309 (2020).
- [21] V. Ranjan, S. Probst, B. Albanese, T. Schenkel, D. Vion, D. Esteve, J. J. L. Morton, and P. Bertet, *Applied Physics Letters* **116**, 184002 (2020).
- [22] A. Bienfait, P. Campagne-Ibarcq, A. H. Küllerich, X. Zhou, S. Probst, J. J. Pla, T. Schenkel, D. Vion, D. Esteve, J. J. L. Morton, K. Moelmer, and P. Bertet, *Phys. Rev. X* **7**, 041011 (2017).
- [23] C. Godfrin, A. Ferhat, R. Ballou, S. Klyatskaya, M. Ruben, W. Wernsdorfer, and F. Balestro, *Physical Review Letters* **119**, 1 (2017).
- [24] R. Vincent, S. Klyatskaya, M. Ruben, W. Wernsdorfer, and F. Balestro, *Nature* **488**, 357 (2012).
- [25] S. Thiele, F. Balestro, R. Ballou, S. Klyatskaya, M. Ruben, and W. Wernsdorfer, *Science* **344**, 1135 (2014).
- [26] D. M. Irber, F. Poggiali, F. Kong, M. Kieschnick, T. Luhmann, D. Kwiatkowski, J. Meijer, J. Du, F. Shi, and F. Reinhard, *Nature Communications* **12**, 532 (2021).
- [27] K. Yang, W. Paul, S. H. Phark, P. Willke, Y. Bae, T. Choi, T. Esat, A. Ardavan, A. J. Heinrich, and C. P. Lutz, *Science* **366**, 509 (2019).
- [28] A. R. Stegner, C. Boehme, H. Huebl, M. Stutzmann, K. Lips, and M. S. Brandt, *Nature Physics* **2**, 835 (2006).
- [29] J. J. Pla, K. Y. Tan, J. P. Dehollain, W. H. Lim, J. J. L. Morton, D. N. Jamieson, A. S. Dzurak, and A. Morello, *Nature* **489**, 541 (2012).
- [30] S. Müllegger, S. Tebi, A. K. Das, W. Schöfberger, F. Faschinger, and R. Koch, *Physical Review Letters* **113**, 133001 (2014).
- [31] N. Kishimoto, K. Morigaki, and K. Murakami, *Journal of the Physical Society of Japan* **50**, 1970 (1981).

- [32] R. Maxwell and A. Honig, *Physical Review Letters* **17**, 188 (1966).
- [33] S. Blundell, *Magnetism in condensed matter* (Oxford University Press, 2001).
- [34] B. Odom, D. Hanneke, B. D’Urso, and G. Gabrielse, *Physical Review Letters* **97**, 6 (2006).
- [35] R. L. Fagaly, *Review of Scientific Instruments* **77**, 101101 (2006).
- [36] M. Buchner, K. Höfler, B. Henne, V. Ney, and A. Ney, *Journal of Applied Physics* **124**, 161101 (2018).
- [37] C. Kittel, *Introduction to solid state physics*, 7th ed. (1996).
- [38] T. Schäpers, *Semiconductor spintronics* (De Gruyter Graduate, 2016).
- [39] F. Rortais, S. Oyarzún, F. Bottegoni, J. C. Rojas-Sánchez, P. Laczkowski, A. Ferrari, C. Vergnaud, C. Ducruet, C. Beigné, N. Reyren, A. Marty, J. P. Attané, L. Vila, S. Gambarelli, J. Widiez, F. Ciccacci, H. Jaffrès, J. M. George, and M. Jamet, *Journal of Physics Condensed Matter* **28**, 165801 (2016).
- [40] E. Y. Tsymlal and I. Zutic, eds., *Spintronics handbook: spin transport and magnetism*, Vol. 2 (CRC Press, 2019).
- [41] J. Fabian, A. Matos-Abiague, C. Ertler, P. Stano, and I. Žutić, *physica acta slovacica* **57**, 565 (2007).
- [42] X. Lou, C. Adelman, S. A. Crooker, E. S. Garlid, J. Zhang, K. S. M. Reddy, S. D. Flexner, C. J. Palmström, and P. A. Crowell, *Nature Physics* **3**, 197 (2007).
- [43] A. Schweiger and G. Jeschke, *Principles of pulse electron paramagnetic resonance* (Oxford University Press, 2001).
- [44] J. A. Weil and J. jR. Bolton, *Electron paramagnetic resonance: elementary theory and practical applications*, 2nd (Wiley, 2007), p. 664.
- [45] S. Stoll and A. Schweiger, *Journal of Magnetic Resonance* **178**, 42 (2006).
- [46] C. Boehme and H. Malissa, “Electrically detected magnetic resonance spectroscopy”, in *eMagRes*, Vol. 6 (John Wiley and Sons, Mar. 2017), pp. 83–100.
- [47] S. M. Sze and K. K. Ng, *Physics of semiconductor devices*, 3rd ed. (John Wiley and Sons, 2007).
- [48] J.-M. Spaeth and H. Overhof, *Point defects in semiconductors and insulators* (Springer-Verlag, 2003).
- [49] C. Boehme and K. Lips, *Applied Physics Letters* **79**, 4363 (2001).
- [50] S. Y. Lee, S. Paik, D. R. McCamey, and C. Boehme, *Physical Review B* **86**, 10.1103/PhysRevB.86.115204 (2012).

- [51] J. Zaumseil and H. Siringhaus, *Chemical Reviews* **107**, 1296 (2007).
- [52] Keithley, *Low Level Measurements Handbook*, 7th ed. (Tektronix, 2013).
- [53] P. H. Sydenham, ed., *Handbook of measurement science* (John Wiley and Sons, 1982).
- [54] S. Bechler, M. Kern, H. S. Funk, G. Colston, I. A. Fischer, D. Weißhaupt, M. Myronov, J. van Slageren, and J. Schulze, *Semiconductor Science and Technology* **33**, 95008 (2018).
- [55] S. Datta and B. Das, *Applied Physics Letters* **56**, 665 (1990).
- [56] S. Sugahara and M. Tanaka, *Applied Physics Letters* **84**, 2307 (2004).
- [57] C. Zeng, S. C. Erwin, L. C. Feldman, A. P. Li, R. Jin, Y. Song, J. R. Thompson, and H. H. Weitering, *Applied Physics Letters* **83**, 5002 (2003).
- [58] M. Gajdzik, C. Sürgers, M. T. Kelemen, and H. von Löhneysen, *Journal of Magnetism and Magnetic Materials* **221**, 248 (2000).
- [59] V. L. Thanh, A. Spiesser, M. T. Dau, S. F. Olive-Mendez, L. A. Michez, and M. Petit, *Advances in Natural Sciences: Nanoscience and Nanotechnology* **4**, 043002 (2013).
- [60] I. A. Fischer, J. Gebauer, E. Rolseth, P. Winkel, L. T. Chang, K. L. Wang, C. Sürgers, and J. Schulze, *Semiconductor Science and Technology* **28**, 125002 (2013).
- [61] T. Nishimura, O. Nakatsuka, S. Akimoto, W. Takeuchi, and S. Zaima, *Microelectronic Engineering* **88**, 605 (2011).
- [62] V. G. Myagkov, V. S. Zhigalov, A. A. Matsynin, L. E. Bykova, Y. L. Mikhlin, G. N. Bondarenko, G. S. Patrin, and G. Y. Yurkin, *Thin Solid Films* **552**, 86 (2014).
- [63] M. Petit, L. Michez, C. E. Dutoit, S. Bertaina, V. O. Dolocan, V. Heresanu, M. Stoffel, and V. L. Thanh, *Thin Solid Films* **589**, 427 (2015).
- [64] O. Abbes, A. Portavoce, V. L. Thanh, C. Girardeaux, and L. Michez, *Applied Physics Letters* **103**, 1 (2013).
- [65] E. Kasper and K. Lyutovich, *Solid-State Electronics* **48**, 1257 (2004).
- [66] S. Bechler, “Spininjektion und Spintransport in Germanium”, PhD thesis (University of Stuttgart, 2020).
- [67] L. A. Michez, A. Spiesser, M. Petit, S. Bertaina, J. F. Jacquot, D. Dufeu, C. Coudreau, M. Jamet, and V. L. Thanh, *Journal of Physics Condensed Matter* **27**, 266001 (2015).

- [68] M. Kern, “Optical setup for torque detected electron spin resonance spectroscopy”, MSc thesis (Brno University of Technology, 2015).
- [69] M. Dörfel, M. Kern, H. Bamberger, P. Neugebauer, K. Bader, R. Marx, A. Cornia, T. Mitra, A. Müller, M. Dressel, L. Bogani, and J. van Slageren, *Magnetochemistry* **2**, 25 (2016).
- [70] I. A. Fischer, L. T. Chang, C. Sürgers, E. Rolseth, S. Reiter, S. Stefanov, S. Chiussi, J. Tang, K. L. Wang, and J. Schulze, *Applied Physics Letters* **105**, 222408 (2014).
- [71] IEEE Press, *International Roadmap for Devices and Systems: Beyond CMOS*, tech. rep. (2018).
- [72] S. P. Dash, S. Sharma, J. C. L. Breton, J. Peiro, H. Jaffrès, J. M. George, A. Lemaître, and R. Jansen, *Physical Review B - Condensed Matter and Materials Physics* **84**, 1 (2011).
- [73] J. C. Hensel, *Phys. Rev. Lett.* **21**, 983 (1968).
- [74] N. A. Skorikov and V. I. Anisimov, *JETP Letters* **107**, 422 (2018).
- [75] D. H. Kim, T.-J. Hwang, K.-S. Ryu, and S.-C. Shin, *Physica Status Solidi (C)* **5**, 405 (2008).
- [76] S. F. O. Méndez, L. A. Michez, A. Spiesser, and V. L. Thanh, *Physica Status Solidi (B)* **252**, 1854 (2015).
- [77] G. A. Lungu, L. E. Stofflea, L. C. Tanase, I. C. Bucur, N. Răduțoiu, F. Vasiliu, I. Mercioniu, V. Kuncser, and C. M. Teodorescu, *Materials* **7**, 106 (2014).
- [78] A. Alvidrez-Lechuga, R. L. Antón, L. E. Fuentes-Cobas, J. T. Holguín-Momaca, Solís-Canto, F. Espinosa-Magaña, and S. F. Olive-Méndez, *Journal of Alloys and Compounds* **762**, 363 (2018).
- [79] Y. Xie, Y. Yuan, M. Wang, C. Xu, R. Hübner, J. Grenzer, Y. J. Zeng, M. Helm, S. Zhou, and S. Prucnal, *Applied Physics Letters* **113**, 1 (2018).
- [80] S. Gregory, *Physical Review Letters* **40**, 723 (1978).
- [81] R. Kalvig, E. Jedryka, P. Aleshkevych, M. Wojcik, W. Bednarski, M. Petit, and L. Michez, *Journal of Physics D: Applied Physics* **50**, 125001 (2017).
- [82] M. Stutzmann, M. S. Brandt, and M. W. Bayerl, *Journal of Non-Crystalline Solids* **266-269 A**, 1 (2000).
- [83] C. Boehme, D. R. McCamey, K. J. van Schooten, W. J. Baker, S. Y. Lee, S. Y. Paik, and J. M. Lupton, *Physica Status Solidi (B)* **246**, 2750 (2009).
- [84] C. Boehme and K. Lips, *Physica Status Solidi (B)* **233**, 427 (2002).

- [85] M. Guéron and I. Solomon, *Physical Review Letters* **15**, 667 (1965).
- [86] T. Hirose, H. Yoshioka, and K. Horai, *Journal of the Physical Society of Japan* **21**, 559 (1966).
- [87] J. Schmidt and I. Solomon, *C. R. Acad. Sci. Paris* **263**, 1016 (1966).
- [88] C. J. Cochrane and P. M. Lenahan, *Journal of Applied Physics* **112**, 123714 (2012).
- [89] G. Joshi, R. Miller, L. Ogden, M. Kavand, S. Jamali, K. Ambal, S. Venkatesh, D. Schurig, H. Malissa, J. M. Lupton, and C. Boehme, *Applied Physics Letters* **109**, 103303 (2016).
- [90] V. Lang, C. C. Lo, R. E. George, S. A. Lyon, J. Bokor, T. Schenkel, A. Ardavan, and J. J. L. Morton, *Review of Scientific Instruments* **82**, 34 (2011).
- [91] W. Akhtar, A. Schnegg, S. Veber, C. Meier, M. Fehr, and K. Lips, *Journal of Magnetic Resonance* **257**, 94 (2015).
- [92] M. Eckardt, J. Behrends, D. Münter, and W. Harneit, *AIP Advances* **5**, 047139 (2015).
- [93] K. Fukuda and N. Asakawa, *Macromolecular Chemistry and Physics* **219**, 1700395 (2018).
- [94] K. Iwamoto, Y. Hayakawa, S. Hatanaka, T. Suzuki, and K. Kanemoto, *The Journal of Physical Chemistry C* **123**, 26116 (2019).
- [95] A. J. Kupijai, K. M. Behringer, F. G. Schaeble, N. E. Galfe, M. Corazza, S. A. Gevorgyan, F. C. Krebs, M. Stutzmann, and M. S. Brandt, *Physical Review B* **92**, 245203 (2015).
- [96] F. Kraffert, R. Steyrlleuthner, C. Meier, R. Bittl, and J. Behrends, *Applied Physics Letters* **107**, 043302 (2015).
- [97] R. T. Henriques, V. Gama, G. Bonfait, I. C. Santos, M. J. Matos, M. Almeida, M. T. Duarte, and L. Alcácer, *Synthetic Metals* **56**, 1846 (1993).
- [98] M. J. Matos, V. Gama, G. Bonfait, and R. T. Henriques, *Synthetic Metals* **56**, 1858 (1993).
- [99] A. Allgaier, “Preparation and investigation of radical doped thin P3HT-films as potential qubit system”, BSc thesis (University of Stuttgart, 2019).
- [100] S. Schott, U. Chopra, V. Lemaury, A. Melnyk, Y. Olivier, R. D. Pietro, I. Romanov, R. L. Carey, X. Jiao, C. Jellett, M. Little, A. Marks, C. R. McNeill, I. McCulloch, E. R. McNellis, D. Andrienko, D. Beljonne, J. Sinova, and H. Sirringhaus, *Nature Physics* **15**, 814 (2019).

- [101] A. Hideo, I. Hiroo, and M. Yoshio, *Nature* **173**, 168–169 (1954).
- [102] V. Gama, R. Henriques, G. Bonfait, L. Pereira, J. C. Waerenborgh, I. Santos, M. T. Duarte, J. Cabral, and M. Almeida, *Inorganic Chemistry* **31**, 2598 (1992).
- [103] M. Almeida and R. T. Henriques, “Perylene based conductors”, in *Handbook of organic conductive molecules and polymers, volume 1*, edited by H. S. Nalwa (John Wiley and Sons, 1997).
- [104] M. J. Matos., M. Almeida., L. Alcacer, and R. T. Henriques, *Synthetic Metals* **86**, 2089 (1997).
- [105] V. Gama, M. Almeida, R. T. Henriques, I. C. Santos, A. Domingos, S. Ravy, and J. P. Pouget, *The Journal of Physical Chemistry* **95**, 4263 (1991).
- [106] J.-P. Pouget, P. Foury-Leylekian, and M. Almeida, *Magnetochemistry* **3**, 13 (2017).
- [107] M. Kern, L. Tesi, D. Neusser, N. Rußegger, M. Winkler, A. Allgaier, Y. M. Gross, S. Bechler, H. S. Funk, L. Chang, J. Schulze, S. Ludwigs, and J. van Slageren, *Advanced Functional Materials* **31**, 2006882 (2021).
- [108] NobelPrize.org, *The nobel prize in chemistry 2000*, Accessed: 01.11.2021, <https://www.nobelprize.org/prizes/chemistry/2000/summary/>.
- [109] V. Dediu, M. Murgia, F. Maticotta, C. Taliani, and S. Barbanera, *Solid State Communications* **122**, 181 (2002).
- [110] Z. H. Xiong, D. Wu, Z. V. Vardeny, and J. Shi, *Nature* **427**, 821 (2004).
- [111] Z. G. Yu, *Physical Review Letters* **111**, 016601 (2013).
- [112] S. J. Wang, D. Venkateshvaran, M. R. Mahani, U. Chopra, E. R. McNellis, R. D. Pietro, S. Schott, A. Wittmann, G. Schweicher, M. Cubukcu, K. Kang, R. Carey, T. J. Wagner, J. N. Siebrecht, D. P. Wong, I. E. Jacobs, R. O. Aboljadayel, A. Ionescu, S. A. Egorov, S. Mueller, O. Zadvorna, P. Skalski, C. Jellett, M. Little, A. Marks, I. McCulloch, J. Wunderlich, J. Sinova, and H. Sirringhaus, *Nature Electronics* **2**, 98 (2019).
- [113] M. Groesbeck, H. Liu, M. Kavand, E. Lafalce, J. Wang, X. Pan, T. H. Tannahwa, H. Popli, H. Malissa, C. Boehme, and Z. V. Vardeny, *Physical Review Letters* **124**, 67702 (2020).
- [114] P. Paoprasert, J. W. Spalenka, D. L. Peterson, R. E. Ruther, R. J. Hamers, P. G. Evans, and P. Gopalan, *Journal of Materials Chemistry* **20**, 2651 (2010).
- [115] H. C. Kolb, M. G. Finn, and K. B. Sharpless, *Angewandte Chemie - International Edition* **40**, 2004 (2001).

- [116] B. Gerlach, “Untersuchung der Spindynamik von Quantenbits in polymeren Matrizen”, BSc thesis (2017).
- [117] N. Rußegger, “Investigations of Molecular Quantum Bits and Conducting Polymer Hybrid Material”, MSc thesis (University of Stuttgart, 2017).
- [118] M. Winkler, “Investigations of Transition Metal Beta-Diketonate Complexes in P3HT Matrices as Potential Qubit Systems”, MSc thesis (University of Stuttgart, 2018).
- [119] D. Neusser, “Dilution of molecular quantum bits in conducting polymer matrices”, Research internship report (University of Stuttgart, 2018).
- [120] A. Tsianaka, “Stability investigations of potential molecular nanomagnet / conducting polymer hybrid materials”, Research internship report (University of Stuttgart, 2018).
- [121] S. Ludwigs, ed., *P3HT revisited – from molecular scale to solar cell devices*, Vol. 265 (Springer Berlin Heidelberg, 2014).
- [122] D. Neusser, C. Malacrida, M. Kern, Y. M. Gross, J. van Slageren, and S. Ludwigs, *Chemistry of Materials* **32**, 6003 (2020).
- [123] V. Vijayakumar, Y. Zhong, V. Untilova, M. Bahri, L. Herrmann, L. Biniak, N. Leclerc, and M. Brinkmann, *Advanced Energy Materials* **9**, 1 (2019).
- [124] S. Lenz, K. Bader, H. Bamberger, and J. van Slageren, *Chemical Communications* **53**, 4477 (2017).
- [125] F. Ciccullo, M. Glaser, M. S. Sättele, S. Lenz, P. Neugebauer, Y. Rechkemmer, J. van Slageren, and M. B. Casu, *Journal of Materials Chemistry C* **6**, 8028 (2018).
- [126] D. Nečas and P. Klapetek, *Central European Journal of Physics* **10**, 181 (2012).
- [127] S. Lenz, B. Kern, M. Schneider, and J. van Slageren, *Chemical Communications* **55**, 7163 (2019).
- [128] I. Tkach, A. Baldansuren, E. Kalabukhova, S. Lukin, A. Sitnikov, A. Tsvir, M. Ischenko, Y. Rosentzweig, and E. Roduner, *Applied Magnetic Resonance* **35**, 95 (2008).
- [129] P. F. Goldsmith, *Quasioptical systems* (IEEE Press, 1998).
- [130] J. R. Rumble, ed., *CRC Handbook of Chemistry and Physics*, 102nd ed. (CRC Press, 2021).
- [131] D. T. Scholes, P. Y. Yee, J. R. Lindemuth, H. Kang, J. Onorato, R. Ghosh, C. K. Luscombe, F. C. Spano, S. H. Tolbert, and B. J. Schwartz, *Advanced Functional Materials* **27**, 1702654 (2017).

- [132] D. T. Scholes, S. A. Hawks, P. Y. Yee, H. Wu, J. R. Lindemuth, S. H. Tolbert, and B. J. Schwartz, *Journal of Physical Chemistry Letters* **6**, 4786 (2015).
- [133] C. C. Chang, C. L. Pai, W. C. Chen, and S. A. Jenekhe, *Thin Solid Films* **479**, 254 (2005).
- [134] K. Tukagoshi, F. Fujimori, T. Minari, T. Miyadera, T. Hamano, and Y. Aoyagi, *Applied Physics Letters* **91**, 113508 (2007).
- [135] N. F. Mott, *Philosophical Magazine* **19**, 835 (1969).
- [136] M. Atzori, L. Tesi, S. Benci, A. Lunghi, R. Righini, A. Taschin, R. Torre, L. Sorace, and R. Sessoli, *Journal of the American Chemical Society* **139**, 4338 (2017).
- [137] L. Tesi, E. Lucaccini, I. Cimatti, M. Perfetti, M. Mannini, M. Atzori, E. Morra, M. Chiesa, A. Caneschi, L. Sorace, and R. Sessoli, *Chemical Science* **7**, 2074 (2016).
- [138] L. J. Berliner, G. R. Eaton, and S. S. Eaton, *Distance Measurements in Biological Systems by EPR*, Vol. 19 (Kluwer Academic Publishers, 2002).
- [139] J. McGuire, H. N. Miras, E. Richards, and S. Sproules, *Chemical Science* **10**, 1483 (2019).

Curriculum Vitae

Personal Data

NAME: Michal Kern

DATE AND PLACE OF BIRTH: 16th February 1991 in Bratislava, Slovakia

Education

2015 - 2021 PhD (Dr. rer. nat.) in Physical Chemistry,
University of Stuttgart, Germany
Supervisor: Prof. Dr. Joris van Slageren

2013 - 2015 Master of Engineering (Ing.) in Physical Engineering
and Nanotechnology, Brno University of Technology, Czech Republic
Thesis: Optical Setup for Torque Detected Electron Spin Resonance
Spectrometer
Graduated with honors.

2014 A 7 month ERASMUS internship at University of Stuttgart, Germany
Experimental work in High Field/High Frequency Electron Paramagnetic
Resonance

2010 - 2013 Bachelor of Science (Bc.) in Physical Engineering and Nanotechnology,
Brno University of Technology, Czech Republic
Thesis: Optimization of a Radiofrequency Atomic Source for Deposition
of GaN.

Awards

- 2021 Best paper award of the International EPR Society
- 2016 Poster prize at the SPP1601 Young researcher workshop, Konstanz
- 2013 Innovation of Interdisciplinary Study Linking Science and Engineering (IMPI) Student Grant - Optimization of a Radiofrequency Dissociation Source
- 2012 IMPI Student Grant - Radiofrequency Source of Atomic Nitrogen

Publications

1. A. Chu, B. Schlecker, M. Kern, J. L. Goodsell, A. Angerhofer and J. Anders, On the modeling of amplitude-sensitive electron spin resonance (ESR) detection using voltage-controlled oscillator (VCO)-based ESR-on-a-chip detectors, *Magnetic Resonance*, 2, 699–713 (2021)
2. A. V. Funes, M. Perfetti, M. Kern, Nadine Rußegger, L. Carella, E. Rentschler, J. van Slageren and P. Alborés, Single Molecule Magnet Features in the Butterfly $[\text{Co}_2^{\text{III}}\text{Ln}_2^{\text{III}}]$ Pivalate Family with Alcohol-Amine Ligands, *European Journal of Inorganic Chemistry*, 31, 3191-3210 (2021)
3. M. A. Hassan, T. Elrifai, A. Sakr, M. Kern, K. Lips and J. Anders, A 14-channel 7 GHz VCO-based EPR-on-a-chip sensor with rapid scan capabilities, *2021 IEEE Sensors*, 1-4 (2021)
4. L. Tesi, D. Bloos, M. Hrtoň, A. Beneš, M. Hentschel, M. Kern, A. Leavesley, R. Hillenbrand, V. Křápek, T. Šíkola and J. van Slageren, Plasmonic Metasurface Resonators to Enhance Terahertz Magnetic Fields for High-Frequency Electron Paramagnetic Resonance, *Small Methods*, 2100376 (2021)
5. D. Weißhaupt, H. S. Funk, M. Kern, M. M. Dettling, D. Schwarz, M. Oehme, C. Suergers, J. van Slageren, I. A. Fischer and J. Schulze, Weak localization and weak antilocalization in doped Ge 1- y Sn y layers with up to 8% Sn, *Journal of Physics: Condensed Matter*, 33, 085703 (2021)
6. M. Kern, L. Tesi, D. Neusser, N. Rußegger, M. Winkler, A. Allgaier, Y. M. Gross, S. Bechler, H. S. Funk, L.-T. Chang, J. Schulze, S. Ludwigs and J. van Slageren, Hybrid Spintronic Materials from Conducting Polymers with Molecular Quantum Bits, *Advanced Functional Materials*, 31, 2006882 (2020)
7. D. Neusser, C. Malacrida, M. Kern, Y. M. Gross, J. van Slageren, and S. Ludwigs, High Conductivities of Disordered P3HT Films by an Electrochemical Doping Strategy, *Chemistry of Materials*, 32, 6003–6013 (2020)
8. S. Liddle, R. Magnall, G. Balazs, E. Lu, M. Kern, J. van Slageren, F. Tuna, A.

- Woolles and M.Scheer, Photolytic and Reductive Activations of 2-Arsaethynolate in a Uranium-Triamidoamine Complex: Decarbonylative Arsenic Group-Transfer Reactions and Trapping of a Highly Bent and Reduced Form, *Chemistry: A European Journal*, 25, 14246 (2019)
9. J. Hrubý, V. T. Santana, D. Kostiuk, M. Bouček, S. Lenz, M. Kern, P. Šiffalovič, J. van Slageren and P. Neugebauer, A graphene-based hybrid material with quantum bits prepared by the double Langmuir–Schaefer method, *RSC Advances*, 9, 24066-2407 (2019)
 10. S. Bechler, M. Kern, H. S. Funk, G. Colston, I. A. Fischer, D. Weißhaupt, M. Myronov, J. van Slageren and J. Schulze, Formation of Mn_5Ge_3 by thermal annealing of evaporated Mn on doped Ge on Si(111), *Semiconductor Science and Technology*, 33, 095008 (2018)
 11. A. Øwre, M. Vinum, M. Kern, J. van Slageren, J. Bendix and M. Perfetti, Chiral, Heterometallic Lanthanide–Transition Metal Complexes by Design, *Inorganics*, 6, 72 (2018)
 12. P. Neugebauer, D. Bloos, R. Marx, P. Lutz, M. Kern, D. A. Aguila, J. Vaverka, O. Laguta, C. Dietrich, R. Clerac and J. van Slageren, Ultra-broadband EPR spectroscopy in field and frequency domains, *Physical Chemistry Chemical Physics*, 20, 15528-15534 (2018)
 13. F. Moro, M. A. Bhuiyan, Z. R. Kudrynskyi, R. Puttock, O. Kazakova, O. Makarovskiy, M. W. Fay, C. Parmenter, Z. D. Kovalyuk, A. J. Fielding, M. Kern, J. van Slageren and A. Patane, Room Temperature Uniaxial Magnetic Anisotropy Induced By Fe-Islands in the InSe Semiconductor Van Der Waals Crystal, *Advanced Science*, 5, 1800257 (2018)
 14. P. Zhang, M. Perfetti, M. Kern, P. P. Hallmen, L. Ungur, S. Lenz, M. R. Ringenberg, W. Frey, H. Stoll, G. Rauhut and J. van Slageren, Exchange Coupling and Single Molecule Magnetism in Redox-active Tetraoxolene-bridged Dilanthanide Complexes, *Chemical Science*, 9, 1221-1230 (2018)
 15. I. Nemeč, R. Herchel, M. Kern, P. Neugebauer, J. van Slageren and Z. Trávníček, Magnetic Anisotropy and Field-induced Slow Relaxation of Magnetization in Tetra-coordinate Co(II) Compound $[Co(CH_3-im)_2Cl_2]$, *Materials*, 10, 249 (2017)
 16. R. Koerner, D. Schwarz, I. A. Fischer, L. Augel, S. Bechler, L. Haenel, M. Kern, M. Oehme, E. Rolseth, B. Schwartz, D. Weisshaupt, W. Zhang and J. Schulze, The Zener-Emitter: A novel superluminescent Ge optical waveguide-amplifier with 4.7 dB gain at 92 mA based on free-carrier modulation by direct Zener tunneling monolithically integrated on Si, *IEEE International Electron Devices Meeting (IEDM)*, San Francisco, CA, pp. 22.5.1-22.5.4 (2016)

17. M. Dörfel, M. Kern, H. Bamberger, P. Neugebauer, K. Bader, R. Marx, A. Cornia, T. Mitra, A. Müller, M. Dressel, L. Bogani and J. van Slageren, Torque-Detected Electron Spin Resonance as a Tool to Investigate Magnetic Anisotropy in Molecular Nanomagnets, *Magnetochemistry*, 2, 25 (2016)